



AG Channel Measurement and Modeling Results for Over-Water and Hilly Terrain Conditions

David W. Matolak and Ruoyu Sun
University of South Carolina, Columbia, South Carolina

NASA STI Program . . . in Profile

Since its founding, NASA has been dedicated to the advancement of aeronautics and space science. The NASA Scientific and Technical Information (STI) Program plays a key part in helping NASA maintain this important role.

The NASA STI Program operates under the auspices of the Agency Chief Information Officer. It collects, organizes, provides for archiving, and disseminates NASA's STI. The NASA STI Program provides access to the NASA Technical Report Server—Registered (NTRS Reg) and NASA Technical Report Server—Public (NTRS) thus providing one of the largest collections of aeronautical and space science STI in the world. Results are published in both non-NASA channels and by NASA in the NASA STI Report Series, which includes the following report types:

- **TECHNICAL PUBLICATION.** Reports of completed research or a major significant phase of research that present the results of NASA programs and include extensive data or theoretical analysis. Includes compilations of significant scientific and technical data and information deemed to be of continuing reference value. NASA counter-part of peer-reviewed formal professional papers, but has less stringent limitations on manuscript length and extent of graphic presentations.
- **TECHNICAL MEMORANDUM.** Scientific and technical findings that are preliminary or of specialized interest, e.g., "quick-release" reports, working papers, and bibliographies that contain minimal annotation. Does not contain extensive analysis.
- **CONTRACTOR REPORT.** Scientific and technical findings by NASA-sponsored contractors and grantees.
- **CONFERENCE PUBLICATION.** Collected papers from scientific and technical conferences, symposia, seminars, or other meetings sponsored or co-sponsored by NASA.
- **SPECIAL PUBLICATION.** Scientific, technical, or historical information from NASA programs, projects, and missions, often concerned with subjects having substantial public interest.
- **TECHNICAL TRANSLATION.** English-language translations of foreign scientific and technical material pertinent to NASA's mission.

For more information about the NASA STI program, see the following:

- Access the NASA STI program home page at <http://www.sti.nasa.gov>
- E-mail your question to help@sti.nasa.gov
- Fax your question to the NASA STI Information Desk at 757-864-6500
- Telephone the NASA STI Information Desk at 757-864-9658
- Write to:
NASA STI Program
Mail Stop 148
NASA Langley Research Center
Hampton, VA 23681-2199



AG Channel Measurement and Modeling Results for Over-Water and Hilly Terrain Conditions

David W. Matolak and Ruoyu Sun
University of South Carolina, Columbia, South Carolina

Prepared under Grant NNX12AR56G

National Aeronautics and
Space Administration

Glenn Research Center
Cleveland, Ohio 44135

Trade names and trademarks are used in this report for identification only. Their usage does not constitute an official endorsement, either expressed or implied, by the National Aeronautics and Space Administration.

Level of Review: This material has been technically reviewed by NASA technical management.

Available from

NASA STI Program
Mail Stop 148
NASA Langley Research Center
Hampton, VA 23681-2199

National Technical Information Service
5285 Port Royal Road
Springfield, VA 22161
703-605-6000

This report is available in electronic form at <http://www.sti.nasa.gov/> and <http://ntrs.nasa.gov/>

AG Channel Measurement and Modeling Results for Over-Water and Hilly Terrain Conditions

David W. Matolak and Ruoyu Sun
University of South Carolina
Columbia, South Carolina 29208

Abstract

This report describes work completed over the past year on our project, entitled “Unmanned Aircraft Systems (UAS) Research: The AG Channel, Robust Waveforms, and Aeronautical Network Simulations.” This project is funded under the NASA project “Unmanned Aircraft Systems (UAS) in the National Airspace System (NAS).” In this report we provide the following: an update on project progress; a description of the over-freshwater and hilly terrain initial results on path loss, delay spread, small-scale fading, and correlations; complete path loss models for the over-water AG channels; analysis for obtaining parameter statistics required for development of accurate wideband AG channel models; and analysis of an atypical AG channel in which the aircraft flies out of the ground site antenna main beam. We have modeled the small-scale fading of these channels with Ricean statistics, and have quantified the behavior of the Ricean K -factor. We also provide some results for correlations of signal components, both intra-band and inter-band. An updated literature review, and a summary that also describes future work, are also included.

1. Introduction

In this report we continue our investigation of the air-ground (AG) channel. Prior reports [1]-[6] reviewed the existing AG channel literature, outlined the plan for flight tests, discussed the channel modeling approach, provided a detailed characterization of our dual-band channel sounder, and reported detailed results for measurements and some model results for the over-sea setting.

The goals of this project are to quantitatively characterize the AG channel in a number of different environments, for contribution to NASA’s work on Unmanned Aircraft Systems (UAS) in the National Airspace System (NAS). The different environments pertain primarily to the type of environment surrounding the ground site (GS) with which the UAS is communicating. For our characterization we have employed measurements in which we have collected data that enables us to estimate the channel’s time varying impulse response. This provides a complete description of the channel, and from this data, we are developing AG channel models for each setting.

The actual measurements collected power delay profiles (PDPs), from which (with associated measured phase information), we can estimate the AG channel impulse response (CIR). From these PDPs and knowledge of other link parameters, we can also determine propagation path loss. We refer the reader to prior reports [1]-[6] for additional background material.

The remainder of this report is organized as follows: in Section 2 we briefly summarize progress made since the last report, and also summarize our data processing procedures. Section 3 describes the over-freshwater measurements. In Section 4 we provide new results for the over-water AG channels, including completed path loss models for both over-sea and over-freshwater conditions, a description of statistical analyses required for obtaining statistical channel characteristics that includes estimation of stationarity distance and correlations, some new over-freshwater channel results, a description of channel characteristics for an over-harbor setting in which the aircraft flew outside the ground site antennas’ main beams, and some initial statistics required for the construction of the wideband AG channel models. Section 5 contains new results for the hilly terrain/suburban environment, and Section 6 contains an update to the literature review. In Section 7 we conclude and discuss planned future work. Several appendices provide supporting detail for the main body of the report.

2. Summary of Project Progress

Since the last report, we have done the following:

- processed the vast majority of the flight test data for the over-freshwater flight tests;
- processed some of the data for the hilly terrain flight tests;
- processed some of the data for the urban setting flight tests;
- conducted a detailed statistical analysis of the over-sea data, which will enable us to use the techniques we have developed for the remaining data sets. This analysis allows us to estimate the AG channel's stationarity distance, which in turn enables computation of correlations among the signals received on the various antennas, computation of small-scale fading statistics, etc.;
- written several papers to publicize our results [7]-[12];
- contributed to a report for the International Civil Aviation Organization (ICAO) working group F [13] (another such contribution is imminent);
- made a presentation to the Radio Technical Commission for Aeronautics (RTCA) Special Committee (SC) 228, apprising them of project progress [14];
- augmented our update to the literature review on UAS and AG channels;
- compiled statistics required for development of detailed statistical wideband tapped-delay line (TDL) models for the over-sea AG channel.

The principal investigator (PI) has also been invited to contribute a paper and give an invited talk at an upcoming conference [15], with another invited talk to occur in April 2015. We are also currently writing a journal paper that will introduce the AG channel characterization project, describe our methods and summarize measurements, and provide complete results for the over-water settings. Additional journal papers are also planned, and will cover results for the remaining GS environments.

At this time, we have largely completed our algorithms for processing the measured flight test data. As noted in prior reports, we have had to account for several non-idealities in the measurements. This includes channel sounder impulse response and noise characteristics, external electronic noise from other aircraft electronics, channel sounder sampling clock drift, and a variable channel sounder PDP output rate (see Appendix D). A few parameters also remain only partially known—primarily the aircraft antenna patterns, which are affected by the airframe itself. Focusing first on the relatively simplest over-water settings has allowed us to develop a thorough and reliable set of algorithms for extracting the actual AG channel characteristics from the measurement data. Figure 1 provides an illustration of the data processing procedure.

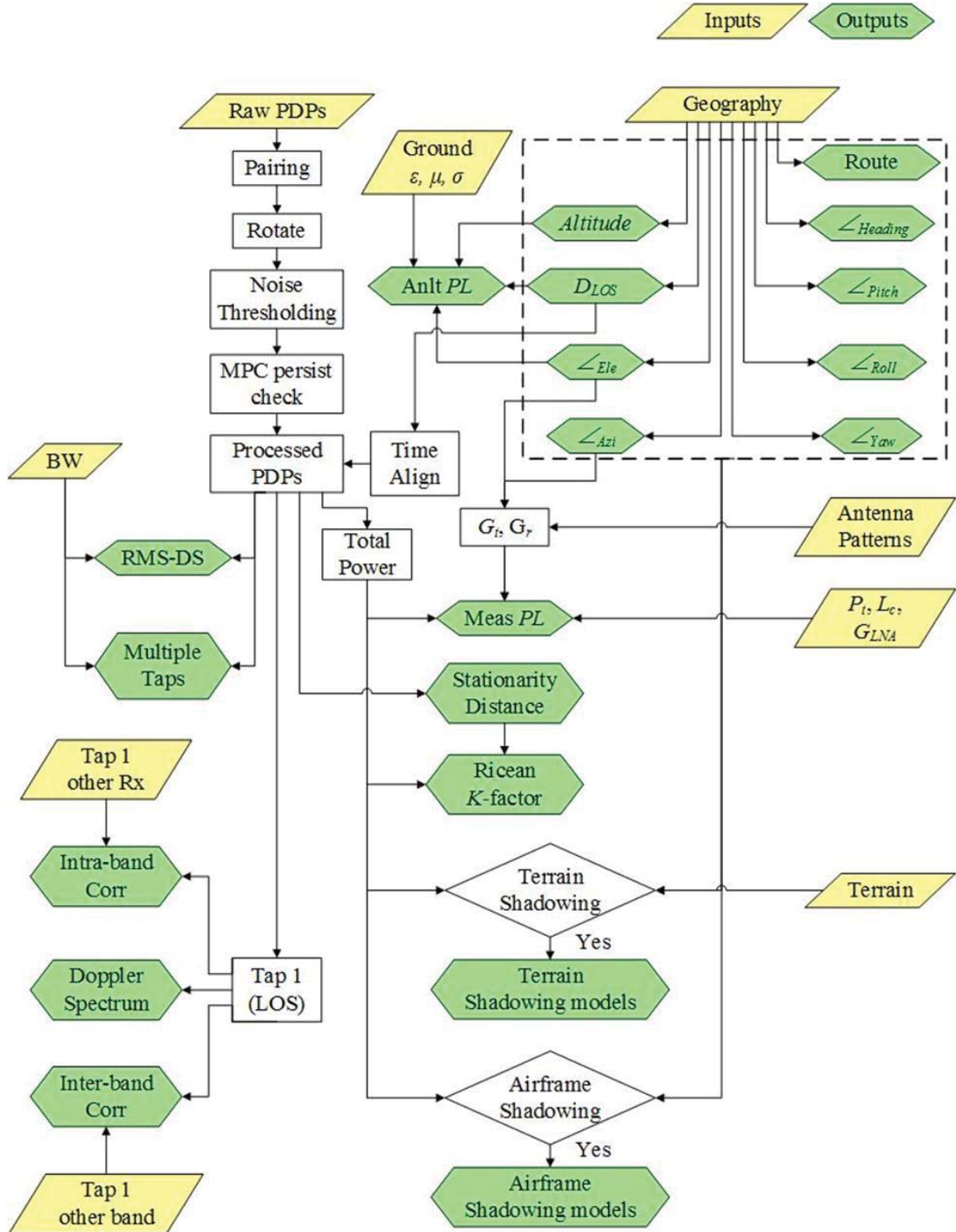


Figure 1. Illustration of data processing procedures.

A corresponding table that describes the status of the flight test data processing appears in Figure 2. As can be observed, the over 315 million PDPs we have recorded provides—to our knowledge—the *largest* set of data ever compiled for analysis of the AG channel.

Index	Location	Date	Terrain	# of Flight Tracks	# of PDPs (Million)	Raw Data Size (GB)	Geometry & Analytical	Pairing & Rotation	Noise Threshold	Persistence Check	Cross Correlation	TDL	SD	K factor	Doppler Shift	Alignment & Results	Total Size (GB)	Backup Date	Note		
1	Cleveland, OH	03/20/13	Suburban	5	12.53	10.6	Status N	P	N	N	N	D	N	N	D	N	10.60	9/19/2014			
							Update Date														
							Size (GB)	--	--	--	--	--	--	--	--	--					
2	Litrope, PA	04/15/13	Hilly	12	26.46	22.8	Status Y	Y	Y	Y	Y	D	P	P	D	Y	50.23	9/19/2014			
							Update Date	9/16/2014	10/19/2013	11/22/2013	11/23/2013	2/23/2014					9/23/2014				
							Size (GB)	1.53E-03	16.90	3.45	3.53	0.16	--	--	--	--	3.39				
3	Oceanside, CA	06/11/13	Over sea & Harbor	12	67.11	26.1	Status Y	Y	Y	Y	Y	D	P	P	D	Y	92/23/2014	101.25	9/19/2014		
							Update Date	9/15/2014	10/17/2013	10/17/2013	11/4/2013	11/15/2013									
							Size (GB)	1.70E-03	33.90	18.50	18.90	0.57	--	--	--	--	3.28				
4	Palmdale, CA	06/12/13	Desert & Hilly	13	52.88	24.0	Status N	Y	Y	Y	Y	D	N	N	D	N	82.85	9/19/2014			
							Update Date	12/4/2013	12/5/2013	12/6/2013	12/5/2013										
							Size (GB)	--	27.30	15.50	15.80	2.49E-01	--	--	--	--	--				
5	Palmdale, CA	06/13/13	Desert & Hilly	13	54.97	18.2	Status N	Y	Y	Y	Y	D	N	N	D	N	55.08	9/19/2014	L-band Rx 2 does not have "DATA FIELDS".		
							Update Date	11/20/2013	11/24/2013	11/24/2013	12/13/2013										
							Size (GB)	--	18.60	8.99	9.18	1.24E-01	--	--	--	--	--				
6	Cleveland, OH	09/05/13	Suburban	6	28.36	10.3	Status N	Y	Y	Y	Y	D	N	N	D	N	40.52	9/19/2014			
							Update Date	11/21/2013	11/23/2013	11/24/2013	12/6/2013										
							Size (GB)	--	13.30	8.32	8.47	1.25E-01	--	--	--	--	--				
7	Telluride, CO	09/12/13	Mountain	12	48.32	22.3	Status N	Y	Y	Y	Y	D	N	N	D	N	76.04	9/19/2014			
							Update Date	11/23/2013	11/23/2013	11/23/2013	11/29/2013										
							Size (GB)	--	24.90	14.20	14.40	0.24	--	--	--	--	--				
8	Cleveland, OH	10/22/13	Over lake & Downtown	6	25.32	11.2	Status Y	Y	Y	Y	Y	D	P	P	D	P	35.74	9/19/2014			
							Update Date	9/15/2014	9/7/2014	9/7/2014	9/7/2014	2/28/2014									
							Size (GB)	8.44E-04	11.00	6.65	6.78	0.11	--	--	--	--	--				
							Total	79	315.95	145.5	4.07E-03	145.90	75.60	77.06	1.58	0.00	0.00	0.00	6.67	452.31	

Figure 2. Summary of flight test data processing to date.

3. Over-Freshwater Measurement Summary

The over-sea measurements were described in detail in [6]. Prior reports also described the channel sounder characteristics in detail, and some detail on portions of the data processing algorithms. Here we describe the over-freshwater measurements.

The over-freshwater flights were conducted on 22 October 2013, over Lake Erie, near Cleveland, OH. The ground site was placed near the lake shore line in Edgewater Park, and as with the over-sea measurements, both straight and oval-shaped flight tracks (FTs) were flown. Figure 3 shows an aerial view of the GS location and a view looking east toward downtown Cleveland.



Figure 3. Views of over-freshwater test area: left, aerial view from south of GS, right, view from aircraft looking eastward.

The GS was located at coordinates latitude 41° 29' 33.8" N, longitude 81 44'5.48" W, with elevation (AMSL) 177.4 m. The GS antennas were 20 m above ground, oriented 352° from geographic north in azimuth, with zero degree elevation angles. The average Lake Erie water level is 174 m AMSL. Figure 4 shows a view from the GS looking east.



Figure 4. View from GS looking eastward.

Over 25 million PDPs were collected over six FTs. Figure 5 shows two example FTs in a Google Maps® view, and in ECEF coordinates. The FT2 was a straight flight path toward the GS with link distance varying from approximately 2.5-29.35 km. The average altitude difference between the GS and aircraft was 566 m (minimum 554 m, maximum 578 m), and the elevation angle ranged from 1.4-13°. The oval-shaped (or, U-shaped) FT4 had link distance ranging from 16.34-21.76 km, average altitude difference 567 m (maximum 578 m, minimum 555 m), with elevation angle from 1.7-2.2°.

Initial results from the over-freshwater measurements appear in Section 4. Detailed FT information and additional results for the other over-freshwater FTs appears in Appendix A.

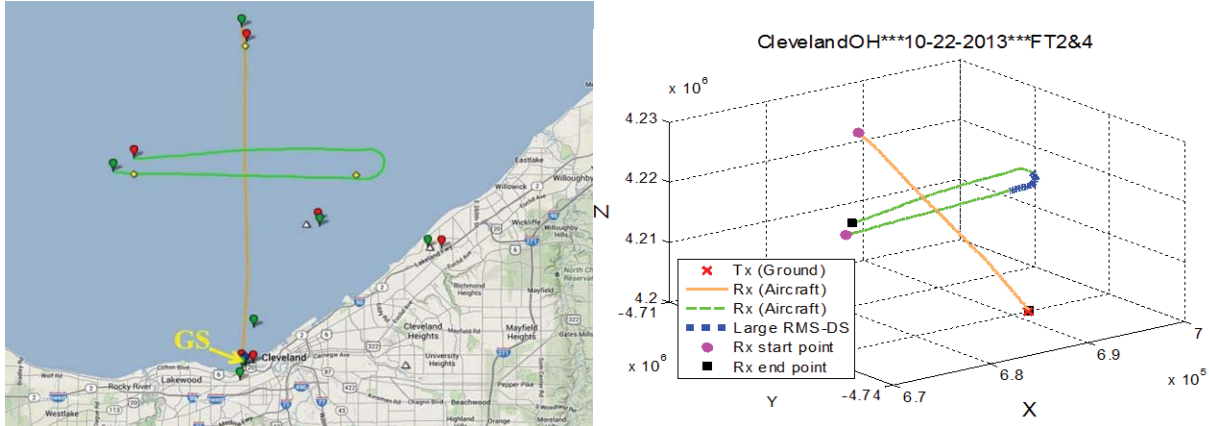


Figure 5. Left: Google Maps® view of FT2 (straight) and FT4 (oval); Right: FTs in ECEF coordinates.

4. Over-Water AG Channel Results

In this section we describe in detail the recent analysis we have done in order to develop models for the over-water AG channels. We provide detailed path loss results for both the over-sea and over-freshwater cases, and some additional preliminary results for the over-freshwater case (with added detail in Appendix A). We also provide results for the atypical condition in which the aircraft was not within the main beams of the GS antennas, but rather in the “backlobe” region (initial results for this case appear in [6]). Although this is not a normal operational condition, it

certainly *can* occur, particularly during early phases of UAS GS deployments, and in any “ad hoc” or anomalous conditions (e.g., when one GS sector has failed). We also provide example statistics that are the next step required for completion of wideband statistical models for the over-sea AG channel.

4.1 Over-Water Path Loss Models

As noted in [6], radio propagation in over-water environments has been studied for many years for communications, radar, and remote sensing applications [16]. In very open coastal ocean and lake settings, obstructions are minimal. We observed no anomalous propagation phenomena during our testing. Specifically, we saw no increased attenuation from hydrometeors or atmospheric gases—effects of hydrometeors (primarily rain) are well known, and can be estimated using established models, with inputs of rain rate and the spatial extent of the rainstorm [17]. Likewise, we saw no enhanced propagation via ducting [18], [19]. Since evaporation ducts are essentially always present over water, when the altitude difference between GS and aircraft is small (difference between transmitter and receiver antenna heights is within tens of meters or less), the effect of these ducts should be taken into account in these conditions. The empirical procedures in [20] can be used for estimating this effect when required.

Numerous example path loss results appear in [6], for both C-band and L-band. From these results, we have determined that the over-water AG channels are best modeled using the curved-earth two-ray (CE2R) model (see [2] for analysis). For short link distances, the simpler flat-earth two-ray model is sufficient. The applicable distance at which one should transition from the flat-earth to the CE2R depends upon frequency and antenna heights, in a rather complicated way. The criterion of when (at what distance) the two model results differ is also somewhat subjective. Nonetheless, one can select some criterion for this and evaluate the transition distance numerically given the carrier frequency and antenna heights. For the antenna heights in our over-sea measurements, the transitions could be set as approximately 2 km for L-band, and approximately 3 km for C-band. Note that because these two-ray models have very rapidly “oscillating” loss values for these short distances, the very need for modeling the transition from flat to curved earth is debatable. In fact, once programmed into a computer for numerical computation, the CE2R is not very computationally-intensive, hence one may use it for all values of distance.

Even though the CE2R model captures the main features of the over-water AG channel, measured results will not follow the analytical model perfectly. Aside from any antenna effects or equipment imperfections, and additional multipath components (which are sparse in the over-water cases) the surface reflection will vary. By this we mean that the sea surface is complex, and temporally (and spatially) varying [21]. Hence the phase—and to a lesser degree the amplitude—of the specular component of the surface reflection can vary because of the changing geometry of the rough sea surface. We do incorporate a simple sea-surface roughness factor into our CE2R model, based upon wind speed, to approximate the effect on the specular reflection’s magnitude, but there is no easy way to model the dynamic effects upon phase. Thus in addition to the deterministic CE2R, we have incorporated random variation to quantify the variation of path loss. Also, since the sea surface is smoother at L-band than at C-band, because the electrical length (relative to wavelength λ) of the sea surface features is smaller at L-band, the CE2R model matches the experimental data better at L-band. Finally on this, for freshwater settings, we expect generally smoother surface conditions, which would enhance the specular reflection, but this is countered in part by the lower conductivity of freshwater compared to that of seawater. Hence the over-freshwater results for path loss are comparable to those for the over-sea case.

The over-sea path loss models for the two bands are composed of two equations (for each band’s model), which apply to different ranges of elevation angle (equivalently, different ranges of link distance). The models for path loss (PL), in units of dB, are as follows:

L-band

$$PL(d, \theta) = \begin{cases} A_{0,L,s} + 10n_{L,s} \log(d) + X_{L,s} + \zeta L_{L,s}, & \theta > \theta_t (d > d_t) \\ CE2R + L_0 + X_{L,\ell} + \zeta L_{L,\ell}, & \theta < \theta_t (d < d_t) \end{cases} \quad (1)$$

where threshold elevation angle $\theta_t = 5$ degrees, $\zeta = -1$ for travel toward the GS and $+1$ for travel away from the GS, $L_{L,s}$ and $L_{L,\ell}$ are small constants, $A_{0,L,s}$ is an intercept value, $n_{L,s}$ is the path loss exponent, distance ranges from $1 \leq d \leq 28$ km for fresh water and $2.2 \leq d \leq 24$ km for sea water. The variable X is a zero-mean Gaussian random variable, with standard deviation σ_X dB, and L_0 is a small offset value. Note that two distinct (both zero-mean) Gaussians pertain to the different segments in (1).

C-band

$$PL(d, \theta) = \begin{cases} A_{0,C,s} + 10n_{C,s} \log(d) + X_{C,s} + \zeta L_{C,s}, & \theta > \theta_t (d > d_t) \\ A_{0,\ell} + 10n_{C,\ell} \log(d) + X_{C,\ell} + \zeta L_{C,\ell}, & \theta < \theta_t (d < d_t) \end{cases} \quad (2)$$

The same parameter definitions in the L-band model apply to the C-band model as well. Model parameters are provided in Tables 1 and 2.

Table 1. L-band path loss parameters for eq. (1) (using CE2R).

Setting	$A_{0,L,s}$ (dB)	$n_{L,s}$	$\sigma_{X,L,s}$ (dB)	$L_{L,s}$ (dB)	L_0 (dB)	$\sigma_{X,L,\ell}$ (dB)	$L_{L,\ell}$ (dB)	d_t (km)
Fresh	57.7	1.4	2.8	1.8	1.1	3.2	1.8	6.6
Sea	50.6	1.5	2.8	1.2	1.0	4.8	1.1	9.1

Table 2. C-band path loss parameters for eq. (2).

Setting	$A_{0,C,s}$ (dB)	$n_{C,s}$	$\sigma_{X,C,s}$ (dB)	$L_{C,s}$ (dB)	$A_{0,\ell}$ (dB)	$n_{C,\ell}$	$\sigma_{X,C,\ell}$ (dB)	$L_{C,\ell}$ (dB)	d_t (km)
Fresh	53.6	1.8	2.6	2.2	53.7	1.8	2.8	1.5	6.6
Sea	60.0	1.6	2.3	1.7	63.9	1.5	2.5	0.5	9.1

We also provide a second model for L-band path loss that uses the log-distance form only (no CE2R), for any who may want a simpler (slightly less accurate) model:

L-band, log-distance

$$PL(d, \theta) = \begin{cases} A_{0,L,s} + 10n_{L,s} \log(d) + X_{L,s} + \zeta L_{L,s}, & \theta > \theta_t (d > d_t) \\ A_{0,\ell} + 10n_{L,\ell} \log(d) + X_{L,\ell} + \zeta L_{L,\ell}, & \theta < \theta_t (d < d_t) \end{cases} \quad (3)$$

with parameters provided in Table 3.

Table 3. L-band path loss parameters for eq. (3) (using log-distance form).

Setting	$A_{0,L,s}$ (dB)	$n_{L,s}$	$\sigma_{X,L,s}$ (dB)	$L_{L,s}$ (dB)	$A_{0,\ell}$ (dB)	$n_{L,\ell}$	$\sigma_{X,L,\ell}$ (dB)	$L_{L,\ell}$ (dB)	d_t (km)
Fresh	57.7	1.4	2.8	1.8	28.6	2.1	3.9	1.8	6.6
Sea	50.6	1.5	2.8	1.2	23.2	2.2	4.6	1.0	9.1

4.2 Stationarity Distance

Aside from intermittent multipath components and variability of the surface reflection, the predominant features of the over-water AG channels are deterministic, and well-approximated by the CE2R model. For more detailed channel characterizations that account for wideband effects such as multipath, and for effects that are difficult to model deterministically (such as airframe shadowing), stochastic approaches are appropriate. Such approaches might also be applied to modeling of the water surface reflection. With a channel that is largely deterministic, stochastic modeling presents something of a conceptual challenge. Yet it is common for communication engineers to employ stochastic models, and their use does increase the realism (accuracy) of the resulting model outputs. Thus we have proceeded to develop statistical models (in addition to that embodied in the path loss models of (1)-(3)) to fully account for the “random” elements in the channel. When employed with the CE2R, this will result in a “mixed” model that has both deterministic and stochastic components.

One of the primary random effects is small-scale fading, attributed mostly to multipath propagation. Physically, in the over-water channels, our intermittent multipath is combined with two-ray effects, which are primarily the phase variation of the surface reflection. Larger scale effects such as airframe shadowing generally vary much more slowly, or equivalently, over larger distances—and these are characterized separately. Small-scale fading is characterized by specifying the distribution of amplitude (sometimes also phase), after removal of large-scale effects such as path loss and shadowing. Small-scale effects must also be considered when evaluating diversity, in our case in both the spatial and temporal domains. Thus we have developed procedures for estimating small-scale fading parameters.

In order to estimate statistical parameters for more detailed channel characterization, it is necessary to determine the region of space over which the channel statistics can be assumed constant¹. We quantify this region as the stationarity distance (SD). (Note strictly that the region should be a volume of space, but for our AG application, the simpler linear distance should suffice.) So-called “rules of thumb” exist for these spatial extents or SDs, but these are based on terrestrial propagation in non-line-of-sight (NLOS) conditions. For example, the rule devised in [22], which yields a stationarity distance of $20\lambda - 40\lambda$, has been extensively used for terrestrial cellular radio channels. Also underlying the derivation in [22] is the assumption of Rayleigh amplitude statistics. Neither the NLOS or Rayleigh conditions apply in our over-water settings, so we should not employ this value of SD in the LOS AG channel.

Before discussing computation of the SD, we briefly describe the channel variation in a two-ray case. Consider the (ideal) two-ray model for a straight flight path. Here, the PDP consists of two components, the LOS, and the surface reflection. Since absolute delay does not affect the shape of the PDP or any statistics of interest, we can fix (shift) the delay of the LOS component to zero. Then for a flight away from the GS, the PDP varies as follows: both the LOS and surface reflection amplitudes decrease with distance ($\sim 1/d$), and the relative delay of the surface reflection also decreases. The opposite variation occurs for a flight toward the GS. This is illustrated in Figure 6.

¹ In general a balance must be struck: it is desirable to have as long a data record as possible in order to obtain reliable statistics, yet the data record should not be long enough to span a period (or distance) over which the statistics change.

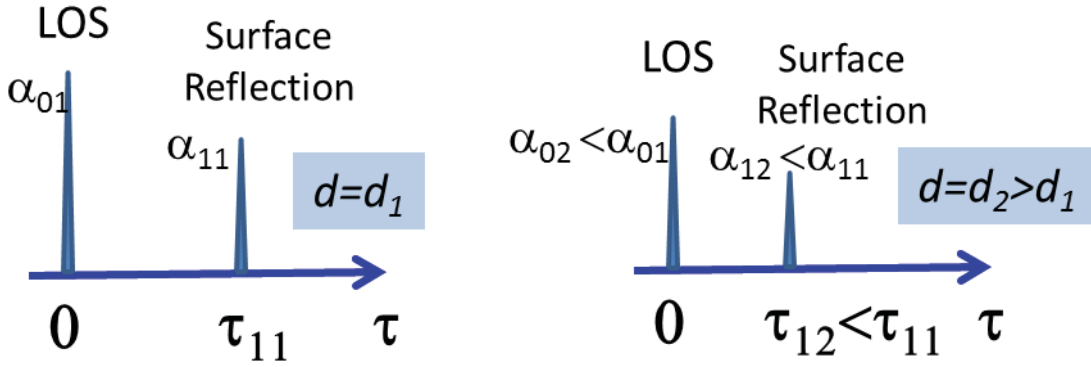


Figure 6. Magnitude of two-ray CIR (or, PDP) for two different distances: left, at time t_1 (distance d_1); right, at time $t_2 > t_1$ (distance $d_2 > d_1$).

Thus in the ideal two-ray case, the PDP is changing *continuously*. Yet for times (or distances) closely separated, the PDP does not change substantially, and in fact changes very slowly as distance increases. As noted though, we do have additional intermittent MPCs that change the PDPs, as well as the change to the surface reflection from ocean surface dynamics, thus the channel will have a quantifiable stationarity distance.

The stationarity distance can be computed in several ways. For our wideband (50 MHz C-band) measurements, we have chosen to use the method in [23], which essentially computes a temporal correlation coefficient for the temporally varying PDP. To begin, the CIR for the i^{th} time instant is given by

$$h(\tau, t_i) = \sum_{k=1}^{L_i} \alpha_{k,i} e^{j\phi_{k,i}} \delta(\tau - \tau_{k,i}) \quad (4)$$

where $\alpha_{k,i}$ represents the k^{th} MPC amplitude at time instant t_i , $\phi_{k,i}$ the k^{th} MPC's phase, and $\tau_{k,i}$ the k^{th} MPC's delay. The i^{th} (instantaneous) PDP is then

$$P(\tau, t_i) = \sum_{k=1}^{L_i} (\alpha_{k,i})^2 \delta(\tau - \tau_{k,i}). \quad (5)$$

The method for computing the PDP temporal correlation coefficient in [23] begins by averaging N PDPs of the form of (5). The averaged PDP is denoted $P_{avg,N}(\tau, t_i)$,

$$P_{avg,N}(\tau, t_i) = \frac{1}{N} \sum_{i=1}^{i+N-1} P(\tau, t_i) \quad (6)$$

with the first PDP in the average the i^{th} . The temporal correlation is easily translated to a spatial correlation via knowledge of platform velocity. The averaging of the instantaneous PDPs is done to smooth somewhat the effects of small scale fading and remove any equipment-related variation, so N should be large enough to do this, without being so large as to include PDPs that are affected by larger scale effects, or PDPs that are—in effect—outside the region of stationarity. Note that this selection involves some assumption regarding the very parameter (stationarity distance) we are trying to estimate! Hence we rely on engineering judgment, including knowledge of our equipment's variation rate, to select N .

From [23], using our average PDP $P_{avg,N}(\tau, t_i)$, we compute a temporal correlation coefficient $c(\Delta t, t_i)$ as follows:

$$c(\Delta t, t_i) = \frac{\int P_{avg,N}(\tau, t_i) P_{avg,N}(\tau, t_i + \Delta t) d\tau}{\max \left\{ \int [P_{avg,N}(\tau, t_i)]^2 d\tau, \int [P_{avg,N}(\tau, t_i + \Delta t)]^2 d\tau \right\}}. \quad (7)$$

This metric quantifies how similar the average PDP at time t_i is to the average PDP at time $t_i+\Delta t$; naturally this is also a function of the starting time t_i (or location, or distance d_i). The denominator of (7) simply normalizes $c(\Delta t, t_i)$ to a maximum value of unity. The coefficient $c(\Delta t, t_i)$ is also not completely equivalent to the usual correlation coefficient definition, since $c(\Delta t, t_i)$ cannot be negative. We compute (7) for a range of Δt , for each value of t_i , and select as the stationarity distance (SD) the value of distance Δx such that $c(\Delta t, t_i)>0.9$, with the translation $\Delta x=v\Delta t$, with v =velocity. The value 0.9 is conservative, i.e., with *very* high probability, the channel is stationary during this time (over this distance). For simplicity we apply these computations to our straight flight tracks.

For the over-sea straight FT1, the aircraft flew straight toward the GS. Average aircraft velocity was 92 m/s, and the PDP update rate was approximately 2900 Hz, for all four receivers. Each receiver recorded more than 670,000 PDPs in this FT. Link distances ranged from 3 to 24.15 km in C-band and from 2.25 to 24.15 km in L-band². Due to periodic variation of our C-band received power, caused by a slow relative drift of the sampling clocks in the Tx and Rx [3], the averaging distance we selected (corresponding to N in (6)) is 200λ .

A selected plot of values of $c(\Delta t, t_i)$ (actually, $c(\Delta x, d_i)$) versus link distance and Δx is shown in Figure 7. The quasi-periodicity one can observe is still under investigation, but at present we are fairly confident that this is also due to the sampling clock drift. The value of Δx in Figure 7 for which $c(\Delta x, d_i)>0.9$ is approximately 6-7 m. To determine an SD we can apply to *all* data in this environment, we collect statistics of $c(\Delta x, d_i)$ over all our data. These statistics appear in Table 4, and Figure 8 shows cumulative distribution functions (cdfs) for SD for FT1. The SD follows a lognormal distribution fairly well. For computation of all channel statistics, the median value of SD is employed: $\sim 250\lambda$ in C-band. This is substantially larger than the 20-40 λ widely used for cellular channels, but this is as expected in this LOS channel. We have also found the 250λ value of SD to hold for the over-freshwater flight tracks.

Note that we did not compute an SD for L-band. This is because the PDP in the over-water channels has multipath components (including the main surface reflection) that are almost always *unresolvable*, hence the coefficient $c(\Delta x, t_i)$ would nearly always be one. Based upon the physical environment, we expect that the SD for L-band (with physically longer wavelength) will not be smaller than the SD for C-band, hence our conservative estimate should apply to the L-band as well. Worth pointing out is that our conservative choice for SD ($c(\Delta x, d_i)>0.9$) is practical in the sense that even if the actual SD is larger than our chosen value, computing statistics over intervals shorter than the true SD still yields valid statistics. Additional results for stationarity distance appear in Appendix B.

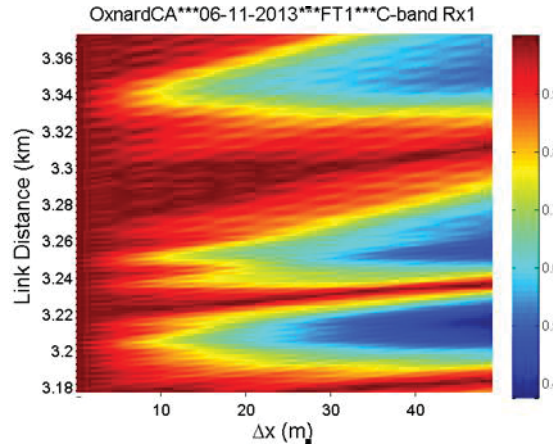


Figure 8. Contour of C-band PDP correlation coefficient $c(\Delta x, d)$ vs. link distance d and Δx for segment of FT1.

² Different minimum link distances result from slightly different GS antenna patterns for the two bands.

Table 4. C-band stationarity distance statistics, over-sea FT1.

		Rx1	Rx2
Lognormal	μ (m)	2.78	2.66
	σ (m)	0.86	0.79
Mean	(m)	23.5	19.0
	(λ 's)	396.6	321.2
Median	(m)	15.2	14.4
	(λ 's)	256.1	242.0
10th percentile	(m)	5.5	5.2
	(λ 's)	92.9	87.3
Min	(m)	0.97	0.91
	(λ s)	16.4	15.4

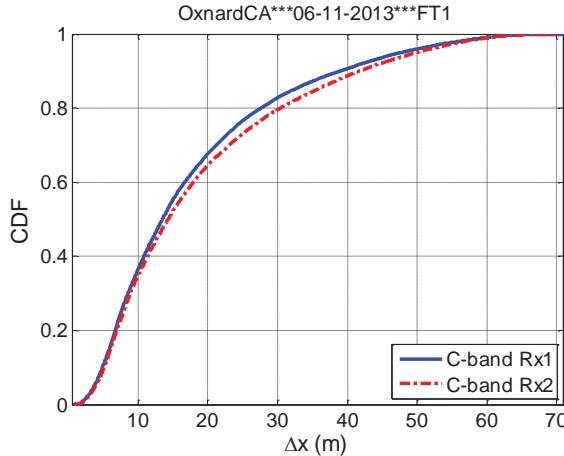


Figure 8. SD CDFs for straight flight track (FT1).

4.3 Correlation Analysis

With our estimate of SD, we can proceed to estimate statistical channel parameters of interest. One of these is the correlation between received signal components. The components in question are in general *all* received signal components, on all four antennas, in both bands. For channels with more multipath components (in addition to the surface reflection), correlations among the MPCs are also of interest. In our over-water channels, we are primarily interested in the correlations of the main (LOS) components, since the vast majority of received power is contained within the LOS components.

In [6] we presented preliminary analysis of the correlations among LOS components for the four antennas for the over-sea case. Specifically, for the correlation between the two C-band antennas, the amplitude correlation is computed by

$$\rho_{A_{C1}, A_{C2}} = \frac{E[(A_{C1} - \mu_{A_{C1}})(A_{C2} - \mu_{A_{C2}})]}{\sigma_{A_{C1}} \sigma_{A_{C2}}} \quad (8)$$

where E denotes expectation, the A 's in the numerator are sample amplitude vectors, and the μ 's are the means of the A vectors. Specifically, $A_{C1} = (A_{C1,1}, A_{C1,2}, \dots, A_{C1,i}, \dots, A_{C1,n})$ is the vector of LOS

amplitude samples for C-band Rx1; analogously, $A_{C2} = (A_{C2,1}, A_{C2,2}, \dots, A_{C2,i}, \dots, A_{C2,n})$ is the vector of Rx2 amplitude samples for its LOS component. Both vectors span only the SD. The σ 's are the standard deviations of the respective sample vectors. Element $A_{Ck,i}$ is the i^{th} amplitude sample (after time alignment, from the i^{th} PDP in a 1 ms delay bin) for Rxm ($m=1$ or 2), and vector length n corresponds to the SD.

In order to gain insight into what we might expect for the cross correlation among signal components of the AG channel, and to check measurement results, we have developed an analysis for the *theoretical* two-ray channel, specifically the CE2R. We apply our analysis to the over freshwater case here. Flight track and measurement details for this case were provided in Section 3, and in this analysis we select parameters close to those of the measurements, e.g., we use an altitude difference of 566.3 m between the GS antenna and aircraft, approximating the value in the over freshwater tests. For the CE2R model, we also require the relative dielectric constant (permittivity) $\varepsilon=81$, and the conductivity $\sigma_{fw}=0.01$ S/m of freshwater (the relative permeability $\mu_r=1$) [24]. Also required for our over-water CE2R is average wind speed, applied to compute the water surface reflection coefficient according to the Miller-Brown surface roughness model [25]. The average wind speed for Lake Erie on 22 October 2013 was 11.16 mph [26]. Finally, the atmospheric refractivity is accounted for via the modified earth radius approach, i.e., the modified earth radius is given by ka , where $k=1/[1+(a/n_0)dn/dh]$, with a the earth radius $a\approx6380$ km, n_0 the index of refraction at the surface level, and dn/dh the refractivity gradient with respect to altitude h . Typically $k=4/3$ is used but one can use a more accurate value if n_0 and dn/dh are available. We used $n_0=1.000315$, and the common exponential form for refractivity gradient $(dn/dh)=315(-0.136)\exp(-0.136h)$, with h in km.

The horizontal distance between aircraft Rx1 and GS is denoted d_{k1} , and for our analysis this ranges from 10-5000 m, with an increment of 0.1 m. The link distance, denoted R_{k1} , ranges from 566.4-5032.1 m, as computed by the CE2R model equations (15)-(20) in [2]. The link distance for Rx2 is $d_{k1}+\Delta d$, where Δd is the relative distance between the two intra-band antennas. Two Δd values of 0.4 m and 1.84 m are used in this analysis, for illustration (actual maximum antenna separation is $\Delta d\sim1.3$ m).

Note that the earth surface reflection is always *unresolvable* at L-band, and is only resolvable within the 20 ns C-band delay resolution for short link distances up to approximately 5 km (analytically of course, we can still compute for both bands for any values of distance). Thus the first five kilometers are of most interest for comparison with measurements. For this analytical flight path, the elevation angle ranges from 89.7 to 6.5 degrees.

We derive the amplitude values required to compute (8) via the CE2R path loss, PL_{CE2R} , used in the following link budget equation,

$$P_r = P_t + G_{PA} + G_{LNA} + G_t + G_r - L_C - PL_{CE2R}, \quad (9)$$

where P_t is 40 dBm (10 Watts), G_{PA} is 7 dB and pertains only to C-band, G_{LNA} is 30 dB in C-band and 15.5 dB in L-band, G_t is 6 dB in C-band and 5 dB in L-band, G_r is 5 dB for both bands, and L_C is 7.5 dB in C-band and 4 dB in L-band. We then obtain the (linear-scale) amplitudes we need for (8) via

$$A = +\sqrt{10^{\frac{Pr}{10}-3}}. \quad (10)$$

Figure 9 shows the analytical CE2R path loss *difference* between the two C-band receivers for the two values of antenna separation Δd . As can clearly be seen, the path loss difference takes its largest values at small link distances, and the antenna separation Δd does affect the magnitude and range of distances where the path loss difference is greater than zero.

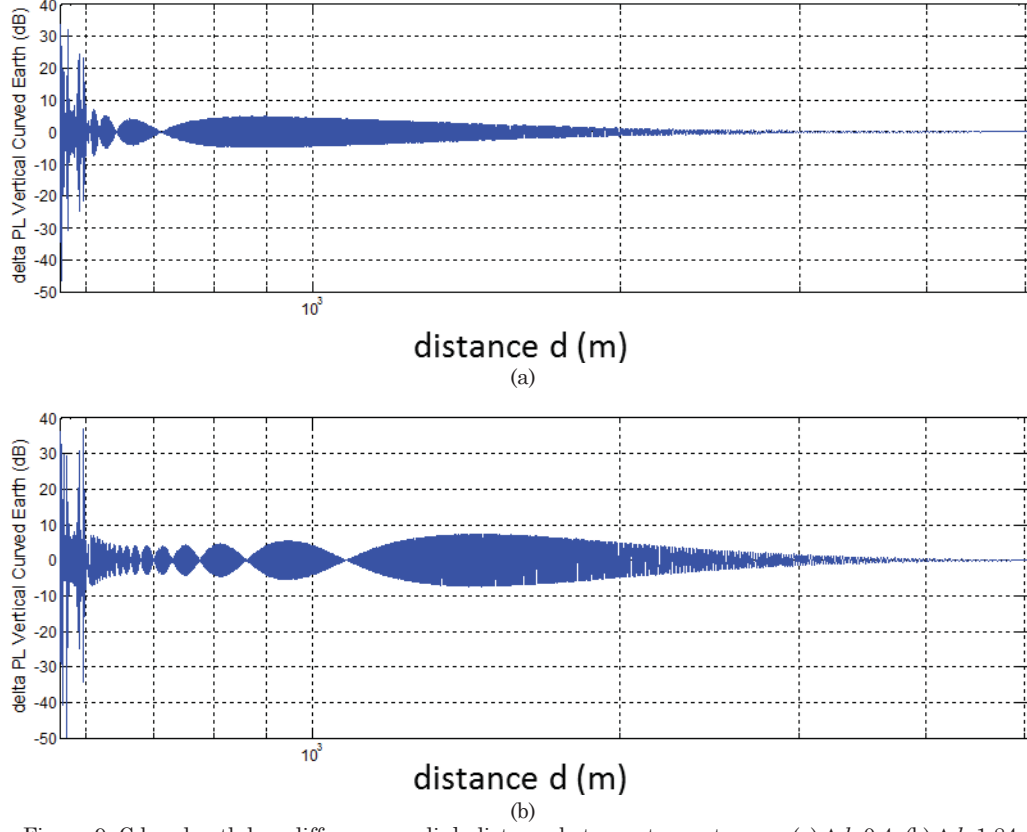


Figure 9. C-band path loss difference vs. link distance between two antennas, (a) $\Delta d=0.4$; (b) $\Delta d=1.84$.

The analytical cross correlation vs. distance for the CE two-ray model is shown in Figures 10 and 11. The correlation is close to one at large values of distance, and varies in an oscillatory fashion between one and negative one at short distances. This oscillation is a direct manifestation of the two-ray effect. Note also that the correlations depend upon the window length, which takes several values in Figures 10 and 11. Detailed behavior also depends somewhat on the distance increment for which the figures are plotted, or the graph's resolution; here this is 0.1 m. Evaluation at smaller distance increments did not change the variation beyond that seen in Figure 12B. For our over water flight velocities and PDP update rates, the SD of 15 m corresponds to $n \sim 144$, thus the results in Figures 10 and 11 for $n=100$ correspond most closely to what we should use to compare with measurements. As shown in Figure 12 (taken from [6]), correlations computed using measured data do exhibit these oscillations, where the negative-valued correlations are seen at values of link distance less than approximately 5 km. Analytical L-band results are similar to those for C-band, since the only things that change are surface reflection coefficients at the different frequency. Thus, our measurement results for correlation are supported by this analysis of the theoretical CE2R channel. Interestingly, even at *large* link distances, the correlation coefficients exhibit periodic variation, and this period increases with link distance. The extent of the variation of the correlation coefficient decreases with vector length: this is illustrated in Figure 12B. Thus when two-ray effects dominate, the intra-band correlation coefficients can be expected to vary significantly over all values of link distance, particularly for small window lengths (or assumed small SDs).

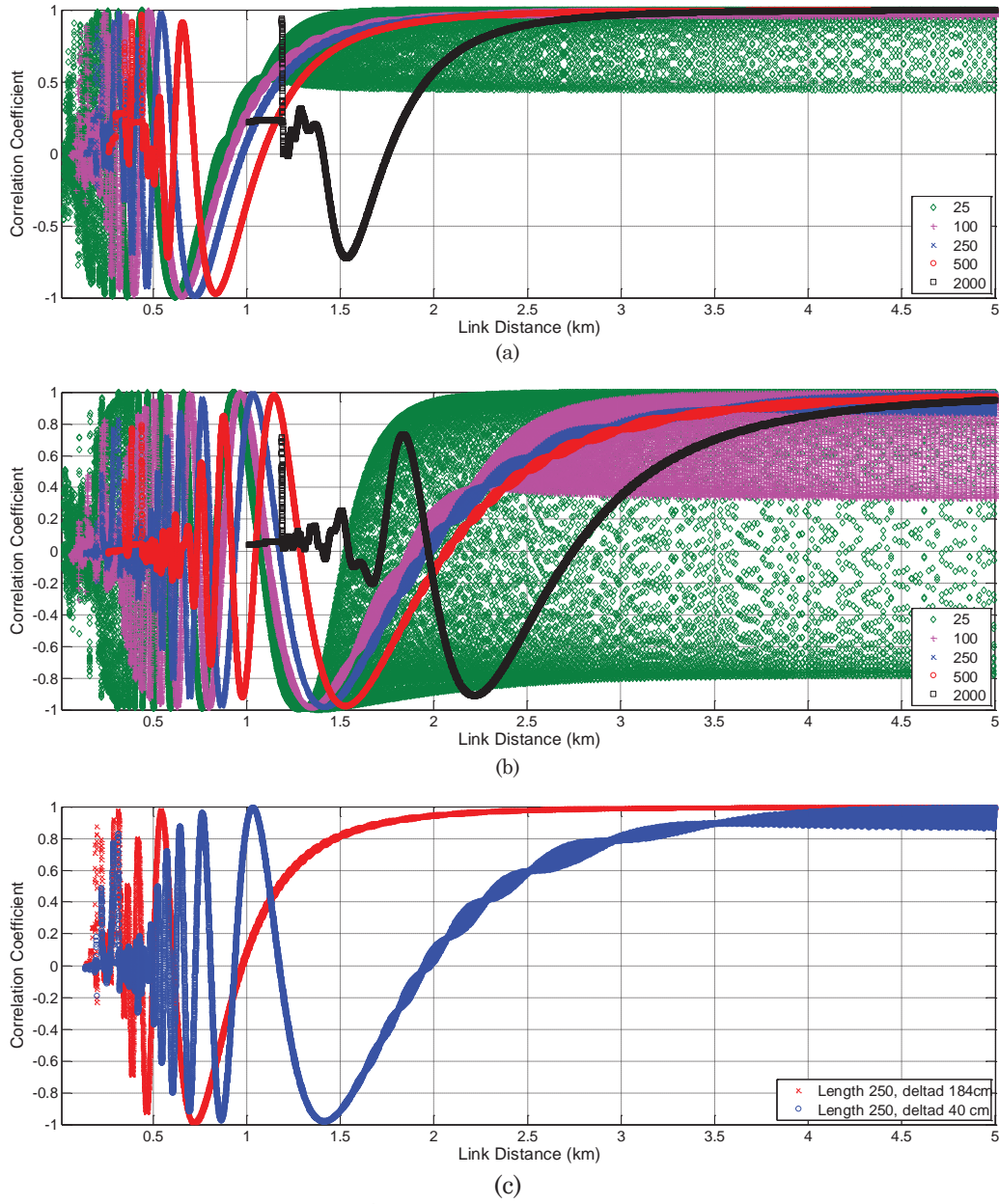


Figure 10. C-band correlation coefficient vs. link distance computed with five vector lengths $n=[25, 100, 250, 500, 2000]$, (a) $\Delta d=0.4$; (b) $\Delta d=1.84$; (c) vector length fixed at $n=250$, comparison between ρ 's for two different Δd 's.

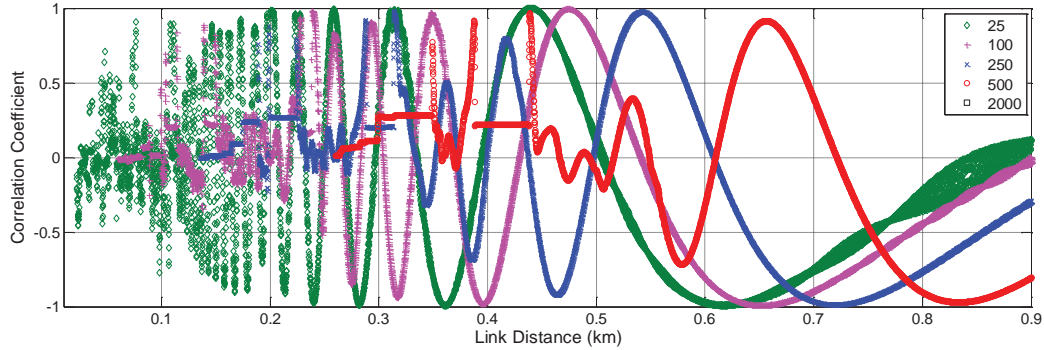


Figure 11. C-band correlation coefficient vs. link distance with five vector lengths $n=[25, 100, 250, 500, 2000]$ (enlarged version of Figure 10(a)), $\Delta d=0.4$.

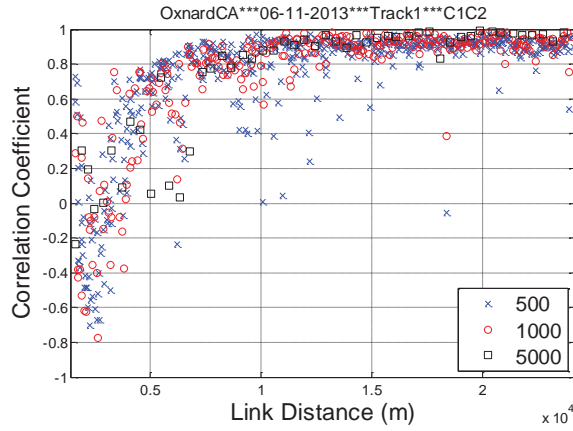


Figure 12. Measured amplitude correlation coefficient between C-band Rx1 and 2 for over-sea FT1, for three different vector lengths, $n=[500, 1000, 5000]$; (Figure 10(a) from [6]).

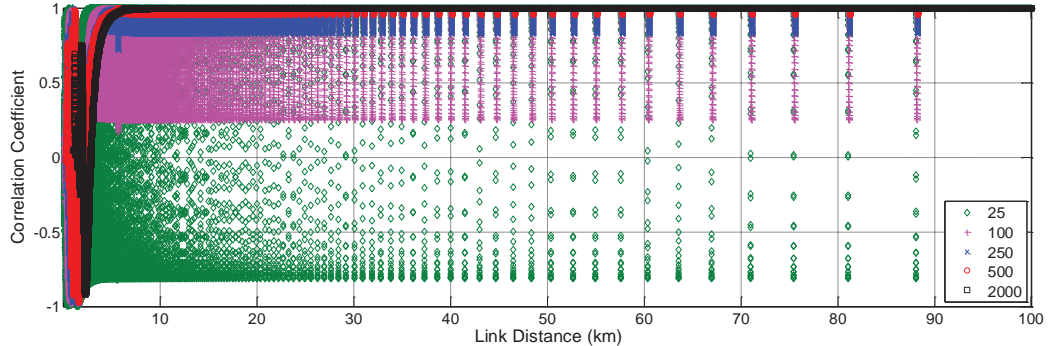


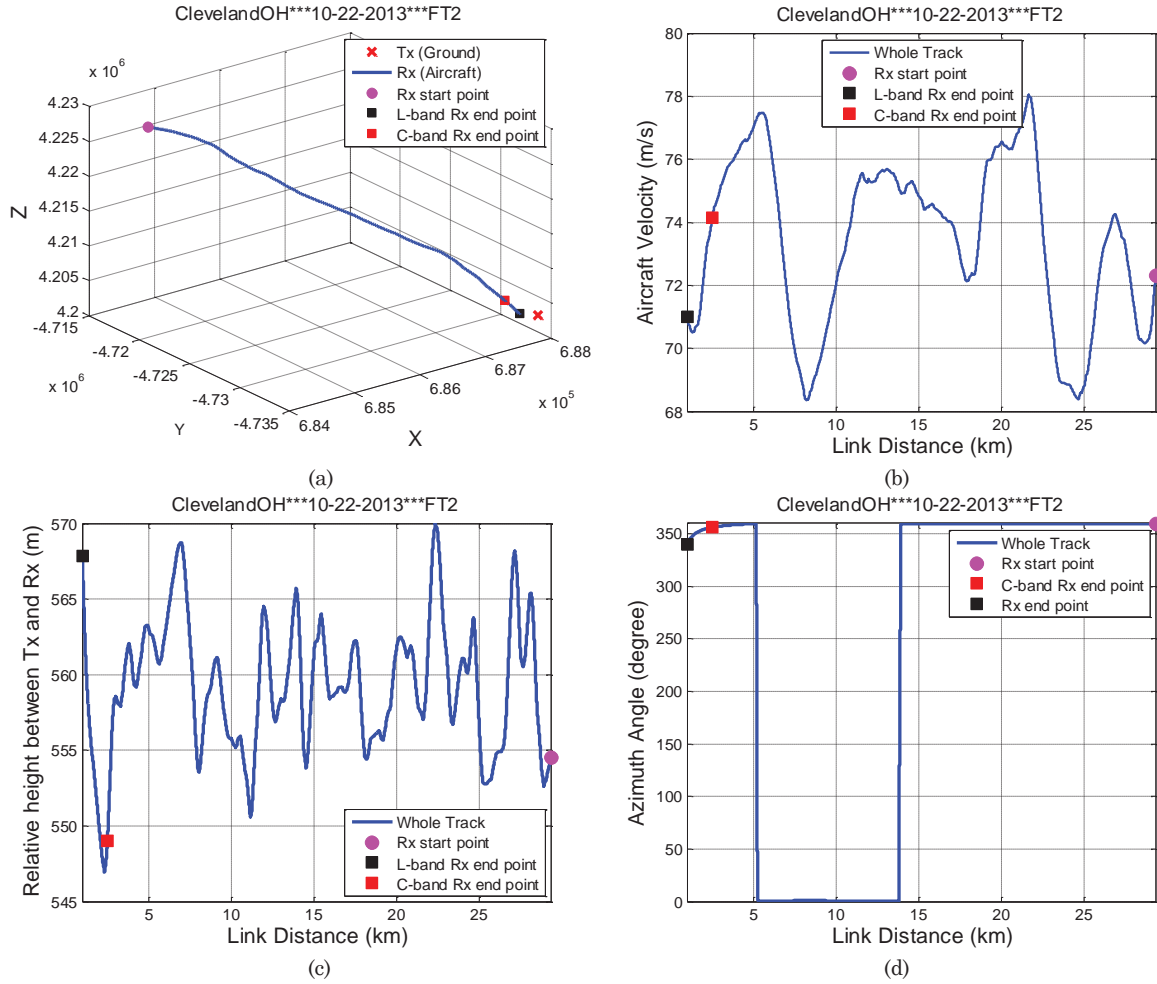
Figure 12B. Analytical CE2R C-band correlation coefficients vs. link distance with antenna separation 2 m, and five vector lengths $n=[25, 100, 250, 500, 2000]$.

4.4 Preliminary Over-Freshwater Results

For the over-freshwater flight tests, measurements were described in Section 3, and final path loss models were described in Section 4.1. Here we provide some analysis of preliminary results, specifically for one flight track: FT2. Results for other FTs appear in Appendix A. Although we do have final path loss models ((1)-(3)) for the over-freshwater setting, we term the results here “preliminary” because we do not yet have complete wideband models for the tapped-delay line over-freshwater setting, nor have we completed all computations of correlations. We also do not have a

final implementation of the Ricean K -factor that varies with link distance d (although we do have the functional forms for $K(d)$ —see subsequent discussion in this section and results in Appendix A).

Figure 13 shows geometric traces for multiple flight parameters for the over-freshwater FT2. This includes the flight path in ECEF coordinates, flight velocity, altitude difference between Tx and Rx, azimuth angle from GS to aircraft, elevation angle from GS to aircraft, aircraft heading (relative to geographic north), and aircraft pitch and roll angles. The latter two parameters are of use in deducing airframe shadowing events.



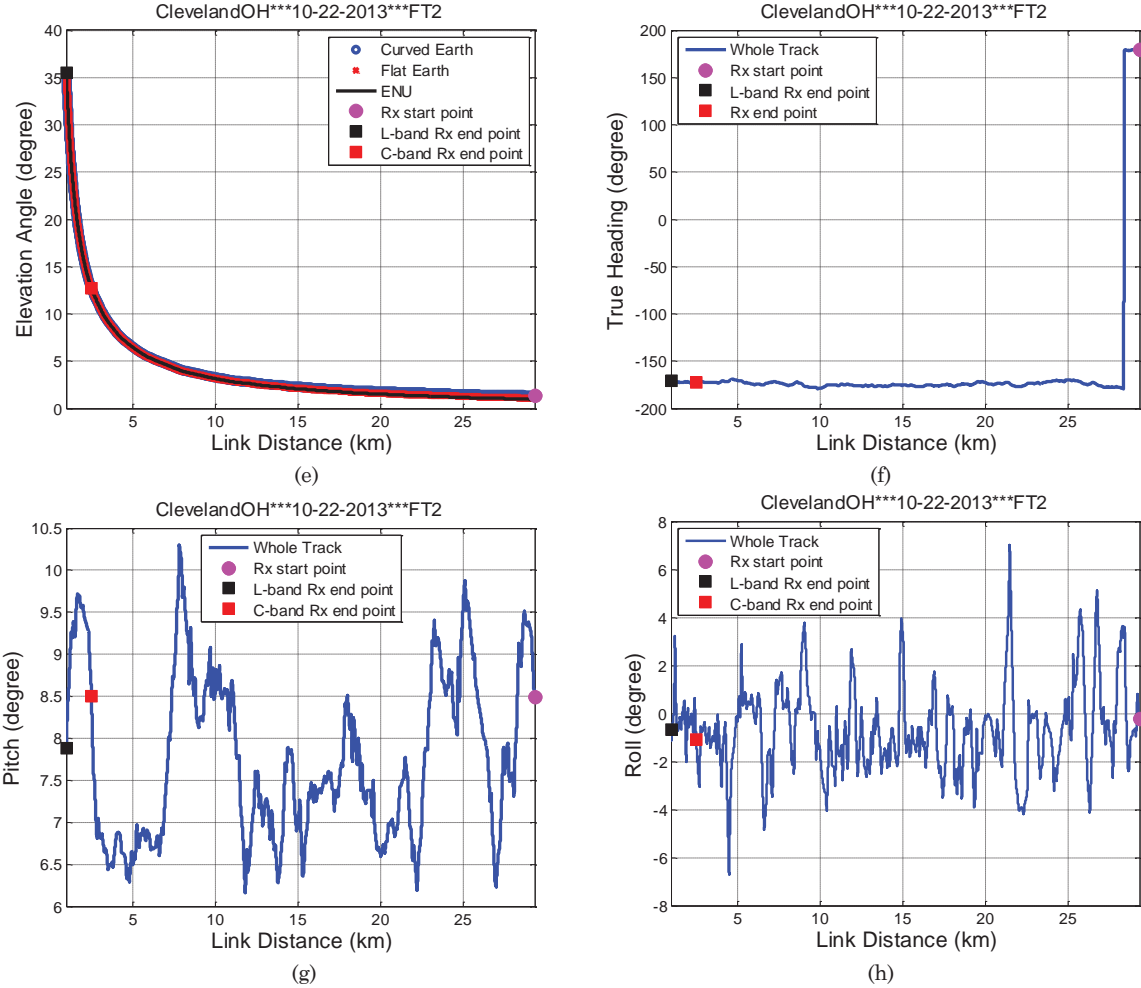


Figure 13. Geometric traces for FT2: (a) flight track in ECEF coordinates; (b) aircraft velocity; (c) altitude difference between aircraft and ground station; (d) azimuth angle; (e) elevation angle; (f) heading of aircraft; (g) pitch angle of aircraft; (h) roll angle of aircraft.

Path loss vs. distance for all four receivers is shown in Figure 14. As with the over-sea case, path loss generally follows the free space path loss line, with variation due to two-ray effects, and increased attenuation at short link distances ($\sim < 5$ km) due to aircraft antenna effects. Just as seen for the over-sea results, in the freshwater case the CE2R model is also better for L-band than for C-band, due to the larger reflection coefficient and the relatively smoother water surface at L-band. Linear fit path loss model lines for this specific FT are also shown in the figure. Note that the path loss models reported in Section 4.1 pertain to the *overall* over-freshwater case, or in other words, the path loss models of (1)-(3) are aggregate models, whereas results here, and those reported in Appendix A, are “per-FT” models. The aggregate models of (1)-(3) are recommended for general use. The “per-FT” models are provided to illustrate some of the variation seen among the various FTs. Table 5 provides the “per-FT2” path loss model parameters.

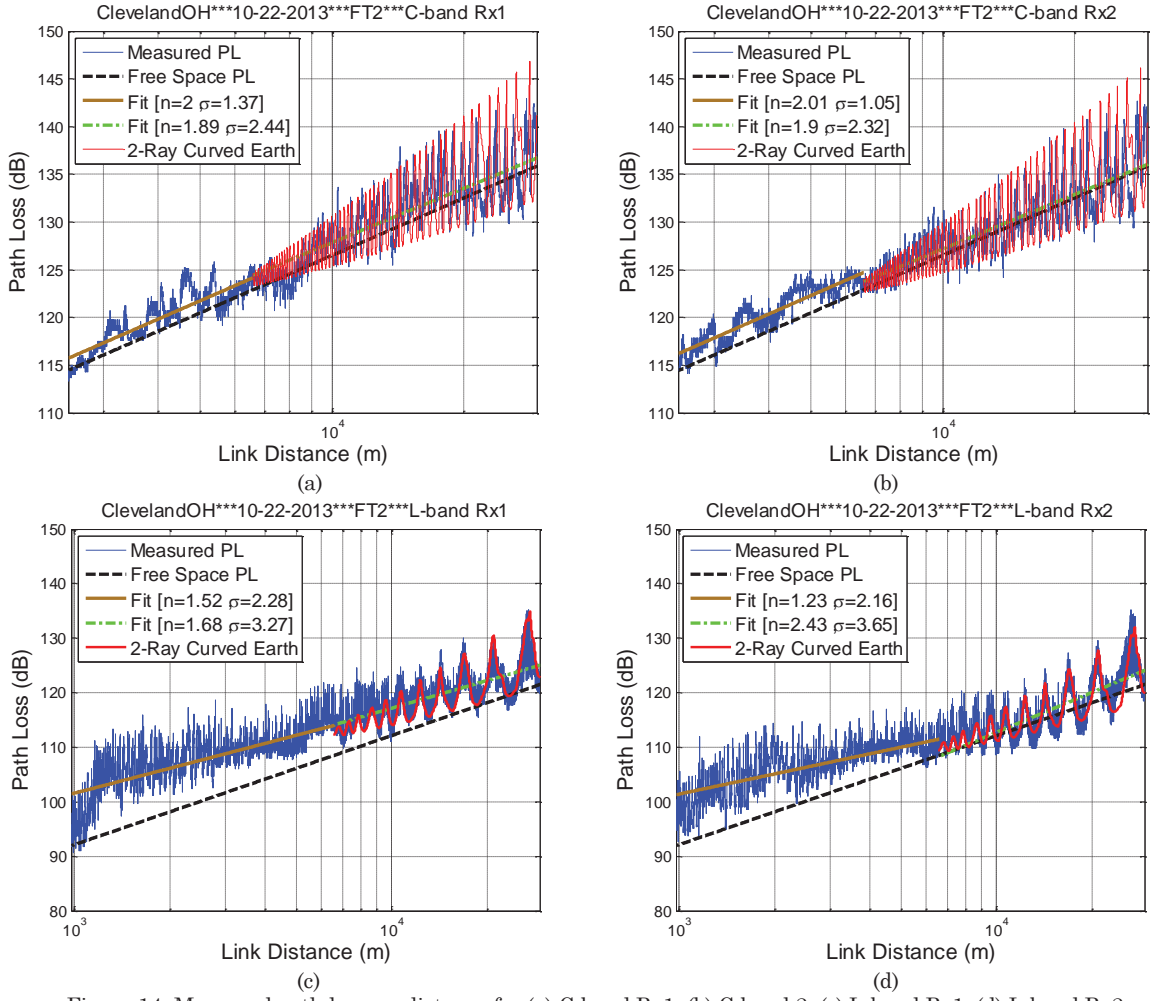


Figure 14. Measured path loss vs. distance for (a) C-band Rx1; (b) C-band 2; (c) L-band Rx1; (d) L-band Rx2.

Table 5. Path loss model parameters for over-freshwater FT2, straight flight toward GS.

Receiver	$d < d_t (\theta > \theta_t)$							$d > d_t (\theta < \theta_t)$									
	Log-distance linear PL model			Elevation angle range (degree)		Distance range (km)		Log-distance linear PL model			CE2R (dB)		Elevation angle range (degree)		Distance range (km)		
	$A_{0,S}$ (dB)	n_S	$\sigma_{XL,S}$ (dB)	$\theta_{min,S}$	$\theta_{max,S}$	$d_{min,S}$	$d_{max,S}$	$A_{0,L}$ (dB)	n_L	$\sigma_{XL,L}$ (dB)	L_0	σ_{X2}	$\theta_{min,L}$	$\theta_{max,L}$	$d_{min,L}$	$d_{max,L}$	
	C-Rx1	47.8	2.0	1.4	5.0	12.7	2.5	6.6	52.1	1.9	2.4	1.0	3.9	1.4	5.0	6.6	29.4
	C-Rx2	47.9	2.0	1.1	5.0	12.7	2.5	6.6	51.4	1.9	2.3	0.4	3.8	1.4	5.0	6.6	29.3
	L-Rx1	56.1	1.5	2.3	5.0	35.5	1.0	6.6	49.9	1.7	3.3	4.1	1.8	1.4	5.0	6.6	29.4
	L-Rx2	64.6	1.2	2.2	5.0	35.5	1.0	6.6	15.4	2.4	3.7	1.2	1.8	1.4	5.0	6.6	29.3

In Figure 15 we show plots of root-mean square delay spread (RMS-DS) vs. link distance for the two C-band receivers. These plots are “post-processing,” as we describe in the following paragraph. The RMS-DS is denoted σ_τ and is given by

$$\sigma_\tau = \sqrt{\frac{\sum_{k=0}^{L-1} \alpha_k^2 \tau_k^2}{\sum_{k=0}^{L-1} \alpha_k^2}} - \mu_\tau, \quad (11)$$

where as in (4), α_k is the k^{th} MPC amplitude out of a total of L MPCs in a PDP, τ_k is the delay of the k^{th} MPC, and μ_k is the mean energy delay, calculated via

$$\mu_\tau = \frac{\sum_{k=0}^{L-1} \alpha_k^2 \tau_k}{\sum_{k=0}^{L-1} \alpha_k^2}. \quad (12)$$

The denominator sum $\sum_{k=0}^{L-1} \alpha_k^2$ in (11) and (12) is the total power in the PDP. This power can be either the power for the average PDP for a given set of data, or for a single PDP; for the latter case the parameters in (11) and (12) are termed the instantaneous RMS-DS and instantaneous mean energy delay, respectively.

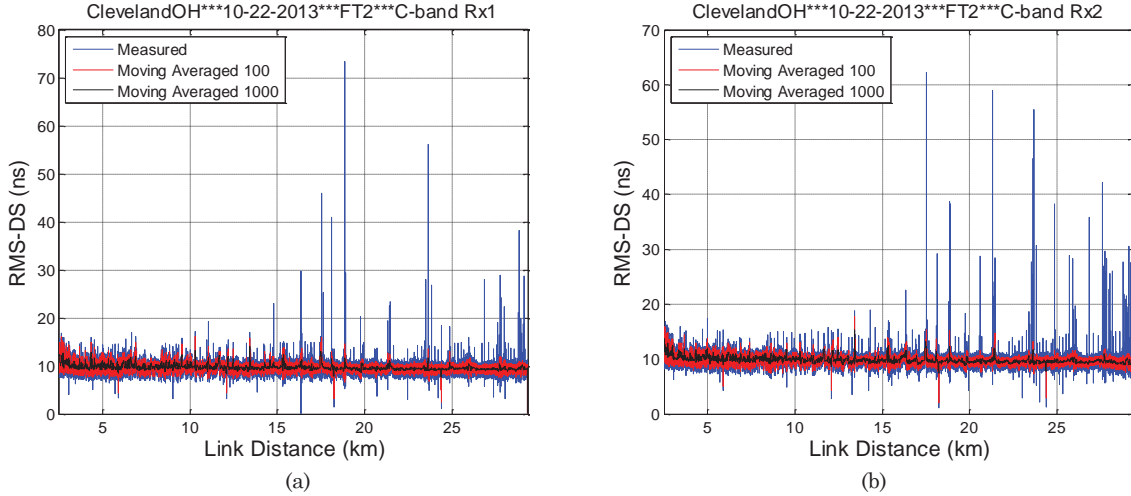


Figure 15. RMS-DS vs. distance for C-band (a) Rx1; (b) Rx2, over-freshwater FT2.

As in the over-sea case, we note the presence of multiple “bumps” in the RMS-DS vs. distance plots, where the geometry was such that reflections from objects on the lake shore presented multipath components (MPCs) that resulted in a temporary increase in RMS-DS. In fact, the *original* RMS-DS vs. distance plots contained many *more* bumps of much *larger* value, due to strong reflections from the large buildings in downtown Cleveland. These large reflections (MPCs) were removed via a delay threshold of 1 μ s.

A closer look at this is presented in Figure 16 where we show the original RMS-DS vs. distance plot before application of the delay threshold. The more numerous and larger RMS-DS bumps are clearly evident. Figure 17 shows a decimated sequence of PDPs for this FT both before and after thresholding. Note that the two figures have different delay scales, but the distant reflections from downtown Cleveland have been removed by thresholding in Fig. 17(b). The original (before-thresholding) PDPs will be of use in developing the urban GS setting channel models.

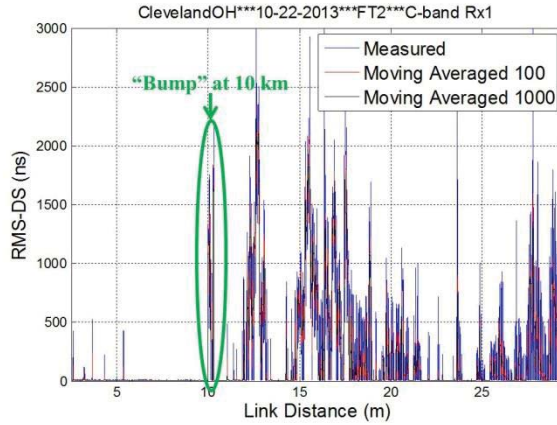


Figure 16. C-band Rx1 RMS-DS vs. distance for FT2, before thresholding.

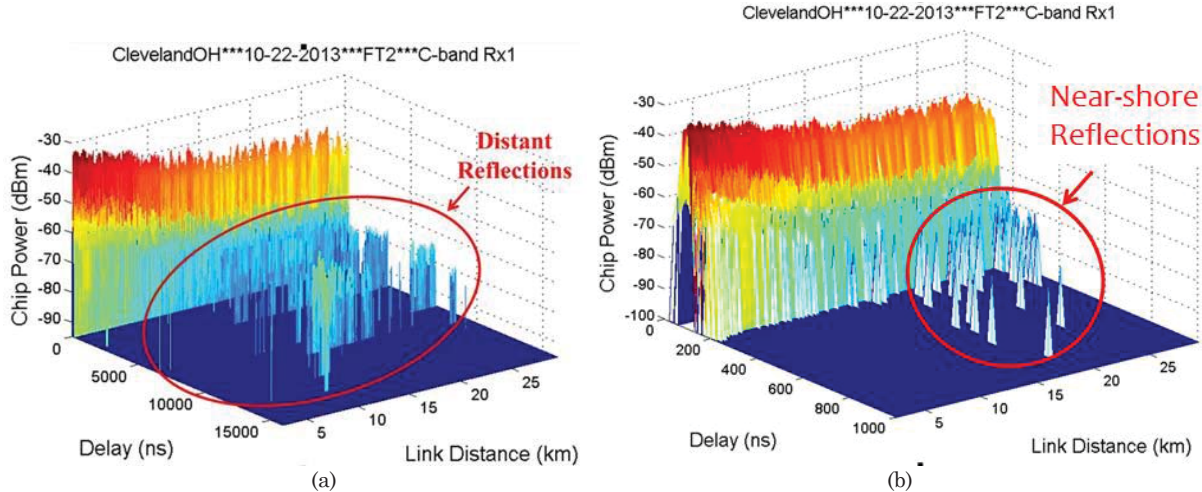


Figure 17. Sequence of C-band Rx1 PDPs for FT2, (a) before thresholding, with distant reflections (MPCs from large buildings in downtown Cleveland) indicated, and (b) after thresholding. Note two different delay ranges.

Figure 18 shows a Google Maps® view in which we have identified the potential short-delay “near-shore” reflecting objects along the lake shore. Several large buildings, three harbors with watercraft, light houses and oil tanks are present. The geometry indicates that these obstacles are likely responsible for the MPCs in Figure 17(b).



Figure 18. Google Maps® view illustrating region of potential near-shore reflectors.

Figure 19 shows histograms of RMS-DS for FT2, both for the original thresholded data set, and a moving-average filtered version of the thresholded instantaneous RMS-DS sequences. The filtering naturally reduces the maximum values, but does not change the means. Although the distribution may not be strictly “heavy-tailed” (hyperbolic), it clearly indicates that a small percentage of PDPs have RMS-DS values well above the mean. Table 6 quantifies the RMS-DS statistics.

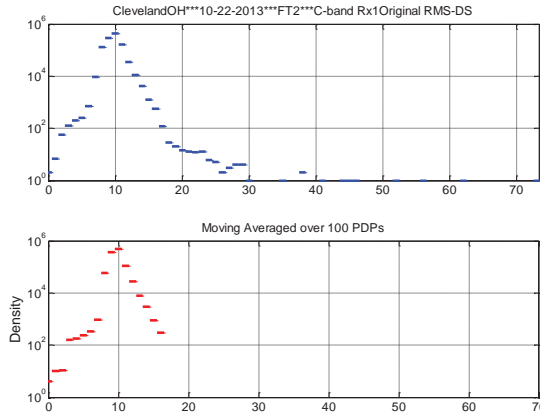


Figure 19. Histogram of RMS-DS for FT2 (straight) after thresholding, C-band Rx 1.

Table 6. Over-freshwater RMS-DS statistics.

RMS-DS (ns)			Mean	Max
FT2	Rx1	Original	9.7	73.3
		Moving Averaged Over 100		16.2
		Moving Averaged Over 1000		14.0
	Rx2	Original	9.9	62.2
		Moving Averaged Over 100		17.7
		Moving Averaged Over 1000		15.3
FT4	Rx1	Original	9.9	161.0
		Moving Averaged Over 100		119.3
		Moving Averaged Over 1000		77.3
	Rx2	Original	10.0	135.8
		Moving Averaged Over 100		116.6
		Moving Averaged Over 1000		96.0

In Figure 20 we show intra-band correlation coefficient results vs. link distance for both C-band and L-band. The C-band results do not strongly resemble those described for the analytical CE2R. This is in part a manifestation of the rapidly-oscillating two-ray effect (and surface reflection variations), but is actually dominated here by equipment stability limitations. Specifically, for some FTs the channel sounder exhibited greater variation (sample clock drift) than others, and this causes the unusual correlation coefficient results of Figure 20. In the results of Figure 20, we actually used a window (vector) length of twice the SD in order to reduce the clock drift effect. The mean value of C-band correlation is 0.5, and the mean value of L-band correlation is 0.66. We are currently working on an algorithm to remove the sample clock drift effects from the data so that accurate correlation results can be obtained for the data from all FTs. As with the over-sea results, inter-band correlations are essentially zero.

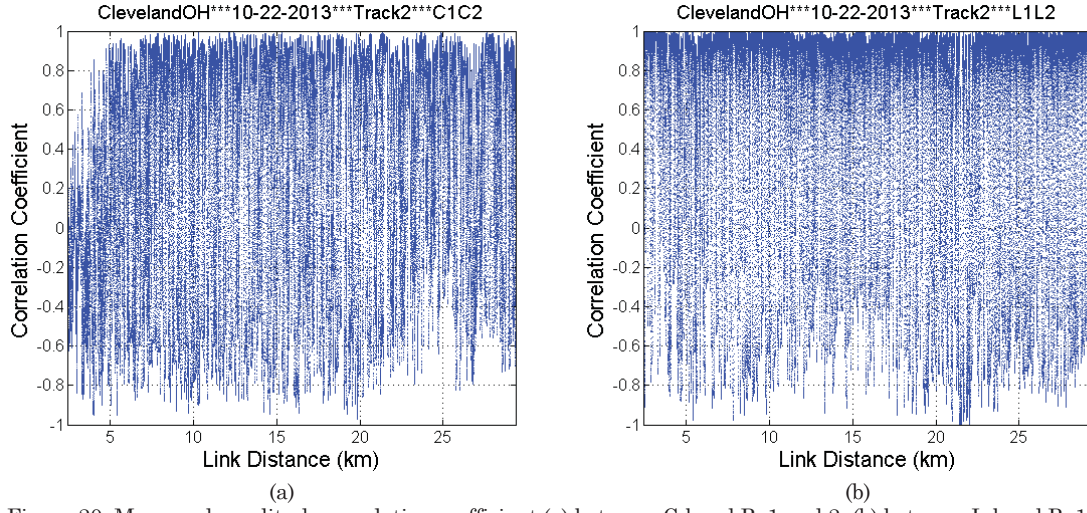
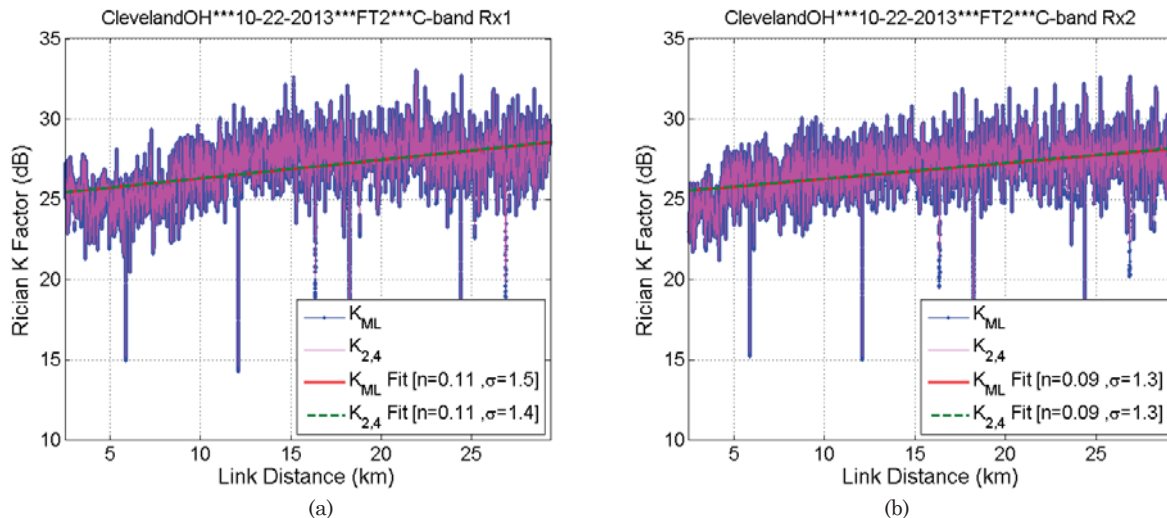


Figure 20. Measured amplitude correlation coefficient (a) between C-band Rx1 and 2; (b) between L-band Rx1 and 2 for FT2.

Our final results in this over-freshwater section pertain to small-scale fading, specifically the distribution of amplitude fading about the mean (where the mean is given by the path loss models). As is common in such LOS channels, we selected the Ricean distribution as the appropriate one to quantify this fading. This is fully described via the Ricean K -factor—see Appendix C for a complete description of the Ricean density function, and estimation methods for K . Using our stationarity distance, we estimated the Ricean K -factor for all four receivers. Plots of K vs. link distance are shown in Figure 21. In general, K increases very slightly with distance for FT2, although for other FTs, K is more nearly constant, or may decrease slightly (see Appendix A). As with the “per-FT2” path loss models, the K -factors here are “per-FT2,” and an aggregate model for K vs. distance will be developed in the future (for over-sea as well as over-freshwater). The L-band K is also smaller than that for C-band, and in addition shows dependence on two-ray effects; as with path loss, this is due to the stronger surface reflection at L-band. Nonetheless, the over-freshwater AG channel has relatively large K -factors of ~ 12 dB for L-band, and ~ 25 dB for C-band, illustrating the weakness of true small-scale fading (aside from the CE2R effects). Table 8 lists the “per-FT2” Ricean K -factor statistics. The K -factor estimated via the maximum-likelihood method, K_{ML} , is the most accurate.



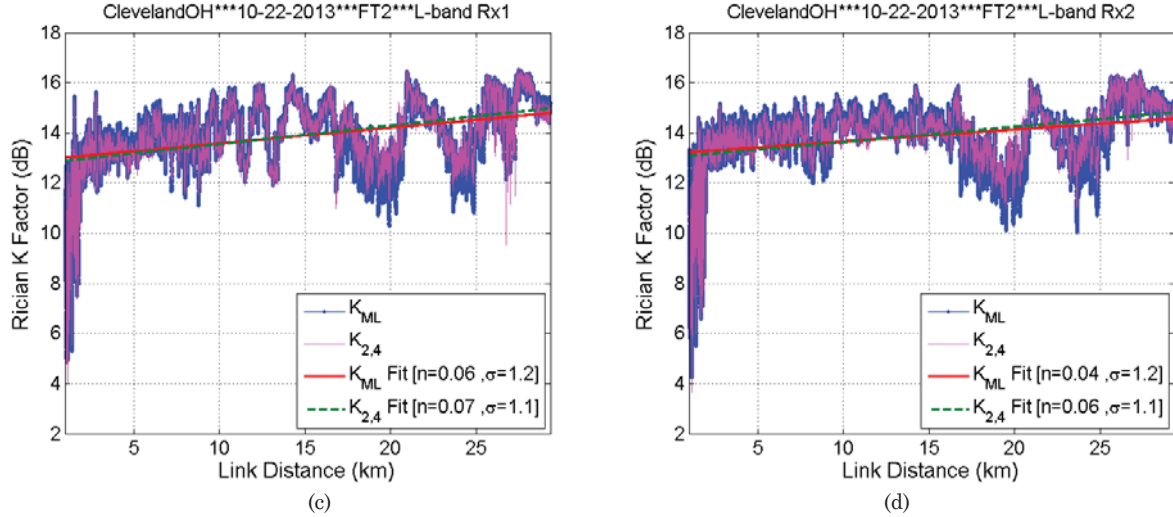


Figure 21. Ricean K factor for over-freshwater FT2 (a) C-band Rx1; (b) C-band 2; (c) L-band Rx1; (d) L-band Rx2.

Table 7. Statistics of over-freshwater Ricean K factor, FT2, Cleveland, OH, 22 October 2013, straight flight toward GS.

	C-band						L-band						
	Rx1			Rx2			Rx1			Rx2			
Moving Window Length	250λ						15 m						
Overall K factor (dB)	26.3			26.3			13.6			13.6			
Methods	K_{ML}	K_2	$K_{2,4}$	K_{ML}	K_2	$K_{2,4}$	K_{ML}	K_2	$K_{2,4}$	K_{ML}	K_2	$K_{2,4}$	
Linear fit of K factor	A (dB)	25.1	23.1	25.1	25.3	23.3	25.3	13.0	12.2	12.8	13.2	12.3	13.0
	n	0.12	0.09	0.12	0.10	0.07	0.10	0.06	0.11	0.07	0.05	0.09	0.06
	σ_x (dB)	1.5	2.9	1.5	1.4	2.9	1.4	1.3	1.5	1.2	1.3	1.5	1.1
Statistics of K factor (dB)	Max	33.0	32.9	33.0	32.6	32.5	32.6	16.5	16.6	16.5	16.5	16.5	16.6
	Min	13.6	11.1	13.9	13.4	11.1	13.9	4.9	-3.5	4.0	4.2	0.0	3.7
	Median	27.0	24.5	27.0	26.8	24.4	26.9	13.9	13.7	13.9	13.9	13.7	14.0
	μ	27.3	25.0	27.3	27.0	24.8	27.1	14.0	13.9	14.0	14.1	14.0	14.1
	σ	1.8	3.0	1.7	1.6	2.9	1.6	1.4	1.8	1.3	1.3	1.7	1.2

4.5 The Over-Harbor “Backlobe” AG Channel

We first described some of these results in [6], which were obtained during an over-sea flight from Oxnard, CA in June 2013. Here we provide more detailed analysis of this atypical case, some of which will appear in [11].

Figure 22 shows the portion of the flight track in question, in both ECEF coordinates (a) and in a Google Maps® view (b). Here the aircraft flew over a harbor. For the portion of the flight track shown in green (C-band) and brown (L-band) in Figure 22(a), the receivers were not in the GS antennas’ main beams, i.e., they were in the GS antennas’ “backlobe” regions. These backlobe areas and flight regions at large elevation angles are often neglected by researchers and system engineers, and in fact these areas are usually intentionally avoided by communication system designers. Yet in cases where the GS does not have an antenna beam directed upward, the aircraft will be out of the antenna main beam at large elevation angles. Similarly, there may be situations such as initial deployment, or equipment failure for one GS sector, in which signals between the aircraft and the backlobes of the GS antenna are of interest. The results here describe the AG channel in such a case.

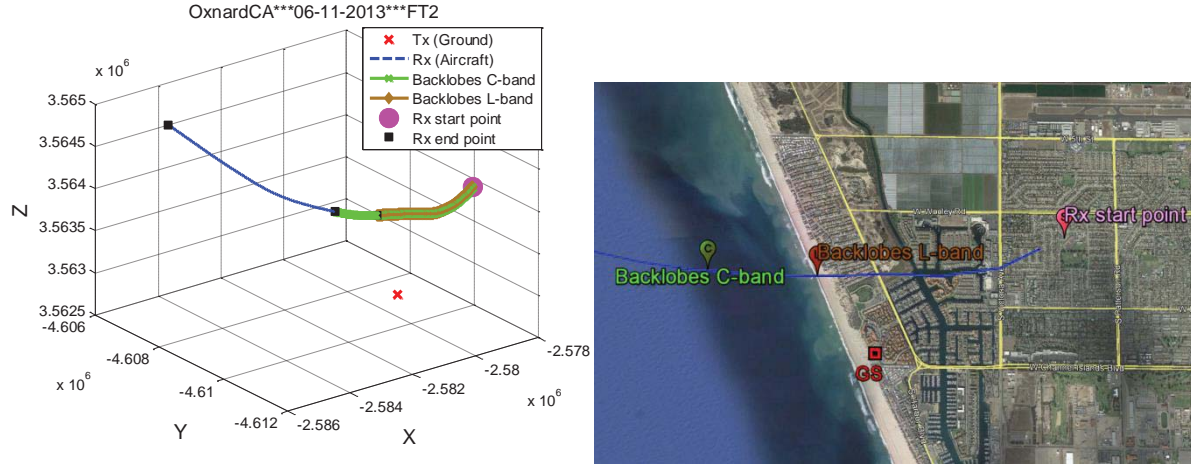


Figure 22. Portion of FT2 with ground site at Oxnard, 11 June 2013.

In the backlobe region, one would expect poor coverage, possibly severe fading and fairly large values of delay spread, and these can dramatically degrade the performance of any CPNC system operating in the backlobe area. Backlobe channel characteristics may also be used in estimating inter-sector interference in sectored antenna schemes. Despite the dependence of these results on our specific antenna patterns, the empirical statistical models provide interesting practical results.

Figure 23 illustrates the situation via a simplified diagram. Region (1) is where the aircraft is out of the main beam of the GS antenna where the GS transmitter antenna gain G_t is only very approximately known, and Region (2) denotes the region where the aircraft is within the half power main beam where G_t is almost a constant. The link distance d between GS and aircraft at the starting point is 2163 m. The green and brown lines in Fig. 22 are the backlobe areas of the C- and L-band antennas, respectively. The link distance at the boundary of the 3 dB main beam is 1857 m in C-band and 1175 m in L-band, due to the slightly different main beam patterns. The minimum link distance d_{min} is 1043 m. The blue line in Fig. 22 is the route for the rest of FT2, within the main beam for both bands. In Region 1, the earth surface reflections are on the ground. Additional potential reflectors include buildings of no higher than three levels, water vehicles in the harbor, the harbor itself, ground vehicles, and the ground itself (areas of sand). The GS antennas were elevated 20 m above the ground, oriented 283° from geographic north with zero elevation angles. In the backlobe area, the altitude difference between the aircraft and the GS ranged from 780.6 to 783.8 m. The azimuth angle ranged from -40 to 60 degrees relative to geographic north. The elevation angle was between 21.2 and 48.5 degrees. Each of the four receivers recorded approximately 70,000 PDPs in Region 1.

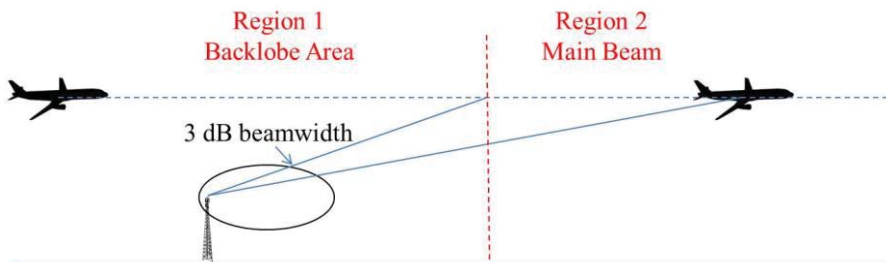


Figure 23. Illustration of main beam and backlobe regions.

The patterns of the directional Tx (GS) antennas are shown in Figure 24, with main beams directed to zero azimuth/elevation angles. The maximum gains are 6 dB in C-band and 5 dB in L-band. The locations of the omni-directional monopole Rx antennas (maximum gain 5 dB) are on the

bottom of the S3-B fuselage in a rectangular pattern; the front-to-rear and left-to-right distances between the Rx antennas are 1.29 and 1.32 m, respectively.

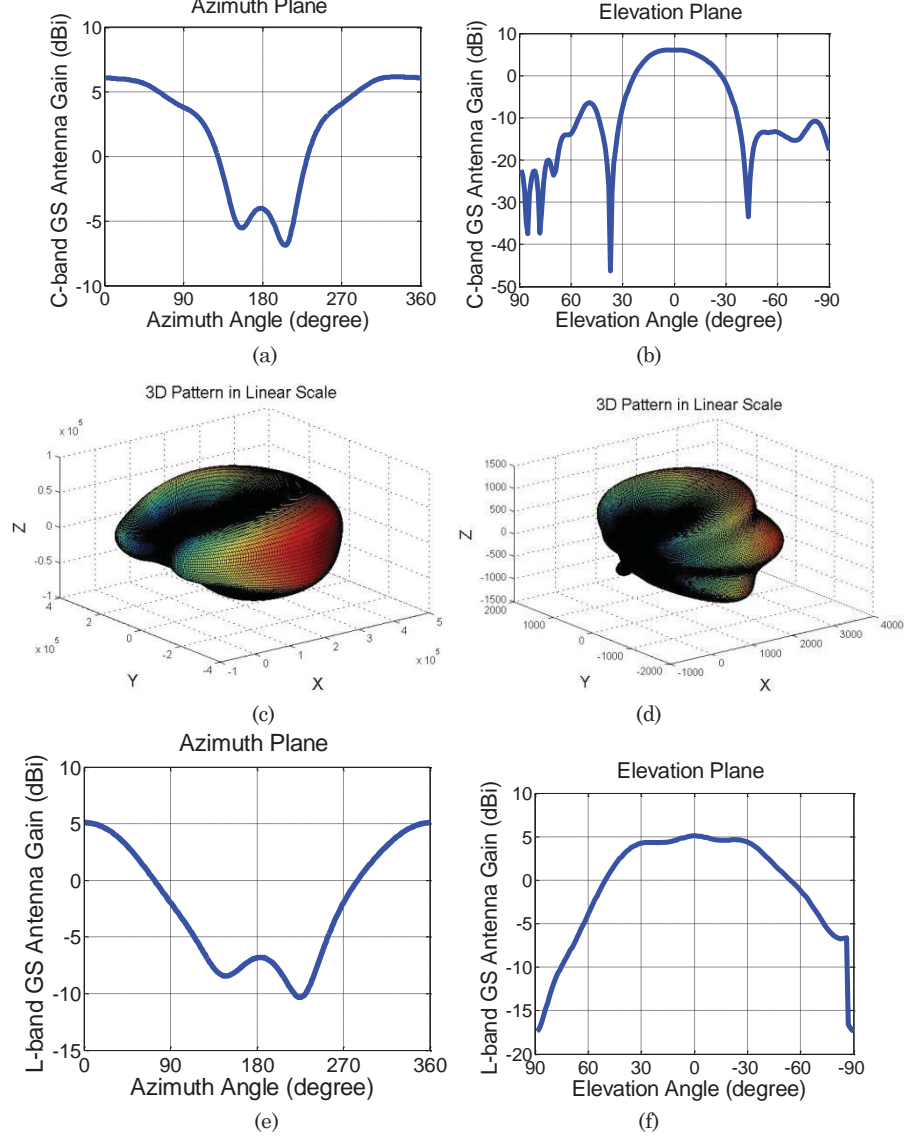


Figure 24. GS antenna patterns. (a) C-band azimuth plane; (b) C-band elevation plane; (c) C-band 3D pattern in linear scale; (d) L-band 3D pattern in linear scale; (e) L-band azimuth plane; (f) L-band elevation plane

We employed the antenna gain patterns in post processing, according to the elevation/azimuth angles and the orientation of the GS antennas with respect to the aircraft. (Note again that the patterns of the aircraft Rx antennas were measured on a metal ground plate in an anechoic chamber, and not while mounted on the aircraft, and the metallic body of the aircraft has a significant effect on these patterns. This introduces additional uncertainties into our measurements.) Both G_r and G_t have a resolution of one degree. The backlobes are always narrow, and the depths and locations of the nulls are sensitive to both angular resolution and the method by which the patterns are estimated. Hence G_r and G_t are only very approximately known at large elevation angles and in the backlobe regions.

In Region 1, the aircraft lies in the backlobes of the GS antennas where it is possible that the LOS component is heavily attenuated in a null but some other multipath components (MPCs) are in

a relatively stronger backlobe. The power of these MPCs can thus be stronger than in the main beam. Compared with the over-sea results in the main beam, results in Region 1 show fast fading and large delay spread.

Propagation path loss in dB vs. link distance for the two C-band receivers is shown in Figure 25. As indicated in Figure 22, the link distance between the aircraft and GS first decreased and then increased (hence in Figure 25 two loss values may occur at a single value of distance). The pink circle and black square are the Rx starting point and ending point within the backlobe areas, respectively, which correspond to the points shown in Figure 22. Compared to the path loss within the main beam, for short distances below approximately 2.5 km (Fig. 25(b)), the path loss in the backlobe areas is up to 15 dB larger than the expected free space path loss, and has large variation. The standard deviation (σ_{PL}) of the measured path loss difference from free space path loss is 6.8 dB for Rx1 and 7.3 dB for Rx2. In contrast, in Region 2 σ_{PL} is less than 2 dB.

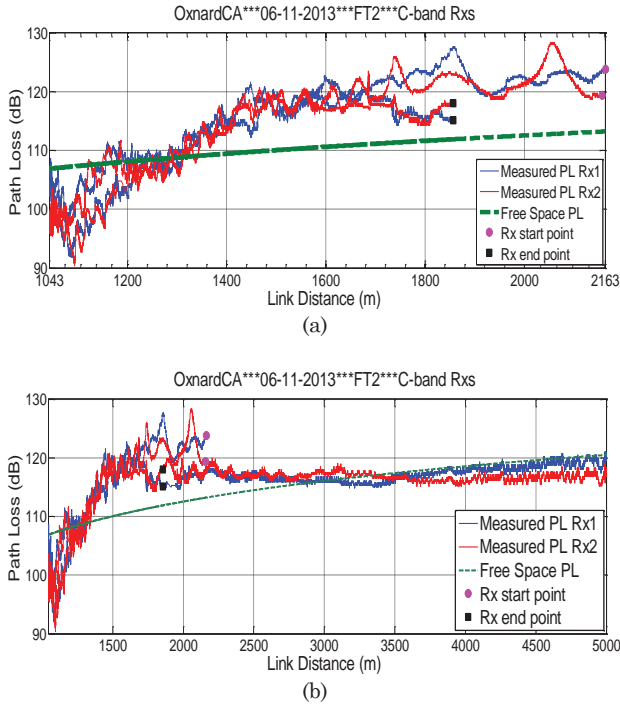
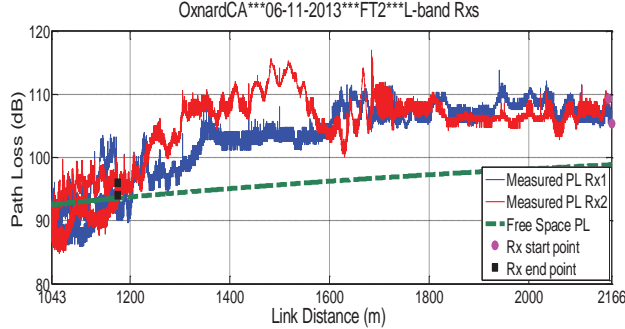
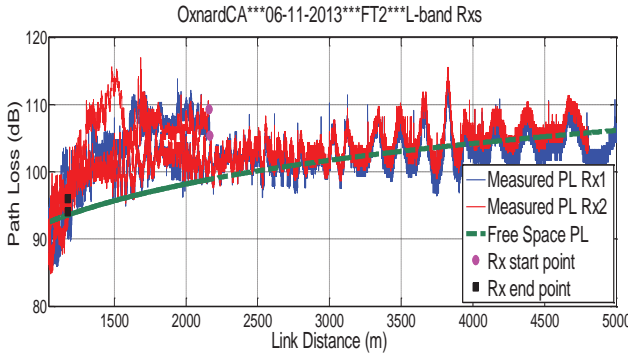


Figure 25. Path loss vs. link distance for C-band receivers. (a) Back lobe areas only; (b) including backlobe areas and part of Region 2 up to 5 km.

The path loss results for L-band are shown in Figure 26. The path loss in the main beam shows clear two-ray behavior, but the path loss in the backlobe area does not, and this is likely due to the presence of more MPCs and backlobe attenuation of the LOS component. Here the measured path loss is up to 20 dB larger than free space path loss. The σ_{PL} of the measured L-band path loss with respect to free space path loss is 5.8 dB for Rx1 and 6.4 dB for Rx2. In the main beam Region 2 the σ_{PL} is approximately 2.3 dB.



(a)



(b)

Figure 26. Path loss vs. link distance for L-band receivers. (a) Back lobe areas only; (b) including backlobe areas and part in Region 2 up to 5 km.

We also extracted amplitude fading data from the path loss measurements, just as we did for the Ricean fading fits in the over-water settings. The fading amplitude distributions are shown in Figure 27. The Generalized Extreme Value (GEV), lognormal, Weibull and Rayleigh distributions are plotted. The probability density function of the GEV distribution is

$$f(x; \mu, \sigma, \xi) = \frac{1}{\sigma} \left[1 + \xi \left(\frac{x-\mu}{\sigma} \right) \right]^{(-1/\xi)-1} \exp \left\{ - \left[1 + \xi \left(\frac{x-\mu}{\sigma} \right) \right]^{(-1/\xi)} \right\}, \quad (13)$$

where ξ is the shape factor, μ is a location parameter, and σ the scale factor. The parameters of the four distributions are listed in Table 8. The Weibull and Rayleigh distributions do not fit the data. Due to the complexity of the backlobe patterns combined with multipath, the distributions show two or three modes, and often fading is severe, or worse than Rayleigh [27].

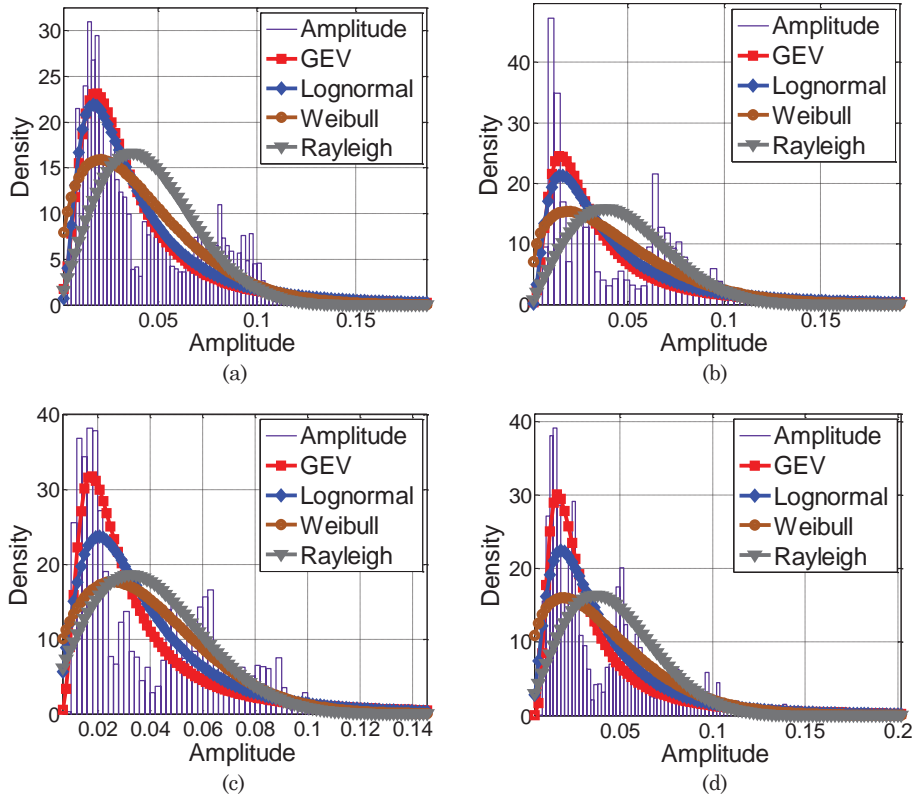


Figure 27. Histogram of received signal envelope amplitude for (a) C-band Rx1; (b) C-band Rx 2; (c) L-band Rx1; (d) L-band Rx2.

Table 8. Distribution parameters for backlobe amplitude fading.

		C-band		L-band	
		Rx1	Rx2	Rx1	Rx2
Generalized Extreme Value	ξ	0.43	0.59	0.58	0.62
	μ	0.02	0.02	0.02	0.02
	σ	0.02	0.02	0.01	0.01
Lognormal	μ	-3.45	-3.45	-3.45	-3.45
	σ	0.78	0.84	0.66	0.74
Weibull	β	1.44	1.38	1.69	1.41
Rayleigh	σ	0.04	0.04	0.03	0.04

The C-band RMS-DS along with its moving averaged version over 1000 PDPs is shown vs. distance in Figure 28. The RMS-DS in the main beam is approximately 10 ns with some “bumps” no larger than 50 ns as seen in Figure 28(b).³ The RMS-DS in the backlobe area has mean 35 ns, maximum 220 ns for Rx1 and mean of 37 ns, maximum of 391 ns for Rx2, i.e., RMS-DS is substantially larger in the backlobe region than in the main beam.

³Due to the present of filters in the channel sounder, the minimum RMS-DS that can be measured (through a back-to-back connection) is 10 ns in C-band.

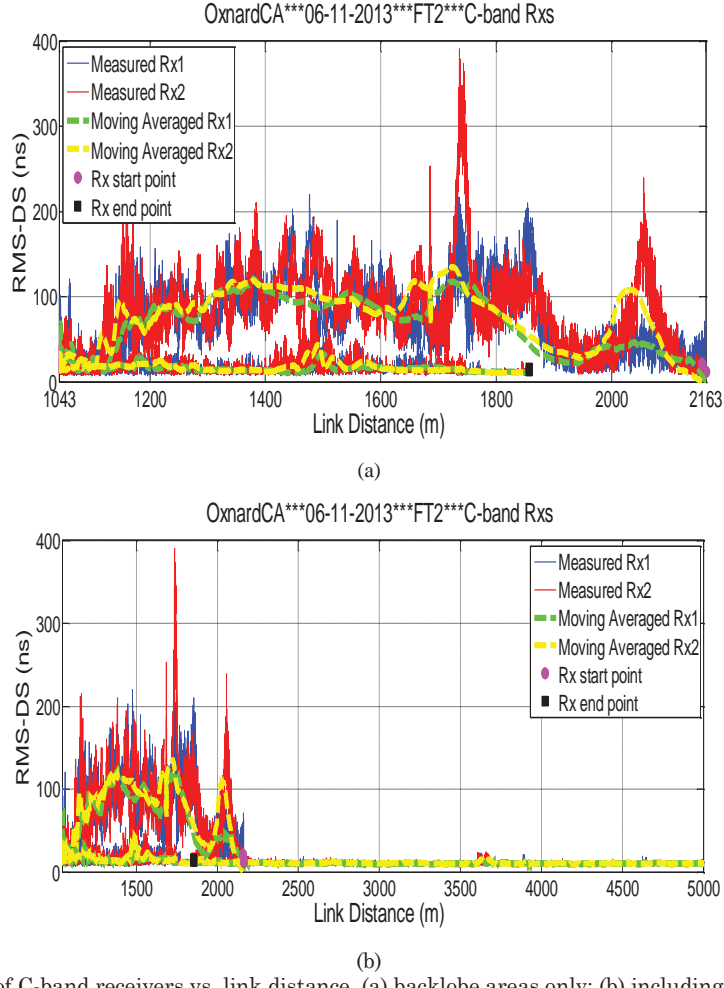


Figure 28. RMS-DS of C-band receivers vs. link distance, (a) backlobe areas only; (b) including backlobe areas and part in region 2 up to 5 km.

Figure 29(a) is the sequence of C-band PDPs for Rx1 from the starting point to the minimum link distance d_{min} . Figure 29(b) shows the sequence of PDPs from d_{min} to approximately 2.5 km. In both plots, the flight path is along the link distance axis from upper right to lower left. The RMS-DS decreases substantially after the half power main beam boundary at approximately 1857 m, as indicated by the white line at the base of the plot in Fig. 29(b). Many MPCs are present in the backlobe area, most within 1000 ns delay, but a few MPCs have delay up to 1820 ns. The power of the strongest (LOS) component increases from the range -40 to -62 dBm up to -31 dBm when the aircraft goes from the backlobe area to the main beam.

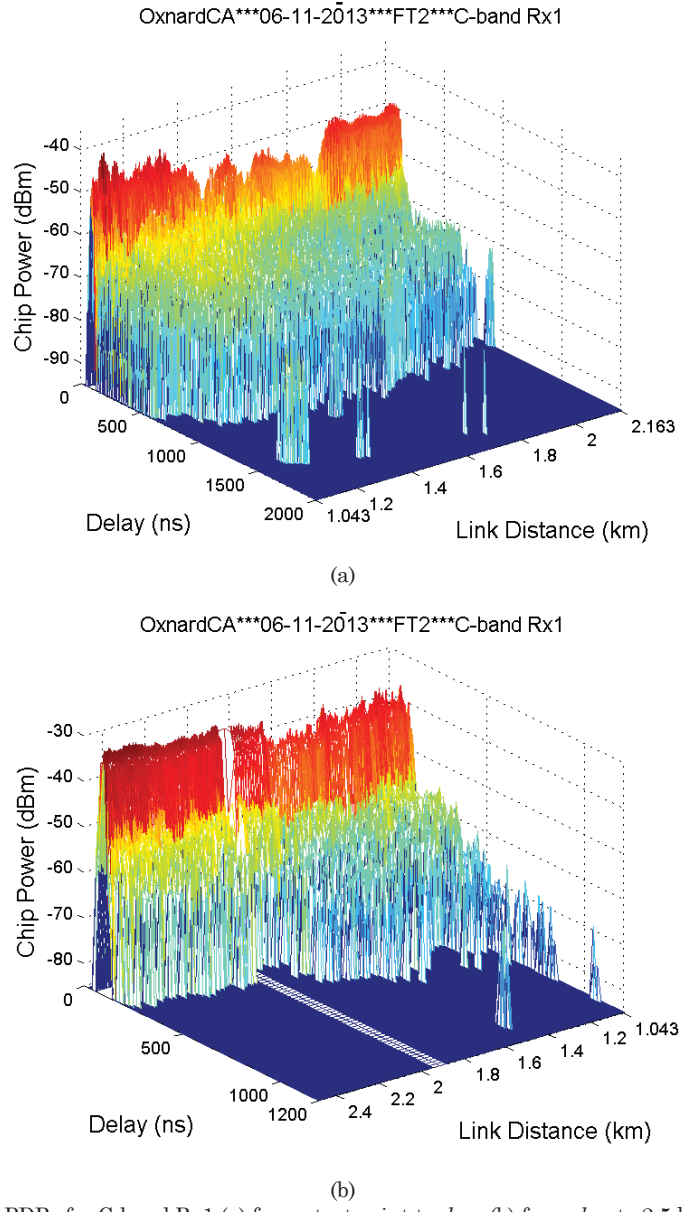


Figure 29. Sequence of PDPs for C-band Rx1 (a) from start point to d_{min} ; (b) from d_{min} to 2.5 km (including part of Region 1 & 2). Flight path in both figures is along link distance axis from upper right toward lower left.

An example individual PDP is shown in Figure 30; the link distance of this 17150th PDP is 1287.8 m, which lies in the segment before d_{min} (Fig. 29(a)). The strongest MPC (likely the LOS) is shifted to a delay value of 100 ns. MPCs are present with a maximum excess delay of 540 ns, with MPC power from 10 to 30 dB smaller than that of the LOS. The instantaneous RMS-DS of this PDP is 61.6 ns.

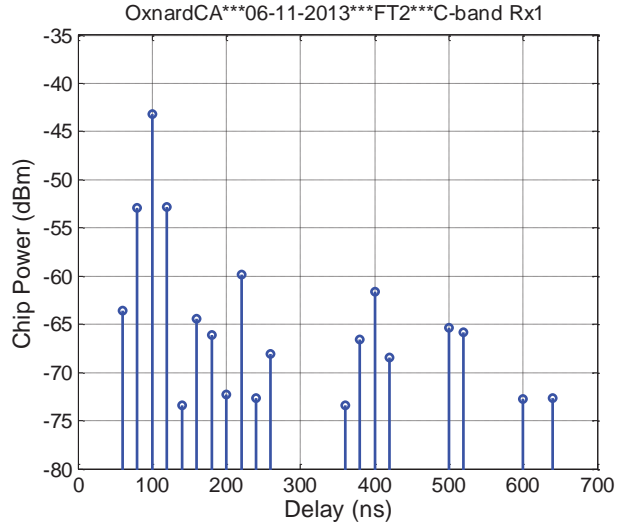


Figure 30. Example individual C-band PDP, 17150th PDP at $d=1287.8$ m.

In summary, for this “backlobe” AG channel when the aircraft is outside the half power main beam of the GS antennas, path loss is up to 15 dB larger than free space path loss in C-band and up to 20 dB larger than free space path loss in L-band. Path loss variation is also much larger and more rapid than that within the main beam. The received signal amplitude fading is fast and severe, or worse than Rayleigh. The C-band RMS-DS is up to 400 ns with mean of 35 ns, whereas the RMS-DS in the main beam (for the flight over the Pacific Ocean) is essentially near the measurement lower limit of 10 ns with a few values near 50 ns and very rare larger values near 200 ns. The sequence of PDPs and example individual PDPs show that the power of the LOS component in the backlobe area is 10-30 dB smaller than that in the main beam, and also has rapid variation. The number of MPCs and their excess delays (up to ~ 1.8 μ s) within the backlobe are much larger than those in the main beam as well.

4.6 Statistics for Over-Sea Channel Models

As reported in [6], we are compiling results that will enable us to develop statistical, tapped-delay (TDL) line models of the wideband over-water AG channels. Although not complete at this time, we are close to the final specification of these models⁴. The basis for the over-water AG channel models is the CE2R. This geometry-based model represents the first two components (“taps”) in the TDL model, and is the deterministic portion of the complete model. The remaining portion is the stochastic part, which is composed of the intermittent MPCs.

In [6] we provided example statistics for these intermittent MPCs, termed the 3rd and 4th rays. Upon a more detailed analysis of the over-sea data, we have concluded that what was termed the 4th ray in some results was actually the 3rd ray at a larger value of relative delay. Thus the presence of the 4th ray is even more rare than previously reported ($\sim 0.29\%$ of the time). Hence the final over-sea TDL models may not have any 4th ray at all. Since the 4th ray’s power level is very small (at least 27 dB down from the LOS component), this simplification will not result in a significant loss of accuracy. For purposes of discussion, we repeat the diagram of the (3-ray) TDL model in Figure 31.

⁴ Progress was delayed in part due to a breakdown of our main processing computer on 18 September 2014. This is currently under repair, and should be ready to resume use in several weeks.

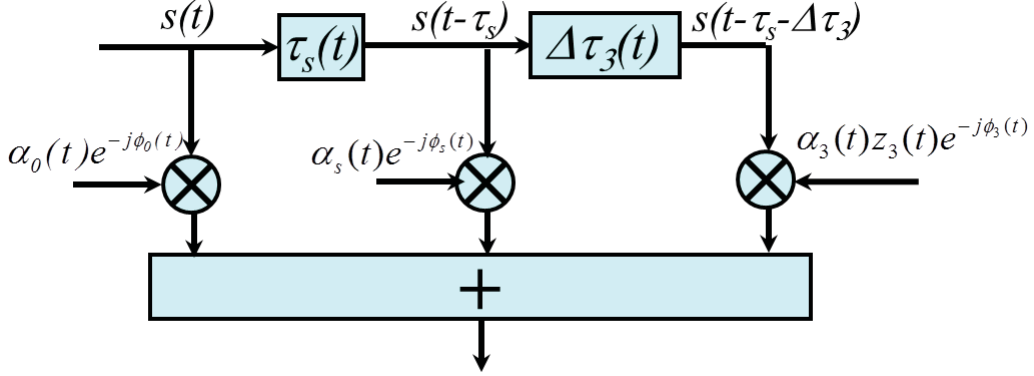


Figure 31. 3-ray TDL for over-sea AG channel.

The impulse response of this channel is given by

$$h(\tau, t) = \alpha_0(t)e^{-j\phi_0(t)}\delta(\tau) + \alpha_s(t)e^{-j\phi_s(t)}\delta(\tau - \tau_s(t)) + z_3(t)\alpha_3(t)e^{-j\phi_3(t)}\delta(\tau - \tau_s(t) - \Delta\tau_3(t)) \quad (14)$$

where again, the α 's denote the MPC amplitudes, the ϕ 's the MPC phases, τ_s denotes the relative delay of the surface reflection, $\Delta\tau_3$ denotes the additional relative delay of the 3rd ray, and z_3 denotes the binary on/off (or, “0/1”) random process that controls the frequency of occurrence and duration of the intermittent 3rd ray. The LOS component delay is set to a value of zero in Fig. 31 and (14).

In addition to the CE2R, to complete the TDL in Fig. 31 requires that we specify the statistics of the 3rd ray, specifically its relative delay $\Delta\tau_3$, its relative amplitude α_3 , its presence and duration (controlled by z_3), and its phase (the phase appears to be well-modeled as uniform on $[0, 2\pi]$). Here we present some of the initial statistics.

Figure 32 shows statistics for the 3rd ray duration vs. link distance, and the excess delay (relative to the LOS component, i.e., $\Delta\tau = \tau_s + \Delta\tau_3$) for the over-sea straight FT1. Duration D_m is provided in units of meters, but this can be translated to an actual time duration via link velocity (duration D_s (seconds)= D_m (meters)/velocity(m/s)).

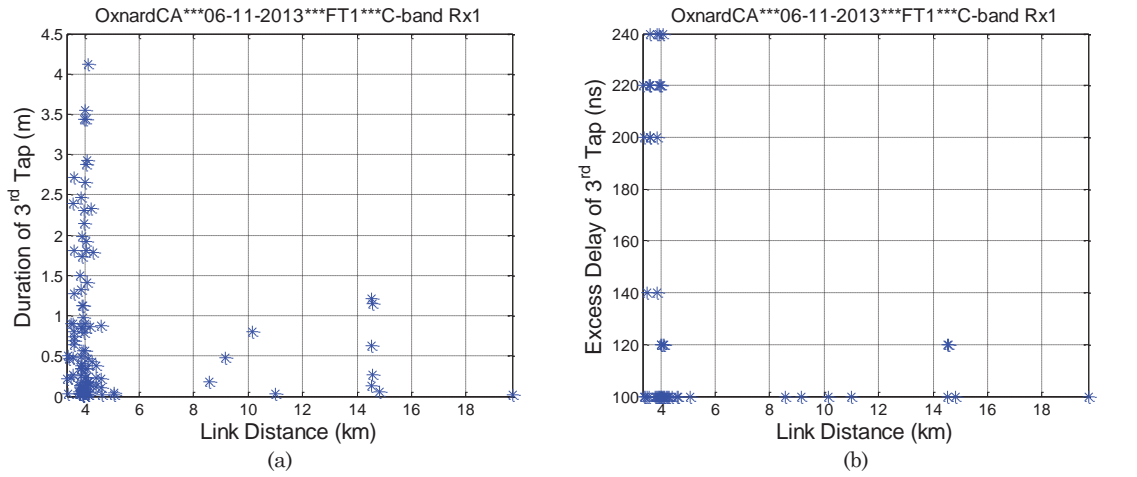


Figure 32. Third-ray statistics vs. distance, (a) duration D_m (m) and (b) excess delay $\Delta\tau$ (ns).

The results in Figure 32 show that “spatial duration” D_m ranges up to only 4.2 m, corresponding to a temporal duration of approximately 5 ms. The 3rd ray duration is greater than zero only for specific values of link distance, and most 3rd ray occurrences are at the smaller values of link distance—where near-shore objects induce MPCs. Similarly for excess delay, since quantized into increments of the sounder’s delay resolution of 20 ns, excess delays take values only in the set

$\{100, 120, 140, 200, 220, 240\}$ ns. Receiver 2's statistics are similar, but not quite identical, and for the final set of valid values of duration and excess delay, we will aggregate results from both receivers.

The dependence on link distance is also evident in a plot of $z_3(d)$, shown in Figure 33. Here again we see more 3rd ray presence in PDPs at short link distances than at large link distances. The results for Rx2 show more 3rd ray presence at larger distances than in Figure 33 for Rx1, but the presence of the 3rd ray is still concentrated at the smaller link distances.

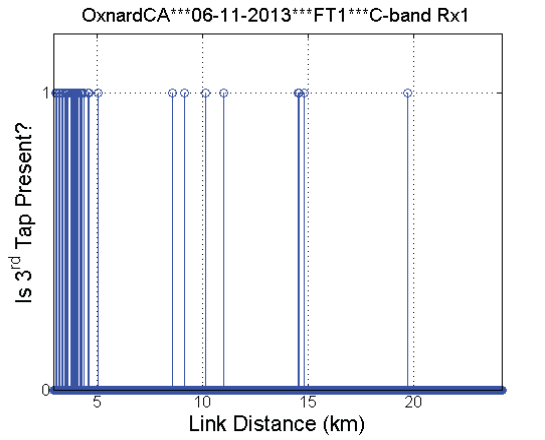


Figure 33. Third-ray “presence” vs. distance: “1” denotes 3rd ray present, “0” denotes 3rd ray absent.

In Figure 34 we show a plot of duration D_m vs. excess delay $\Delta\tau$. This can be viewed as analogous to a joint distribution of these variables, which illustrates their dependence. From plots like that in Figure 34 we can count the instances of each pair $(D_m, \Delta\tau)$ to construct a histogram that represents the actual joint probability mass function of these two variables. One such plot is shown in Figure 35.

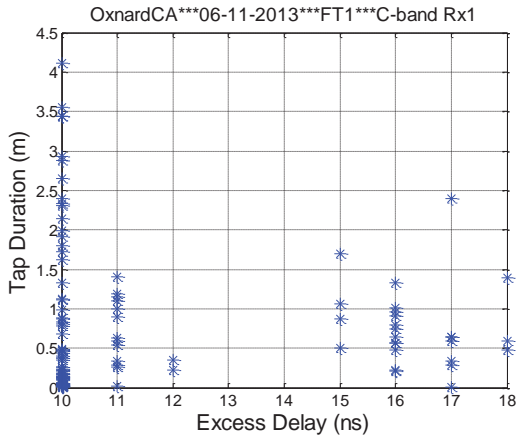


Figure 34. Third-ray duration D_m vs. excess delay $\Delta\tau$.

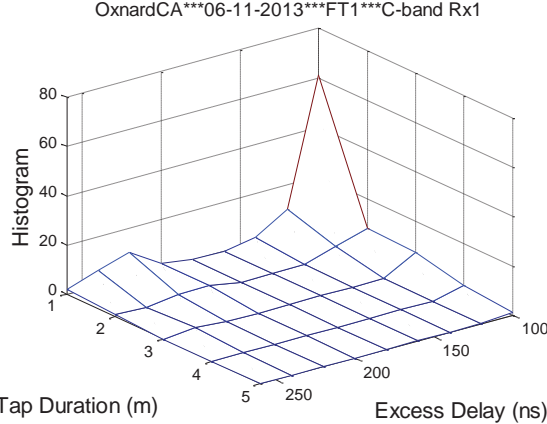


Figure 35. Third-ray joint distribution for duration D_m and excess delay $\Delta\tau$.

The results in Figure 35 can be used along with another histogram, of excess delay vs. distance, shown in Figure 36, to obtain the joint probability mass function of duration and excess delay vs. distance.

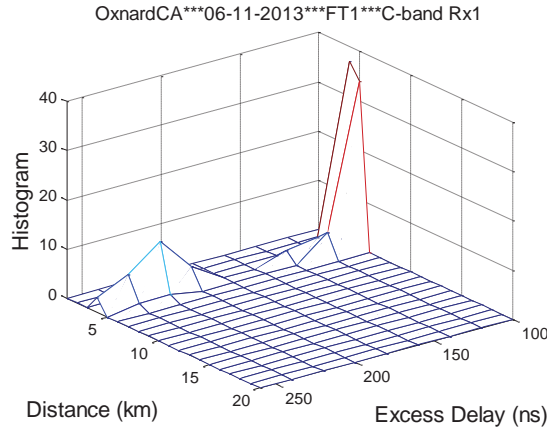


Figure 36. Third-ray distribution for excess delay $\Delta\tau$ as a function of link distance.

With these results, one algorithm for generating the wideband 3-ray over-sea channel model is as follows:

1. Run CE2R (vs. distance d);
2. Given distance d , based upon a model similar to that in Figure 33, draw random variable to declare 3rd ray present or absent. Go to Step 3;
3. If 3rd ray absent, model output=CE2R(d), and return to Step 1;
If 3rd ray present, draw random variable with distribution similar to that in Figure 36 to determine excess delay. Go to Step 4;
4. With excess delay of Step 3, draw random variable to set duration D_m according to distribution similar to that in Figure 35. Return to Step 1 and continue running CE2R (with added 3rd ray) until distance $d+D_m$ is reached. For first value of distance $d > d+D_m$, resume Steps 1, 2,

Although this algorithm should yield the required dependencies between the variables (based upon measurements), it is not the only way to generate the 3-ray TDL. We might instead model the “persistence” process z_3 via a (statistically non-stationary) discrete Markov chain, with a dependence on distance. We are also currently compiling a joint probability mass function that represents the third ray’s duration, distance, and excess delay all together (in a sense, combining Figures 35 and 36)—this will not be representable by diagram, but will instead be in tabular form. Each of these alternatives is being explored to determine the procedure that best mimics the actual measurement

results. As noted, we are aggregating results from both receivers for this. Finally on this wideband model algorithm, we have not stated anything about the 3rd ray amplitude α_3 . From our measured data, this value is nearly constant at approximately 25 dB down from the LOS component. We will investigate the amplitude variation of the 3rd ray during its “on” periods, but if this variation is minimal, it should be sufficient to model α_3 as a constant. The remaining part of the wideband model would be a model for airframe shadowing—although we did not have any such shadowing in the over-sea flights, it was observed in some of the over-freshwater and hilly terrain flights, hence it could be incorporated when flight maneuvers (primarily roll angle) can cause such shadowing.

Also of interest for CNPC is a narrowband over-water AG channel model. This can be constructed as shown in Figure 37, and consists of the CE2R plus a Ricean fader, plus the shadowing model. A Ricean fader that has a K -factor varying with distance is easy to construct. The only remaining characteristic of the Ricean fader that must be specified is its fading rate. This rate should be relatively easy to determine from our results on the Ricean K -factor (see Section 4.4 and Appendix A), and once determined, the Ricean fader can be completed by specifying the appropriate lowpass filter.

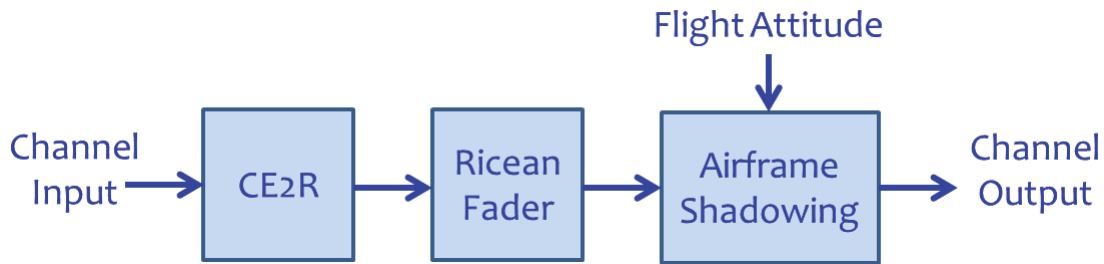


Figure 37. Narrowband over-sea AG channel model.

5. Initial Results for the Hilly Terrain AG Channel

Flight tests were conducted with the GS in a hilly terrain/suburban environment on 15 April 2013. These tests were made in southwestern Pennsylvania, near the town of Latrobe. All link parameters (transmit powers, antenna gains and GS antenna height, etc.) were identical to those used in the over-water flight tests.

Multiple FTs were flown along both straight and oval-shaped paths, with two orientations relative to the predominant ridgeline. Example FTs are shown in Figure 38: FT1 (straight toward GS from 17 km - 2.2 km), and FT6 (oval, link distance 16 to 24 km) are shown in a Google Earth® view. The average altitude difference between Tx and Rx was 602 m. Elevation angle ranged from 1.6-16°. Based upon curved-earth computations, the maximum link distance at which the surface reflection is resolvable is 4150 m for C-band, and 615 m for L-band (thus the L-band surface reflection was essentially never resolvable since the altitude difference was only 602 m). Figure 39 shows a view of the GS near the Latrobe airport, and geometric flight track traces for FT1 are shown in Figure 40. Traces for the remaining FTs appear in Appendix A, along with additional hilly terrain FT channel measurement results.



Figure 38. FT1 (brown), FT6 (blue), and ridgeline (double-green), Google Earth®.

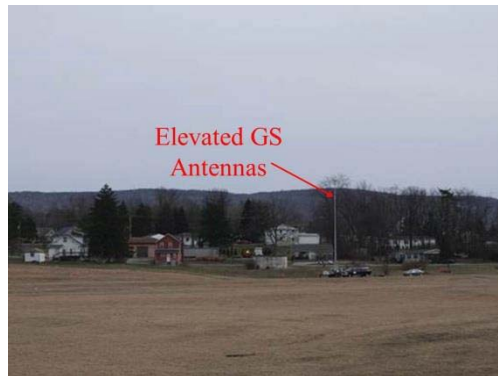
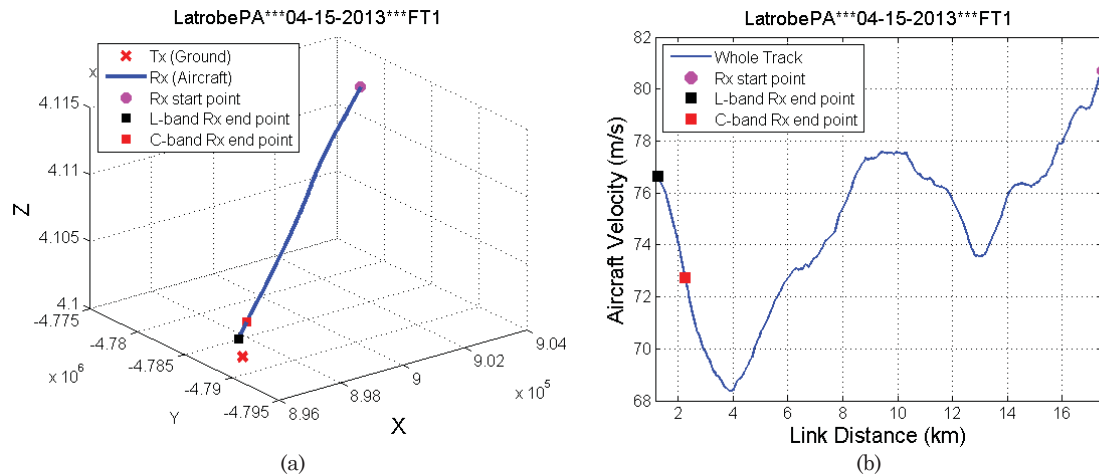


Figure 39. GS location, Latrobe, PA: view toward 137° from magnetic north.



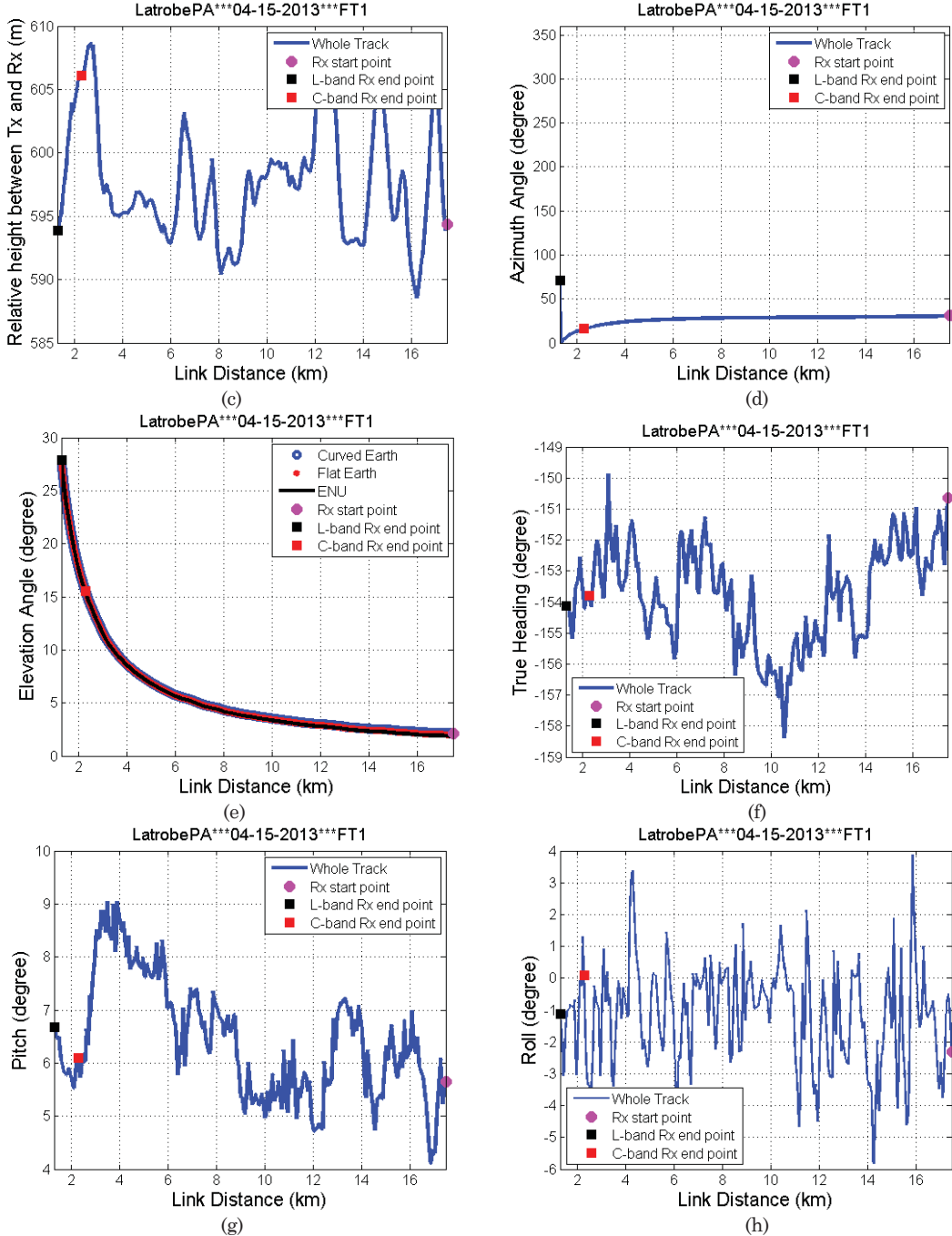


Figure 40. Geometric traces for FT1, Latrobe, PA: (a) flight track in ECEF coordinates; (b) aircraft velocity; (c) altitude difference between aircraft and ground station; (d) azimuth angle; (e) elevation angle; (f) heading of aircraft; (g) pitch angle of aircraft; (h) roll angle of aircraft.

Propagation path loss results are shown in Figure 41. As with the over-water results, path loss generally follows the free space path loss lines, with larger attenuation at small link distances from aircraft antenna effects. The two-ray model does not fit the measured data as well as in the over-water cases, but this is expected because of the lower reflectivity of dry ground as compared to that of water, and also to the generally rougher surface. Figure 41 also shows linear least-squares fit lines to the measured path loss data (two segments, for two ranges of elevation angle, or equivalently two ranges of link distance). The “per-FT” path loss model parameters for these linear fits appear in Table 9.

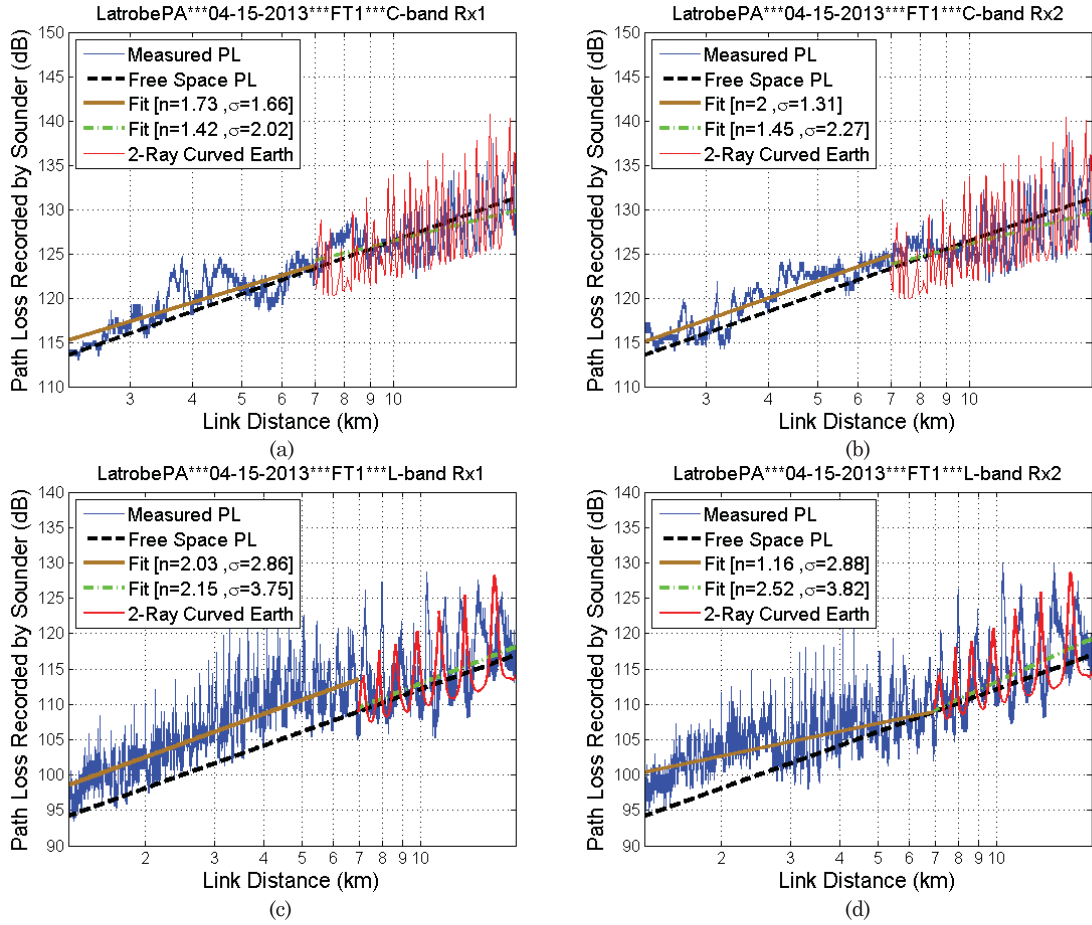


Figure 41. Measured path loss vs. distance for FT1, Latrobe, PA (a) C-band Rx1; (b) C-band 2; (c) L-band Rx1; (d) L-band Rx2.

Table 9. Path loss model parameters, FT1, Latrobe, PA, 15 April 2013, straight flight toward GS.

		$d < d_t (\theta < \theta_t)$						$d > d_t (\theta < \theta_t)$									
		Log-distance linear PL model			Elevation angle range (degrees)		Distance range (km)		Log-distance linear PL model			CE2R (dB)		Elevation angle range (degree)		Distance range (km)	
		$A_{0,S}$ (dB)	n_s	σ_{XLS} (dB)	$\theta_{min,S}$	$\theta_{max,S}$	$d_{min,S}$	$d_{max,S}$	$A_{0,L}$ (dB)	n_L	σ_{XLL} (dB)	L_0	σ_{X2}	$\theta_{min,L}$	$\theta_{max,L}$	$d_{min,L}$	$d_{max,L}$
	C-Rx1	5.6	1.7	1.7	5.0	15.5	2.3	6.9	27.4	1.4	2.0	-0.4	4.3	2.1	5.0	6.9	17.5
	C-Rx2	-11.8	2.0	1.3	5.0	15.5	2.3	6.9	24.5	1.5	2.3	-0.7	4.4	2.1	5.0	6.9	17.4
	L-Rx1	-25.1	2.0	2.9	5.0	27.9	1.3	6.9	-37.6	2.2	3.7	1.4	6.1	2.1	5.0	6.9	17.5
	L-Rx2	29.5	1.2	2.9	5.0	27.9	1.3	6.9	-63.2	2.5	3.8	1.8	6.2	2.1	5.0	6.9	17.5

Figure 42 shows plots of RMS-DS vs. link distance for this FT. As seen in the over-freshwater results where near-shore obstacles induced multipath components and caused temporary increases in RMS-DS, similar RMS-DS “bumps” can be observed for this hilly terrain environment. RMS-DS values of larger than 500 ns are evident. Figure 43 shows sequences of PDPs where we have identified the MPCs for two of the RMS-DS bumps, with the detailed PDPs for the bump at link distance 5.8 km shown in Fig. 43(b).

In this environment, using maps and geometry, we have identified the likely reflectors that cause the MPCs as large buildings in/near the town of Latrobe. Some moderate reflections may also arise from portions of the hillsides [28]. Statistics for RMS-DS for two FTs are provided in Table 10.

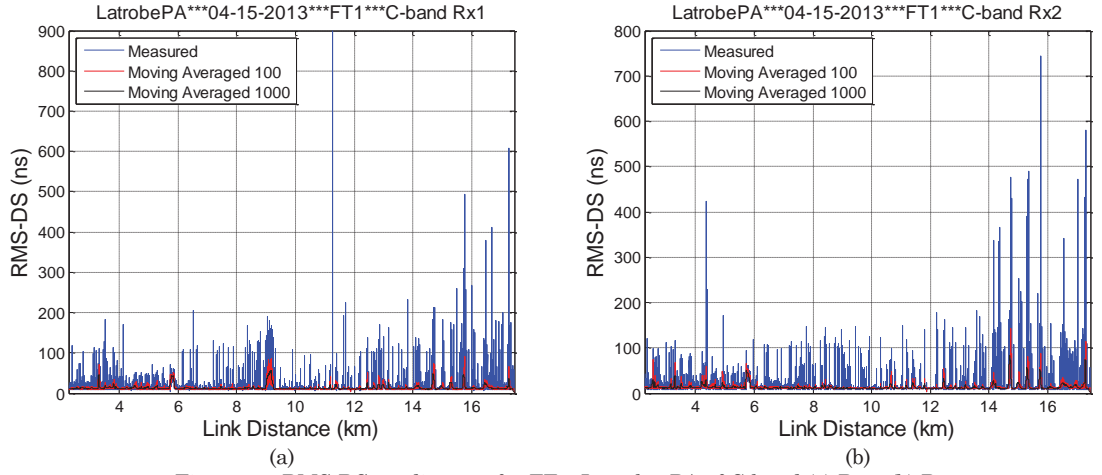


Figure 42. RMS-DS vs. distance for FT1, Latrobe, PA of C-band (a) Rx1; (b) Rx2.

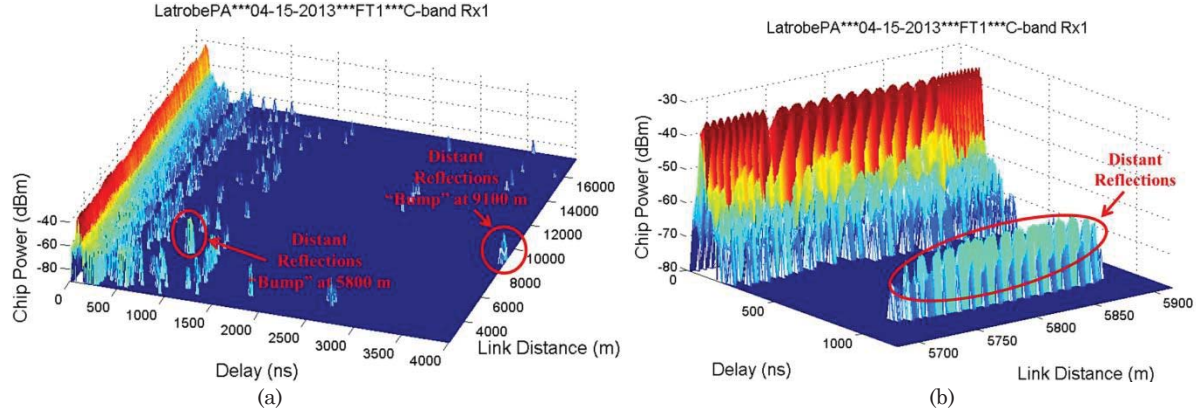


Fig. 43. Sequence of PDPs for C-band Rx1 FT1, hilly terrain: (a) entire FT1; (b) portion of FT1 near 5.8 km.

Table 10. RMS-DS statistics for hilly terrain, two FTs.

RMS Delay Spread		Mean (ns)	Median (ns)	Max (ns)	Standard Deviation (ns)
FT1	Original	12.9	10.9	267.2	9.8
	Moving Averaged over 100 PDPs		11.1	87.0	6.6
	Moving Averaged over 1000 PDPs		11.2	57.0	5.7
FT6	Original	35.7	10.9	995.7	55.7
	Moving Averaged over 100 PDPs		18.6	371.8	42.9
	Moving Averaged over 1000 PDPs		19.3	349.2	40.4

Plots of the correlation coefficient vs. link distance are not presented here—the data is still being processed to compute those. The statistics of correlations for FT1 are shown in Table 11.

Table 11. Statistics of spatial correlation, FT1, Latrobe, PA.

	C1C2	L1L2	CIL1	C1L2	C2L1	C2L2
Window Length	101	101	101	101	101	101
Mean	0.33	0.62	0.03	-0.01	-0.01	-0.02
Median	0.66	0.92	0.07	-0.02	-0.02	-0.05
Max	1.00	1.00	1.00	1.00	1.00	1.00
Min	-1.00	-1.00	-1.00	-1.00	-1.00	-1.00
Standard deviation	0.71	0.54	0.78	0.79	0.79	0.79

Our final results for the hilly terrain AG channel are the Ricean K -factors, shown in Figure 44. Very similar to the results for over-water, the Ricean K -factors increase very slightly with link distance, and are approximately 12 dB for L-band, and 25 dB for C-band. Two-ray behavior is again evident for the L-band results as well. The (“per-FT”) K -factor statistics are listed in Table 12.

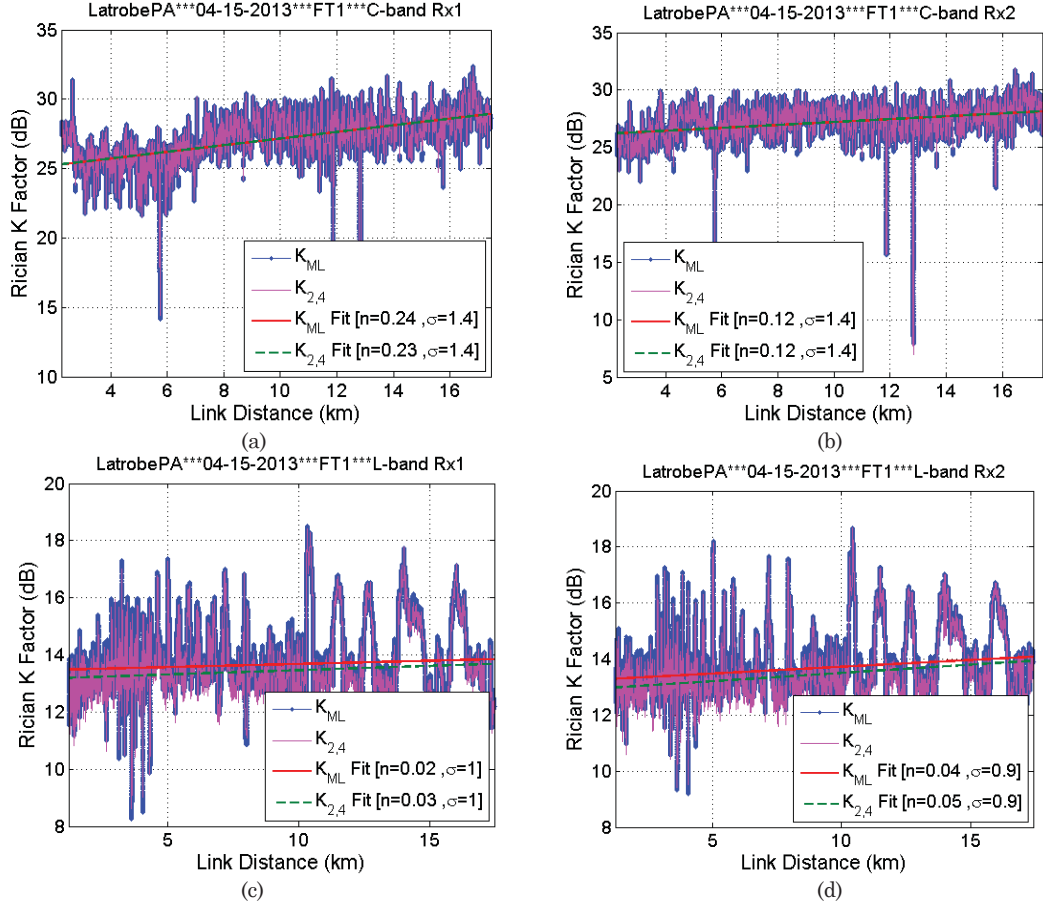


Figure 44. Ricean K factor for FT1, Latrobe, PA (a) C-band Rx1; (b) C-band 2; (c) L-band Rx1; (d) L-band Rx2.

Table 12. Statistics of Ricean K factor, FT1, Latrobe, PA, 15 April 2013, straight flight toward GS.

		C-band						L-band						
		Rx1			Rx2			Rx1			Rx2			
Moving Window Length		250λ						15 m						
Overall K factor (dB)		26.5			26.6			13.5			13.5			
Linear fit of K factor		K_{ML}	K_2	$K_{2,4}$	K_{ML}	K_2	$K_{2,4}$	K_{ML}	K_2	$K_{2,4}$	K_{ML}	K_2	$K_{2,4}$	
		A(dB)	24.8	24.6	24.8	26.0	25.8	26.0	13.5	11.9	13.2	13.2	11.6	12.9
		n	0.24	0.09	0.24	0.13	-0.04	0.13	0.02	0.12	0.03	0.05	0.15	0.06
		σ_X (dB)	1.5	2.5	1.5	1.4	2.7	1.4	1.0	1.3	1.0	0.9	1.2	1.0
		D_{max} (km)	2.2	2.2	2.2	2.2	2.2	2.2	1.2	1.2	1.2	1.2	1.2	1.2
Statistics of K factor (dB)		D_{Min} (km)	17.5	17.5	17.5	17.4	17.4	17.4	17.5	17.5	17.5	17.5	17.5	17.5
		Max	32.4	32.1	32.3	31.8	31.8	31.8	18.5	17.0	18.4	18.7	17.1	18.7
		Min	12.5	2.6	12.0	7.9	0.0	6.9	8.2	2.4	8.6	9.2	0.9	9.4
		Median	27.1	25.4	27.1	27.2	25.4	27.2	13.7	13.0	13.4	13.7	12.9	13.4
		μ	27.2	25.7	27.2	27.4	25.9	27.4	13.5	13.0	13.3	13.5	13.0	13.2
		σ	1.8	2.5	1.8	1.5	2.7	1.5	1.0	1.4	1.1	0.9	1.4	1.0

6. Literature Review Update

This section provides an update to the ongoing project literature review. With the growing popularity of UAS, it is not hard to find material. In fact, articles related to UAS appear in the popular press daily. For example, the American Institute of Aeronautics and Astronautics (AIAA) provides regular daily email news articles, which often address various aspects of UAS, including policies, experiments, applications, etc. One recent article noted that the popular social media company Facebook is looking to expand internet access via solar powered UAS [29]. The same issue of the AIAA email had an article that stated UAS will be used for aerial photography at future major sporting events. Another recent online article that received worldwide publicity appeared on the CNN website [30], and described how a tourist crashed a UAS into the largest hot spring in Yellowstone National Park. An airline magazine [31] predicted “personal UAS” in the future. Since much of the reporting in the popular press tends toward non-technical issues, henceforth we will limit review of such articles to only those that have sufficient technical content, and direct bearing on the UAS in the NAS project.

The establishment of six FAA UAS test sites in the United States is also generating publicity [32], as is the public’s reaction to UAS in general [33]. Reputable popular media are also contributing, often identifying clear challenges to UAS safety and security [34].

In terms of more technical literature, this too is expanding, with publications on networking, multiple antenna techniques, and some on the air-ground wireless channel as well. Reference [35] is a good review article on the challenges in designing airborne tactical networks. These challenges include an expectation of significantly increasing data rates in the future, latency for long-range links and networks, mobility-induced network topology changes, scarcity of spectrum, and “body blockage” or airframe shadowing. Interference resilient waveforms (e.g., spread spectrum) were cited as critical for these tactical networks.

The authors of [36] describe the L-band Digital Aeronautical Communication System-1 (LDACS1). This article does not compare LDACS1 with competing technologies (as reported in [6], several publications have already done so, with, for example, LDACS1 being superior to LDACS2). Rather, the article provides an overview of the system, and how it has been designed to effectively coexist with existing ground-based distance measuring equipment (DME) transmitters.

In [37], the authors describe how UAS can be used in rescue services after natural disasters. The article provides an overview, and some description of image processing to locate victims. Reference [38] also describes the use of UAS in military settings, with a custom spread-spectrum waveform based upon the 3rd-generation cellular standard WCDMA. The authors briefly discuss required antenna characteristics for their Ku-band system, and show a few example results from a field trial.

Reference [39] provides a summary of UAS network topologies and recommends several protocols for their effective operation. Little technical detail is provided. The authors of [40] consider the use of UAS for serving as LTE base stations. Simulation results are provided for throughput and delay, but unfortunately the channel employed in the simulations is a terrestrial cellular-like channel, so results are of questionable validity.

The effects of interference between aircraft (UAS as well as piloted) and terrestrial systems are addressed in [41]. The authors employ simplified path loss models, plus models for fuselage attenuation, to estimate interference densities and the consequent effects on system capacity. Although not an exceptionally clear treatment of the problem, the analysis does illustrate the potential degradations to both airborne and cellular systems if spectrum management is not enforced.

In [42], the authors describe experiments conducted with very small, or “micro” UAS. Interesting results obtained with WiFi (IEEE 802.11b) radios address the effects of different antenna types on the radio throughput. Their main conclusion is that allowing the WiFi radios to employ their normal adaptation (for physical layer parameters, e.g., modulation and coding), does not yield the largest throughput when the UAS are moving. This is simply because the WiFi system was not

designed with mobility in mind, i.e., the adaptation is not fast enough. The authors also identify shadowing as a significant degrading effect that should be characterized.

Reference [43] describes experiments with UAS in a 200 nautical mile link. Two different radios were used: one a Ku-band radio with a steerable beam antenna, and the other an L-band frequency hopping radio. Both radios had data rates above 1 Mbps. The authors characterize link availability with the two radios for both air-air and air-ground links. Availabilities ranged from as high as 99.9% to as low as 63%, depending on link and flight patterns. Statistics on latency and throughput were also provided.

In [44] the authors analyze the maximum achievable capacity in airborne multiple-input/multiple-output (MIMO) air-air links. The channel model is a pure free space channel, and the analysis is geometry-based, with the assumption of equal aircraft altitudes. No shadowing or multipath propagation was considered, and one main conclusion is that capacity decreases with link distance (as SNR decreases). This paper was an extension of similar work in [45].

The author of [46] conducts a comparison of the spectral efficiency of several types of systems and levels of signal processing complexity in interference limited environments. One system is an air-ground system with 4 by 4 MIMO links. The comparison is via simulation, and the AG channel was modeled as a free space channel without any shadowing or multipath propagation. Results were in terms of spectral efficiency as a function of antennas and cell radius.

A slightly older treatment of MIMO in the AG channel appears in [47]. This paper analyzes MIMO capacity as a function of distance (coming to conclusions similar to those in [44], but with a less rigorous analysis). Another older paper on AG MIMO is [48], in which the authors also assume the same Ricean channel as in [47]. Their main conclusion is that MIMO capacity can approach that of the uncorrelated Rayleigh channel as antenna separation increases, in general agreement with results in [44].

In [49] the authors address the effects of rain on a satellite to ground channel in both L- and C-bands. The most interesting results in this paper show that during heavy rain events, C-band attenuation can increase by up to 4 dB (in general agreement with predictions available via ITU recommendations), and that the differential delay between L-band and C-band signals can reach approximately 68 mm (only 22 ps) during these rain events.

Reference [50] describes measurements made with IEEE 802.11a radios in AG links. The authors characterized throughput versus link distance, with some results resembling two-ray channel variations. The most substantial paper addressing AG channel characteristics we have recently found is [51]. The authors configured an OFDM system to measure channel impulse responses at 2.3 GHz over the island of Oahu, Hawaii. Multiple flight tracks were flown at altitudes 500-1500 m. A large number of multipath components (up to 20) were seen in some flights over populated urban areas, and some with extremely large values of excess delay, up to 30 μ s. No data on path loss or delay spreads were reported.

7. Summary, Conclusions, and Future Work

In this report we provided additional measurement and modeling results on the AG channel. Over-water, hilly/suburban, and over-harbor backlobe environments were addressed. We also described procedures for estimating statistical channel characteristics, namely, our procedure for estimation of the stationarity distance, over which other channel parameters can be estimated, and procedures for estimating small-scale fading (Ricean K -factors) and inter-antenna correlations. We also described our evaluation of the inter-antenna correlations for an analytical (two-ray) channel, for comparison with measurements. Some initial statistics compiled for development of the wideband over-sea channel models were also provided, and the literature review was updated.

The AG channel path loss is best described by the curved-earth two-ray (CE2R) model, plus a Gaussian random variable to account for deviations from this geometric model. The CE2R model pertains best to the over-water channels, and is slightly less accurate for the hilly terrain setting. Complete path loss models for the over-water channels were provided.

In terms of channel dispersion, quantified by RMS-DS σ_{τ} , our results show the expected relationship $\sigma_{\tau,\text{urban}} > \sigma_{\tau,\text{hilly}} > \sigma_{\tau,\text{over-water}}$, and because of the greater number of large obstacles in the freshwater Lake Erie environment than in the ocean area near Oxnard, CA, we also have the relationship $\sigma_{\tau,\text{over-freshwater}} > \sigma_{\tau,\text{over-sea}}$ for our results. The RMS-DS values were quantified for all FTs.

Intra-band correlations should be large in the LOS environments for straight FTs, with rapid variation from -1 to +1 at shorter link distances, and slower variation at longer link distances, in general agreement with measurements. Some the difference between measured and analytical correlations emanates from channel sounder instability, i.e., the varying sample clock drift between Tx and Rx. This does not affect absolute power values significantly, hence it does not affect path loss or RMS-DS, and it has little effect on Ricean K -factors. Inter-band correlations are near zero, as expected.

Fairly large Ricean K -factors were found for both bands, with slight variation with distance in some FTs. As with path loss, the L-band K -factors (smaller than C-band) are more strongly affected by the stronger surface reflection, in both over-water and hilly terrain settings. Stationarity distances computed in the three environments, and for some urban GS data, are all similar at approximately 250 C-band wavelengths, or ~ 15 m.

Future work includes the following:

1. continuation of data processing for the remaining GS environments: desert, urban, and mountainous terrain;
2. completion of computations of inter-antenna correlations after development of a method to remove effects of channel sounder sample clock drift for selected FTs;
3. development of aggregate Ricean K -factor vs. distance models for over-water and hilly terrains;
4. quantification of Ricean fading rates for completion of Ricean fading models;
5. development of hilly terrain path loss models;
6. completion of wideband tapped-delay line statistical models for the over-sea setting;
7. validation of Ricean fading and wideband tapped-delay line simulation models with measurements.

For tasks 3, 5, and 6, model development for the remaining GS environments will also be done, following the model development for the settings specified in these tasks.

References

- [1] D. W. Matolak, "AG Channel Measurements & Modeling: Initial Report on Flight Test Planning and Narrowband Measurements," Report #1 for NASA Glenn Research Center, Grant #NNX12AD53G, 20 March 2012.
- [2] D. W. Matolak, R. Sun, "AG Channel Measurements & Modeling: Initial Analysis & Flight Test Planning," (Report #2) NASA Grant #NNX12AD53G, 8 June 2012.
- [3] D. W. Matolak, R. Sun, "AG Channel Measurements & Modeling: Initial Channel Sounder Laboratory & Flight Tests," (Report #3) NASA Grant # NNX12AR56G, 29 January 2013.
- [4] D. W. Matolak, R. Sun, "AG Channel Measurements & Modeling: Initial Channel Sounder Laboratory & Flight Tests—Supplementary Report," (Report #4) NASA Grant #NNX12AR56G, 1 March 2013.
- [5] D. W. Matolak, R. Sun, "AG Channel Measurements & Modeling: BVS Channel Sounder Performance: Measurement Stability," (Report #5) NASA Grant #NNX12AR56G, 19 April 2013.
- [6] D. W. Matolak, R. Sun, "AG Channel Measurement & Modeling Results for Over-Sea Conditions," (Report #6) NASA Grant #NNX12AR56G, 3 December 2013.
- [7] D. W. Matolak, R. Sun, "Initial Results for Air-Ground Channel Measurements & Modeling for Unmanned Aircraft Systems: Over Sea," *IEEE Aerospace Conference*, Big Sky, MT, 1-8 March 2014.
- [8] D. W. Matolak, R. Sun, "Air-Ground Channel Characterization for Unmanned Aircraft Systems: the Over-Freshwater Setting," *Proc. IEEE Integrated Communications, Navigation, & Surveillance Conf.*, Herndon, VA, 8-10 April 2014. (*Winner of best paper in track.*)
- [9] D. W. Matolak, R. Sun, "Air-Ground Channel Characterization for Unmanned Aircraft Systems: the Hilly Suburban Environment," *IEEE Fall Veh. Tech. Conf.*, Vancouver, BC, Canada, 14-17 Sep. 2014.
- [10] D. W. Matolak, R. Sun, "Antenna and Frequency Diversity in the Unmanned Aircraft Systems Bands for the Over Sea Setting," to appear, *IEEE/AIAA Digital Avionics Systems Conference*, Colorado Springs, CO, 5-9 October 2014
- [11] R. Sun, D. W. Matolak, "Over-Harbor Channel Modeling with Directional Ground Station Antennas for the Air-Ground Channel," to appear, *MILCOM 2014*, Baltimore, MD, 6-8 October 2014.
- [12] D. W. Matolak, R. Sun, "Air-Ground Channel Measurements & Modeling for UAS," to appear, *IEEE Aerospace & Electronic Systems Magazine*, vol. 29, no. 11, November 2014.
- [13] D. W. Matolak, K. Shalkhauser, R. Kerczewski, "L-Band and C-Band Air-Ground Channel Measurement and Modeling for Over-Sea Conditions," International Civil Aviation Organization (ICAO), Aeronautical Communications Panel, WG-F, Bangkok, Thailand, 13 – 19 March 2014.
- [14] D. W. Matolak, "Air-Ground Channel Measurements and Modeling for Unmanned Aircraft Systems," presentation given to RTCA SC-228, Washington, DC, 19 May 2014.
- [15] (*Invited Paper*) D. W. Matolak, "Unmanned Aerial Vehicles: Communications Challenges and Future Aerial Networking," to appear, *International Conference on Computing, Networking and Communications*, Anaheim, CA, 16-19 February 2015.
- [16] E. D. R. Shearman, "Radio Science and Oceanography," *Radio Science*, vol. 18, no. 3, pp. 299-320, May-June 1983.
- [17] C. A. Levis, J. T. Johnson, F. L. Teixeira, *Radiowave Propagation: Physics and Applications*, John Wiley & Sons, Hoboken, NJ, 2010.
- [18] H. V. Hitney, "Refractive Effects from VHF to EHF Part A: Propagation Mechanisms," *Advisory Group for Aerospace Research and Development (AGARD) Lecture Series*, 1994.
- [19] H. V. Hitney, "Refractive Effects from VHF to EHF Part B: Propagation Models," *Advisory Group for Aerospace Research and Development (AGARD) Lecture Series*, 1994.
- [20] International Telecommunications Union (ITU), "Prediction Procedure for the Evaluation of Interference between Stations on the Surface of the Earth at Frequencies Above About 0.1 GHz," *ITU Recommendation ITU-R P.452-15*, September 2013.
- [21] I. J. Timmins, S. O'Young, "Marine Communications Channel Modeling Using the Finite-Difference Time-Domain Method," *IEEE Trans. Veh. Tech.*, vol. 58, no. 6, pp. 2626-2637, July 2009.

[22] W. C. Y. Lee, "Estimate of Local Average Power of a Mobile Radio Signal," *IEEE Trans. Veh. Tech.*, vol. VT-34, no. 1, pp. 22-27, February 1985.

[23] A. Gehring, M. Steinbauer, I. Gaspard, M. Grigat, "Empirical Channel Stationarity in Urban Environments," *4th European Personal & Mobile Comm. Conf. (EPMCC 2001)*, Vienna, Austria, 20-22 February 2001.

[24] J. D. Parsons, *The Mobile Radio Propagation Channel*, 2nd ed., John Wiley & Sons, New York, NY, 2000.

[25] H. V. Hitney, "Refractive Effects from VHF to EHF Part B: Propagation Models," *Advisory Group for Aerospace Research and Development (AGARD) Lecture Series*, 1994.

[26] National Climatic Data Center, website, www.ncdc.noaa.gov, 20 March 2014.

[27] D. W. Matolak; J. Frolik, "Worse-than-Rayleigh fading: Experimental results and theoretical models," *IEEE Comm. Mag.*, vol.49, no.4, pp.140-146, April 2011.

[28] P. F. Driessen, "Prediction of Multipath Delay Profiles in Mountainous Terrain," *IEEE Journ. Selected Areas Comm.*, vol. 18, no. 3, pp. 336-346, March 2000.

[29] American Institute of Aeronautics and Astronautics, "Daily Launch" AIAA news email, 24 September 2014.

[30] Cable News Network (CNN), "Tourist Reportedly Crashes Drone into Yellowstone National Park's Largest Hot Spring," CNN website, http://www.cnn.com/2014/08/07/us/drones-yellowstone/index.html?hpt=hp_t2 , 7 August 2014.

[31] United Airlines, "Tech Special, The Technology: Personal Drones," *Hemispheres Magazine*, pp. 94, April 2014.

[32] D. Werner, "Preparing for the Era of Unmanned Planes," *Aerospace America*, AIAA, pp. 38-42, September 2014.

[33] D. Schneider, "Open Season on Drones," *IEEE Spectrum*, pp. 32-33, January 2014.

[34] K. Wesson, T. Humphreys, "Hacking Drones," *Scientific American*, pp. 55-59, November 2013.

[35] B. N. Cheng, F. J. Block, B. R. Hamilton, D. Ripplinger, C. Timmerman, L. Veytser, A. N. Tam, "Design Considerations for Next-Generation Airborne Tactical Networks," *IEEE Comm. Mag.*, vol. 52, no. 5, pp. 138-145, May 2014.

[36] M. Schnell, U. Epple, D. Shutin, N. Schneckenberger, "LDACS: Future Aeronautical Communications for Air Traffic Management," *IEEE Comm. Mag.*, vol. 52, no. 5, pp. 104-110, May 2014.

[37] L. Apvrille, T. Tanzi, J. L. Dugelay, "Autonomous Drones for Assisting Rescue Services within the Context of Natural Disasters," *Proc. URSI General Assembly*, Beijing, China, 17-23 August 2014.

[38] M. S. Jean-Christophe, M. M. Francois, M. Melanie, M. P. Guy, "The Airborne Communication Node: the Backbone of the Theatre for Network Centric Operations," *Proc. NATO Symp. Military Communications*, RTO-MP-IST-083, April 2008.

[39] J. Li, Y. Zhou, L. Lamont, "Communication Architectures and Protocols for Networking Unmanned Aerial Vehicles," *Proc. Globecom 2013, Workshop on Wireless Networking and Control for Unmanned Autonomous Vehicles*, Atlanta, GA, 9-13 December 2013.

[40] K. Gomez, T. Rasheed, L. Reynau, S. Kandeepan, "On the Performance of Aerial LTE Base Stations for Public Safety and Emergency Rescue," *Proc. Globecom 2013, Workshop on Wireless Networking and Control for Unmanned Autonomous Vehicles*, Atlanta, GA, 9-13 December 2013.

[41] N. Moraitis, A. D. Panagopoulos, "Multiple Airborne Radio Interference to Cellular Networks: a Statistical Approach," *IEEE Aerospace & Electronics Systems Magazine*, pp. 21-27, November 2013.

[42] M. Asadpour, B. VandenBergh, D. Giustiniano, K. A. Hummel, S. Pollin, B. Plattner, "Micro Aerial Vehicle Networks: An Experimental Analysis of Challenges and Opportunities," *IEEE Comm. Mag.*, vol. 52, no. 7, pp. 141-149, July 2014.

[43] B. N. Cheng, R. Charland, P. Christensen, L. Veytser, J. Wheeler, "Evaluation of Multihop Airborne IP Backbone with Heterogeneous Radio Technologies," *IEEE Trans. Mobile Computing*, vol. 13, no. 2, pp. 299-310, February 2014.

[44] W. Su, J. D. Matyjas, M. J. Gans, S. Batalama, "Maximum Achievable Capacity in Airborne MIMO Communications with Arbitrary Alignments of Linear Transceiver Antenna Arrays," *IEEE Trans. Wireless Comm.*, vol. 12, no. 11, pp. 5584-5593, November 2013.

- [45] M. J. Gans, "Aircraft Free-Space MIMO Communications," *Proc. Asilomar Conf. on Signals, Systems, & Computers*, Pacific Grove, CA, November 2009.
- [46] B. F. McGuffin, "Spectral Efficiency of Signal Processing Radios in Interference Limited Environments: Array Processing, MIMO, and MUD," *Proc. Milcom 2012*, Orlando, FL, 29 October-1 November 2012.
- [47] C. Zhang, Y. Hui, "Broadband Air-to-Ground Communications with Adaptive MIMO Datalinks," *Proc. DASC*, Seattle, WA, 16-20 October 2011.
- [48] J. Rasool, G. E. Oien, J. E. Hakegard, T. A. Myrvoll, "On Multiuser MIMO Capacity Benefits in Air-to-Ground Communication for Air Traffic Management," *Proc. 6th Int. Symp. on Wireless Comm. Systems*, Siena, Italy, 7-10 September 2009.
- [49] M. Schonhuber, S. Junker, I. Bartunkova, K. Plimon, R. O. Perez, "Synchronized Measurements of L- and C-band Tropospheric Propagation Parameters," *Proc. EuCAP 2014*, The Hague, Netherlands, 6-11 April 2014.
- [50] E. Yanmaz, R. Kuschnig, C. Bettstetter, "Channel Measurements over 802.11a-based UAV-to-Ground Links," *Proc. Globecom 2011*, Houston, Tx, 5-9 December 2011.
- [51] K. Tekizawa, F. Ono, M. Suzuki, H. Tsuji, R. Miura, "Measurement on S-band Radio Propagation Characteristics for Unmanned Aircraft Systems," *Proc. EuCAP 2014*, The Hague, Netherlands, 6-11 April 2014.
- [52] J. G. Proakis, *Digital Communications*, 4th ed., McGraw-Hill, New York, NY, 2001.
- [53] L. J. Greenstein, S. S. Ghassemzadeh, V. Erceg, D. G. Michelson, "Ricean K-Factors in Narrow-Band Fixed Wireless Channels: Theory, Experiments, and Statistical Models," *IEEE Trans. Vehicular Tech.*, vol. 58, no. 8, pp. 4000-4012, Oct. 2009.
- [54] C. Tepedelenlioglu, A. Abdi, G. B. Giannakis, "The Ricean K factor: estimation and performance analysis," *IEEE Trans. Wireless Comm.*, vol. 2, no. 4, pp. 799-810, July 2003.
- [55] G. Dyer, T. Gilbert, S. Hendrickson, E. Sayadian, "Mobile Propagation Measurements using CW and Sliding Correlator Techniques," *Proc. IEEE Ant. Propagation Symposium*, Atlanta, GA, 1998.

Appendix A: Results from Additional Flight Tracks

This appendix contains path loss, delay spread, spatial correlation and Ricean K -factor results for the over-freshwater and hilly terrain settings, for the remaining flight tracks not described in the main body of the report. New K -factor results, and some new correlation results for the over-sea FTs, are also provided. Most of the results are presented without discussion because of their similarity to those for FTs reported in the report's main body (or in that of [6]), but some atypical results are briefly described. The analysis of all results here has *not* been completed, and this will be done in the near future. Also, complete results for all FTs in this Appendix are not yet available: for examples, for the hilly terrain FT10, much of the data may be invalid, since the sounder PDP update rate was unusually small, and significant terrain shadowing was present. Note also that all tabulated results in this appendix, for path loss parameters, correlations, and K -factors, are “per-FT. For data in this appendix that we are confident is *invalid*, we have highlighted table entries or figure captions in grey.

In Tables A1 and A2 we list the basic information of the over-freshwater and hilly terrain FTs including shape, range of distances, velocity and number of PDPs. We also provide an expanded description of the over-sea FTs in Table A3. Note that the over-freshwater FT2 in Table A1 was already described in detail in the main body of the report; the FT details are shown here in Table A1 for completeness.

Table A1. Descriptions of FTs for over freshwater FTs, Cleveland, OH, 22 October 2013.

	Band	Rx Index	# PDPs	Time duration Δt (s)	Average velocity (m/s)	PDP update rate (Hz)	d_{min} (km)	d_{max} (km)
FT2, flew straight toward GS	C-band	Rx1	1080854	367	73.1	2942	2.51	29.35
		Rx2	1077204	367	73.1	2933	2.51	29.34
	L-band	Rx1	1109829	390	65.3	2843	0.97	29.35
		Rx2	1136858	390	65.3	2912	0.97	29.35
FT3, flew straight away from GS	C-band	Rx1	1039849	353	76.9	2948	1.21	28.09
		Rx2	912903	353	76.9	2588	1.21	28.09
	L-band	Rx1	974564	360	76.8	2708	0.76	28.09
		Rx2	995626	360	76.9	2766	0.76	28.09
FT4, Oval FT	C-band	Rx1	1691453	586	76.6	2884	16.31	21.76
		Rx2	1632930	586	76.5	2785	16.31	21.76
	L-band	Rx1	1513727	586	76.3	2581	16.31	21.76
		Rx2	1599337	586	76.4	2727	16.31	21.76

Table A2. Descriptions of FTs in hilly terrain, Latrobe, PA, 15 April 2013.

	Band	Rx Index	# PDPs	Time duration Δt (s)	Average velocity (m/s)	PDP update rate (Hz)	d_{min} (km)	d_{max} (km)
FT1, flew straight toward GS	<i>C-band</i>	Rx1	443224	205	74.6	2157	2.27	17.46
		Rx2	411707	205	74.6	2005	2.27	17.45
	<i>L-band</i>	Rx1	455082	222	74.6	2054	1.27	17.46
		Rx2	478889	221	74.5	2162	1.27	17.45
FT2, flew straight away from GS	<i>C-band</i>	Rx1	352034	170	91.9	2072	1.39	16.91
		Rx2	309421	170	91.8	1820	1.39	16.91
	<i>L-band</i>	Rx1	385010	179	92.1	2153	0.79	16.91
		Rx2	403085	179	92.0	2254	0.79	16.91
FT3, flew straight toward GS	<i>C-band</i>	Rx1	425798	195	74.3	2184	2.25	16.60
		Rx2	396254	195	74.3	2033	2.25	16.60
	<i>L-band</i>	Rx1	467080	214	74.2	2187	1.03	16.60
		Rx2	446435	213	74.2	2091	1.03	16.60
FT4, flew straight away from GS	<i>C-band</i>	Rx1	338902	164	90.0	2069	1.28	15.80
		Rx2	301524	164	89.9	1841	1.28	15.81
	<i>L-band</i>	Rx1	337449	171	89.9	1979	0.79	15.80
		Rx2	313380	171	89.8	1837	0.79	15.80
FT5, flew straight away from GS	<i>C-band</i>	Rx1	286055	272	90.0	1052	17.01	41.49
		Rx2	181805	272	90.1	669	17.02	41.49
	<i>L-band</i>	Rx1	493141	272	90.0	1814	17.00	41.49
		Rx2	453757	272	90.0	1670	17.01	41.49
FT6, Oval FT	<i>C-band</i>	Rx1	1131539	731	83.2	1549	15.60	24.00
		Rx2	894030	730	81.5	1224	15.60	24.00
	<i>L-band</i>	Rx1	1244883	731	82.4	1704	15.60	24.00
		Rx2	1285370	731	82.6	1760	15.60	24.00
FT7, Oval FT	<i>C-band</i>	Rx1	974889	672	81.2	1452	15.83	23.76
		Rx2	814172	672	79.4	1212	15.83	23.76
	<i>L-band</i>	Rx1	1219353	672	81.5	1815	15.83	23.76
		Rx2	1257997	672	81.4	1873	15.83	23.76
FT8, flew straight toward GS	<i>C-band</i>	Rx1	293118	165	90.5	1772	2.50	17.52
		Rx2	279700	121	90.4	2319	2.50	13.33
	<i>L-band</i>	Rx1	219470	180	91.3	1219	1.24	17.53
		Rx2	223819	180	91.2	1244	1.24	17.51
FT9, flew straight away from GS	<i>C-band</i>	Rx1	357710	200	75.9	1792	1.98	17.02
		Rx2	323670	200	76.0	1621	1.98	17.02
	<i>L-band</i>	Rx1	259612	212	76.8	1225	1.22	17.02
		Rx2	263313	212	76.8	1242	1.22	17.02
FT10, Oval FT	<i>C-band</i>	Rx1	23545	196	85.8	120	19.19	23.95
		Rx2	14600	196	87.2	75	19.20	23.95
	<i>L-band</i>	Rx1	39826	196	86.9	203	19.19	23.95

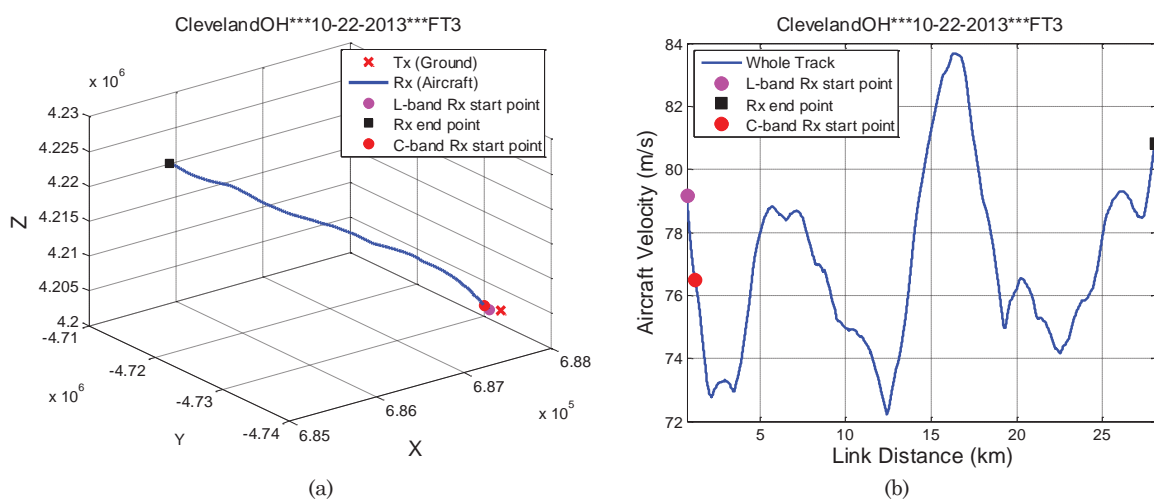
		Rx2	46449	196	86.7	237	19.19	23.95
FT11, Oval FT	<i>C-band</i>	Rx1	616485	641	85.9	962	13.28	19.84
		Rx2	514186	641	86.6	803	13.28	19.84
	<i>L-band</i>	Rx1	690892	641	85.5	1078	13.28	19.84
		Rx2	786794	641	85.4	1228	13.28	19.84
FT12, Oval FT	<i>C-band</i>	Rx1	668296	522	90.2	1281	12.34	19.58
		Rx2	561444	521	90.7	1077	12.34	19.58
	<i>L-band</i>	Rx1	798047	522	89.0	1530	12.34	19.58
		Rx2	861001	522	88.5	1651	12.34	19.58
FT13, flew straight toward GS	<i>C-band</i>	Rx1	288092	157	94.8	1836	2.50	17.16
		Rx2	271241	157	94.8	1730	2.50	17.16
	<i>L-band</i>	Rx1	260000	161	95.0	1619	2.24	17.17
		Rx2	250000	156	95.0	1598	2.57	17.16

Table A3. Descriptions of FTs for over sea FTs, Oxnard, CA, 11 June 2013.

	Band Index	Rx Index	# PDPs	Time duration Δt (s)	Average velocity (m/s)	PDP update rate (Hz)	d_{min} (km)	d_{max} (km)
FT1, flew straight towards the GS	<i>C-band</i>	Rx1	693717	235	94.8	2954	2.50	24.15
		Rx2	690832	235	94.8	2943	2.50	24.15
	<i>L-band</i>	Rx1	683450	240	94.8	2850	2.22	24.15
		Rx2	679470	240	94.8	2834	2.22	24.15
FT2, flew straight away from the GS	<i>C-band</i>	Rx1	1360107	460	94.9	2955	1.88	45.24
		Rx2	1333364	460	94.9	2896	1.88	45.25
	<i>L-band</i>	Rx1	1338635	470	94.8	2847	1.18	45.24
		Rx2	1361656	470	94.8	2896	1.18	45.25
FT3, flew straight towards the GS	<i>C-band</i>	Rx1	976201	330	91.8	2954	18.81	48.99
		Rx2	976374	330	91.8	2955	18.81	48.98
	<i>L-band</i>	Rx1	950131	330	91.8	2875	18.82	48.99
		Rx2	958074	330	91.8	2899	18.81	48.99
FT4, Oval FT	<i>C-band</i>	Rx1	1926266	686	88.4	2809	19.52	26.79
		Rx2	1841367	686	88.5	2686	19.52	26.79
	<i>L-band</i>	Rx1	1999086	686	88.4	2915	19.52	26.79
		Rx2	2013971	686	88.4	2937	19.52	26.79
FT5, Oval FT	<i>C-band</i>	Rx1	1834243	645	89.0	2844	19.33	26.76
		Rx2	1662261	645	89.1	2577	19.33	26.76
	<i>L-band</i>	Rx1	1859686	645	89.0	2883	19.33	26.76
		Rx2	1878599	645	89.0	2912	19.33	26.76
FT6, Oval FT	<i>C-band</i>	Rx1	1810296	645	89.8	2807	18.91	27.33
		Rx2	1664753	645	90.0	2582	18.91	27.33
	<i>L-band</i>	Rx1	1863404	645	89.8	2889	18.91	27.33
		Rx2	1886979	645	89.8	2926	18.91	27.33
FT7, Oval FT	<i>C-band</i>	Rx1	1827301	645	90.0	2832	19.32	27.75

		Rx2	1609671	645	90.2	2495	19.32	27.75
FT8, flew straight towards the GS	L-band	Rx1	1798433	645	90.1	2788	19.32	27.75
		Rx2	1838679	645	90.0	2850	19.32	27.75
	C-band	Rx1	795032	268	87.8	2966	2.50	25.76
FT9, flew straight away from the GS	L-band	Rx1	785290	268	87.8	2930	2.50	25.75
		Rx2	818696	284	87.8	2885	1.29	25.76
	C-band	Rx1	825874	284	87.8	2911	1.29	25.75
		Rx2	1528210	520	86.2	2937	1.79	46.04
FT10, flew straight towards the GS	L-band	Rx1	1470922	520	86.1	2827	1.79	46.05
		Rx2	1549847	531	86.1	2916	1.04	46.04
	C-band	Rx1	1556759	532	86.1	2929	1.04	46.05
		Rx2	876770	305	90.1	2871	19.15	45.18
FT11, Oval FT	L-band	Rx1	873236	305	90.1	2860	19.15	45.18
		Rx2	886269	305	90.1	2902	19.15	45.18
	C-band	Rx1	893365	305	90.1	2926	19.15	45.18
		Rx2	1357075	706	79.6	1922	19.28	26.56
FT12, Oval FT	C-band	Rx1	1422747	706	79.6	2015	19.28	26.56
		Rx2	1656305	755	79.8	2195	19.27	27.09
	L-band	Rx1	1461223	755	79.9	1936	19.27	27.09
		Rx2	1505207	755	79.9	1995	19.27	27.09
			1550215	755	79.9	2054	19.27	27.09

A.1 Over Fresh Water Flight Track 3



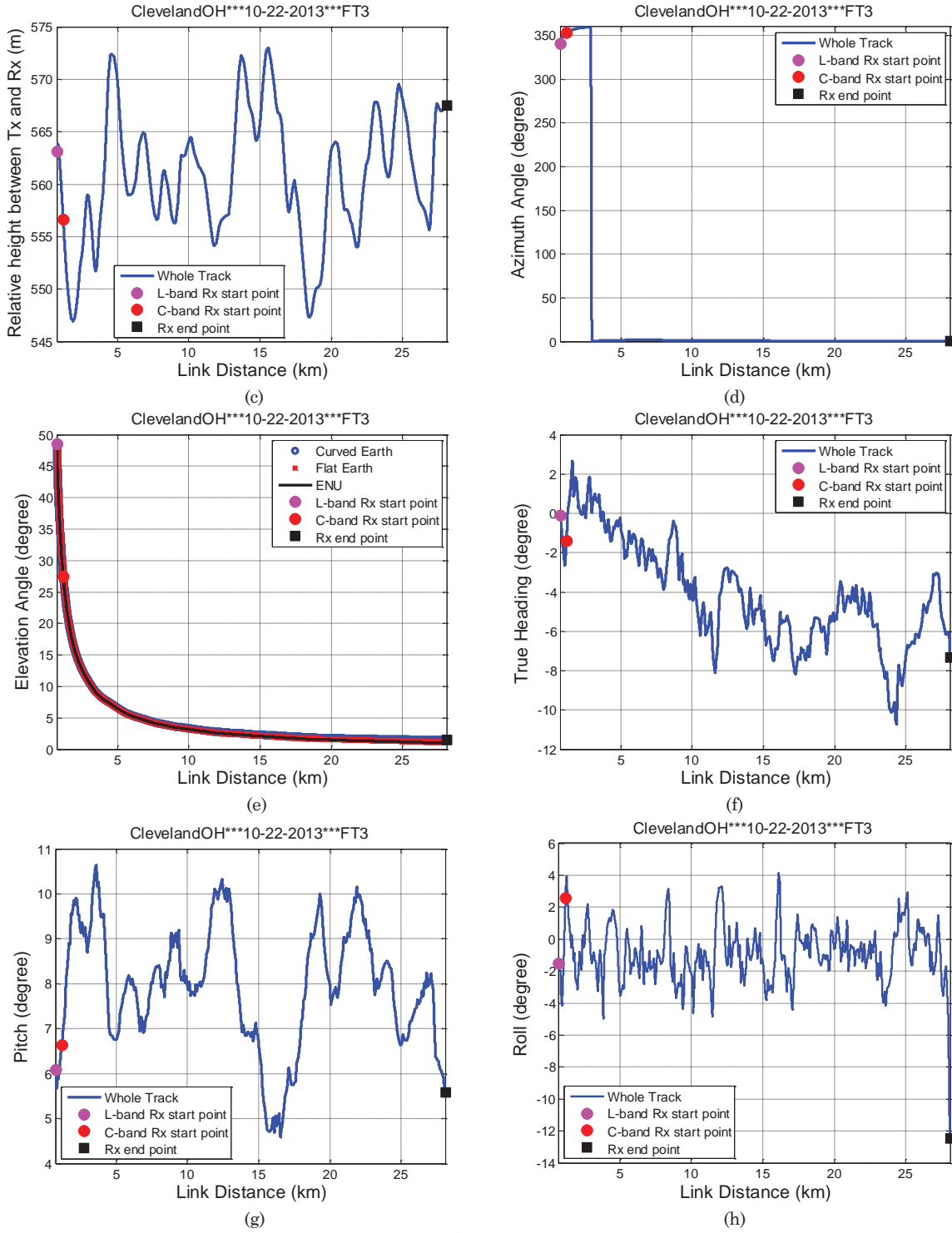


Figure A1. Geometric traces for FT3: (a) flight track in ECEF coordinates; (b) aircraft velocity; (c) altitude difference between aircraft and ground station; (d) azimuth angle; (e) elevation angle; (f) heading of aircraft; (g) pitch angle of aircraft; (h) roll angle of aircraft.

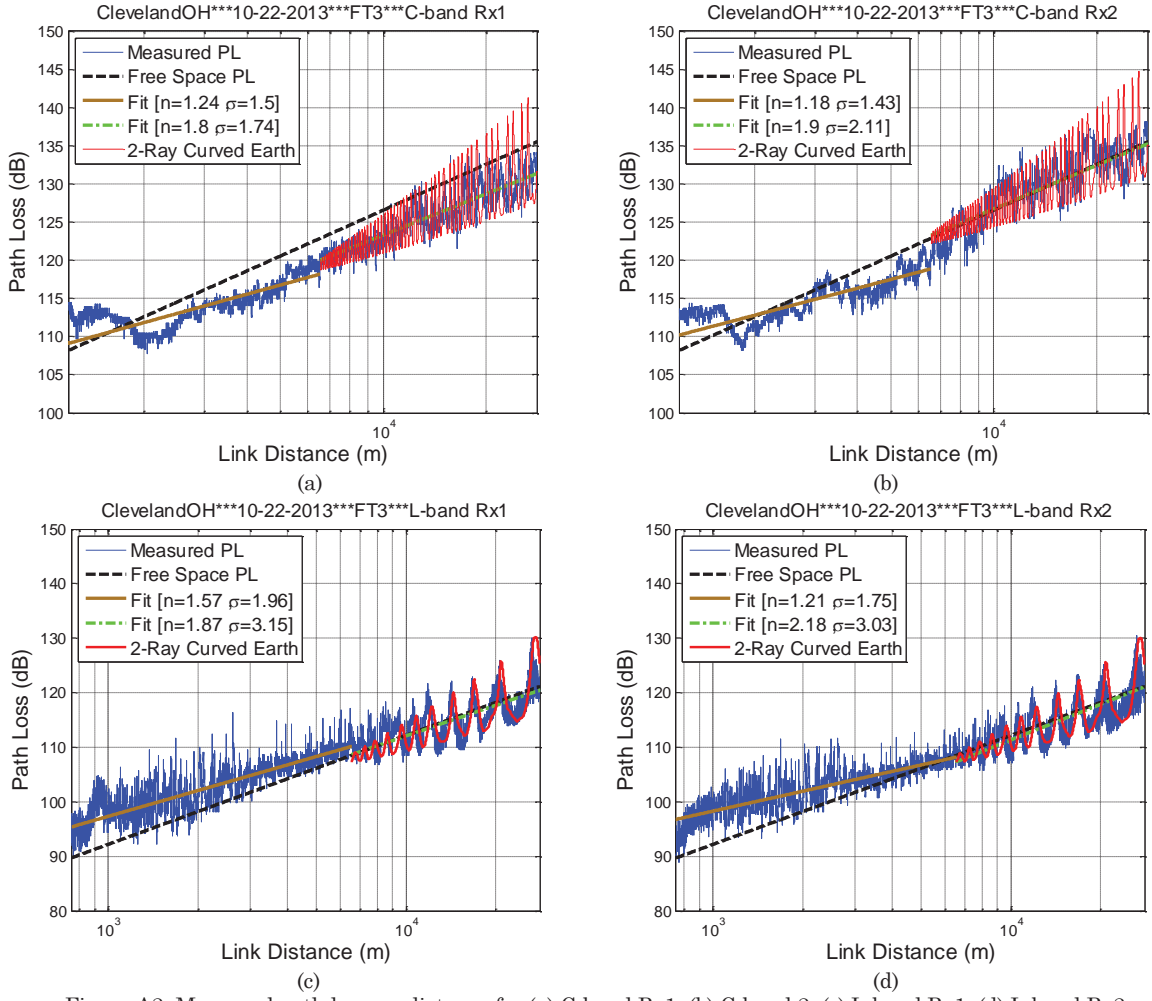


Figure A2. Measured path loss vs. distance for (a) C-band Rx1; (b) C-band 2; (c) L-band Rx1; (d) L-band Rx2.

Table A4. Path Loss Model, FT3, Cleveland, OH, 22 October 2013, straight flight away from GS.

		$d < d_t (\theta > \theta_i)$						$d > d_t (\theta < \theta_i)$									
		Log-distance linear PL model			Elevation angle range (degree)		Distance range (km)		Log-distance linear PL model			CE2R (dB)		Elevation angle range (degree)		Distance range (km)	
		$A_{0,S}$ (dB)	n_S	$\sigma_{XL,S}$ (dB)	$\theta_{min,S}$	$\theta_{max,S}$	$d_{min,S}$	$d_{max,S}$	$A_{0,L}$ (dB)	n_L	$\sigma_{XL,L}$ (dB)	L_0	σ_{X2}	$\theta_{min,L}$	$\theta_{max,L}$	$d_{min,L}$	$d_{max,L}$
	C-Rx1	71.0	1.2	1.5	5.0	27.5	1.2	6.6	51.3	1.8	1.7	-3.5	4.1	1.4	5.0	6.6	28.1
	C-Rx2	73.8	1.2	1.4	5.0	27.5	1.2	6.6	50.8	1.9	2.1	0.0	3.9	1.4	5.0	6.6	28.1
	L-Rx1	50.2	1.6	2.0	5.0	48.5	0.8	6.6	37.3	1.9	3.2	-0.6	3.0	1.4	5.0	6.6	28.1
	L-Rx2	61.9	1.2	1.7	5.0	48.5	0.8	6.6	24.3	2.2	3.0	-0.8	2.9	1.4	5.0	6.6	28.1

Note that some of the RMS-DS results in Fig. A.3 show values below our minimum value of 10 ns (near zero). This may be due to a very weak signal at large distances, in which case only the LOS component was above our threshold. It may also be attributable to variation in the channel sounder. In any case, such small values are inconsequential.

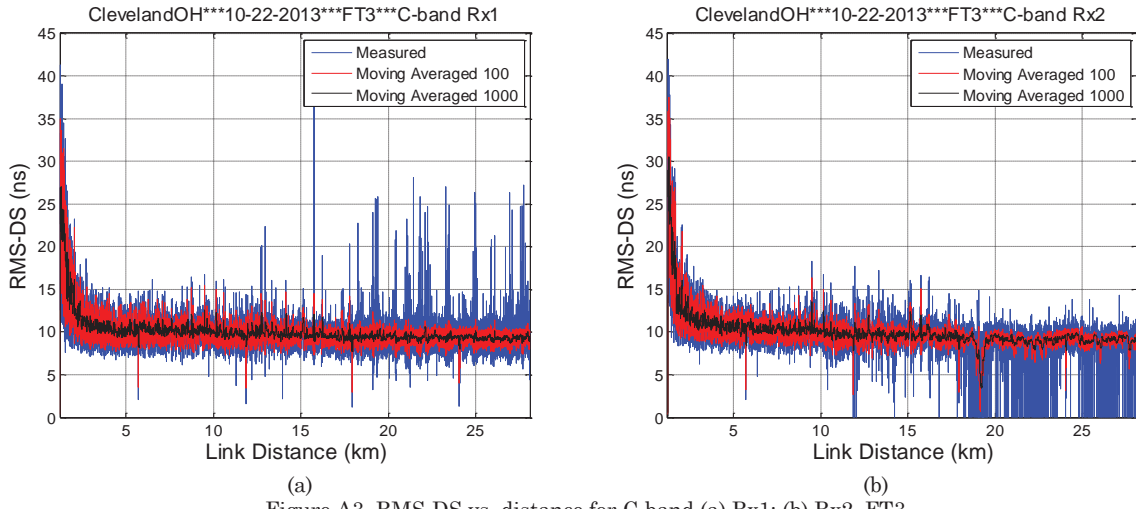


Figure A3. RMS-DS vs. distance for C-band (a) Rx1; (b) Rx2, FT3.

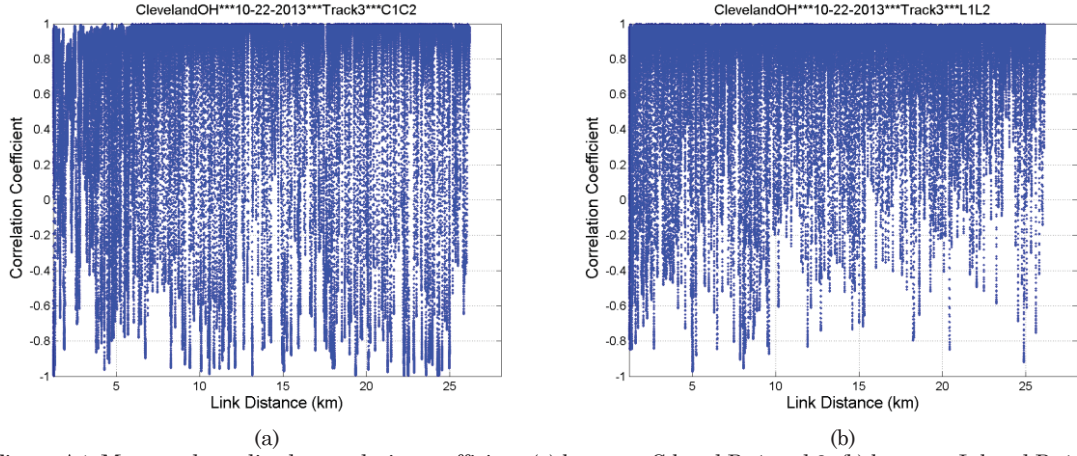


Figure A4. Measured amplitude correlation coefficient (a) between C-band Rx1 and 2; (b) between L-band Rx1 and 2 for FT3.

Table A5. Statistics of Spatial Correlation, FT3, Cleveland, OH, 22 October 2013.

	C1C2	L1L2	C1L1	C1L2	C2L1	C2L2
Window Length	98	98	98	98	98	98
Mean	0.62	0.76	0.03	0.01	0.02	0.01
Median	0.94	0.96	0.00	0.01	0.00	0.00
Max	1.00	1.00	1.00	0.78	1.00	1.00
Min	-1.00	-0.97	-1.00	-0.78	-1.00	-1.00
Standard deviation	0.55	0.39	0.77	0.16	0.77	0.77

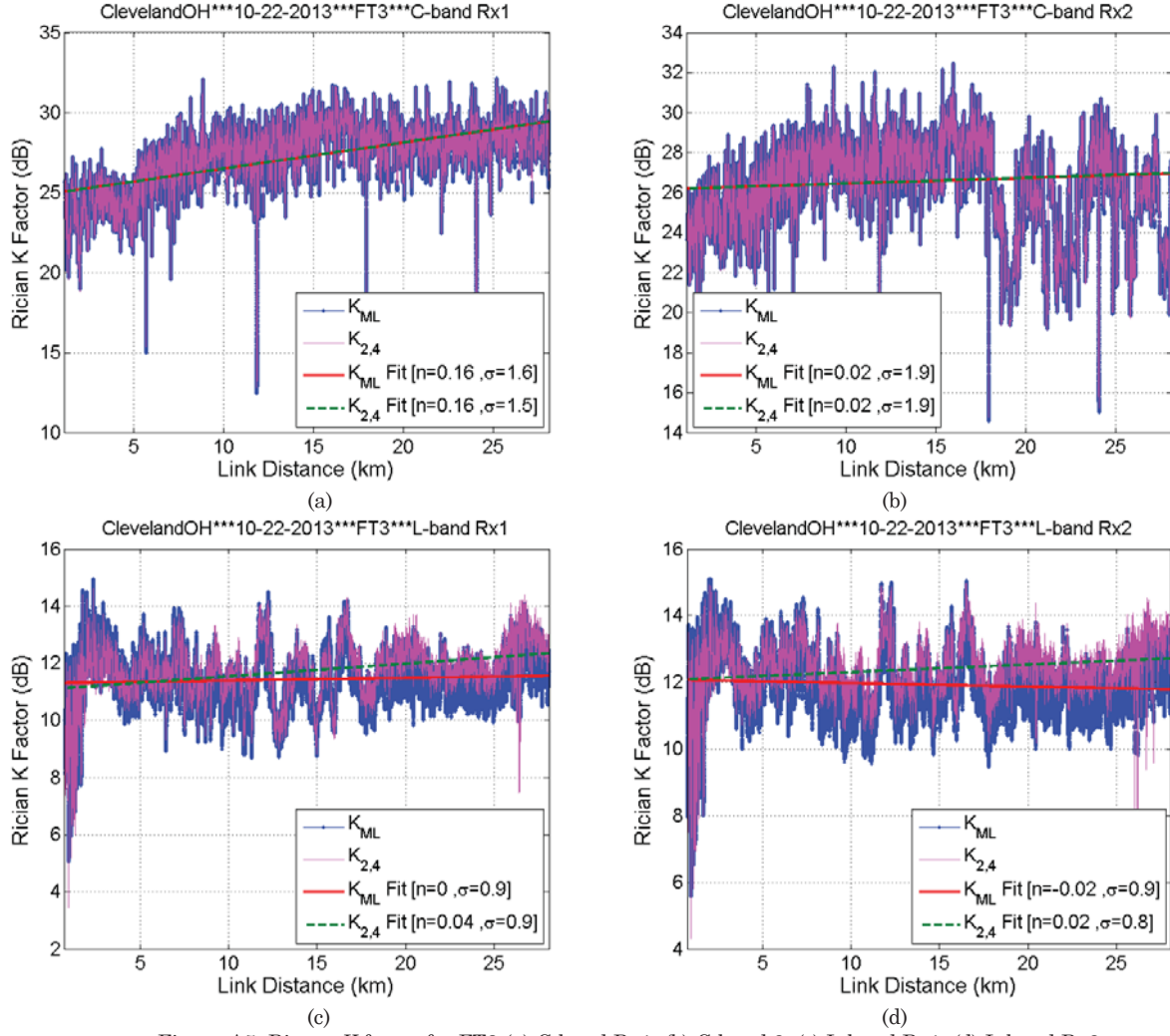
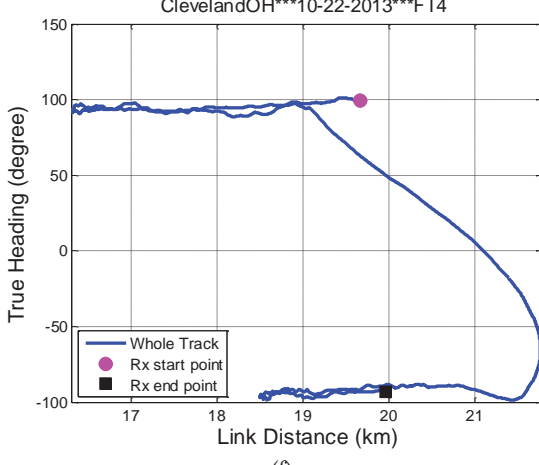
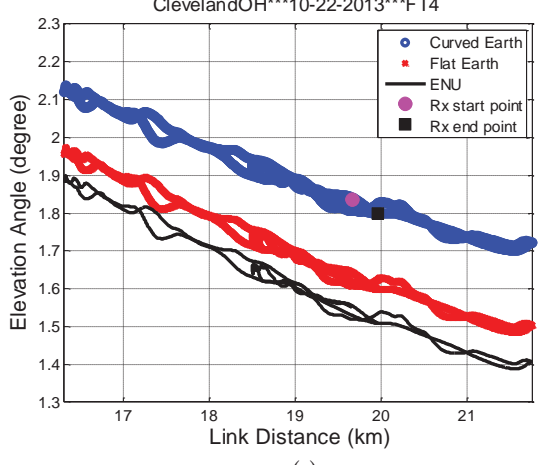
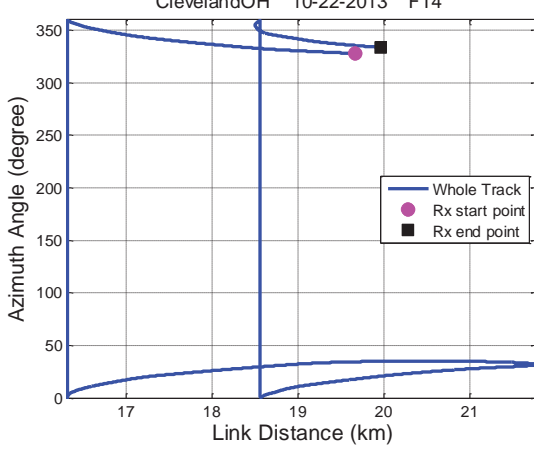
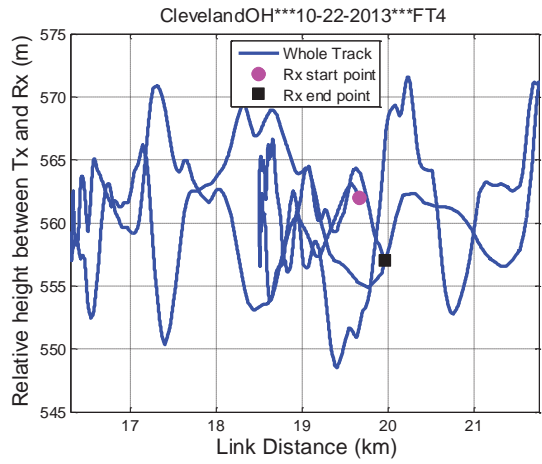
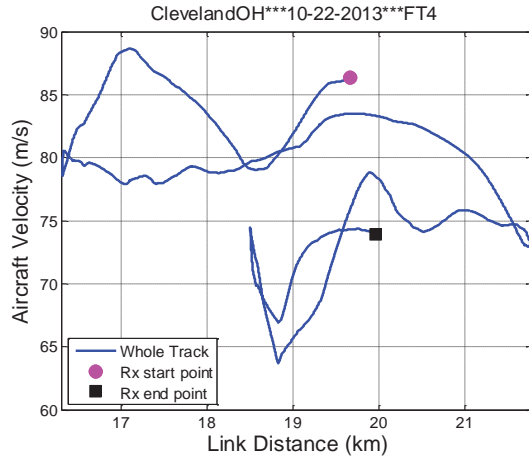
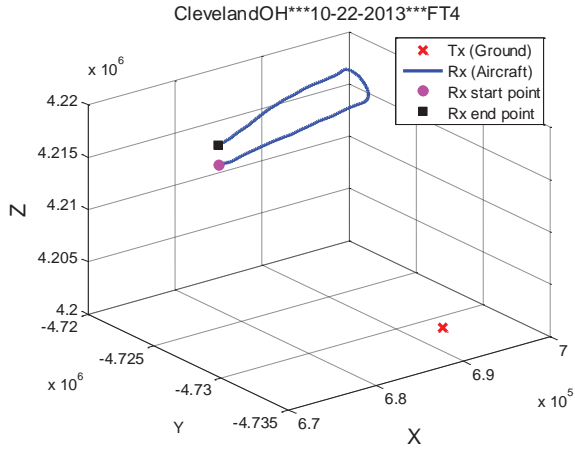


Figure A5. Ricean K factor for FT3 (a) C-band Rx1; (b) C-band 2; (c) L-band Rx1; (d) L-band Rx2.

Table A6. Statistics of Ricean K factor, FT3, Cleveland, OH, 22 October 2013, straight flight away from GS

			C-band						L-band						
			Rx1			Rx2			Rx1			Rx2			
Moving Window Length			250λ						15 m						
Overall K factor (dB)			26.4			25.7			11.3			11.8			
Methods	K_{ML}	K_2	$K_{2,4}$	K_{ML}	K_2	$K_{2,4}$	K_{ML}	K_2	$K_{2,4}$	K_{ML}	K_2	$K_{2,4}$	K_{ML}	K_2	$K_{2,4}$
Linear fit of K factor	A (dB)	24.9	22.5	24.9	26.2	23.7	26.2	11.3	10.6	11.1	12.1	11.6	12.1	11.6	12.1
	n	0.16	0.13	0.16	0.03	0.01	0.03	0.01	0.07	0.04	-0.01	0.05	0.02		
	σ_x (dB)	1.6	3.0	1.6	2.0	3.3	2.0	1.0	1.2	1.0	0.9	1.1	0.9		
Statistics of K factor (dB)	Max	32.1	32.1	32.1	32.5	32.0	32.5	14.9	-17.5	14.6	15.1	15.0	15.0		
	Min	12.4	10.0	12.8	14.6	10.3	14.8	5.0	0.0	3.5	5.6	-1.9	4.3		
	Median	27.2	24.4	27.2	26.5	23.7	26.5	11.4	11.6	11.7	11.9	12.2	12.4		
	μ	27.7	24.7	27.7	26.8	24.3	26.8	11.4	11.7	11.8	11.9	12.4	12.4		
	σ	2.0	3.2	2.0	2.0	3.3	2.0	1.0	1.3	1.0	1.0	1.2	0.9		

A.2 Over Fresh Water Flight Track 4



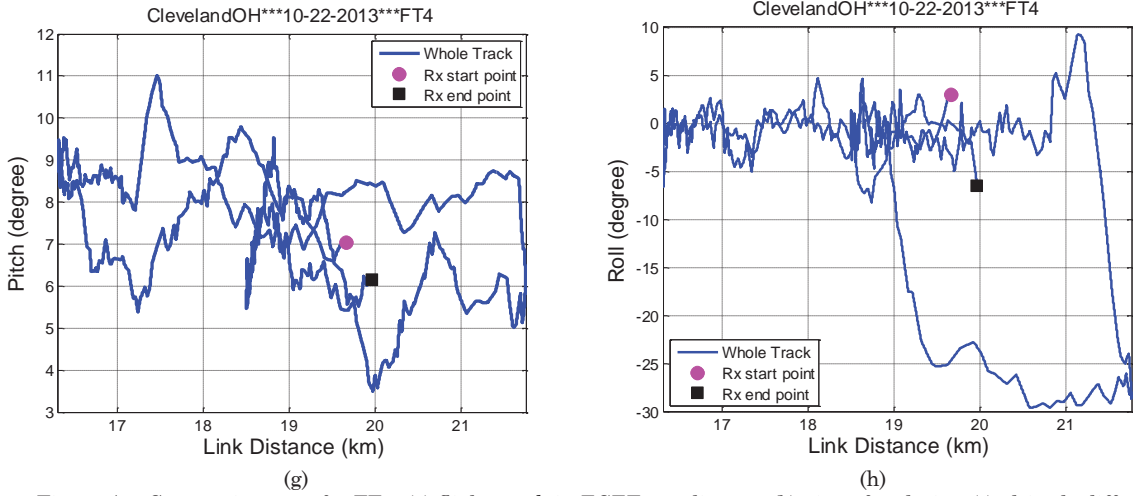


Figure A6. Geometric traces for FT4: (a) flight track in ECEF coordinates; (b) aircraft velocity; (c) altitude difference between aircraft and ground station; (d) azimuth angle; (e) elevation angle; (f) heading of aircraft; (g) pitch angle of aircraft; (h) roll angle of aircraft.

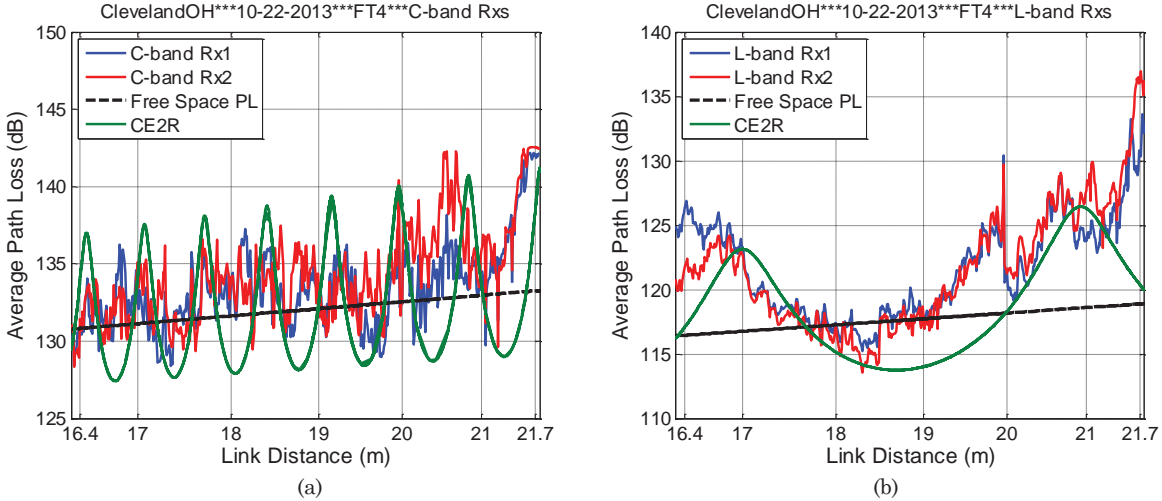


Figure A7. Measured path loss vs. distance for (a) C-band Rx1 & 2; (b) L-band Rx1 & 2.

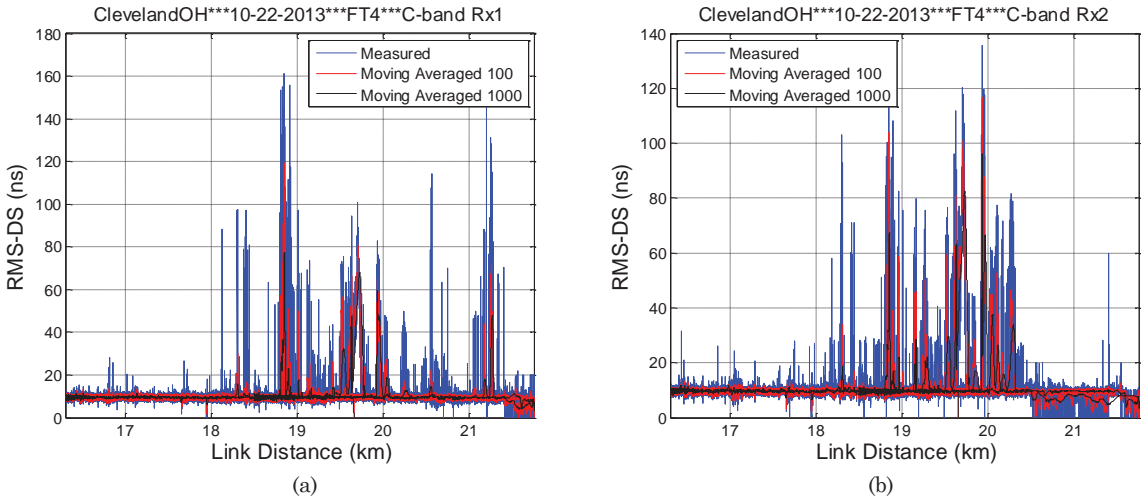


Figure A8. RMS-DS vs. distance for C-band (a) Rx1; (b) Rx2, FT4.

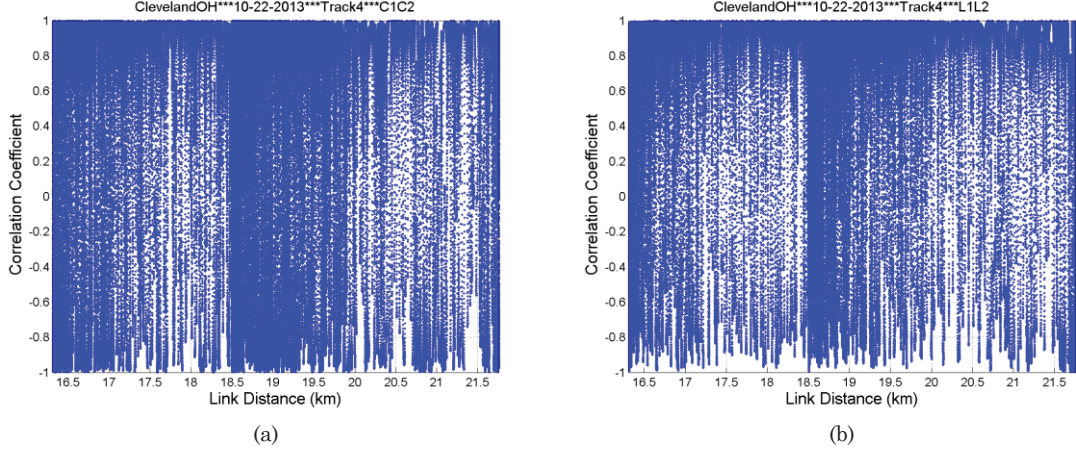
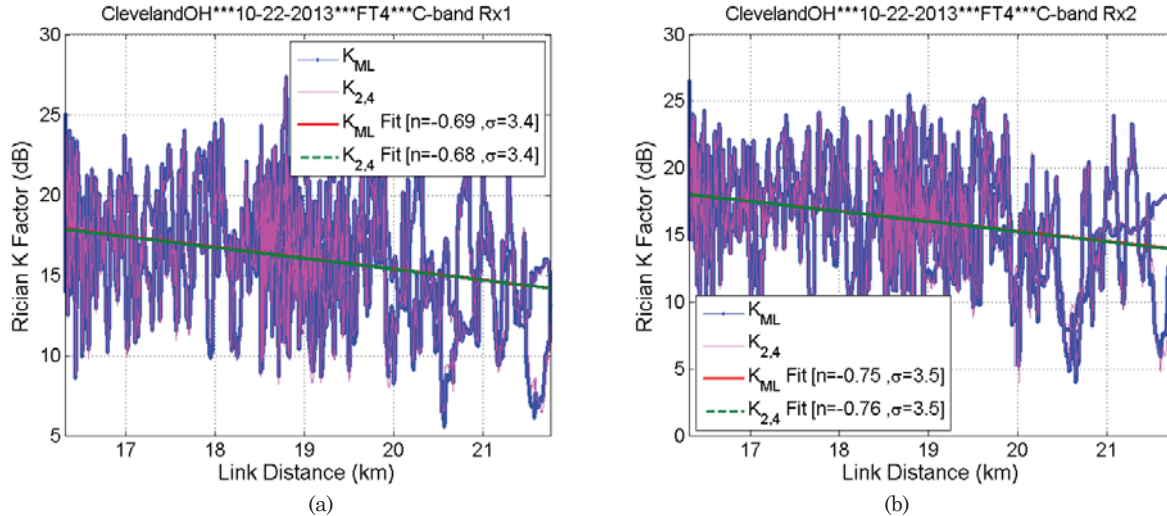


Figure A9. Measured amplitude correlation coefficient (a) between C-band Rx1 and 2; (b) between L-band Rx1 and 2 for FT4.

Table A7. Statistics of Spatial Correlation, FT4, Cleveland, OH, 22 October 2013.

	C1C2	L1L2	C1L1	C1L2	C2L1	C2L2
Window Length	98	98	98	98	98	98
Mean	0.42	0.59	0.01	0.00	0.02	0.00
Median	0.85	0.91	0.03	0.00	0.06	0.00
Max	1.00	1.00	1.00	0.58	1.00	0.61
Min	-1.00	-1.00	-1.00	-0.58	-1.00	-0.73
Standard deviation	0.72	0.59	0.80	0.13	0.80	0.13

The small K -factors at large distances in Figure A.15 are likely due to wing (fuselage) shadowing since the roll angle was near -30 degrees, thus significantly attenuating the LOS component. The L-band path loss is also larger than expected as a result of this shadowing. The C-band K -factor is smaller than the values in the straight FTs, whereas the C-band path loss is larger than in the straight FTs. Interestingly, the shadowing effect appears to be less severe in C-band, and this is unexpected—we expect shadowing to more strongly attenuate the C-band signal. This is a topic for future investigation of shadowing.



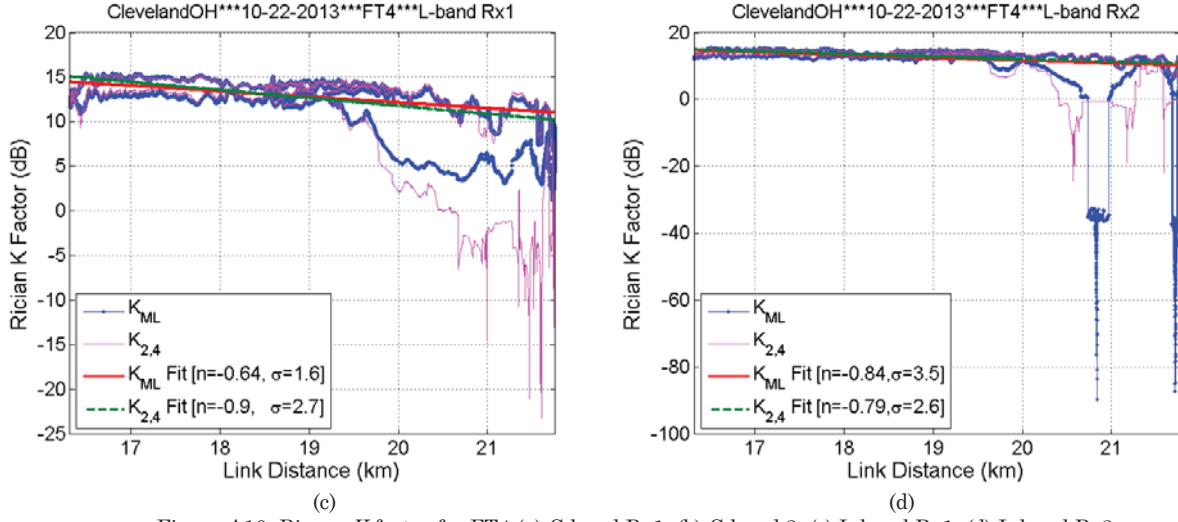
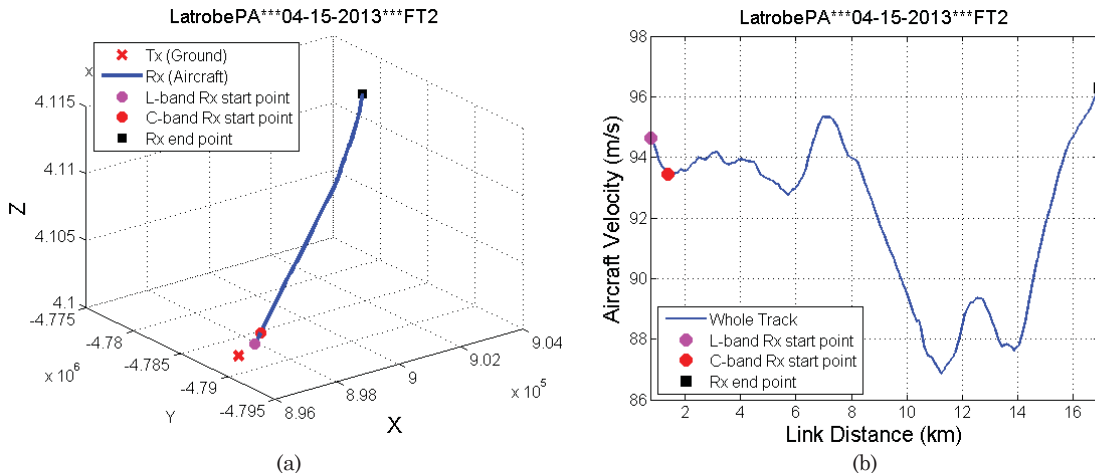


Figure A10. Ricean K factor for FT4 (a) C-band Rx1; (b) C-band 2; (c) L-band Rx1; (d) L-band Rx2.

Table A8. Statistics of Ricean K factor, FT4, Cleveland, OH, 22 October 2013, oval-shaped FT.

	C-band						L-band						
	Rx1			Rx2			Rx1			Rx2			
Moving Window Length	250λ						15 m						
Overall K factor (dB)	14.7			14.5			12.5			12.5			
Methods	K_{ML}	K_2	$K_{2,4}$	K_{ML}	K_2	$K_{2,4}$	K_{ML}	K_2	$K_{2,4}$	K_{ML}	K_2	$K_{2,4}$	
Linear fit of K factor	$A(\text{dB})$	29.0	27.9	28.9	30.3	28.9	30.4	24.8	30.3	29.6	28.3	28.8	27.8
	n	-0.68	-0.73	-0.67	-0.75	-0.82	-0.75	-0.63	-0.95	-0.89	-0.83	-0.86	-0.78
	$\sigma_X (\text{dB})$	3.4	4.0	3.4	3.5	4.4	3.5	1.6	2.8	2.7	3.6	2.6	2.6
Statistics of K factor (dB)	Max	28.1	27.8	28.1	26.5	25.2	26.5	15.5	-24.0	-23.2	15.6	-22.0	-24.5
	Min	5.5	0.0	6.4	4.0	0.0	4.0	1.1	0.0	0.0	-89.7	0.0	0.4
	Median	16.4	14.4	16.4	16.5	13.8	16.4	13.1	12.8	13.1	12.9	12.8	13.2
	μ	16.5	14.7	16.5	16.7	14.2	16.7	13.4	13.5	13.8	13.2	13.3	13.6
	σ	3.6	4.1	3.5	3.7	4.6	3.7	1.8	3.1	3.0	3.8	2.9	2.9

A.3 Hilly Terrain Flight Track 2



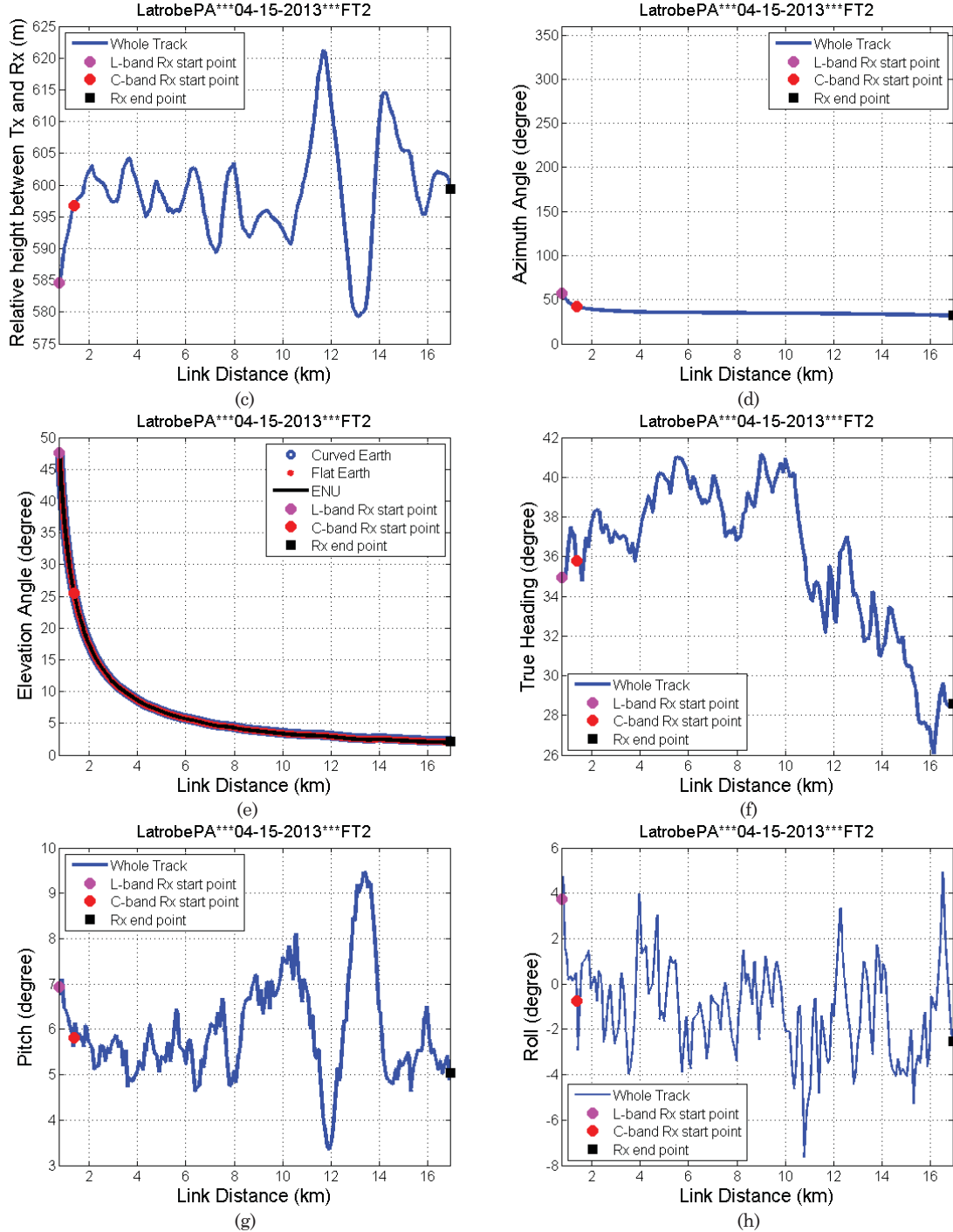


Figure A11. Geometric traces for FT2, Latrobe, PA: (a) flight track in ECEF coordinates; (b) aircraft velocity; (c) altitude difference between aircraft and ground station; (d) azimuth angle; (e) elevation angle; (f) heading of aircraft; (g) pitch angle of aircraft; (h) roll angle of aircraft.

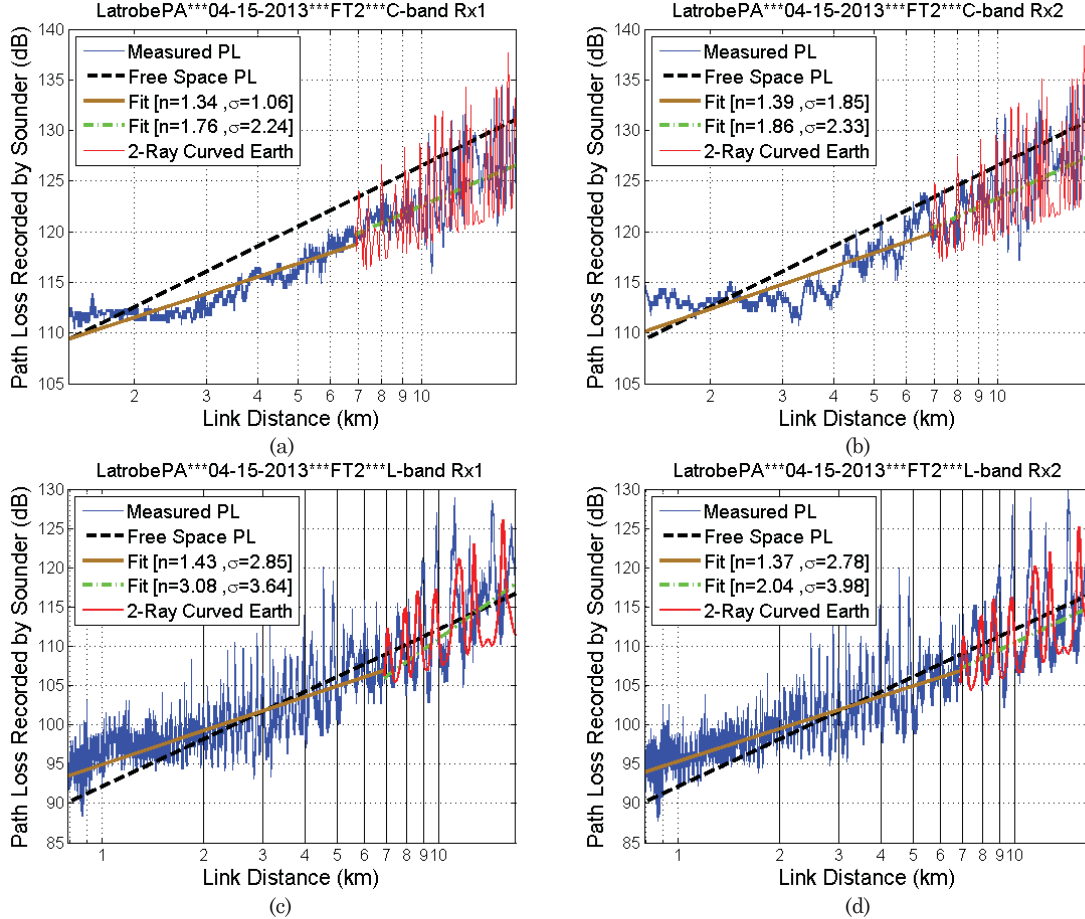


Figure A12. Measured path loss vs. distance for FT2, Latrobe, PA (a) C-band Rx1; (b) C-band 2; (c) L-band Rx1; (d) L-band Rx2.

Table A9. Path loss model parameters, FT2, Latrobe, PA, 15 April 2013, flight straight away from GS.

		$d < d_t(\theta > \theta_i)$							$d > d_t(\theta < \theta_i)$										
		Log-distance linear PL model			Elevation angle range (degree)		Distance range (km)		Log-distance linear PL model			CE2R (dB)		Elevation angle range (degree)		Distance range (km)			
		$A_{0,S}$ (dB)	n_S	σ_{XLS} (dB)	$\theta_{min,S}$	$\theta_{max,S}$	$d_{min,S}$	$d_{max,S}$	$A_{0,L}$ (dB)	n_L	$\sigma_{XL,L}$ (dB)	L_0	σ_{X2}	$\theta_{min,L}$	$\theta_{max,L}$	$d_{min,L}$	$d_{max,L}$		
	C-Rx1	27.3	1.3	1.1	5.0	25.5	1.4	6.9	-0.4	1.8	2.2	-	4.1	4.1	2.2	5.0	6.9	16.9	
	C-Rx2	24.6	1.4	1.9	5.0	25.5	1.4	6.9	-6.8	1.9	2.3	-	3.3	4.3	2.2	5.0	6.9	16.9	
	L-Rx1	9.0	1.4	2.8	5.0	47.5	0.8	6.9	-	104.4	3.1	3.6	-	0.7	5.9	2.2	5.0	6.9	16.9
	L-Rx2	12.9	1.4	2.8	5.0	47.5	0.8	6.9	-32.5	2.0	4.0	-	1.7	6.1	2.2	5.0	6.9	16.9	

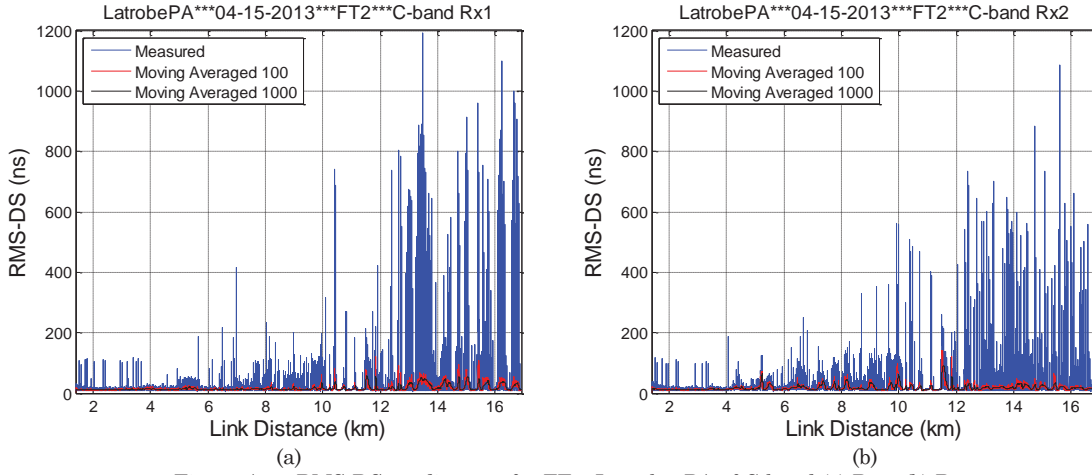
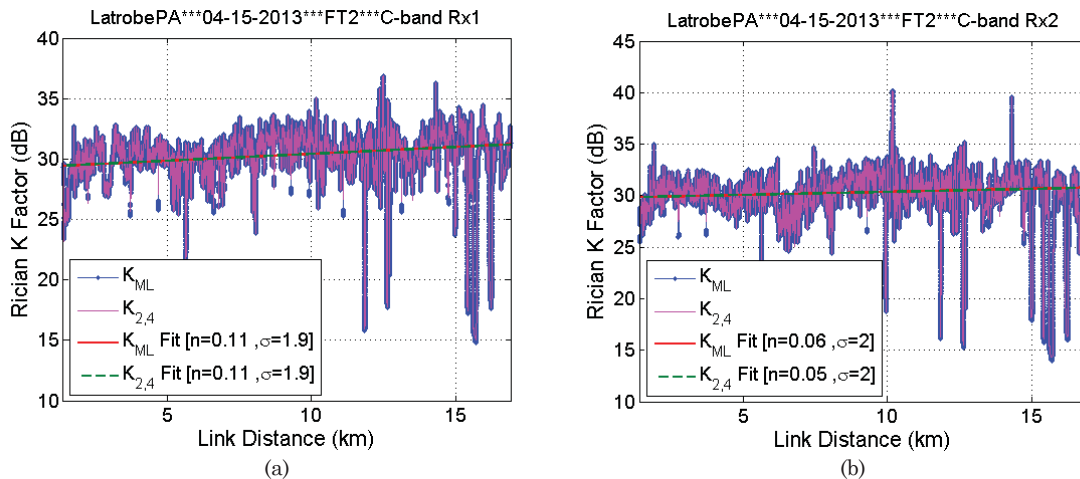


Figure A13. RMS-DS vs. distance for FT2, Latrobe, PA of C-band (a) Rx1; (b) Rx2.

Table A10. Statistics of spatial correlation, FT2, Latrobe, PA.

	C1C2	L1L2	C1L1	C1L2	C2L1	C2L2
Window Length	82	82	82	82	82	82
Mean	0.38	0.70	0.01	0.01	0.01	0.05
Median	0.82	0.96	0.04	0.02	0.02	0.19
Max	1.00	1.00	1.00	1.00	1.00	1.00
Min	-1.00	-1.00	-1.00	-1.00	-1.00	-1.00
Standard deviation	0.73	0.51	0.80	0.80	0.80	0.82



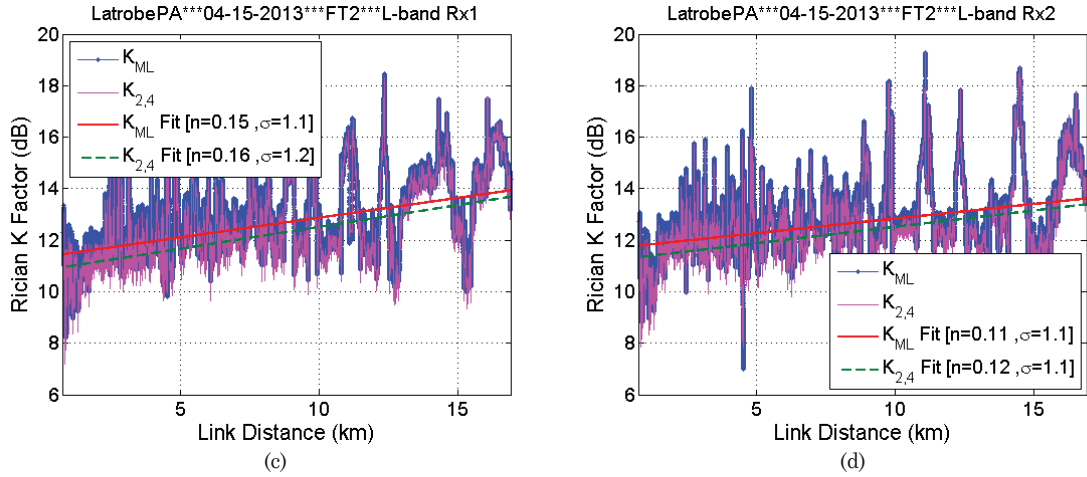
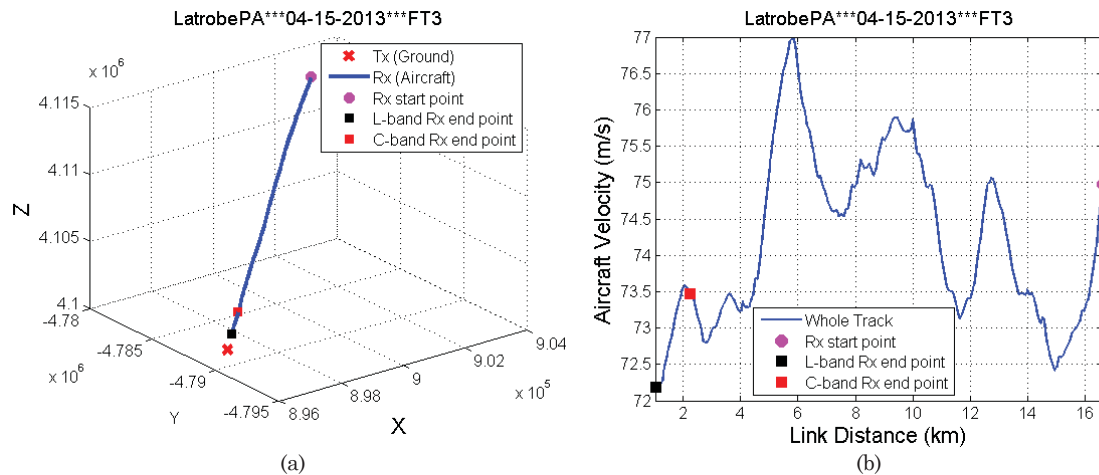


Figure A14. Ricean K factor for FT2, Latrobe, PA (a) C-band Rx1; (b) C-band 2; (c) L-band Rx1; (d) L-band Rx2.

Table A11. Statistics of Ricean K factor, FT2, Latrobe, PA, 15 April 2013, flight straight away from GS.

			C-band			L-band								
			Rx1		Rx2	Rx1		Rx2						
Moving Window Length			250λ						15 m					
Overall K factor (dB)			29.1			28.9			12.4		12.5			
Methods			K_{ML}	K_2	$K_{2,4}$	K_{ML}	K_2	$K_{2,4}$	K_{ML}	K_2	$K_{2,4}$			
Linear fit of K factor	A(dB)	29.3	28.8	29.3	29.8	28.7	29.8	11.3	9.8	10.8	11.7	10.2	11.2	
	n	0.12	-0.21	0.11	0.06	-0.21	0.06	0.15	0.24	0.17	0.11	0.20	0.13	
	σ_X (dB)	2.0	4.0	2.0	2.1	4.1	2.0	1.2	1.4	1.3	1.1	1.2	1.2	
	D_{max} (km)	1.4	1.4	1.4	1.4	1.4	1.4	0.8	0.8	0.8	0.8	0.8	0.8	
	D_{Min} (km)	16.9	16.9	16.9	16.9	16.9	16.9	16.9	16.9	16.9	16.9	16.9	16.9	
Statistics of K factor (dB)	Max	36.9	36.0	36.9	40.2	34.8	40.2	18.4	18.2	18.3	19.3	18.5	19.3	
	Min	12.8	7.9	13.6	12.9	7.6	13.4	8.2	-0.1	7.2	7.0	0.9	7.8	
	Median	30.3	26.9	30.3	30.3	26.8	30.3	12.6	11.8	12.3	12.7	11.9	12.3	
	μ	30.6	27.9	30.5	30.5	27.9	30.5	12.3	11.7	11.9	12.5	11.9	12.1	
	σ	2.1	4.1	2.0	2.1	4.2	2.1	1.4	1.8	1.5	1.2	1.5	1.3	

A.4 Hilly Terrain Flight Track 3



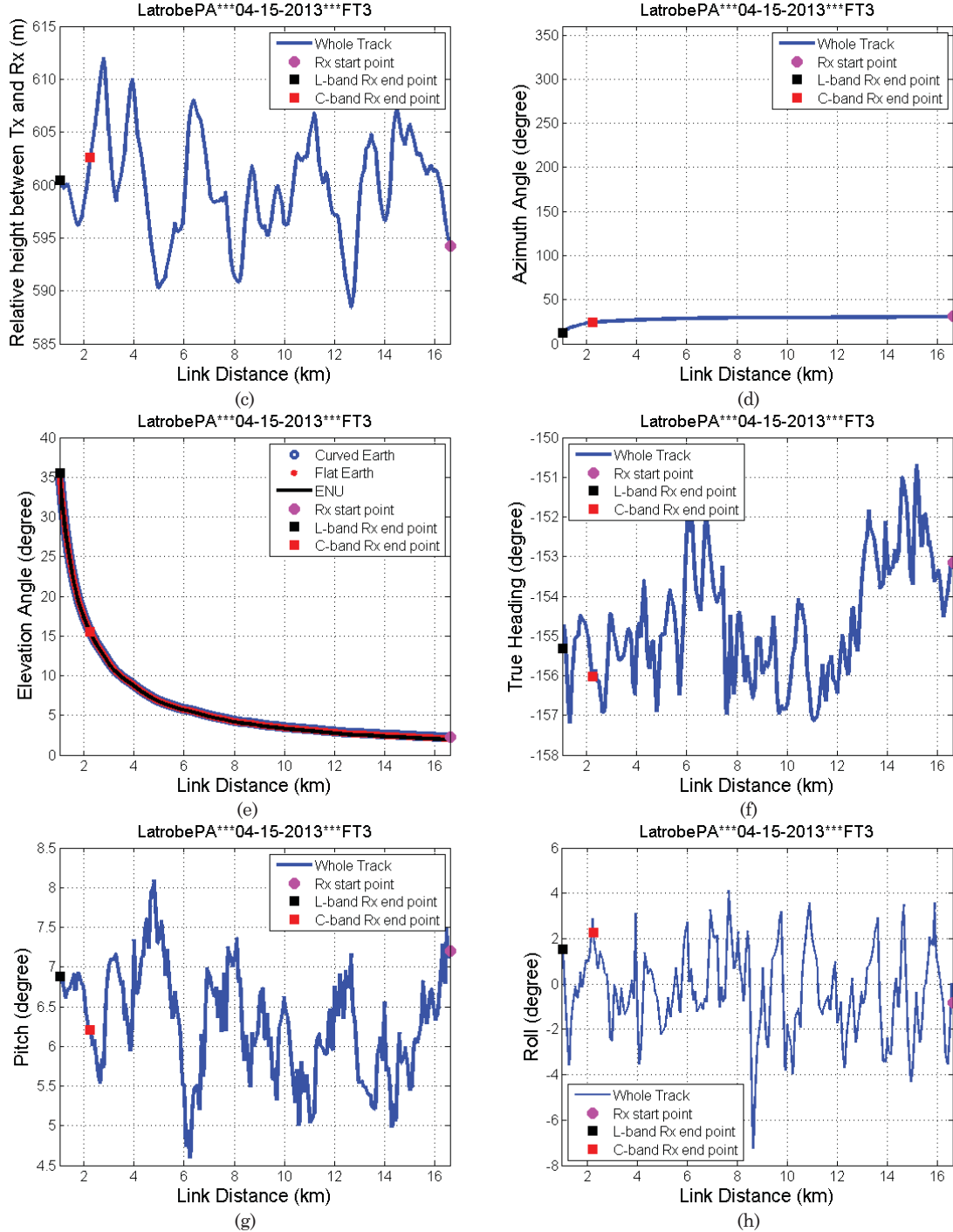


Figure A15. Geometric traces for FT3, Latrobe, PA: (a) flight track in ECEF coordinates; (b) aircraft velocity; (c) altitude difference between aircraft and ground station; (d) azimuth angle; (e) elevation angle; (f) heading of aircraft; (g) pitch angle of aircraft; (h) roll angle of aircraft.

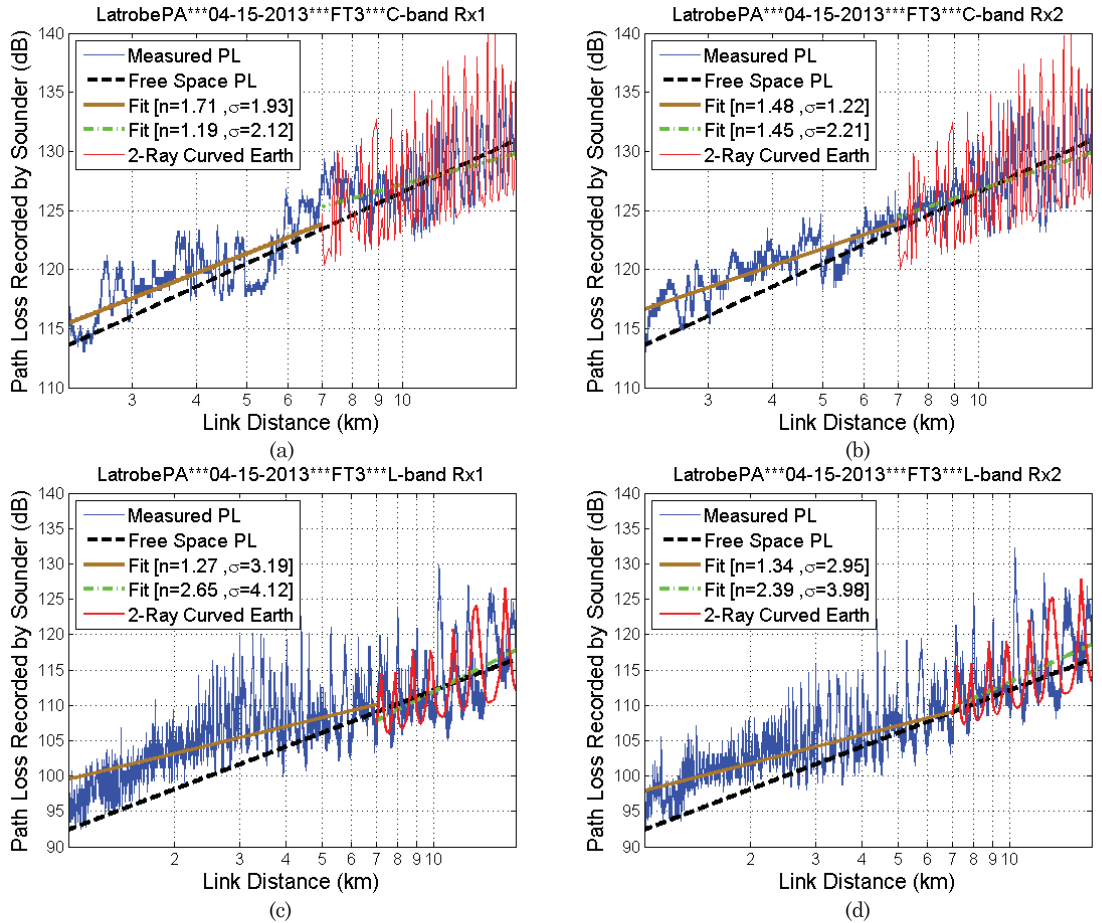


Figure A16. Measured path loss vs. distance for FT1, Latrobe, PA (a) C-band Rx1; (b) C-band 2; (c) L-band Rx1; (d) L-band Rx2.

Table A12. Path loss model parameters, FT3, Latrobe, PA, 15 April 2013, flight straight toward GS.

	$d < d_t (\theta > \theta)$							$d > d_t (\theta < \theta)$								
	Log-distance linear PL model			Elevation angle range (degree)		Distance range (km)		Log-distance linear PL model			CE2R (dB)		Elevation angle range (degree)		Distance range (km)	
	$A_{0,S}$ (dB)	n_S	$\sigma_{XL,S}$ (dB)	$\theta_{min,S}$	$\theta_{max,S}$	$d_{min,S}$	$d_{max,S}$	$A_{0,L}$ (dB)	n_L	$\sigma_{XL,L}$ (dB)	L_0	σ_{X2}	$\theta_{min,L}$	$\theta_{max,L}$	$d_{min,L}$	$d_{max,L}$
C-Rx1	7.1	1.7	1.9	5.0	15.5	2.3	7.0	43.9	1.2	2.1	0.2	4.3	2.2	5.0	7.0	16.6
	22.4	1.5	1.2	5.0	15.5	2.3	7.0	25.5	1.4	2.2	-0.1	4.1	2.2	5.0	7.0	16.6
	23.0	1.3	3.2	5.0	35.5	1.0	7.0	-73.7	2.7	4.1	-0.1	6.7	2.2	5.0	7.0	16.6
	17.2	1.3	2.9	5.0	35.5	1.0	7.0	-54.3	2.4	4.0	1.1	6.7	2.2	5.0	7.0	16.6

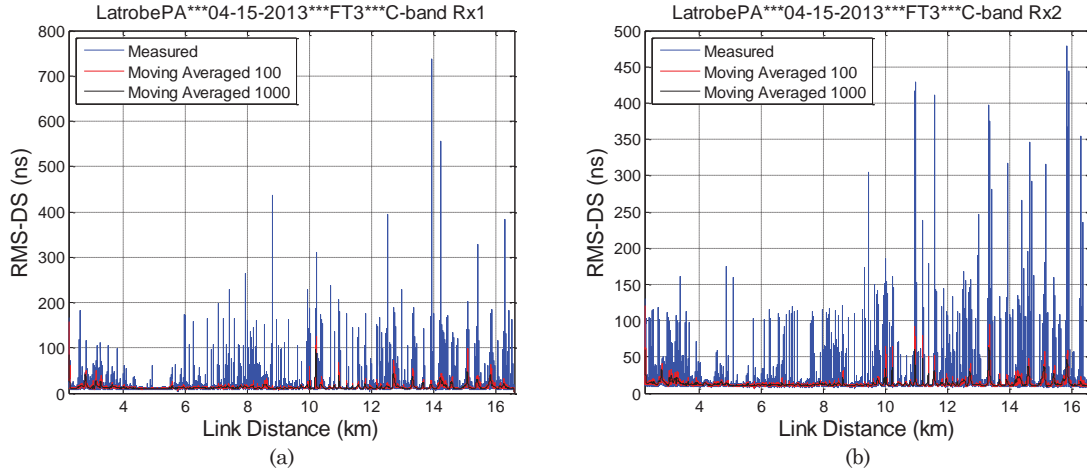
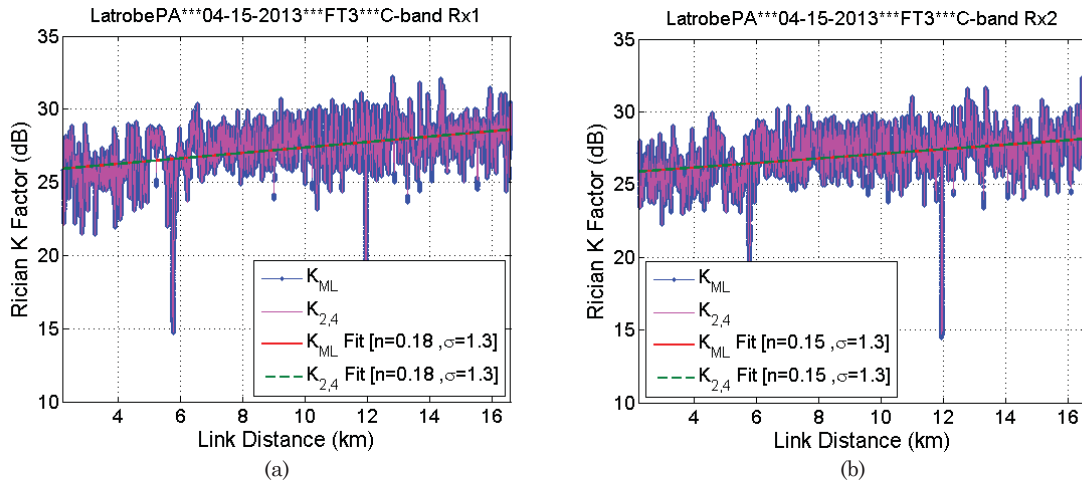


Figure A17. RMS-DS vs. distance for FT3, Latrobe, PA of C-band (a) Rx1; (b) Rx2.

Table A13. Statistics of spatial correlation, FT3, Latrobe, PA.

	C1C2	L1L2	CIL1	C1L2	C2L1	C2L2
Window Length	101	101	101	101	101	101
Mean	0.38	0.61	0.00	0.00	0.00	0.01
Median	0.90	0.93	0.00	0.03	0.03	0.04
Max	1.00	1.00	1.00	1.00	1.00	1.00
Min	-1.00	-1.00	-1.00	-1.00	-1.00	-1.00
Standard deviation	0.78	0.54	0.84	0.83	0.83	0.82



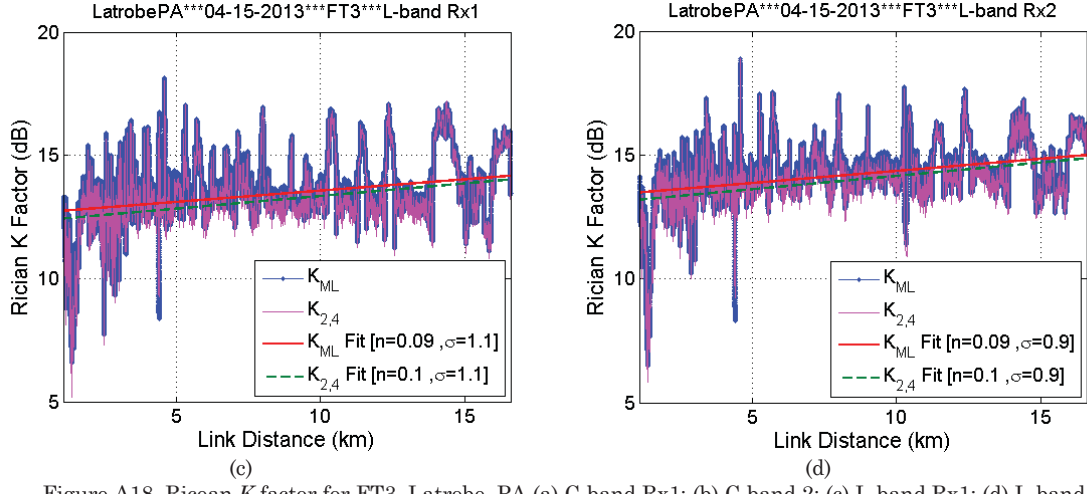
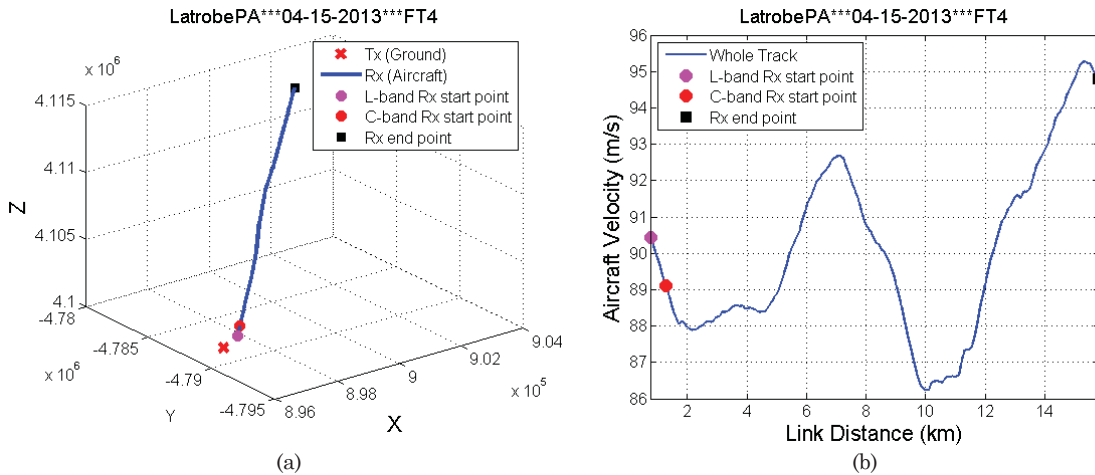


Figure A18. Ricean K factor for FT3, Latrobe, PA (a) C-band Rx1; (b) C-band 2; (c) L-band Rx1; (d) L-band Rx2.

Table A14. Statistics of Ricean K factor, FT3, Latrobe, PA, 15 April 2013, flight straight toward GS.

		C-band						L-band					
		Rx1			Rx2			Rx1			Rx2		
Moving Window Length		250 λ											
Overall K factor (dB)		26.9			26.7			13.3			14.1		
Methods		K_{ML}	K_2	$K_{2,4}$	K_{ML}	K_2	$K_{2,4}$	K_{ML}	K_2	$K_{2,4}$	K_{ML}	K_2	$K_{2,4}$
Linear fit of K factor	A(dB)	25.5	24.6	25.5	25.6	25.1	25.6	12.7	11.2	12.3	13.4	11.9	13.1
	n	0.19	0.08	0.19	0.16	0.02	0.16	0.09	0.18	0.10	0.10	0.20	0.11
	σ_X (dB)	1.4	2.5	1.4	1.4	2.4	1.3	1.1	1.3	1.2	0.9	1.2	1.0
	D_{max} (km)	2.2	2.2	2.2	2.2	2.2	2.2	1.1	1.1	1.1	1.1	1.1	1.1
	D_{Min} (km)	16.6	16.6	16.6	16.6	16.6	16.6	16.6	16.6	16.6	16.6	16.6	16.6
Statistics of K factor (dB)	Max	32.2	31.6	32.2	32.4	32.3	32.3	18.1	17.1	18.0	18.9	17.2	18.9
	Min	13.7	9.8	14.0	14.5	10.1	14.7	6.5	2.0	5.2	6.5	1.9	5.8
	Median	27.3	25.3	27.3	27.0	25.3	27.1	13.5	12.8	13.2	14.3	13.6	14.0
	μ	27.5	25.7	27.5	27.2	25.6	27.2	13.3	12.9	13.1	14.2	13.8	14.0
	σ	1.6	2.5	1.6	1.5	2.4	1.5	1.2	1.5	1.3	1.0	1.5	1.1

A.56 Hilly Terrain Flight Track 4



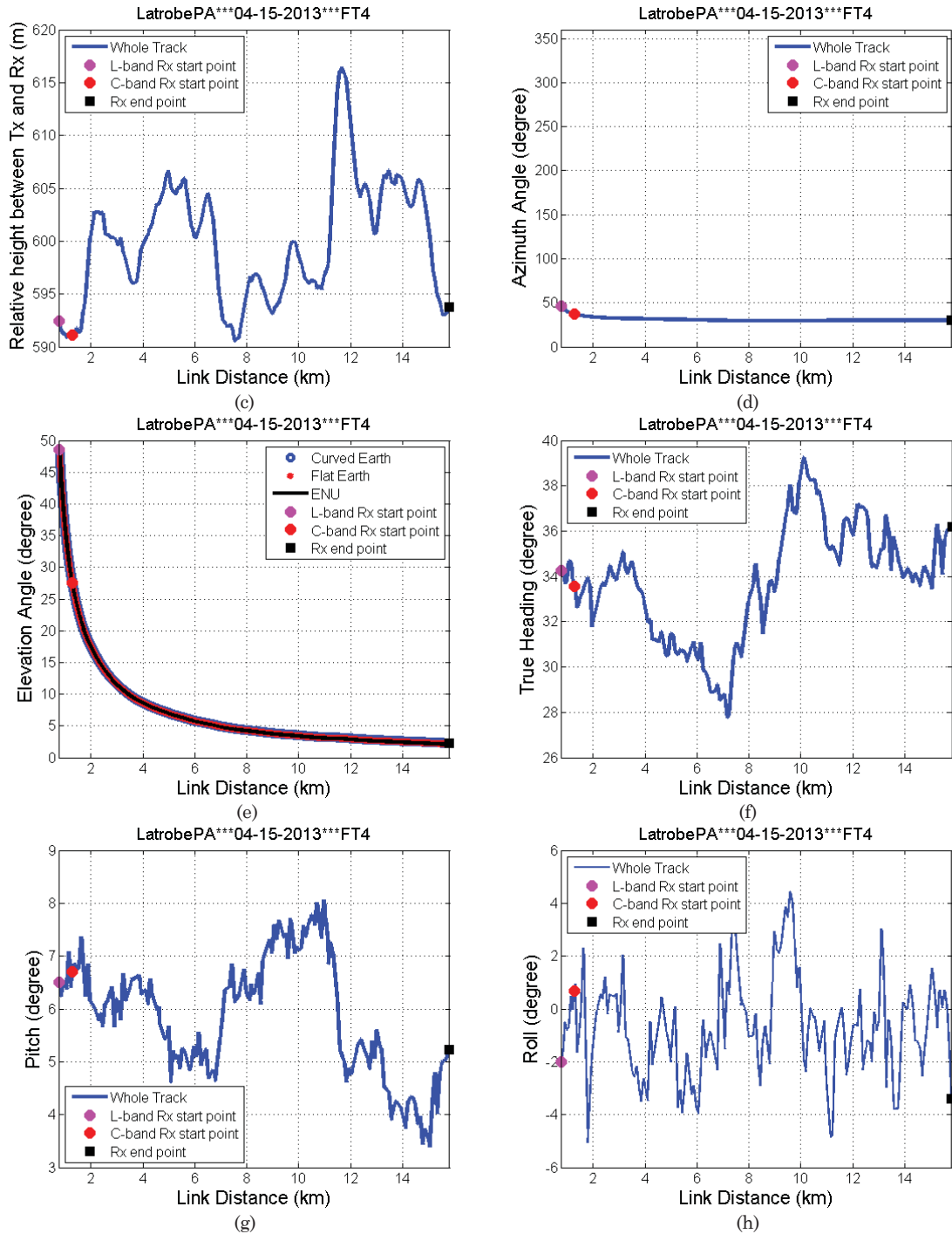


Figure A19. Geometric traces for FT4, Latrobe, PA: (a) flight track in ECEF coordinates; (b) aircraft velocity; (c) altitude difference between aircraft and ground station; (d) azimuth angle; (e) elevation angle; (f) heading of aircraft; (g) pitch angle of aircraft; (h) roll angle of aircraft.

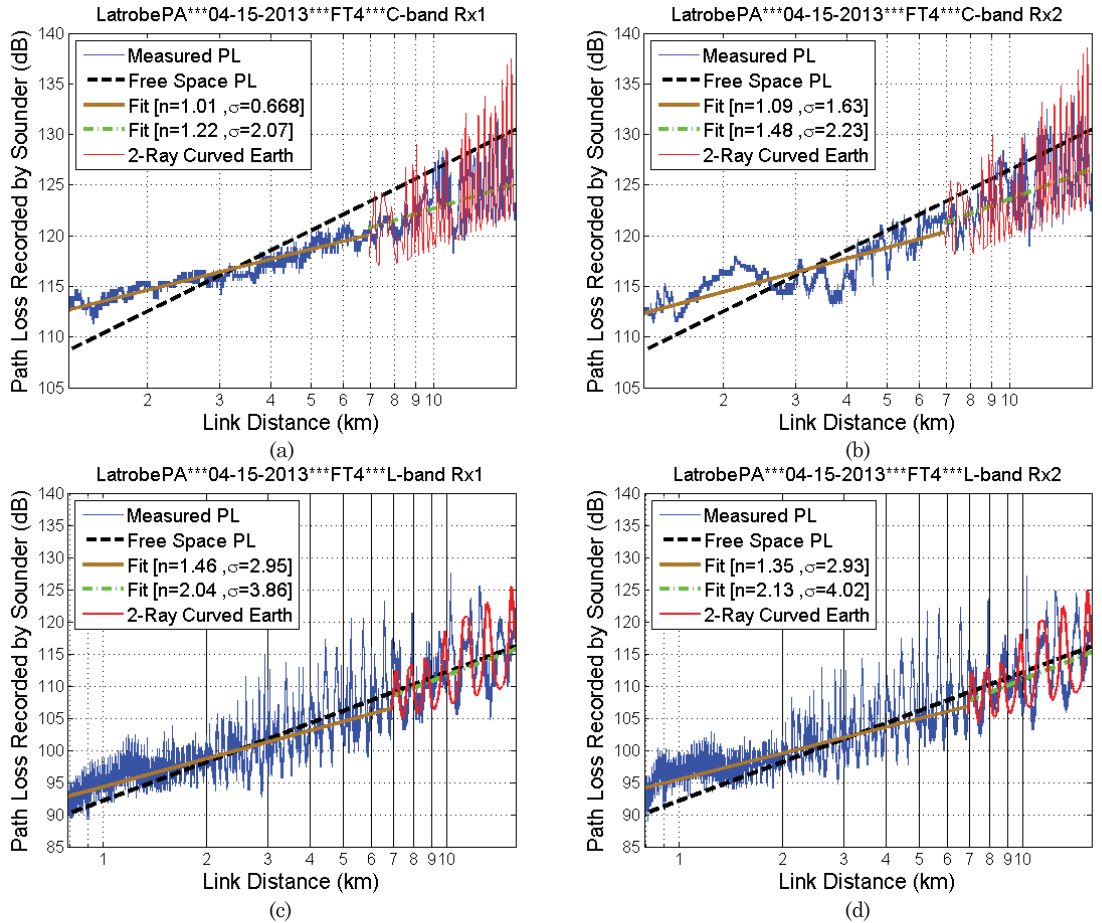


Figure A20. Measured path loss vs. distance for FT4, Latrobe, PA (a) C-band Rx1; (b) C-band 2; (c) L-band Rx1; (d) L-band Rx2.

Table A15. Path Loss Model, FT4, Latrobe, PA, 15 April 2013, flight straight away from GS.

		d < d _r ($\theta > \theta_r$)							d > d _r ($\theta < \theta_r$)									
		Log-distance linear PL model			Elevation angle range (degree)		Distance range (km)		Log-distance linear PL model			CE2R (dB)		Elevation angle range (degree)		Distance range (km)		
		A _{0,S} (dB)	n _S	σ _{XL,S} (dB)	θ _{min,S}	θ _{max,S}	d _{min,S}	d _{max,S}	A _{0,L} (dB)	n _L	σ _{XL,L} (dB)	L ₀	σ _{X2}	θ _{min,L}	θ _{max,L}	d _{min,L}	d _{max,L}	
	C-Rx1	50.8	1.0	0.7	5.0	27.5	1.3	6.9	37.4	1.2	2.1	-	3.9	2.3	5.0	6.9	15.8	
	C-Rx2	45.6	1.1	1.6	5.0	27.5	1.3	6.9	19.7	1.5	2.2	-	2.8	4.0	2.3	5.0	6.9	15.8
	L-Rx1	6.9	1.5	2.9	5.0	48.6	0.8	6.9	-30.9	2.0	3.9	-	1.1	6.1	2.3	5.0	6.9	15.8
	L-Rx2	14.3	1.4	2.9	5.0	48.6	0.8	6.9	-38.1	2.1	4.0	-	1.7	6.2	2.3	5.0	6.9	15.8

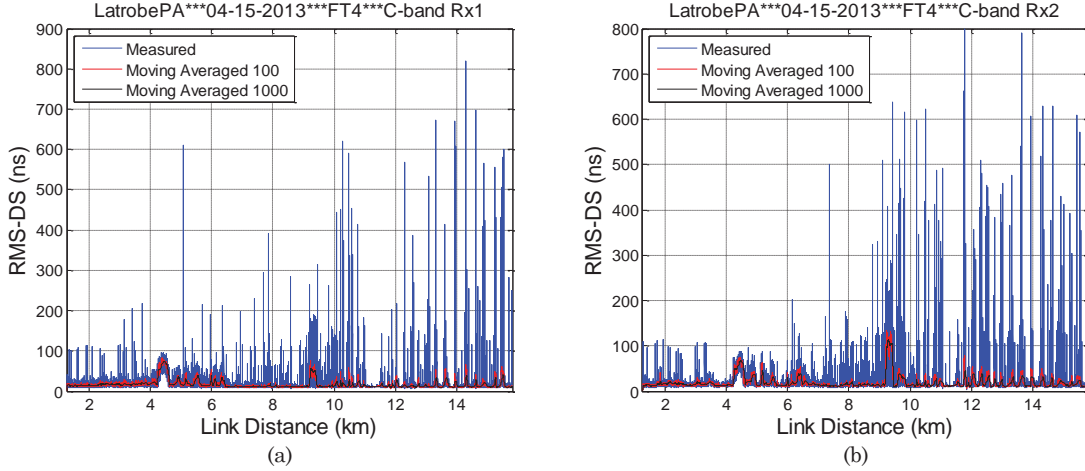
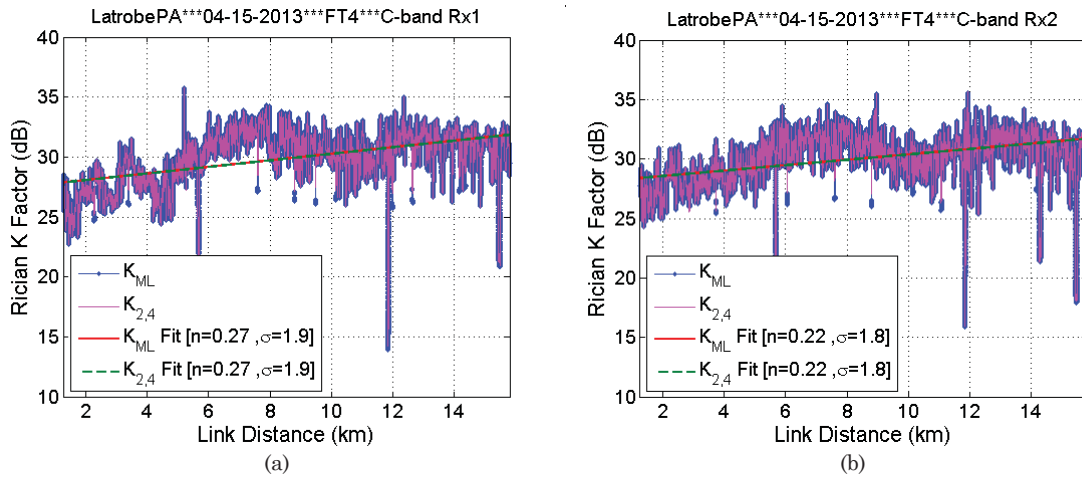


Figure A21. RMS-DS vs. distance for FT4, Latrobe, PA of C-band (a) Rx1; (b) Rx2.

Table A16. Statistics of spatial correlation, FT4, Latrobe, PA.

	C1C2	L1L2	C1L1	C1L2	C2L1	C2L2
Window Length	83	83	83	83	83	83
Mean	0.44	0.70	-0.06	-0.06	-0.06	-0.04
Median	0.83	0.96	-0.18	-0.19	-0.19	-0.11
Max	1.00	1.00	1.00	1.00	1.00	1.00
Min	-1.00	-1.00	-1.00	-1.00	-1.00	-1.00
Standard deviation	0.68	0.49	0.78	0.77	0.77	0.80



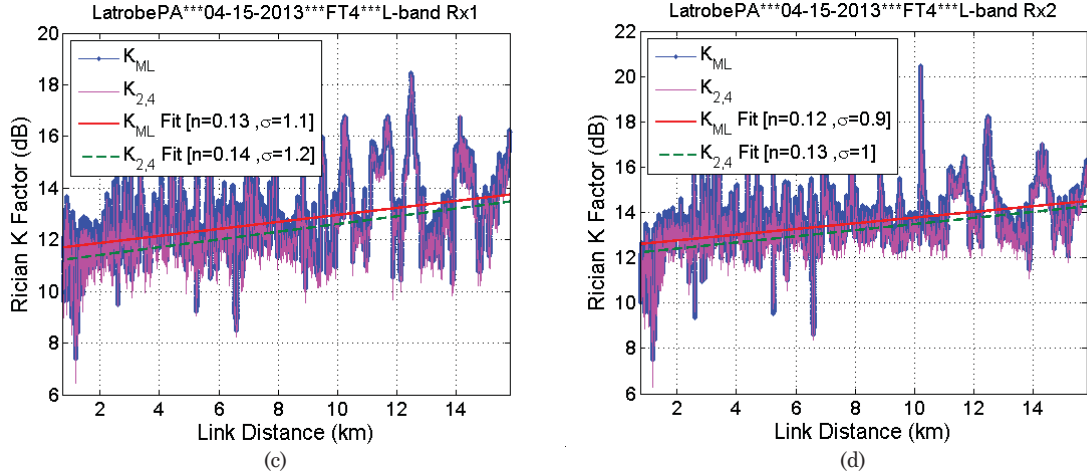
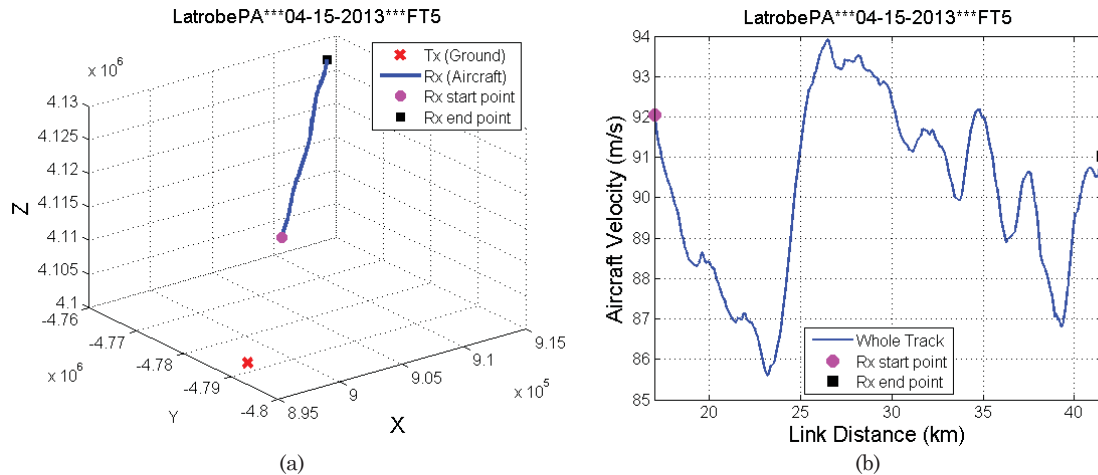


Figure A22. Ricean K factor for FT4, Latrobe, PA (a) C-band Rx1; (b) C-band 2; (c) L-band Rx1; (d) L-band Rx2.

Table A17. Statistics of Ricean K factor, FT4, Latrobe, PA, 15 April 2013, flight straight toward GS.

	C-band						L-band						
	Rx1			Rx2			Rx1			Rx2			
Moving Window Length	250λ						15 m						
Overall K factor (dB)	28.9			29.1			12.4			13.3			
Methods	K_{ML}	K_2	$K_{2,4}$	K_{ML}	K_2	$K_{2,4}$	K_{ML}	K_2	$K_{2,4}$	K_{ML}	K_2	$K_{2,4}$	
Linear fit of K factor	A (dB)	27.5	27.9	27.5	28.1	28.0	28.1	11.6	10.0	11.1	12.5	10.9	12.1
	n	0.27	-0.12	0.27	0.23	-0.17	0.23	0.14	0.23	0.15	0.13	0.22	0.14
	σ_X (dB)	2.0	3.5	1.9	1.8	3.7	1.8	1.1	1.4	1.2	1.0	1.4	1.0
	D_{max} (km)	1.3	1.3	1.3	1.3	1.3	1.3	0.8	0.8	0.8	0.8	0.8	0.8
	D_{Min} (km)	15.8	15.8	15.8	15.8	15.8	15.8	15.8	15.8	15.8	15.8	15.8	15.8
Statistics of K factor (dB)	Max	35.8	34.3	35.8	35.6	33.7	35.6	18.4	17.5	18.4	20.5	17.7	20.4
	Min	13.9	11.8	14.2	13.9	10.6	14.4	7.4	0.3	6.4	7.5	0.2	6.3
	Median	29.9	26.8	29.9	30.0	26.6	30.0	12.6	11.8	12.3	13.5	12.6	13.2
	μ	30.3	27.3	30.3	30.3	27.2	30.3	12.4	11.6	12.0	13.4	12.8	13.1
	σ	2.3	3.5	2.2	2.1	3.8	2.0	1.3	1.7	1.4	1.1	1.7	1.2

A.6 Hilly Terrain Flight Track 5



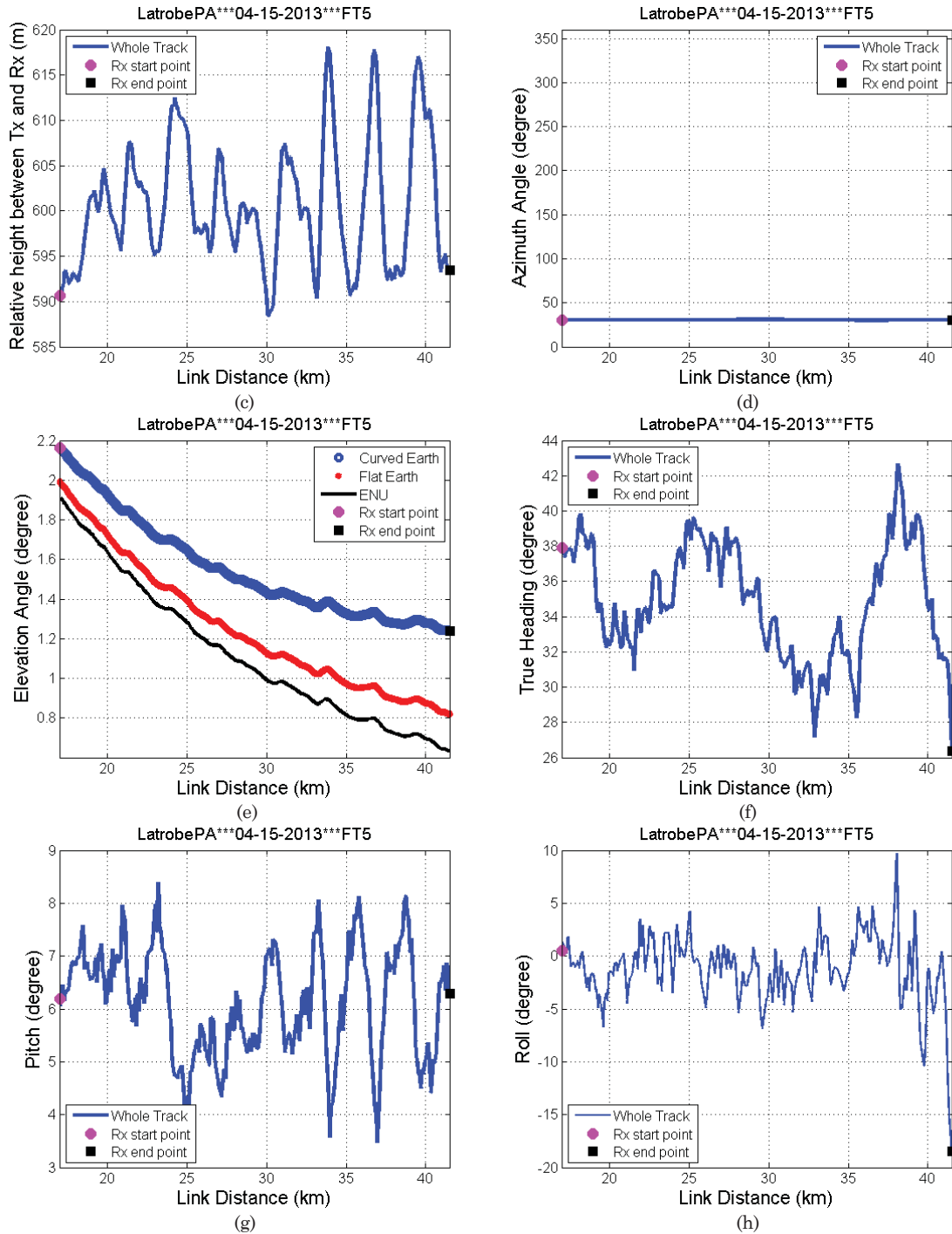


Figure A23. Geometric traces for FT5, Latrobe, PA: (a) flight track in ECEF coordinates; (b) aircraft velocity; (c) altitude difference between aircraft and ground station; (d) azimuth angle; (e) elevation angle; (f) heading of aircraft; (g) pitch angle of aircraft; (h) roll angle of aircraft.

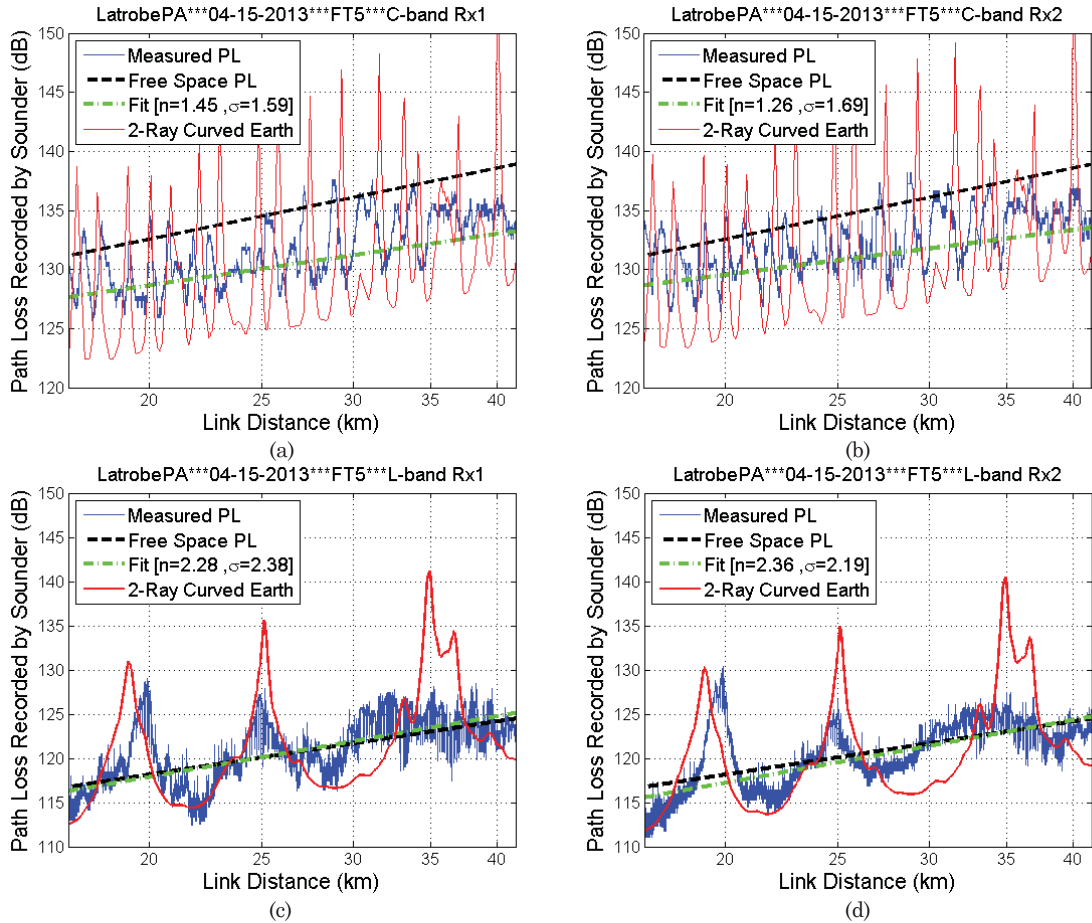


Figure A24. Measured path loss vs. distance for FT5, Latrobe, PA (a) C-band Rx1; (b) C-band 2; (c) L-band Rx1; (d) L-band Rx2.

Table A18. Path loss model parameters, FT5, Latrobe, PA, 15 April 2013, flight straight away from GS.

		$d > d_t (\theta < \theta_t)$								
		Log-distance linear PL model			CE2R (dB)		Elevation angle range (degree)		Distance range (km)	
		$A_{0,L}$ (dB)	n_L	σ_{XLL} (dB)	L_o	σ_{X2}	$\theta_{min,L}$	$\theta_{max,L}$	$d_{min,L}$	$d_{max,L}$
	C-Rx1	23.1	1.4	1.6	-4.6	5.7	1.2	2.2	17.0	41.5
	C-Rx2	37.7	1.3	1.7	-3.6	5.5	1.2	2.2	17.0	41.5
	L-Rx1	-48.9	2.3	2.4	0.6	4.4	1.2	2.2	17.0	41.5
	L-Rx2	-55.1	2.4	2.2	-0.1	4.3	1.2	2.2	17.0	41.5

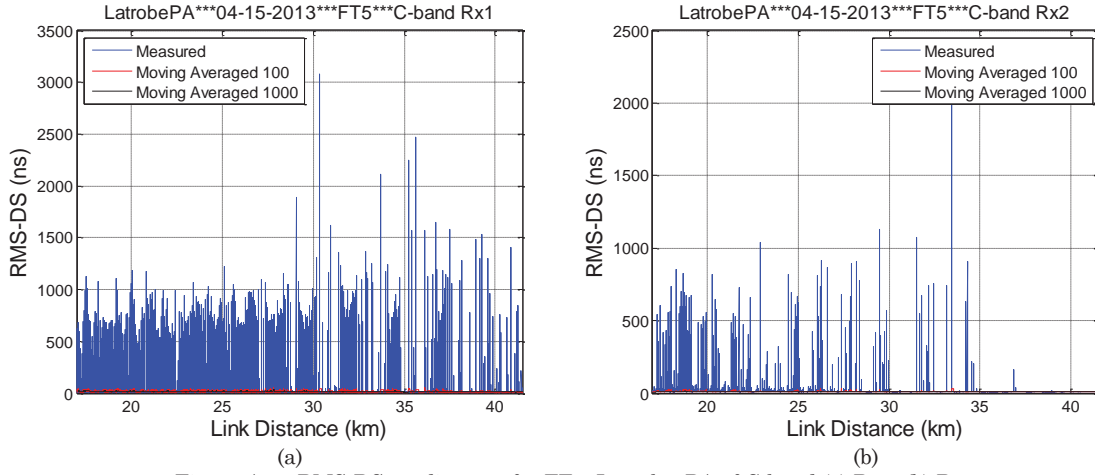
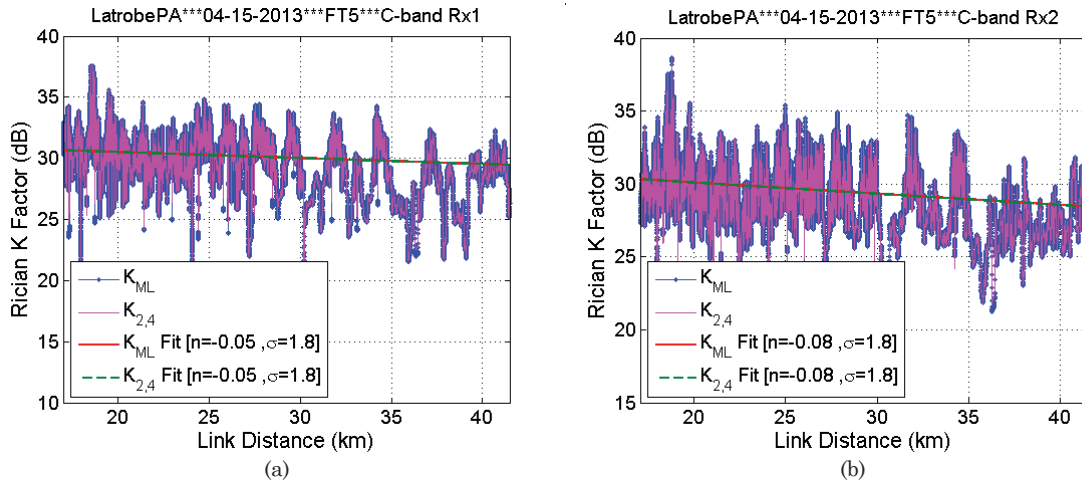


Figure A25. RMS-DS vs. distance for FT5, Latrobe, PA of C-band (a) Rx1; (b) Rx2.

Table A19. Statistics of Spatial Correlation, FT5, Latrobe, PA.

	C1C2	L1L2	CIL1	C1L2	C2L1	C2L2
Window Length	83	83	83	83	83	83
Mean	0.27	0.81	0.27	0.25	0.25	0.15
Median	0.67	0.97	0.64	0.63	0.63	0.40
Max	1.00	1.00	1.00	1.00	1.00	1.00
Min	-1.00	-0.88	-1.00	-1.00	-1.00	-1.00
Standard deviation	0.76	0.35	0.75	0.76	0.76	0.77



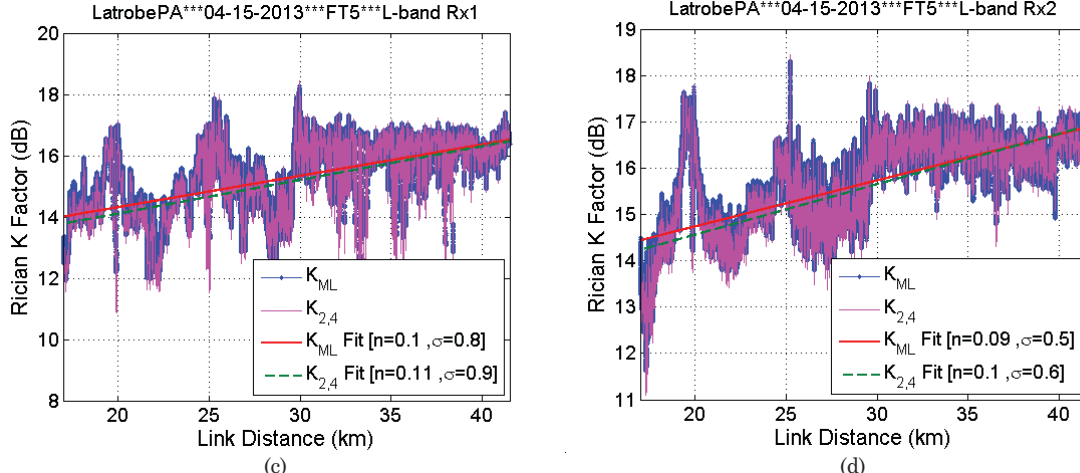
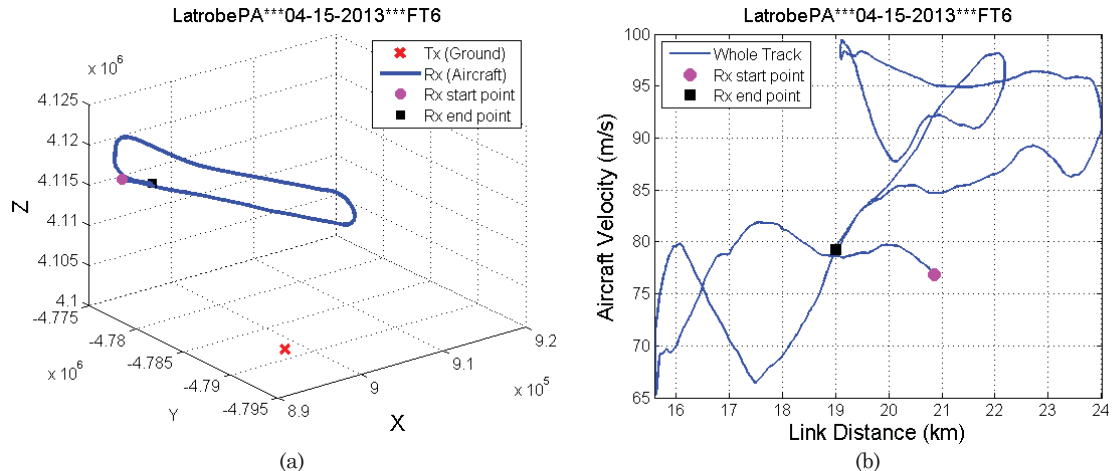


Figure A26. Ricean K factor for FT5, Latrobe, PA (a) C-band Rx1; (b) C-band 2; (c) L-band Rx1; (d) L-band Rx2.

Table A20. Statistics of Ricean K factor, FT5, Latrobe, PA.

		C-band						L-band					
		Rx1			Rx2			Rx1			Rx2		
Moving Window Length		250 λ						15 m					
Overall K factor (dB)		29.6			29.1			15.0			15.5		
Methods		K_{ML}	K_2	$K_{2,4}$	K_{ML}	K_2	$K_{2,4}$	K_{ML}	K_2	$K_{2,4}$	K_{ML}	K_2	$K_{2,4}$
Linear fit of K factor	A(dB)	31.5	31.4	31.5	31.6	31.5	31.6	12.3	11.9	11.9	12.7	12.3	12.4
	n	-0.05	-0.08	-0.05	-0.08	-0.11	-0.08	0.10	0.11	0.11	0.10	0.11	0.11
	σ_X (dB)	1.9	2.6	1.9	1.8	2.7	1.8	0.9	1.0	1.0	0.6	0.6	0.6
	D_{max} (km)	17.0	17.0	17.0	17.0	17.0	17.0	17.0	17.0	17.0	17.0	17.0	17.0
	D_{Min} (km)	41.5	41.5	41.5	41.5	41.5	41.5	41.5	41.5	41.5	41.5	41.5	41.5
Statistics of K factor (dB)	Max	37.5	37.2	37.6	38.6	38.1	38.6	18.3	18.5	18.4	18.3	18.5	18.4
	Min	13.8	11.2	14.0	17.0	13.7	17.8	11.8	8.6	8.9	11.6	11.1	11.1
	Median	30.2	29.5	30.2	29.7	28.8	29.7	15.2	15.0	15.0	15.6	15.5	15.5
	μ	30.5	30.1	30.5	29.8	29.2	29.8	15.2	15.0	15.0	15.6	15.5	15.5
	σ	1.9	2.6	1.9	1.9	2.8	1.9	1.1	1.2	1.3	0.9	1.0	1.0

A.7 Hilly Terrain Flight Track 6



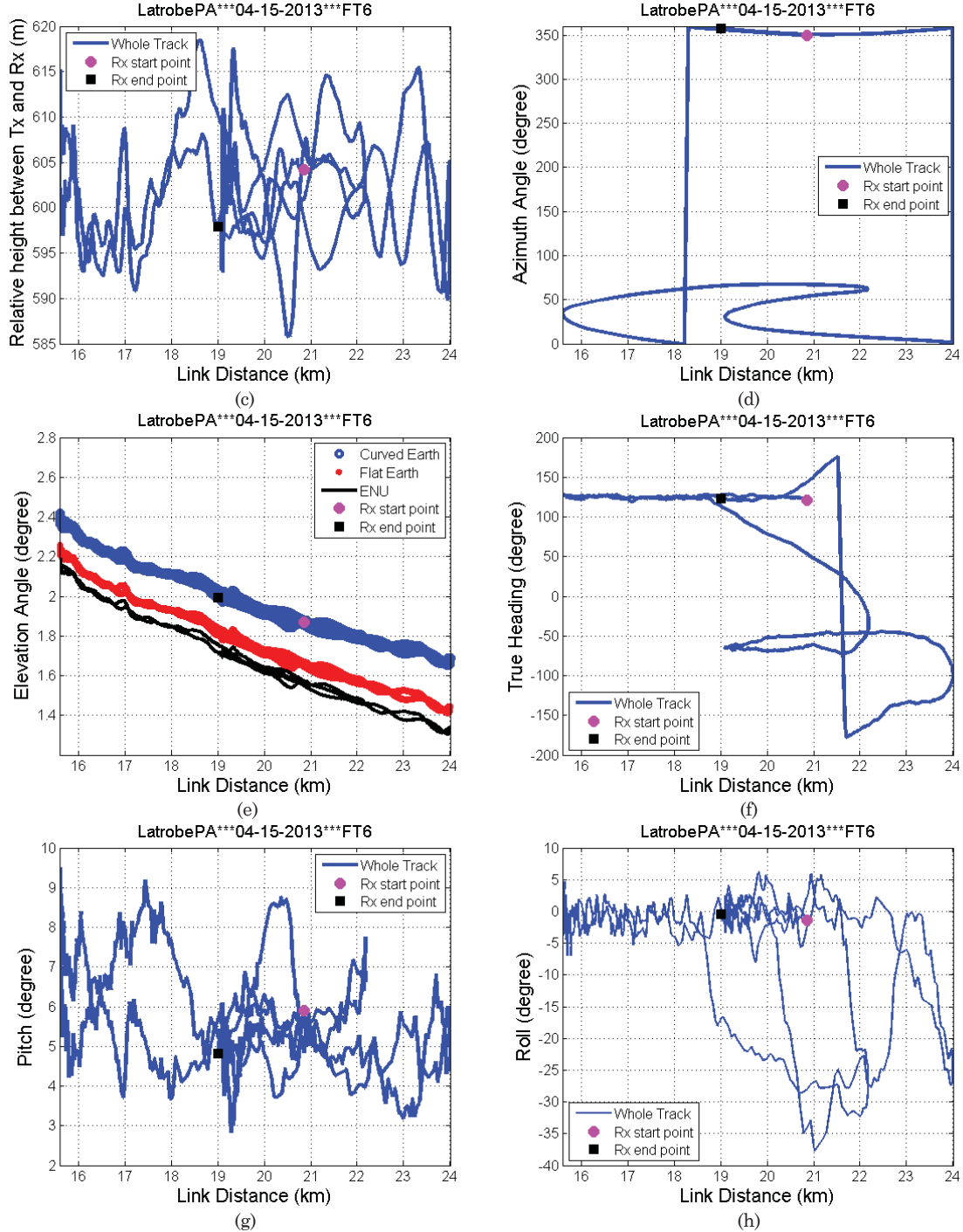


Figure A27. Geometric traces for FT6, Latrobe, PA: (a) flight track in ECEF coordinates; (b) aircraft velocity; (c) altitude difference between aircraft and ground station; (d) azimuth angle; (e) elevation angle; (f) heading of AC; (g) pitch angle of AC; (h) roll angle of AC.

As in the over-freshwater FT4, the hilly terrain FT6 likely also has airframe shadowing due to the large values of roll angle for link distances from $\sim 19\text{--}22.5$ km. Increased path loss and reduced K -factors result. Similar comments apply to hilly terrain FT7.

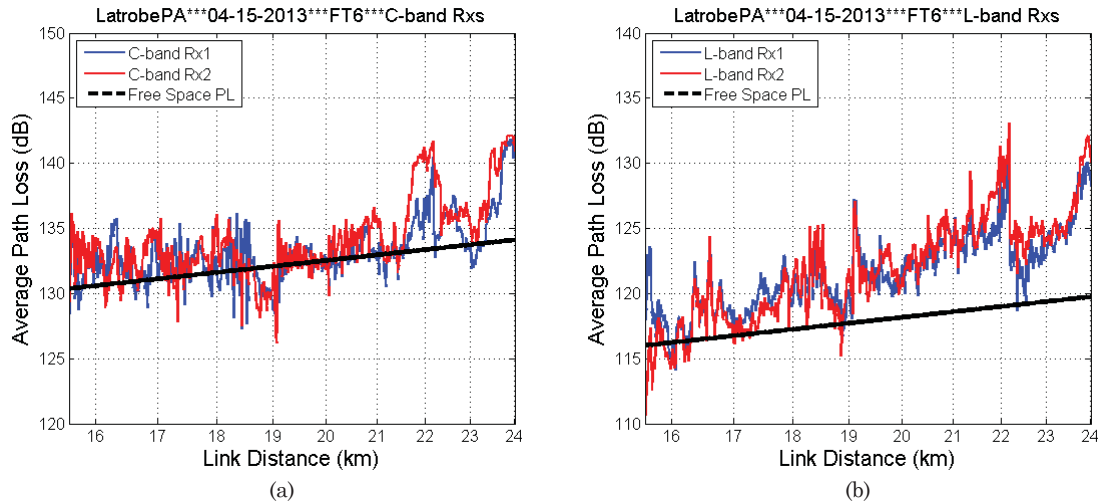


Figure A28. Measured path loss vs. distance for FT6, Latrobe, PA (a) C-band Rx1 & 2; (b) L-band Rx1 & 2.

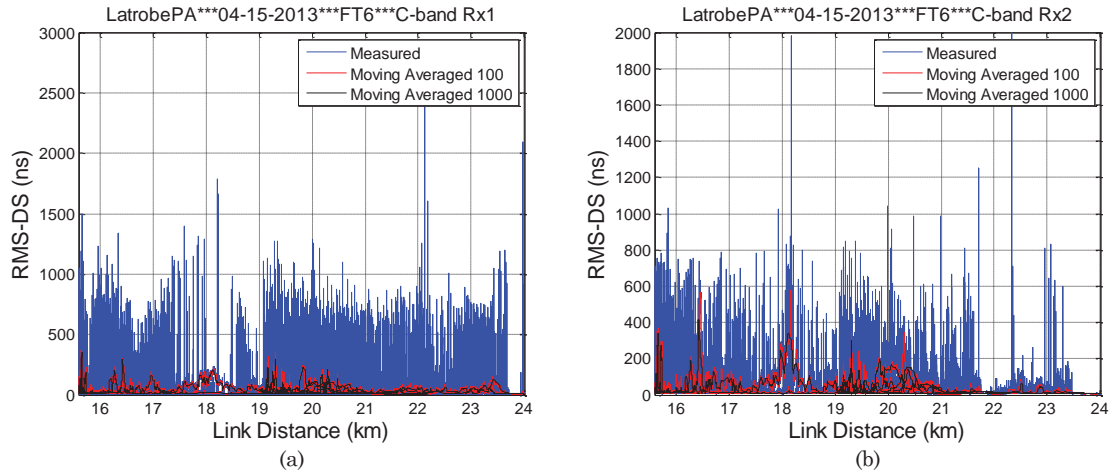


Figure A29. RMS-DS vs. distance for FT6, Latrobe, PA of C-band (a) Rx1; (b) Rx2.

Table A21. Statistics of spatial correlation, FT6, Latrobe, PA.

	C1C2	L1L2	C1L1	C1L2	C2L1	C2L2
Window Length	90	90	90	90	90	90
Mean	0.15	0.61	0.03	0.02	0.02	0.04
Median	0.39	0.95	0.10	0.05	0.05	0.12
Max	1.00	1.00	1.00	1.00	1.00	1.00
Min	-1.00	-1.00	-1.00	-1.00	-1.00	-1.00
Standard deviation	0.76	0.60	0.77	0.77	0.77	0.79

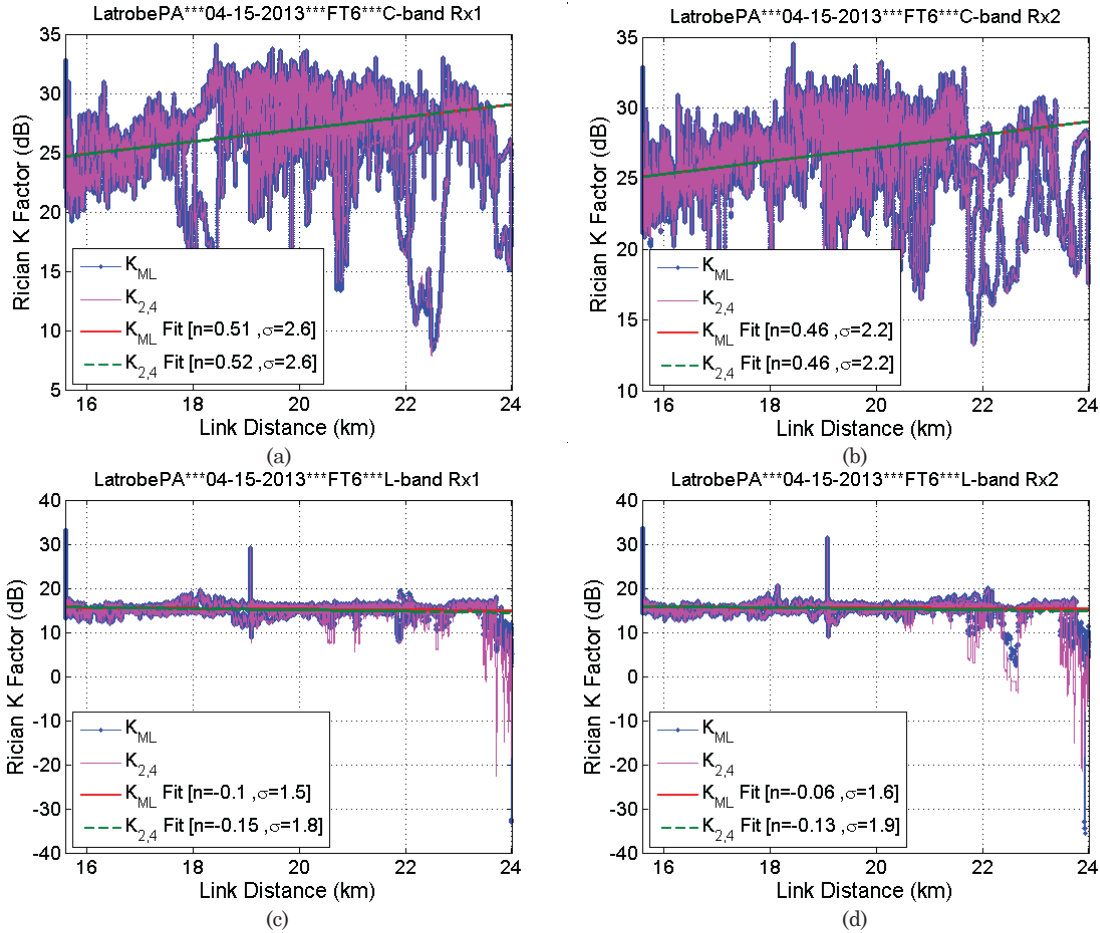
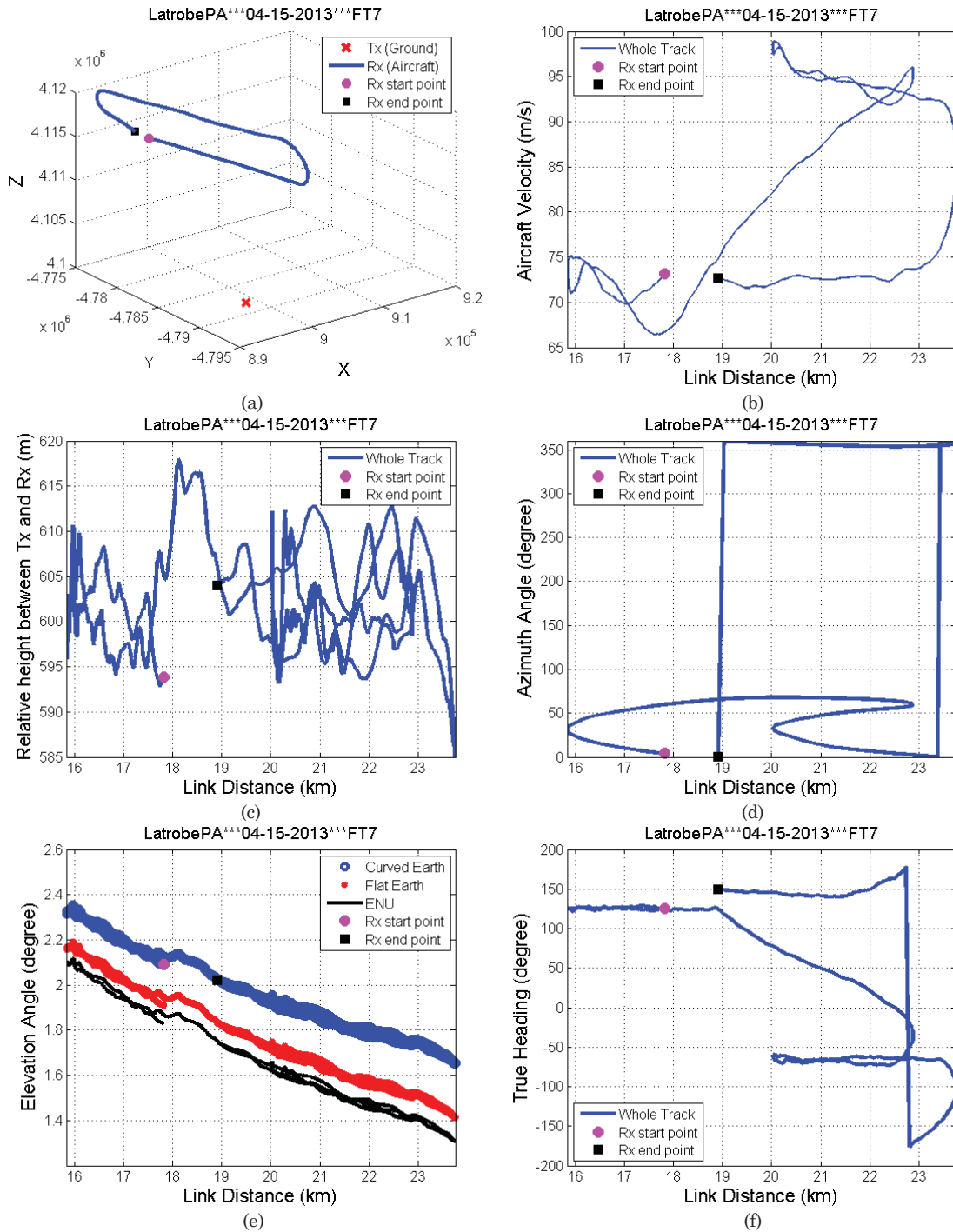


Figure A30. Ricean K factor for FT6, Latrobe, PA (a) C-band Rx1; (b) C-band 2; (c) L-band Rx1; (d) L-band Rx2.

Table A22. Statistics of Ricean K factor, FT6, Latrobe, PA.

		C-band						L-band					
		Rx1			Rx2			Rx1			Rx2		
Moving Window Length		250λ						15 m					
Overall K factor (dB)		25.1			25.6			15.1			15.3		
Methods		K_{ML}	K_2	$K_{2,4}$									
Linear fit of K factor	A(dB)	16.6	17.8	16.5	17.9	18.1	17.9	17.2	17.4	18.1	16.7	17.0	17.9
	n	0.52	0.39	0.52	0.46	0.38	0.47	-0.10	-0.13	-0.15	-0.06	-0.10	-0.13
	σ_x (dB)	2.6	3.1	2.6	2.2	2.8	2.2	1.6	1.7	1.8	1.6	1.8	2.0
	D_{max} (km)	15.6	15.6	15.6	15.6	15.6	15.6	15.6	15.6	15.6	15.6	15.6	15.6
	D_{Min} (km)	24.0	24.0	24.0	24.0	24.0	24.0	24.0	24.0	24.0	24.0	24.0	24.0
Statistics of K factor (dB)	Max	34.1	34.1	34.1	34.5	33.3	34.5	33.4	30.4	33.4	33.9	34.0	33.8
	Min	8.4	2.8	7.8	13.3	8.8	13.2	-33.2	0.0	0.0	-35.6	0.0	0.0
	Median	26.3	25.1	26.3	26.4	25.1	26.4	15.4	15.0	15.3	15.6	15.2	15.5
	μ	26.4	25.2	26.4	26.4	25.2	26.5	15.4	15.2	15.4	15.6	15.4	15.6
	σ	2.9	3.2	2.9	2.4	2.9	2.4	1.6	1.7	1.8	1.6	1.8	2.0

A.8 Hilly Terrain Flight Track 7



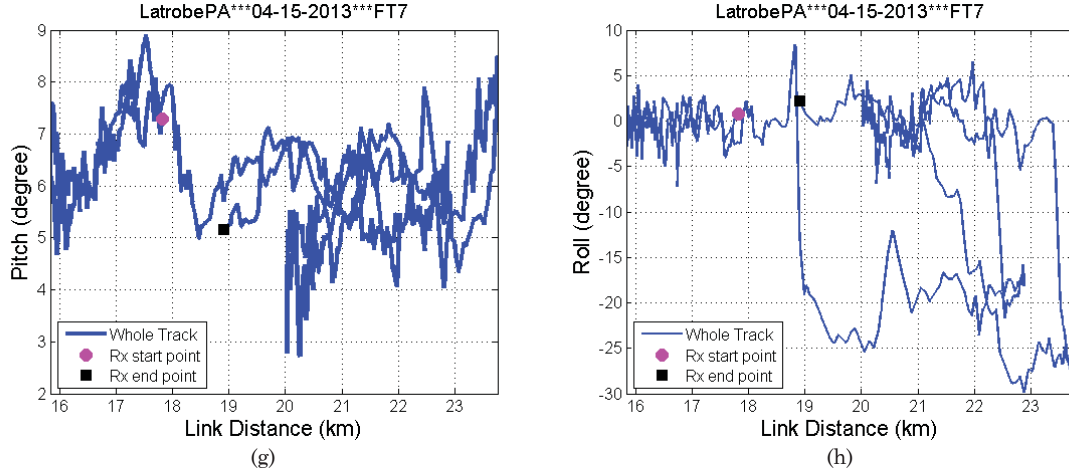


Figure A31. Geometric traces for FT7, Latrobe, PA: (a) flight track in ECEF coordinates; (b) aircraft velocity; (c) altitude difference between aircraft and ground station; (d) azimuth angle; (e) elevation angle; (f) heading of AC; (g) pitch angle of AC; (h) roll angle of AC.

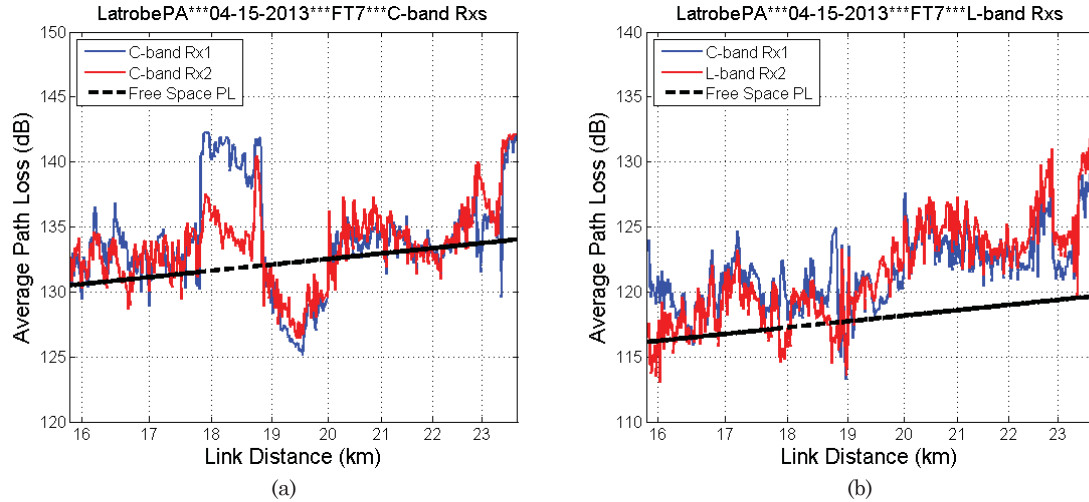


Figure A32. Measured path loss vs. distance for FT7, Latrobe, PA (a) C-band Rx1 & 2; (b) L-band Rx1 & 2.

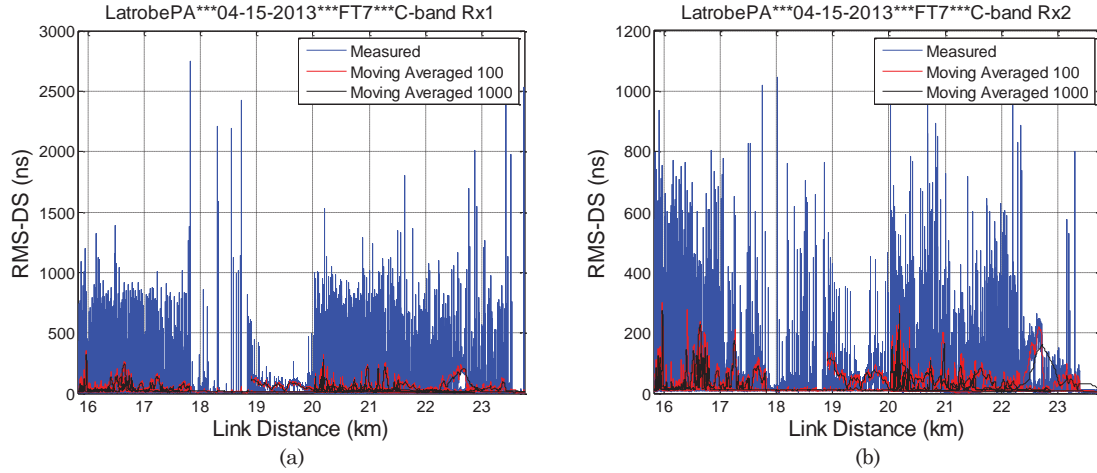


Figure A33. RMS-DS vs. distance for FT7, Latrobe, PA of C-band (a) Rx1; (b) Rx2.

Table A23. Statistics of spatial correlation, FT5, Latrobe, PA.

	C1C2	L1L2	C1L1	C1L2	C2L1	C2L2
Window Length	92	92	92	92	92	92
Mean	0.16	0.64	0.06	0.05	0.05	0.04
Median	0.37	0.95	0.18	0.12	0.12	0.12
Max	1.00	1.00	1.00	1.00	1.00	1.00
Min	-1.00	-1.00	-1.00	-1.00	-1.00	-1.00
Standard deviation	0.75	0.57	0.78	0.77	0.77	0.78

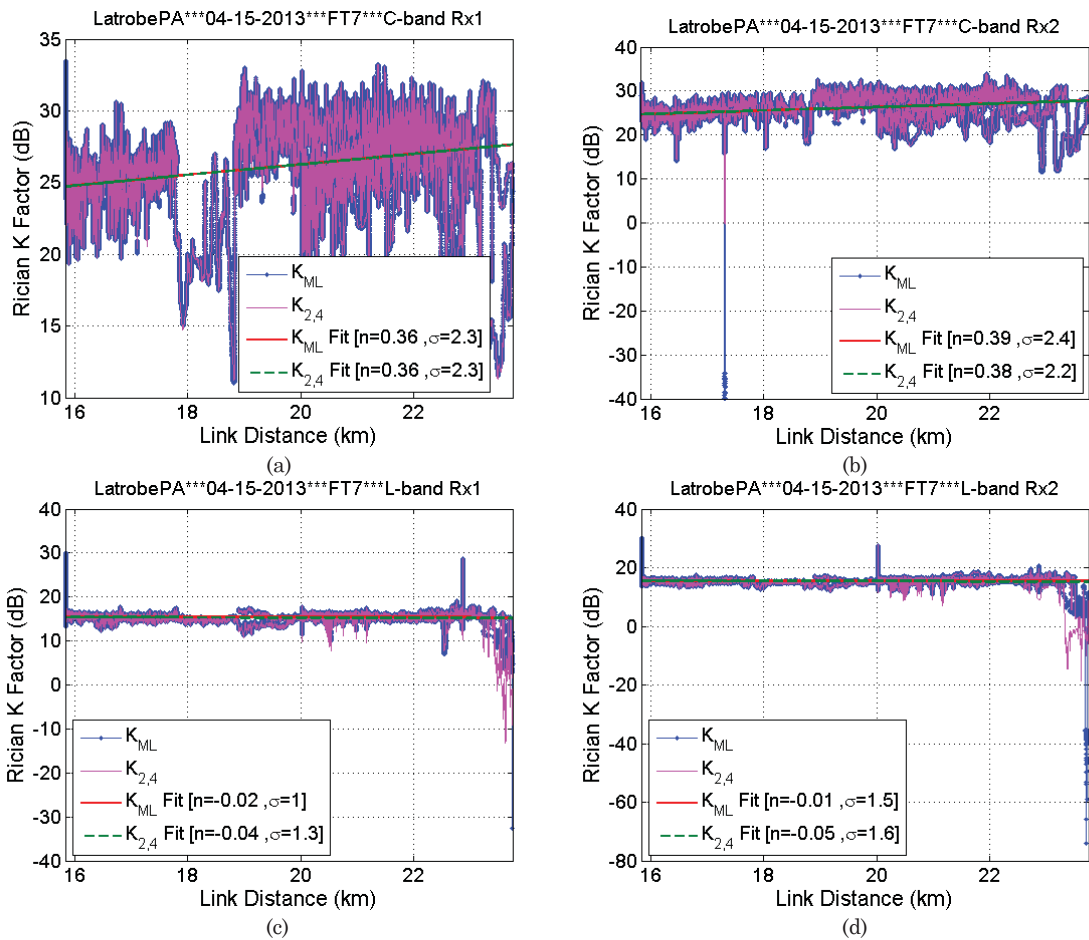
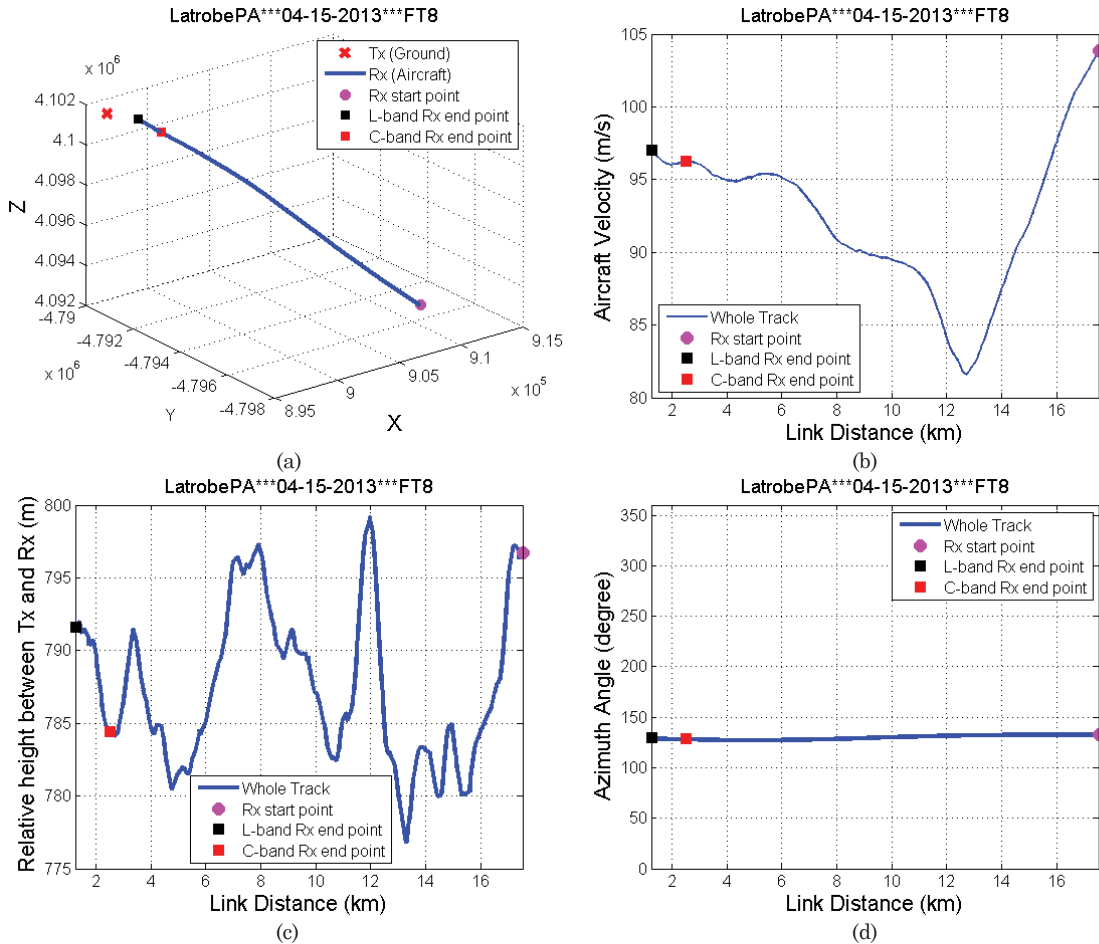


Figure A34. Ricean K factor for FT7, Latrobe, PA (a) C-band Rx1; (b) C-band 2; (c) L-band Rx1; (d) L-band Rx2.

Table A24. Statistics of Ricean K factor, FT7, Latrobe, PA.

		C-band						L-band					
		Rx1			Rx2			Rx1			Rx2		
Moving Window Length		250λ						15 m					
Overall K factor (dB)		25.0			14.2			15.3			15.3		
Methods		K_{ML}	K_2	$K_{2,4}$									
Linear fit of K factor	A(dB)	18.9	20.2	18.9	18.5	19.2	18.6	15.7	15.9	16.1	15.6	15.8	16.3
	n	0.37	0.25	0.37	0.39	0.30	0.39	-0.01	-0.04	-0.04	0.00	-0.03	-0.04
	σ_X (dB)	2.3	2.6	2.3	2.4	2.6	2.2	1.0	1.4	1.4	1.5	1.6	1.7
	D_{max} (km)	15.8	15.8	15.8	15.8	15.8	15.8	15.8	15.8	15.8	15.8	15.8	15.8
	D_{Min} (km)	23.8	23.8	23.8	23.8	23.8	23.8	23.8	23.8	23.8	23.8	23.8	23.8
Statistics of K factor (dB)	Max	33.5	33.3	33.5	33.9	34.1	33.9	30.1	29.5	30.1	30.2	29.6	30.1
	Min	11.0	0.5	11.2	-39.8	5.9	11.8	-32.6	0.0	0.0	-74.0	0.0	0.0
	Median	25.9	24.9	25.9	25.8	24.8	25.8	15.4	15.1	15.3	15.5	15.3	15.5
	μ	25.9	25.0	25.9	25.6	24.7	25.6	15.5	15.3	15.5	15.6	15.5	15.6
	σ	2.5	2.7	2.5	2.6	2.7	2.4	1.0	1.4	1.4	1.5	1.6	1.7

A.9 Hilly Terrain Flight Track 8



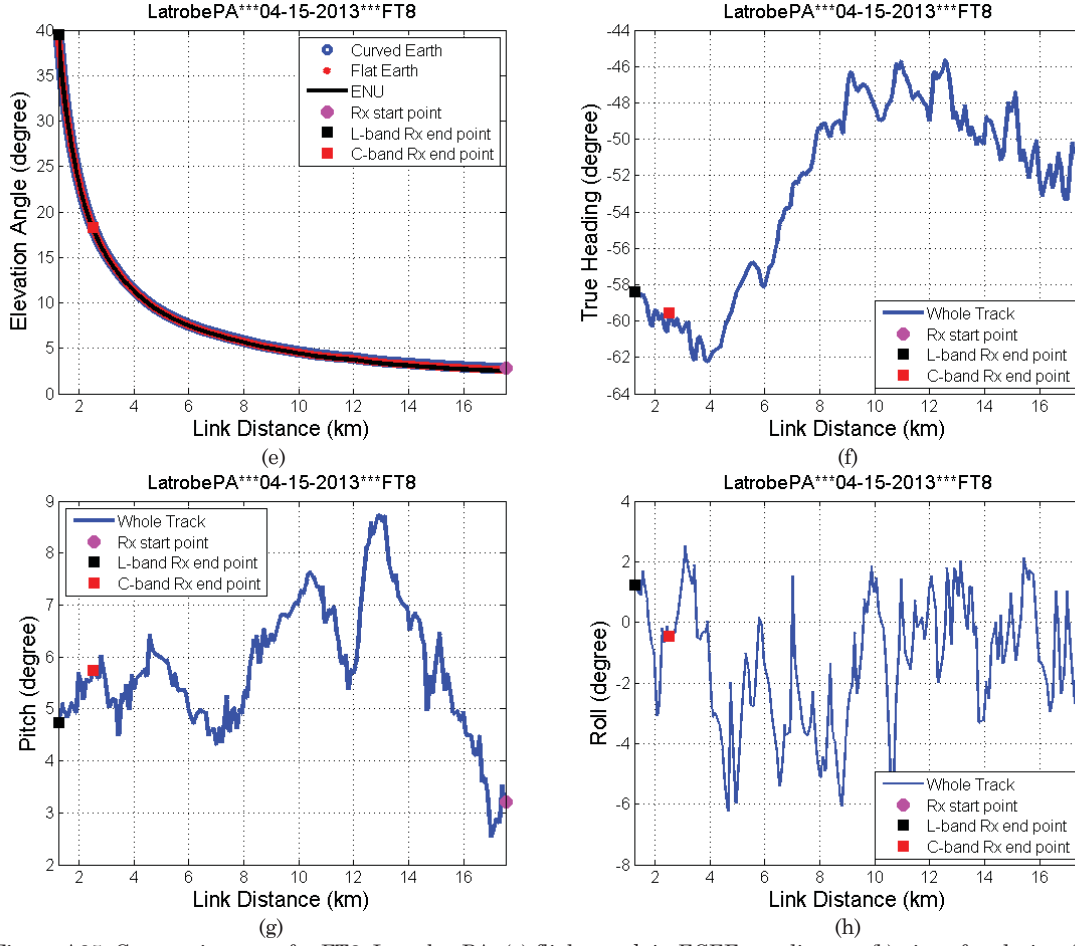
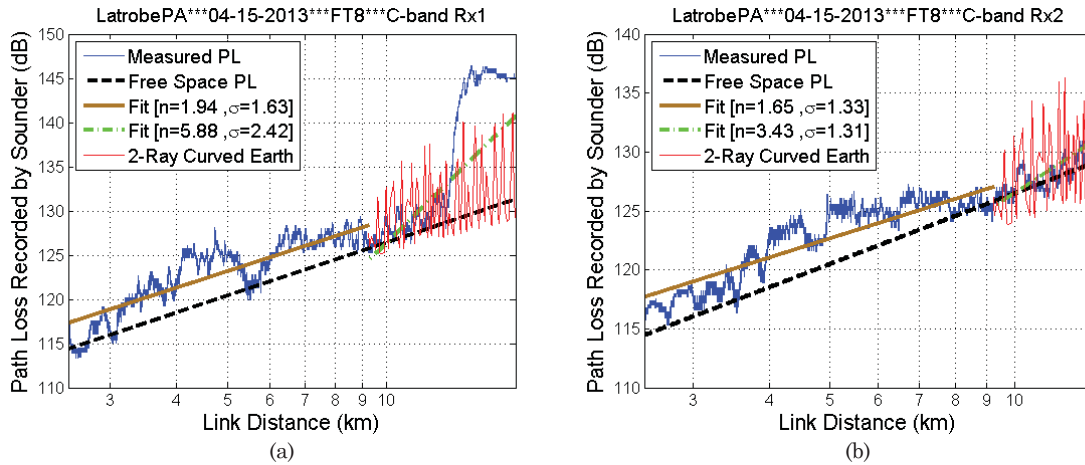


Figure A35. Geometric traces for FT8, Latrobe, PA: (a) flight track in ECEF coordinates; (b) aircraft velocity; (c) altitude difference between aircraft and ground station; (d) azimuth angle; (e) elevation angle; (f) heading of aircraft; (g) pitch angle of AC; (h) roll angle of aircraft.



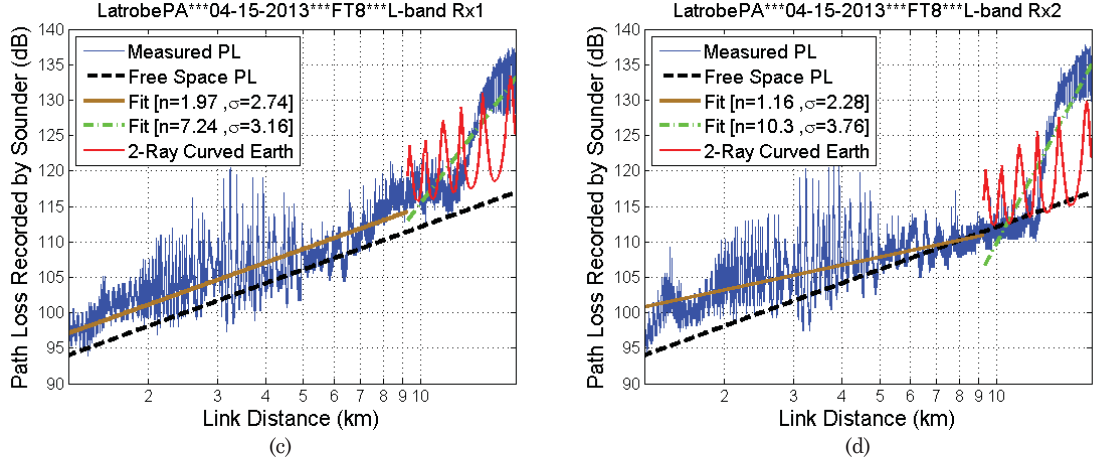


Figure A36. Measured path loss vs. distance for FT8, Latrobe, PA (a) C-band Rx1; (b) C-band 2; (c) L-band Rx1; (d) L-band Rx2.

In FTs 8, 9, and 13, the aircraft flew over a mountain ridge, and the LOS component was blocked. Mountain ridge shadowing can clearly be seen in the path loss figures. The C-band path loss reached its “ceiling” of approximately 145 dB (the limit of our sounder). Hence the path loss models for these FTs for the larger distance segments are NOT valid, but are shown for completeness. The results for RMS-DS and K -factors at the largest distances are also likely invalid.

Table A25. Path loss model parameters, FT8, Latrobe, PA, 15 April 2013, flight straight toward GS.

	$d < d_t(\theta > \theta_i)$							$d > d_t(\theta < \theta_i)$								
	Log-distance linear PL model			Elevation angle range (degree)		Distance range (km)		Log-distance linear PL model			CE2R (dB)		Elevation angle range (degree)		Distance range (km)	
	$A_{0,S}$ (dB)	n_S	$\sigma_{XL,S}$ (dB)	$\theta_{min,S}$	$\theta_{max,S}$	$d_{min,S}$	$d_{max,S}$	$A_{0,L}$ (dB)	n_L	$\sigma_{XL,L}$ (dB)	L_0	σ_{X2}	$\theta_{min,L}$	$\theta_{max,L}$	$d_{min,L}$	$d_{max,L}$
C-Rx1	-6.9	1.9	1.6	5.0	18.3	2.5	9.2	-284.8	5.9	2.4	2.2	4.4	2.8	5.0	9.2	17.5
	12.5	1.6	1.3	5.0	18.3	2.5	9.2	-113.8	3.4	1.3	0.9	3.4	3.5	5.0	9.2	13.3
	-23.0	2.0	2.7	5.0	39.6	1.2	9.2	-391.4	7.2	3.2	7.0	6.1	2.8	5.0	9.2	17.5
	30.1	1.2	2.3	5.0	39.6	1.2	9.2	-613.9	10.3	3.8	3.5	8.0	2.8	5.0	9.2	17.5

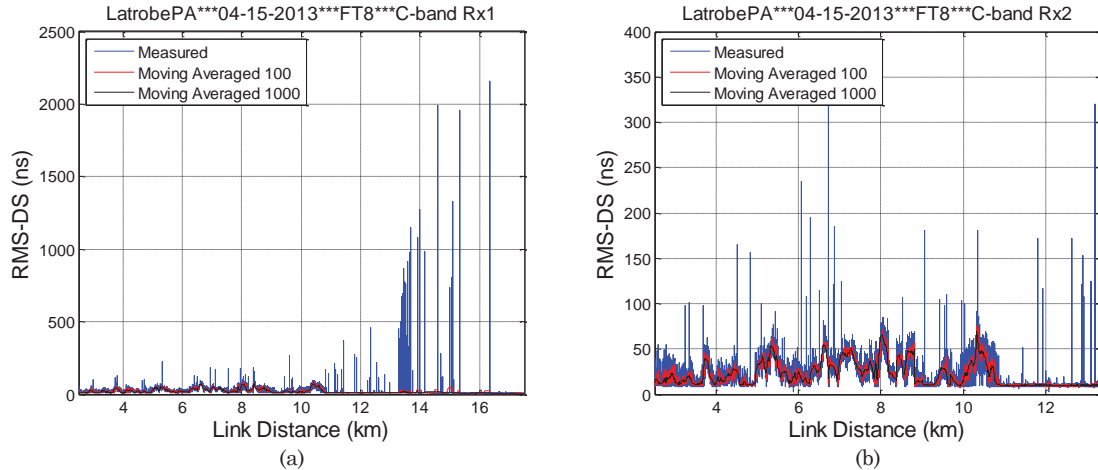


Figure A37. RMS-DS vs. distance for FT8, Latrobe, PA of C-band (a) Rx1; (b) Rx2.

Table A26. Statistics of spatial correlation, FT8, Latrobe, PA.

	C1C2	L1L2	CIL1	C1L2	C2L1	C2L2
Window Length	82	82	82	82	82	82
Mean	-0.03	0.53	0.02	-0.01	-0.01	0.02
Median	-0.06	0.83	0.03	-0.04	-0.04	0.05
Max	1.00	1.00	1.00	1.00	1.00	1.00
Min	-1.00	-0.99	-1.00	-1.00	-1.00	-1.00
Standard deviation	0.72	0.57	0.76	0.76	0.76	0.73

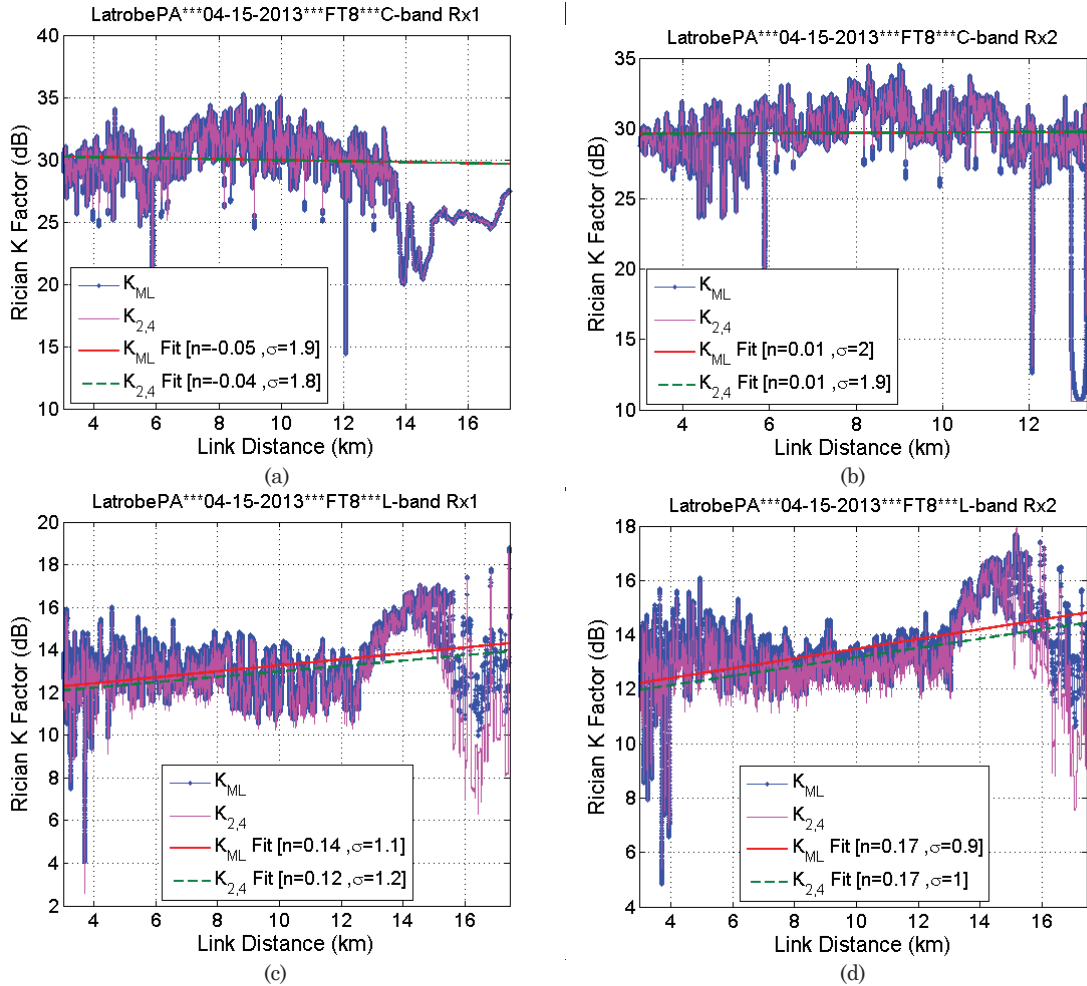
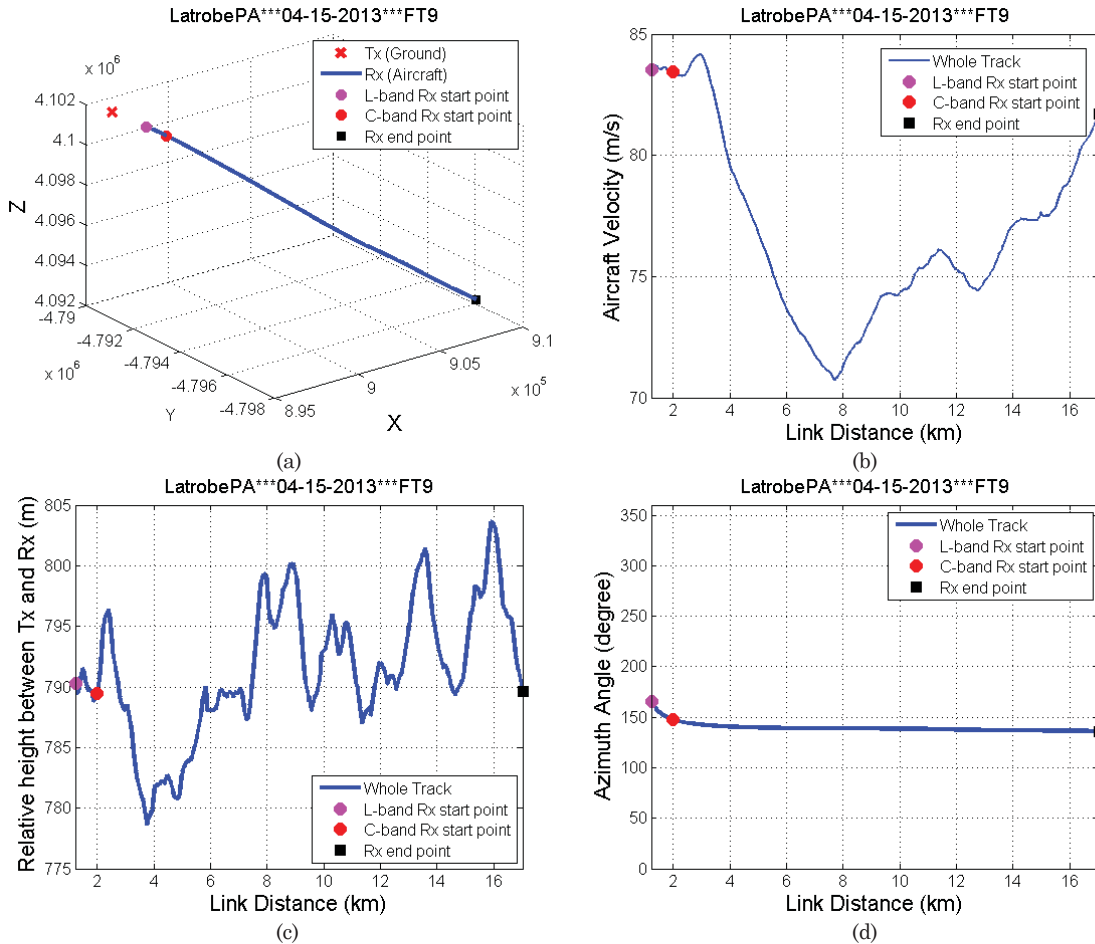


Figure A38. Ricean K factor for FT8, Latrobe, PA (a) C-band Rx1; (b) C-band 2; (c) L-band Rx1; (d) L-band Rx2.

Table A27. Statistics of Ricean K factor, FT8, Latrobe, PA.

		C-band						L-band					
		Rx1			Rx2			Rx1			Rx2		
Moving Window Length		250λ						15 m					
Overall K factor (dB)		29.3			28.5			13.0			13.2		
Methods		K_{ML}	K_2	$K_{2,4}$									
Linear fit of K factor	A (dB)	30.4	27.9	30.4	29.6	27.5	29.6	11.9	10.2	11.7	11.7	9.9	11.5
	n	-0.04	0.12	-0.04	0.01	0.14	0.01	0.14	0.26	0.13	0.18	0.31	0.17
	σ_X (dB)	1.9	2.6	1.9	2.0	2.5	2.0	1.2	1.7	1.3	0.9	1.5	1.0
	D_{max} (km)	3.0	3.0	3.0	3.0	3.0	3.0	3.0	3.0	3.0	3.0	3.0	3.0
	D_{Min} (km)	17.5	17.5	17.5	13.3	13.3	13.3	17.5	17.5	17.5	17.5	17.5	17.5
Statistics of K factor (dB)	Max	35.3	34.5	35.3	34.5	34.6	34.5	18.8	18.5	18.6	17.7	17.7	18.0
	Min	14.1	10.7	14.3	10.7	3.7	10.4	4.0	0.0	2.6	4.8	0.0	5.4
	Median	30.0	28.9	30.0	29.7	28.7	29.7	13.2	12.6	12.9	13.3	12.7	13.0
	μ	30.2	29.3	30.1	29.8	29.0	29.8	13.1	12.7	12.8	13.1	12.7	12.8
	σ	1.9	2.6	1.9	2.0	2.5	2.0	1.3	1.9	1.3	1.1	1.8	1.2

A.10 Hilly Terrain Flight Track 9



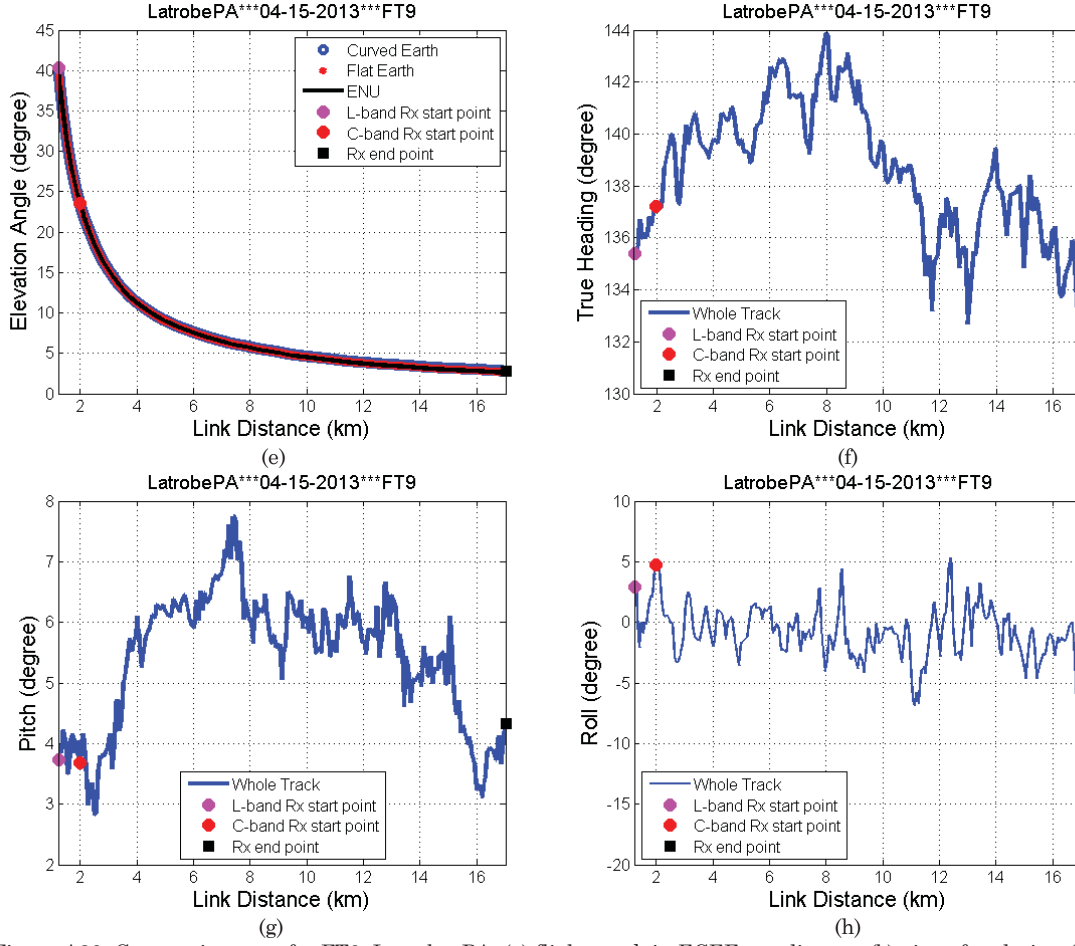
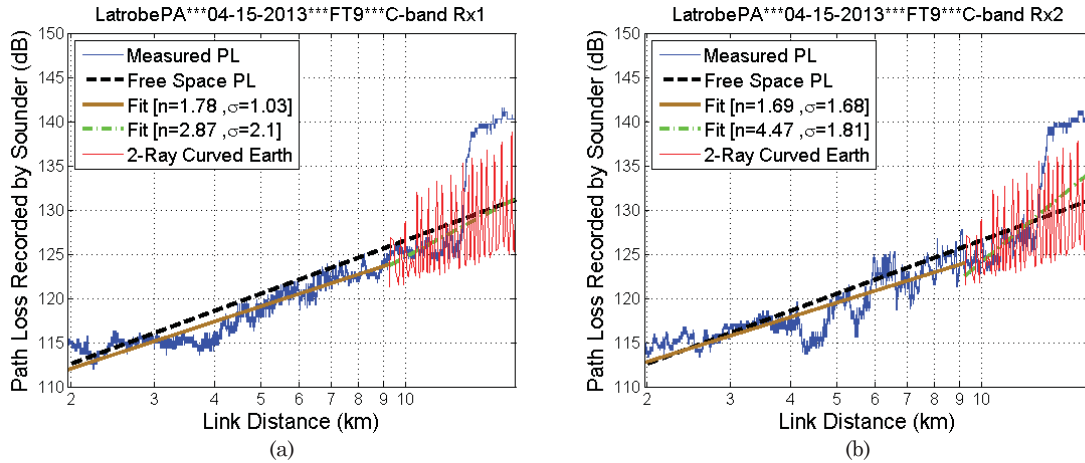


Figure A39. Geometric traces for FT9, Latrobe, PA: (a) flight track in ECEF coordinates; (b) aircraft velocity; (c) altitude difference between aircraft and ground station; (d) azimuth angle; (e) elevation angle; (f) heading of aircraft; (g) pitch angle of aircraft; (h) roll angle of aircraft.



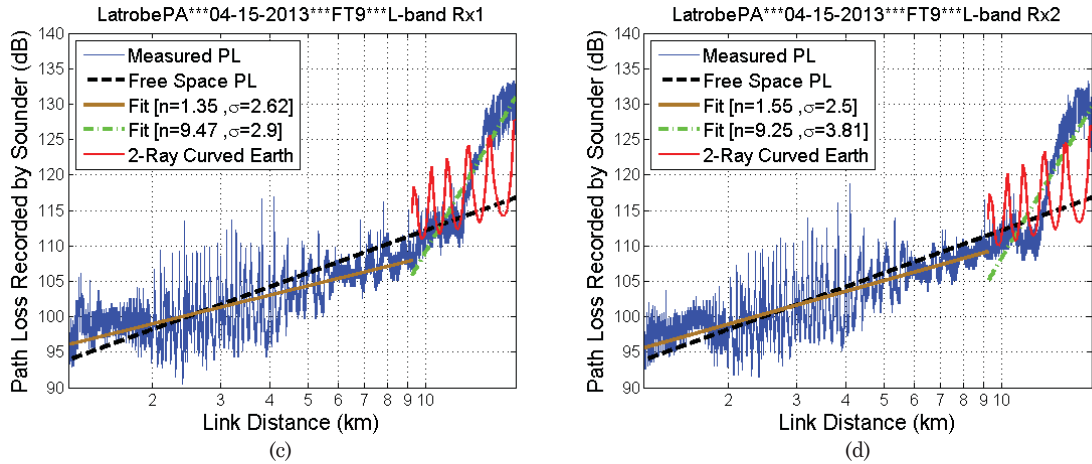


Figure A40. Measured path loss vs. distance for FT9, Latrobe, PA (a) C-band Rx1; (b) C-band 2; (c) L-band Rx1; (d) L-band Rx2.

Table A28. Path loss model parameters, FT9, Latrobe, PA, 15 April 2013, flight straight away from GS.

	$d < d_t (\theta > \theta_t)$							$d > d_t (\theta < \theta_t)$								
	Log-distance linear PL model			Elevation angle range (degree)		Distance range (km)		Log-distance linear PL model			CE2R (dB)		Elevation angle range (degree)		Distance range (km)	
	$A_{0,S}$ (dB)	n_S	σ_{XLS} (dB)	$\theta_{min,S}$	$\theta_{max,S}$	$d_{min,S}$	$d_{max,S}$	$A_{0,L}$ (dB)	n_L	$\sigma_{XL,L}$ (dB)	L_0	σ_{X2}	$\theta_{min,L}$	$\theta_{max,L}$	$d_{min,L}$	$d_{max,L}$
C-Rx1	0.1	1.8	1.0	5.0	23.5	2.0	9.3	-76.5	2.9	2.1	-	3.3	2.8	5.0	9.3	17.0
	6.5	1.7	1.7	5.0	23.5	2.0	9.3	189.1	4.5	1.8	-	3.3	2.8	5.0	9.3	17.0
	13.8	1.4	2.6	5.0	40.3	1.2	9.3	554.2	9.5	2.9	2.4	6.3	2.8	5.0	9.3	17.0
	1.5	1.5	2.5	5.0	40.3	1.2	9.3	539.6	9.3	3.8	1.5	6.8	2.8	5.0	9.3	17.0

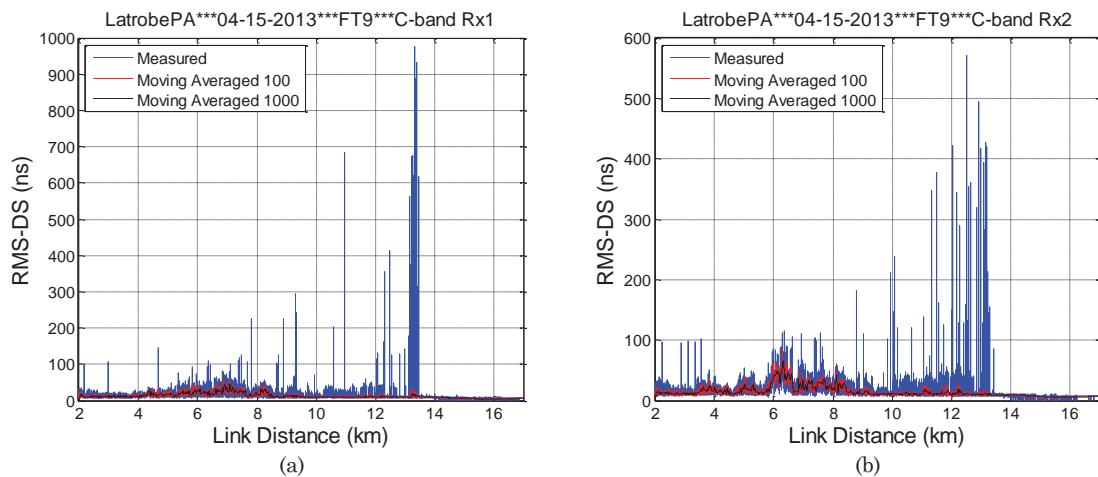


Figure A41. RMS-DS vs. distance for FT9, Latrobe, PA of C-band (a) Rx1; (b) Rx2.

Table A29. Statistics of spatial correlation, FT9, Latrobe, PA.

	C1C2	L1L2	CIL1	C1L2	C2L1	C2L2
Window Length	98	98	98	98	98	98
Mean	0.44	0.65	0.04	0.05	0.05	0.08
Median	0.82	0.89	0.09	0.11	0.11	0.25
Max	1.00	1.00	1.00	1.00	1.00	1.00
Min	-1.00	-1.00	-1.00	-1.00	-1.00	-1.00
Standard deviation	0.68	0.49	0.73	0.73	0.73	0.76

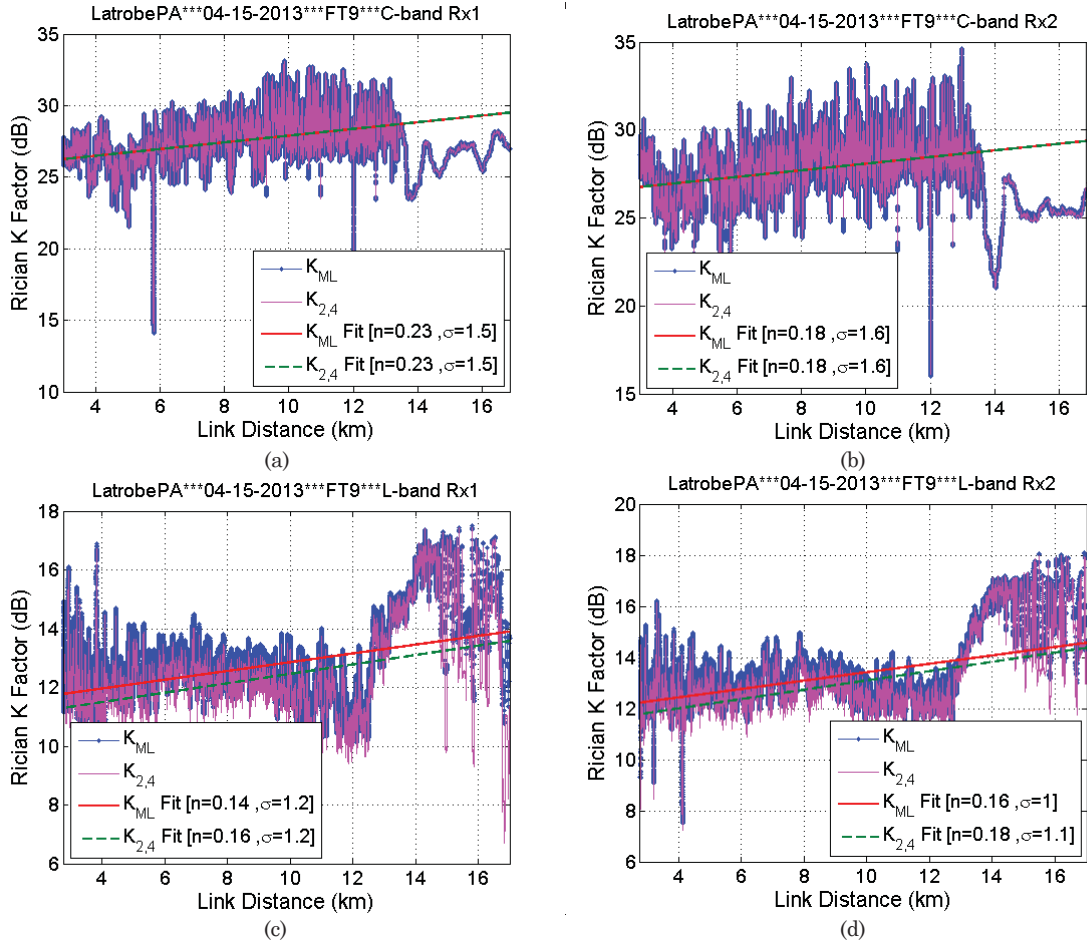
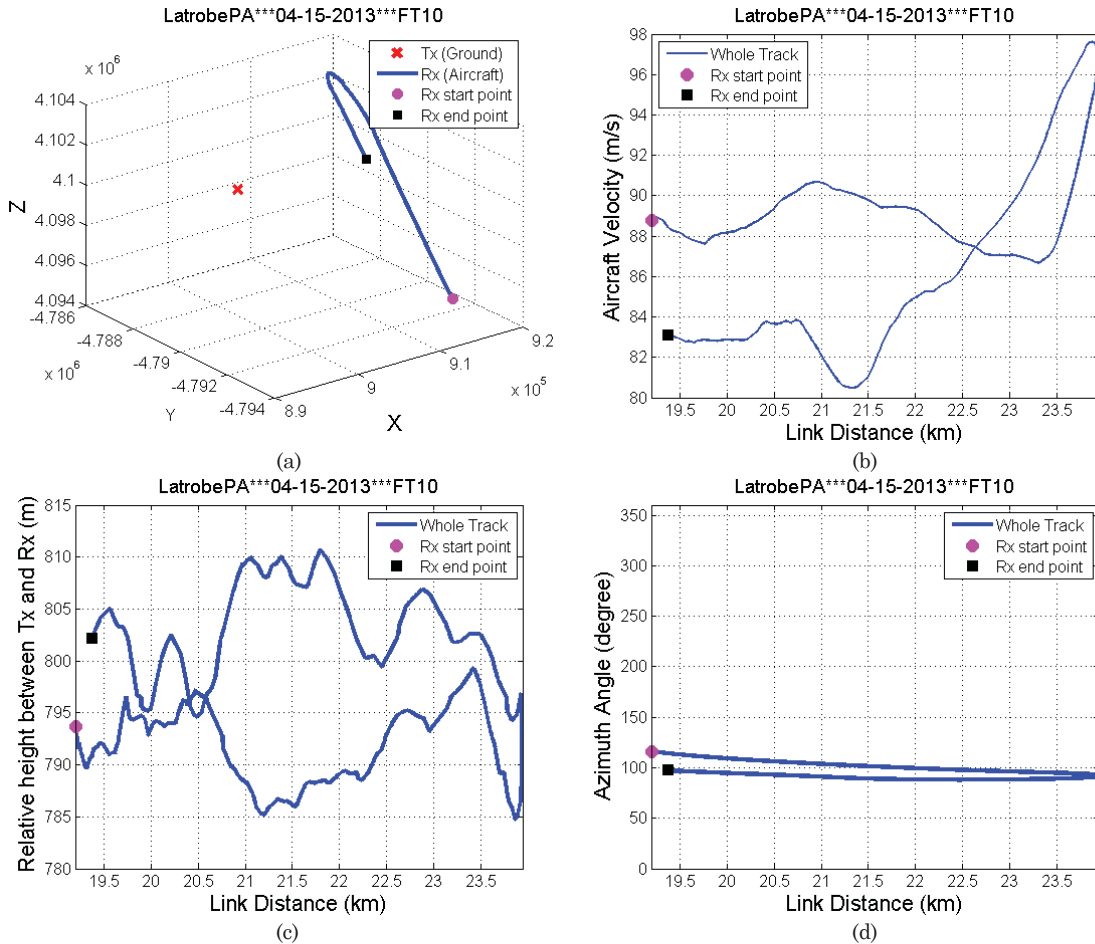


Figure A42. Ricean K factor for FT9, Latrobe, PA (a) C-band Rx1; (b) C-band 2; (c) L-band Rx1; (d) L-band Rx2.

Table A30. Statistics of Ricean K factor, FT9, Latrobe, PA.

		C-band						L-band					
		Rx1			Rx2			Rx1			Rx2		
Moving Window Length		250λ						15 m					
Overall K factor (dB)		27.1			27.3			12.5			13.1		
Methods		K_{ML}	K_2	$K_{2,4}$									
Linear fit of K factor	A (dB)	25.6	24.2	25.5	26.2	24.7	26.2	11.4	9.8	10.9	11.8	10.1	11.3
	n	0.23	0.31	0.24	0.19	0.26	0.19	0.15	0.25	0.16	0.16	0.28	0.18
	σ_X (dB)	1.5	2.0	1.5	1.6	2.3	1.6	1.2	1.4	1.3	1.1	1.3	1.1
	D_{max} (km)	3.0	3.0	3.0	3.0	3.0	3.0	2.8	2.8	2.8	2.8	2.8	2.8
	D_{Min} (km)	17.0	17.0	17.0	17.0	17.0	17.0	17.0	17.0	17.0	17.0	17.0	17.0
Statistics of K factor (dB)	Max	33.1	33.0	33.1	34.6	34.7	34.6	17.5	19.5	19.1	18.1	18.4	18.5
	Min	14.1	10.6	14.3	15.6	9.5	15.7	6.5	-0.4	6.7	7.5	-5.7	7.2
	Median	27.5	26.8	27.5	27.8	26.9	27.8	12.7	12.1	12.3	13.3	12.7	13.0
	μ	27.5	27.0	27.5	27.9	27.2	27.9	12.5	11.9	12.1	13.0	12.5	12.6
	σ	1.7	2.2	1.7	1.7	2.4	1.7	1.3	1.7	1.4	1.2	1.7	1.3

A.11 Hilly Terrain Flight Track 10



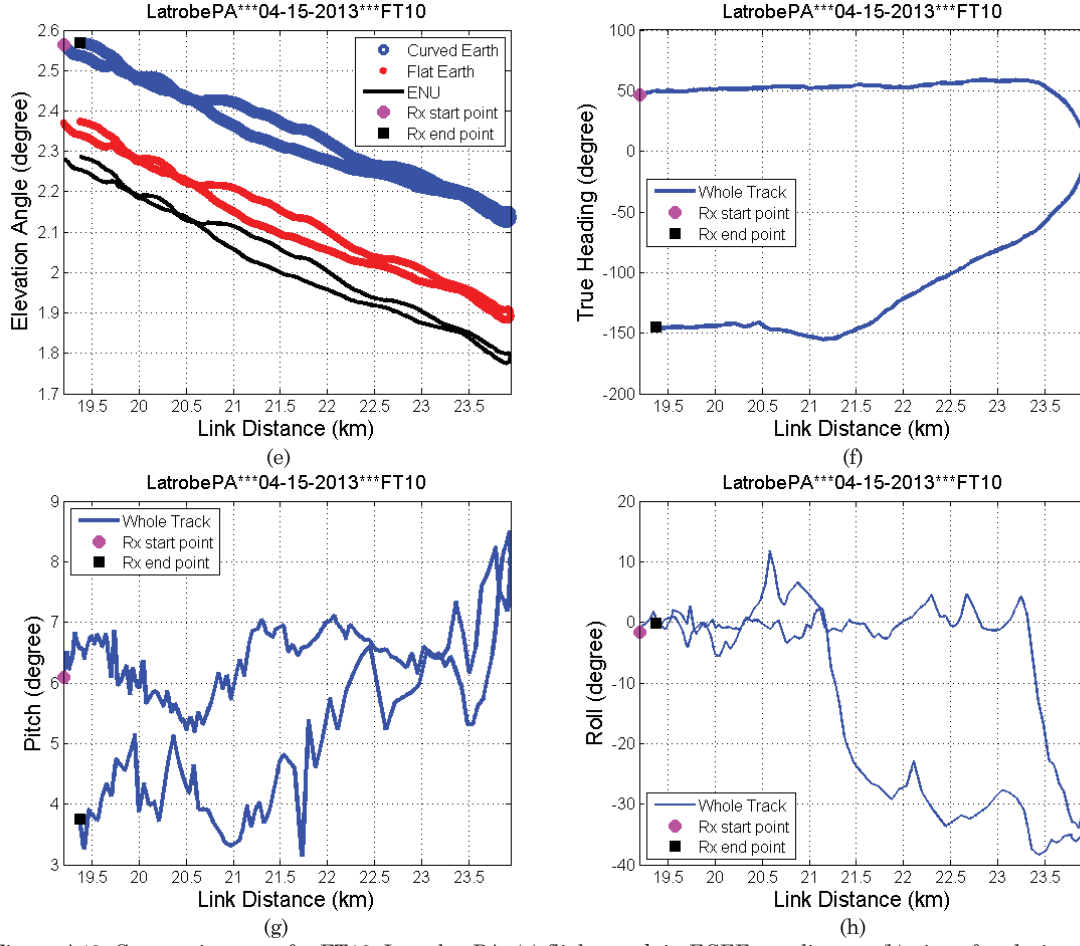


Figure A43. Geometric traces for FT10, Latrobe, PA: (a) flight track in ECEF coordinates; (b) aircraft velocity; (c) altitude difference between aircraft and ground station; (d) azimuth angle; (e) elevation angle; (f) heading of aircraft; (g) pitch angle of aircraft; (h) roll angle of aircraft.

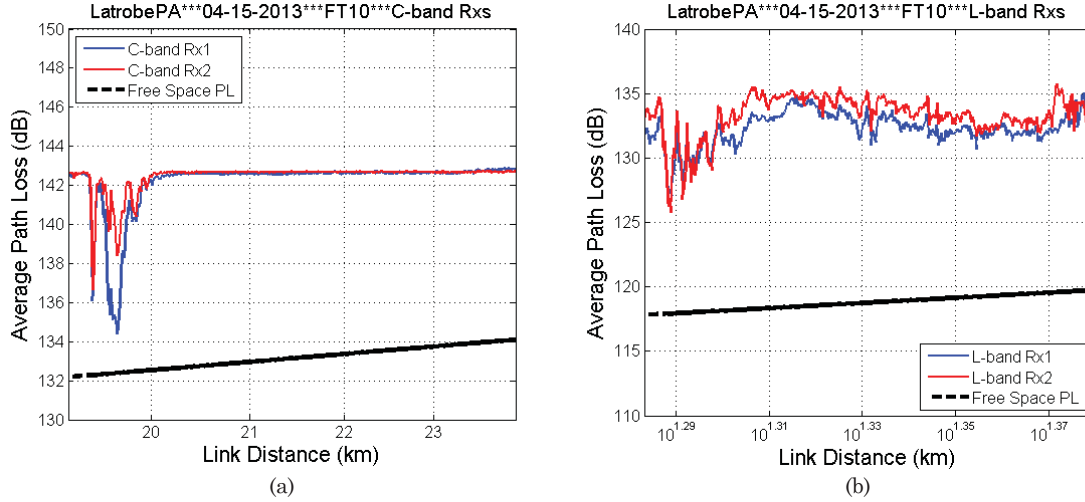


Figure A44. Measured path loss vs. distance for FT10, Latrobe, PA (a) C-band Rx1 & 2; (b) L-band Rx1 & 2.

As seen from Figure A.44, the C-band attenuation also hit its “ceiling” in FT10. Thus the C-band path loss and RMS-DS results for this FT are likely invalid. Because of the smaller number of PDPs and much slower PDP update rate from this FT, the K-factors as well are likely inaccurate.

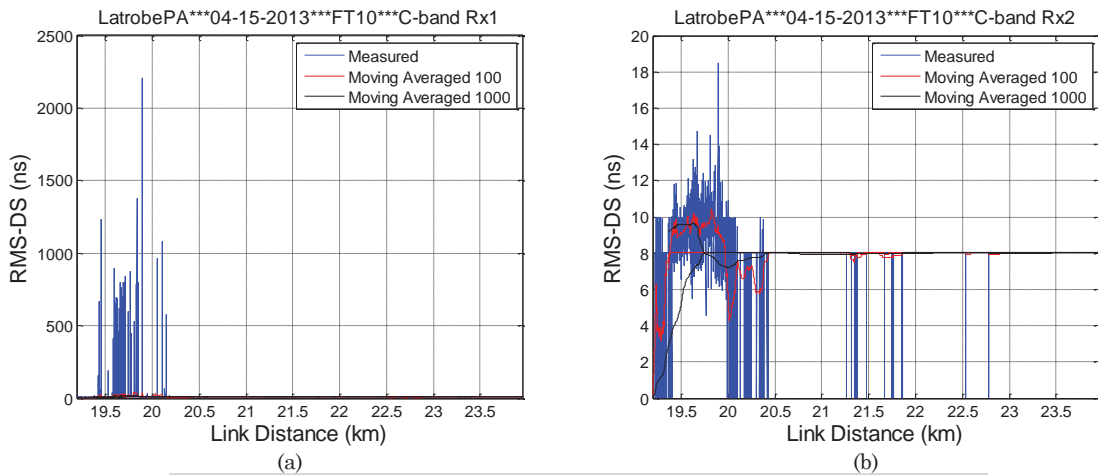
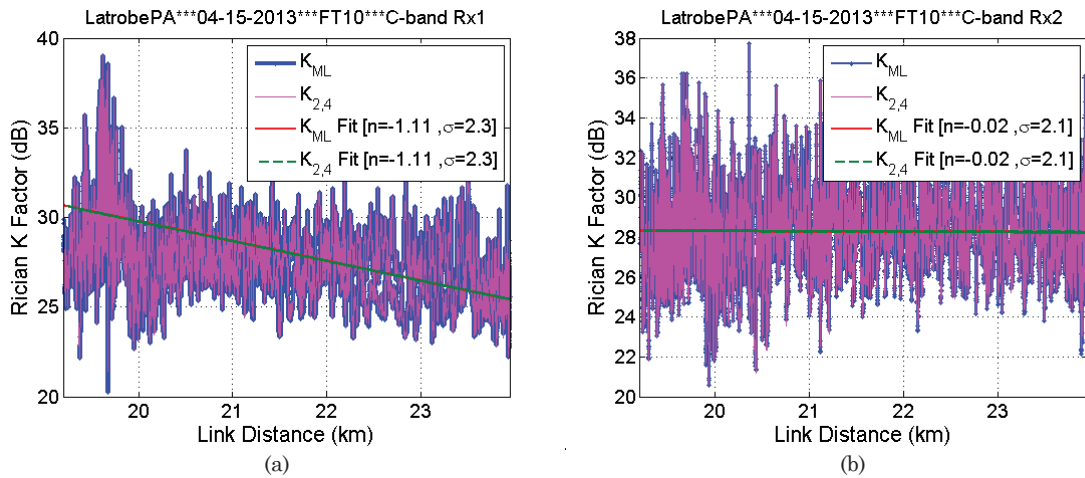


Figure A45. RMS-DS vs. distance for FT10, Latrobe, PA of C-band (a) Rx1; (b) Rx2.

Table A31. Statistics of spatial correlation, FT10, Latrobe, PA.

	C1C2	L1L2	C1L1	C1L2	C2L1	C2L2
Window Length	87	87	87	87	87	87
Mean	0.31	0.61	0.35	0.19	0.19	0.26
Median	0.34	0.93	0.73	0.43	0.43	0.61
Max	1.00	1.00	1.00	1.00	1.00	1.00
Min	-0.82	-0.99	-1.00	-1.00	-1.00	-1.00
Standard deviation	0.53	0.57	0.72	0.74	0.74	0.74



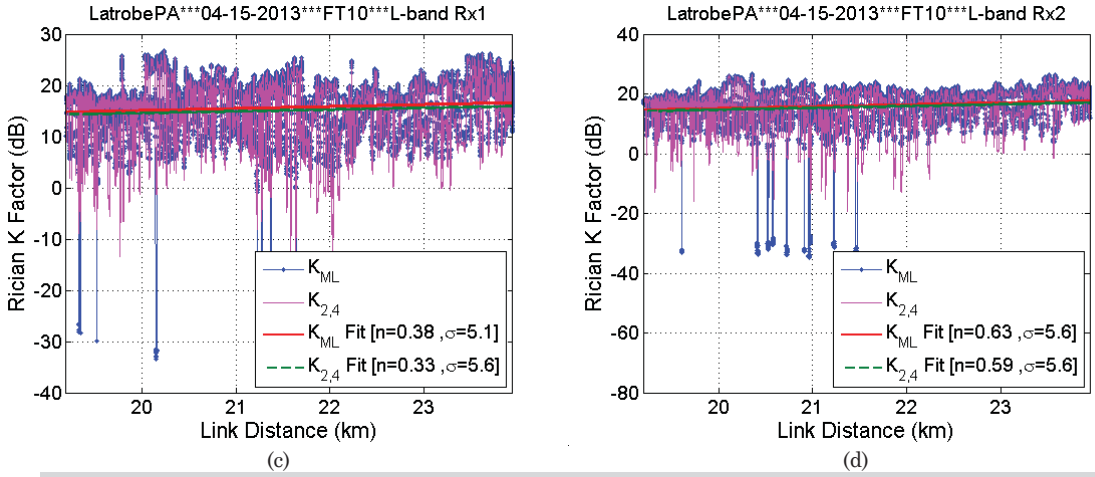
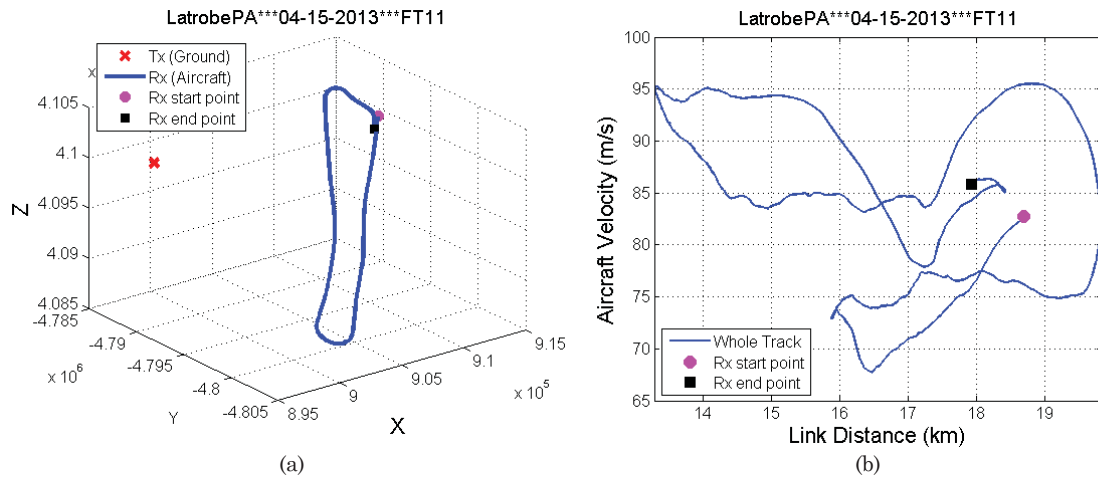


Figure A46. Ricean K factor for FT10, Latrobe, PA (a) C-band Rx1; (b) C-band 2; (c) L-band Rx1; (d) L-band Rx2.

Table A32. Statistics of Ricean K factor, FT10, Latrobe, PA.

		C-band						L-band					
		Rx1			Rx2			Rx1			Rx2		
Moving Window Length		250λ						15 m					
Overall K factor (dB)		28.1			27.7			13.1			13.4		
Methods		K_{ML}	K_2	$K_{2,4}$									
Linear fit of K factor	A(dB)	51.9	50.2	51.8	28.7	26.4	28.6	7.4	7.7	7.9	2.5	2.7	2.8
	n	-1.10	-1.03	-1.10	-0.02	0.08	-0.01	0.38	0.34	0.34	0.63	0.60	0.60
	σ_X (dB)	2.3	2.5	2.3	2.1	2.2	2.1	5.1	5.6	5.6	5.7	5.6	5.6
	D_{max} (km)	19.2	19.2	19.2	19.2	19.2	19.2	19.2	19.2	19.2	19.2	19.2	19.2
	D_{Min} (km)	23.9	23.9	23.9	23.9	23.9	23.9	23.9	23.9	23.9	23.9	23.9	23.9
Statistics of K factor (dB)	Max	39.0	38.4	39.0	37.7	37.2	37.7	26.8	26.8	26.8	26.6	26.7	26.5
	Min	20.2	16.2	21.4	20.6	16.8	20.6	-33.4	0.0	0.0	-61.8	0.0	0.0
	Median	29.0	28.8	29.0	28.3	28.1	28.3	15.5	14.8	15.0	15.8	15.2	15.3
	μ	28.7	28.5	28.7	28.2	28.1	28.2	16.3	16.1	16.2	16.4	16.3	16.3
	σ	2.8	2.9	2.8	2.1	2.2	2.1	5.1	5.6	5.6	5.8	5.7	5.7

A.12 Hilly Terrain Flight Track 11



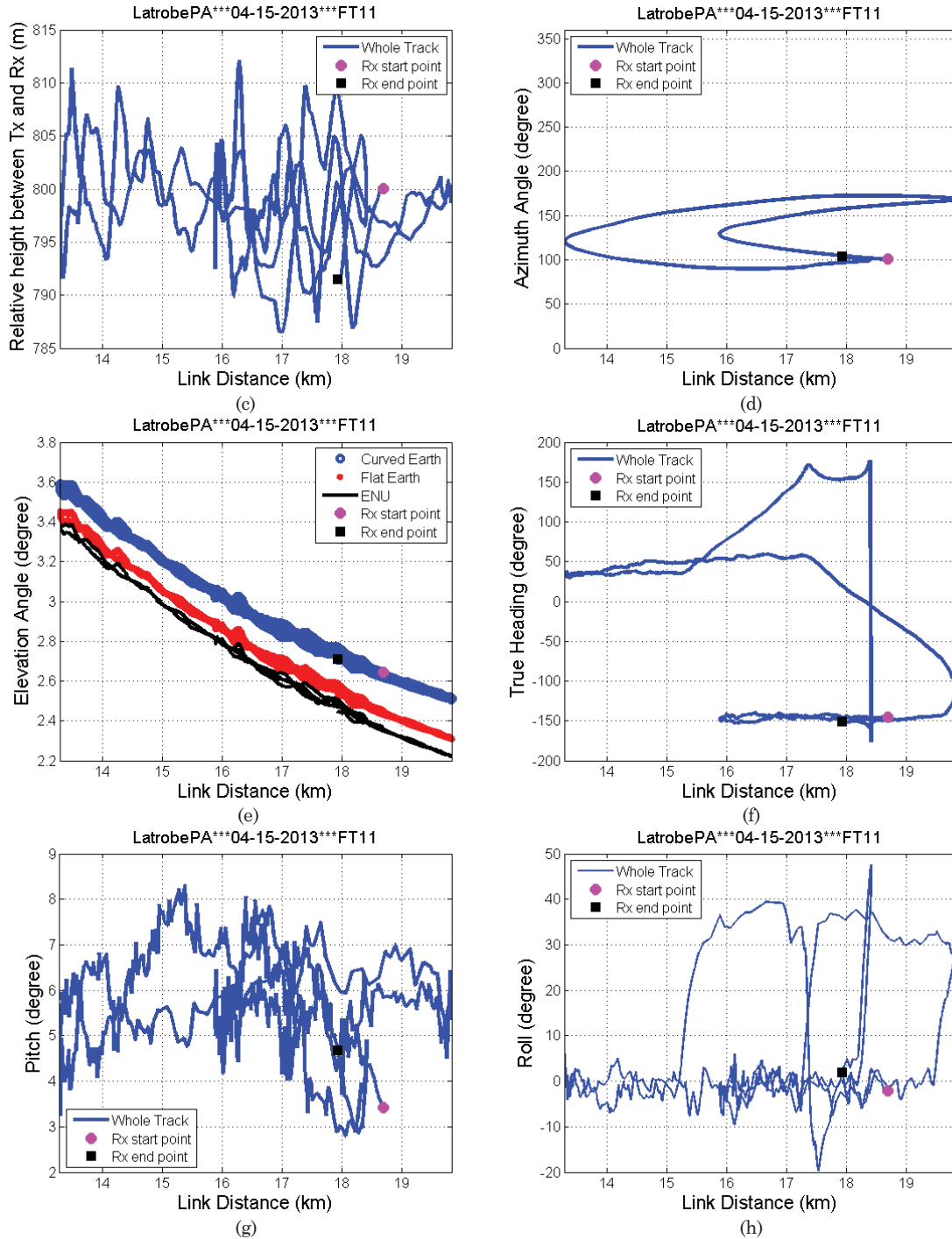


Figure A47. Geometric traces for FT11, Latrobe, PA: (a) flight track in ECEF coordinates; (b) aircraft velocity; (c) altitude difference between aircraft and ground station; (d) azimuth angle; (e) elevation angle; (f) heading of AC; (g) pitch angle of AC; (h) roll angle of AC.

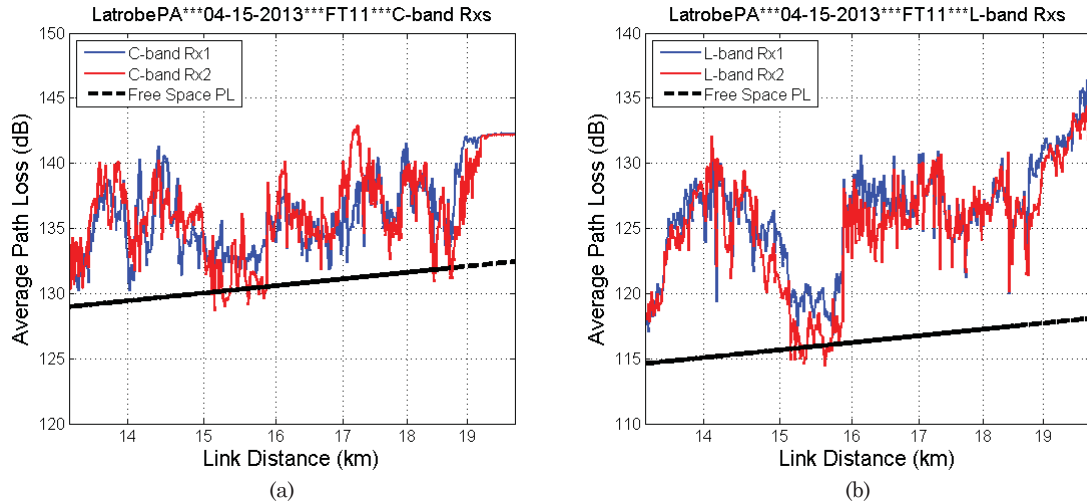


Figure A48. Measured path loss vs. distance for FT11, Latrobe, PA (a) C-band Rx1 & 2; (b) L-band Rx1 & 2.

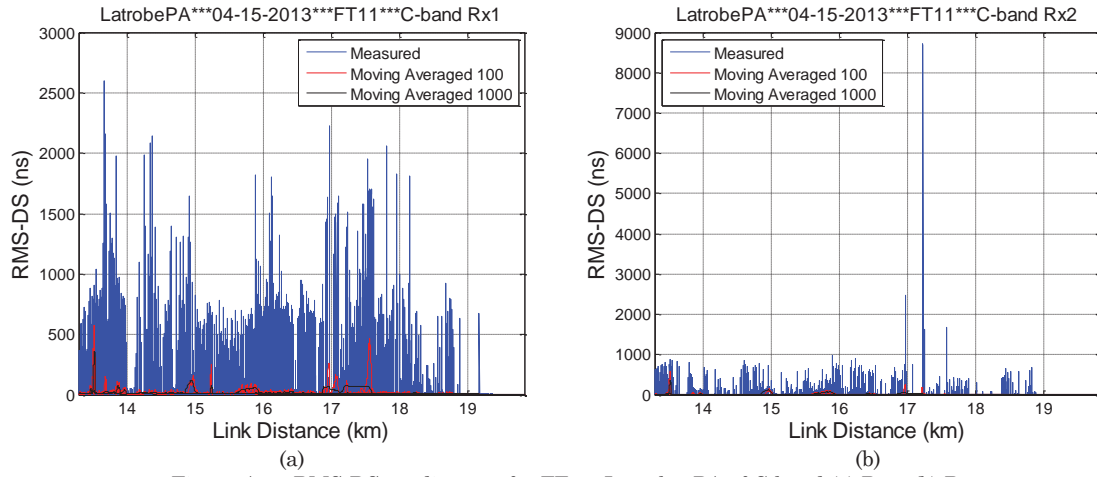


Figure A49. RMS-DS vs. distance for FT11, Latrobe, PA of C-band (a) Rx1; (b) Rx2.

Table A33. Statistics of spatial correlation, FT11, Latrobe, PA.

	C1C2	L1L2	C1L1	C1L2	C2L1	C2L2
Window Length	87	87	87	87	87	87
Mean	0.12	0.63	0.03	0.03	0.03	0.12
Median	0.31	0.95	0.08	0.09	0.09	0.37
Max	1.00	1.00	1.00	1.00	1.00	1.00
Min	-1.00	-1.00	-1.00	-1.00	-1.00	-1.00
Standard deviation	0.76	0.60	0.79	0.78	0.78	0.79

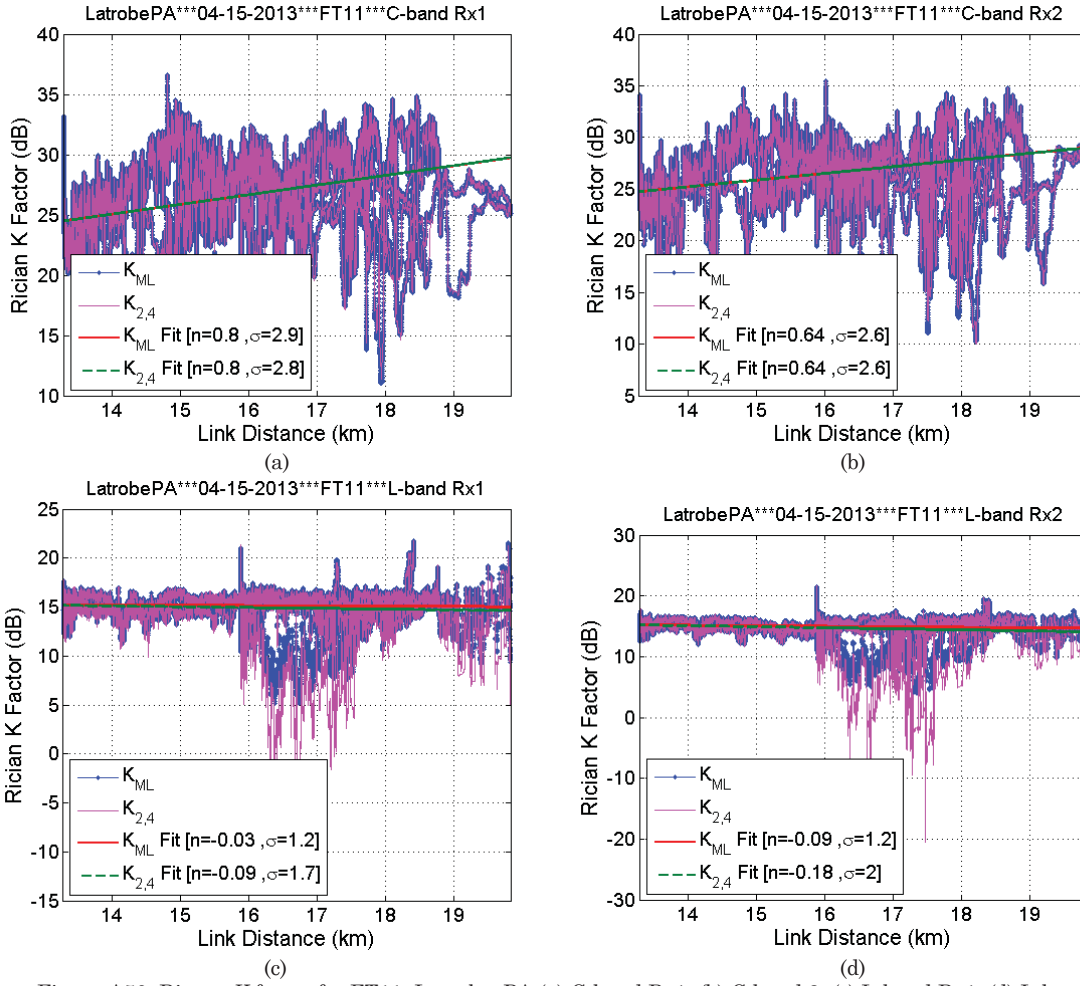
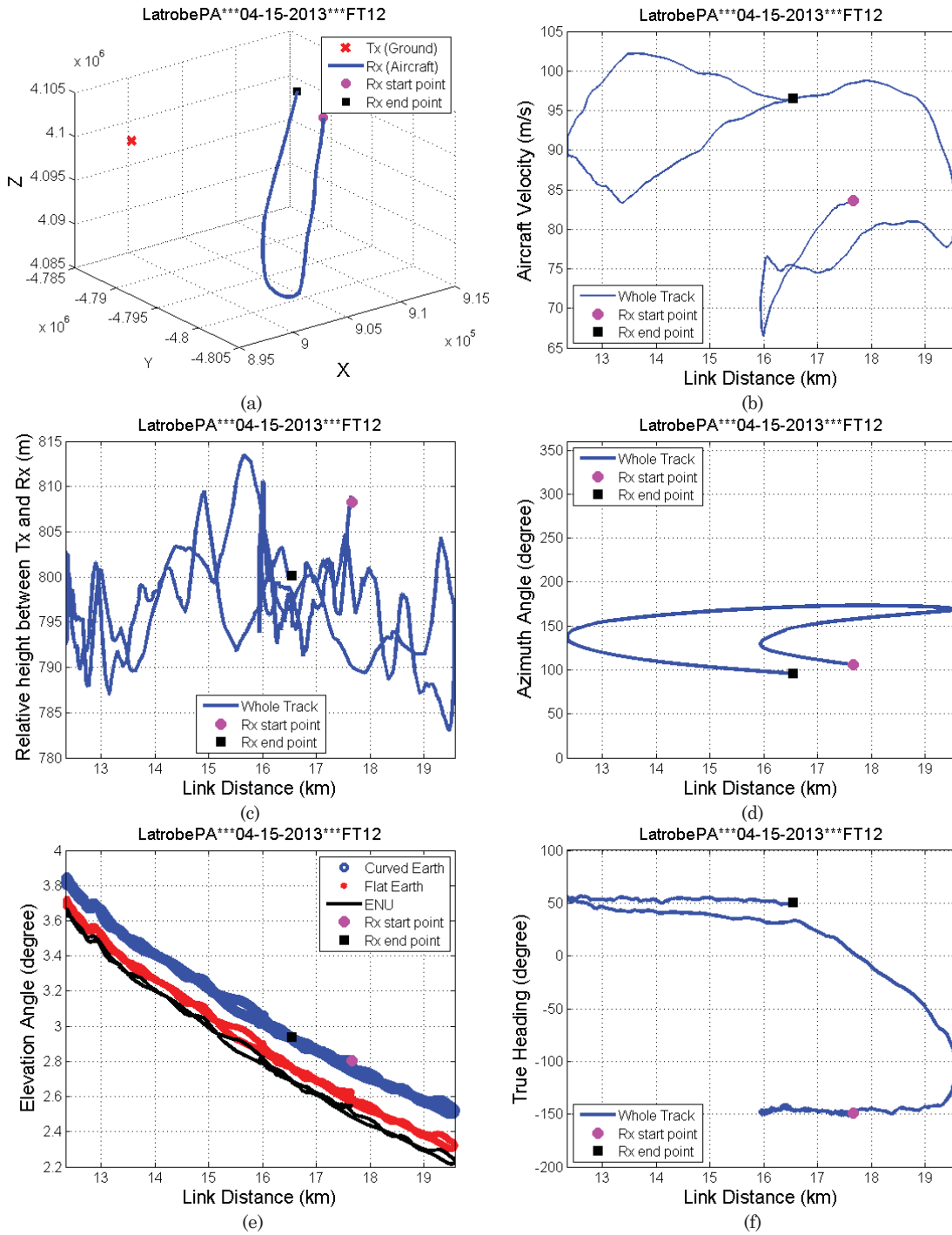


Figure A50. Ricean K factor for FT11, Latrobe, PA (a) C-band Rx1; (b) C-band 2; (c) L-band Rx1; (d) L-band Rx2.

Table A34. Statistics of Ricean K factor, FT11, Latrobe, PA.

		C-band						L-band					
		Rx1			Rx2			Rx1			Rx2		
Moving Window Length		250λ						15 m					
Overall K factor (dB)		25.0			25.1			14.9			14.8		
Methods		K_{ML}	K_2	$K_{2,4}$									
Linear fit of K factor	A(dB)	13.9	14.3	13.8	16.1	17.8	16.1	15.6	16.5	16.3	16.3	17.8	17.5
	n	0.80	0.69	0.80	0.65	0.47	0.65	-0.03	-0.11	-0.08	-0.08	-0.20	-0.17
	σ_X (dB)	2.9	3.2	2.9	2.7	3.1	2.6	1.2	1.8	1.8	1.3	2.1	2.1
	D_{max} (km)	13.3	13.3	13.3	13.3	13.3	13.3	13.3	13.3	13.3	13.3	13.3	13.3
	D_{Min} (km)	19.8	19.8	19.8	19.8	19.8	19.8	19.8	19.8	19.8	19.8	19.8	19.8
Statistics of K factor (dB)	Max	36.6	36.7	36.6	35.5	35.2	35.5	21.8	22.1	22.1	21.5	-24.4	21.8
	Min	11.0	9.2	11.4	10.2	8.1	10.0	5.1	0.0	0.0	4.0	0.0	0.0
	Median	26.3	25.1	26.3	26.2	25.1	26.2	15.2	14.8	15.0	15.0	14.6	14.8
	μ	26.3	25.0	26.3	26.2	25.1	26.2	15.4	15.2	15.3	15.2	15.0	15.1
	σ	3.2	3.3	3.1	2.9	3.2	2.8	1.2	1.8	1.8	1.3	2.1	2.1

A.13 Hilly Terrain Flight Track 12



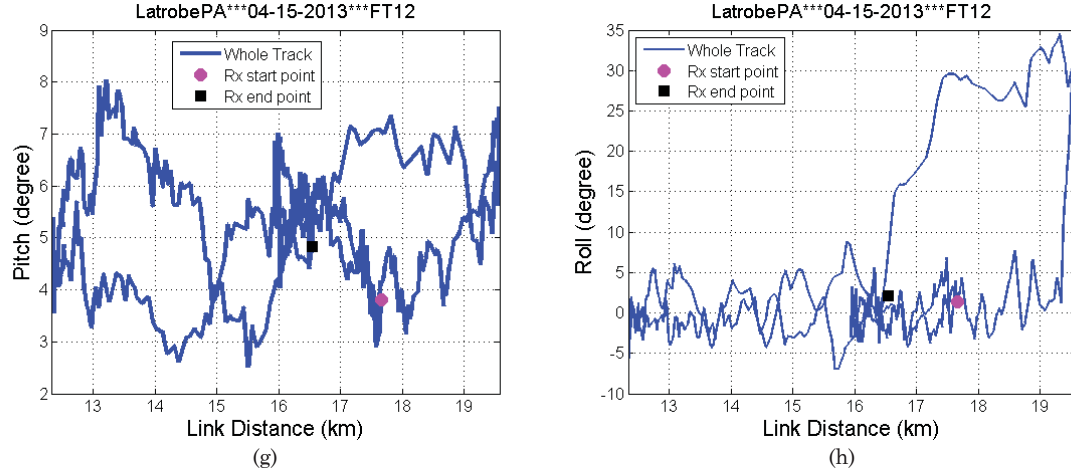


Figure A51. Geometric traces for FT12, Latrobe, PA: (a) flight track in ECEF coordinates; (b) aircraft velocity; (c) altitude difference between aircraft and ground station; (d) azimuth angle; (e) elevation angle; (f) heading of AC; (g) pitch angle of AC; (h) roll angle of AC.

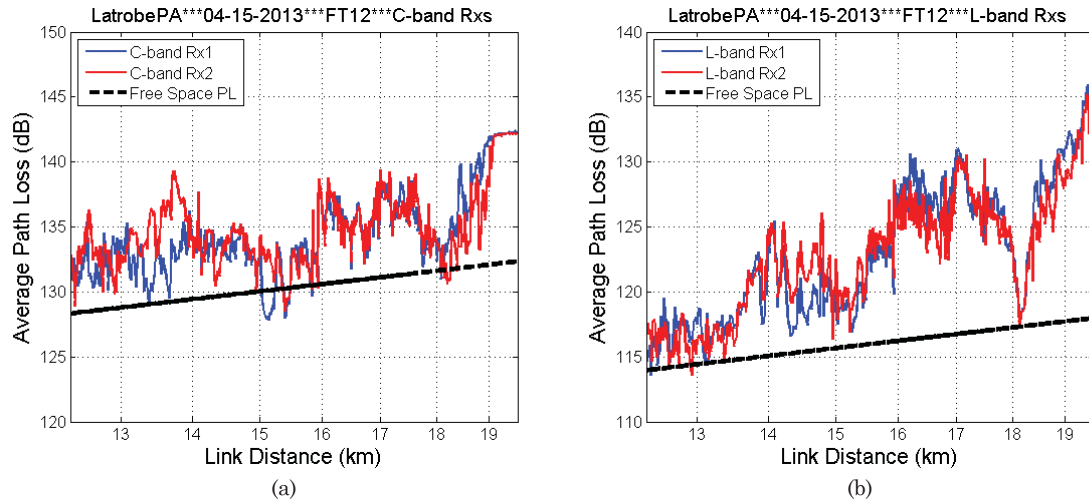


Figure A52. Measured path loss vs. distance for FT12, Latrobe, PA (a) C-band Rx1 & 2; (b) L-band Rx1 & 2.

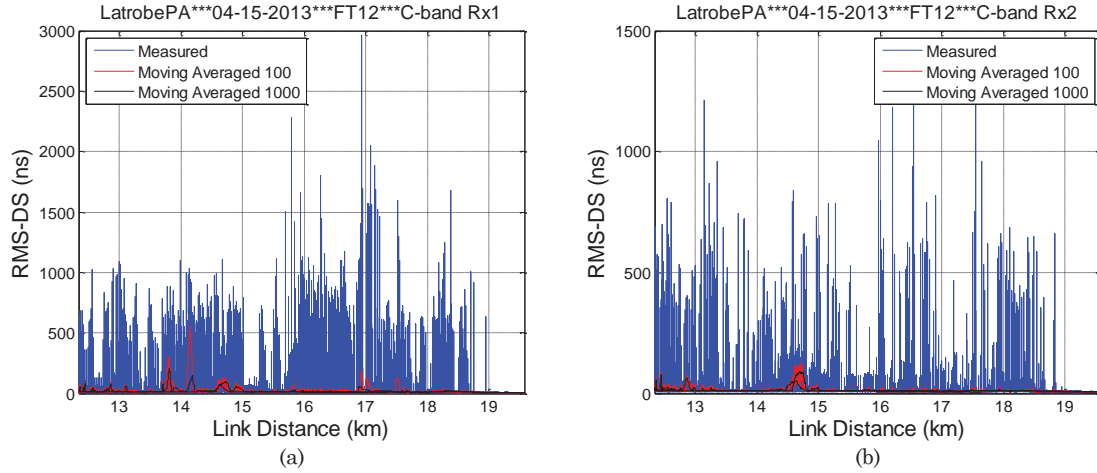


Figure A53. RMS-DS vs. distance for FT12, Latrobe, PA of C-band (a) Rx1; (b) Rx2.

Table A35. Statistics of spatial correlation, FT12, Latrobe, PA.

	C1C2	L1L2	C1L1	C1L2	C2L1	C2L2
Window Length	83	83	83	83	83	83
Mean	0.15	0.66	0.03	0.04	0.04	0.08
Median	0.38	0.95	0.10	0.11	0.11	0.23
Max	1.00	1.00	1.00	1.00	1.00	1.00
Min	-1.00	-1.00	-1.00	-1.00	-1.00	-1.00
Standard deviation	0.76	0.55	0.79	0.79	0.79	0.78

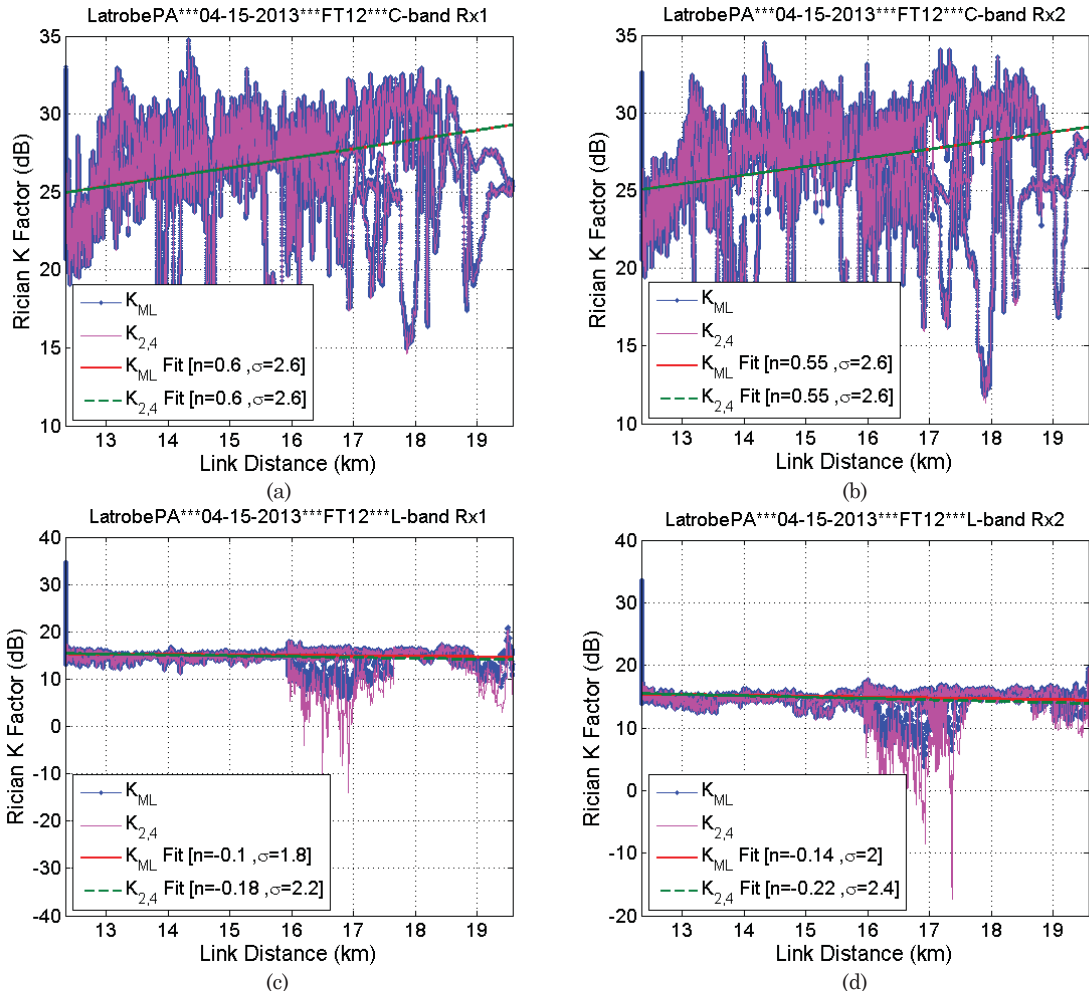
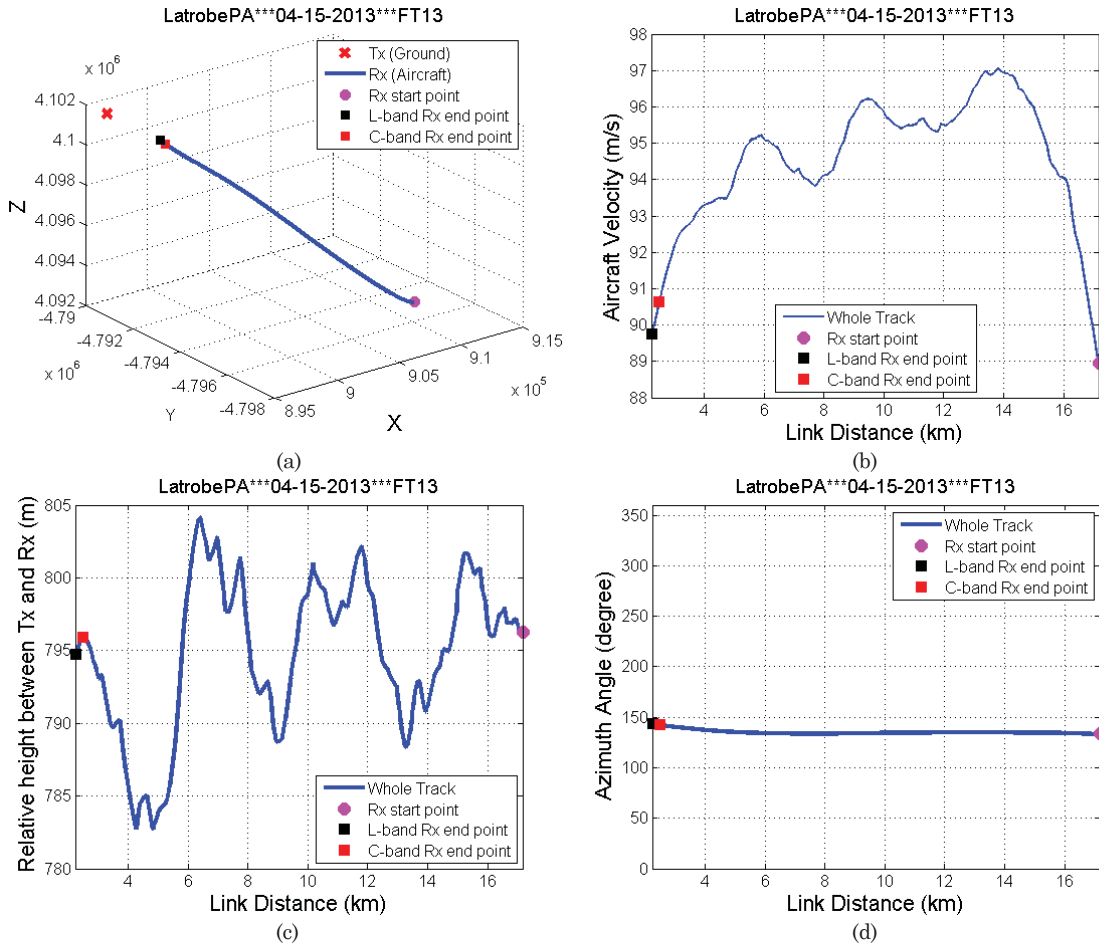


Figure A54. Ricean K factor for FT12, Latrobe, PA (a) C-band Rx1; (b) C-band 2; (c) L-band Rx1; (d) L-band Rx2.

Table A36. Statistics of Ricean K factor, FT12, Latrobe, PA.

		C-band						L-band					
		Rx1			Rx2			Rx1			Rx2		
Moving Window Length		250λ						15 m					
Overall K factor (dB)		25.1			25.2			14.8			14.7		
Methods		K_{ML}	K_2	$K_{2,4}$									
Linear fit of K factor	A(dB)	17.6	18.0	17.5	18.2	19.2	18.2	16.6	17.2	17.6	17.1	17.7	18.2
	n	0.60	0.47	0.60	0.55	0.40	0.56	-0.10	-0.16	-0.18	-0.13	-0.20	-0.22
	σ_X (dB)	2.6	3.0	2.6	2.6	3.0	2.6	1.8	2.1	2.2	2.1	2.2	2.4
	D_{max} (km)	12.3	12.3	12.3	12.3	12.3	12.3	12.3	12.3	12.3	12.3	12.3	12.3
	D_{Min} (km)	19.6	19.6	19.6	19.6	19.6	19.6	19.6	19.6	19.6	19.6	19.6	19.6
Statistics of K factor (dB)	Max	34.8	33.4	34.8	34.5	34.3	34.5	34.9	32.7	34.9	33.7	34.0	33.7
	Min	12.5	7.4	12.4	11.8	8.8	11.4	-30.7	0.0	0.0	3.8	0.0	0.0
	Median	26.3	24.9	26.3	26.4	25.1	26.4	15.2	14.8	15.0	15.1	14.7	15.0
	μ	26.6	25.0	26.6	26.5	25.1	26.5	15.1	14.9	15.0	15.0	14.9	15.0
	σ	2.9	3.1	2.9	2.9	3.1	2.9	1.8	2.1	2.3	2.1	2.3	2.5

A.14 Hilly Terrain Flight Track 13



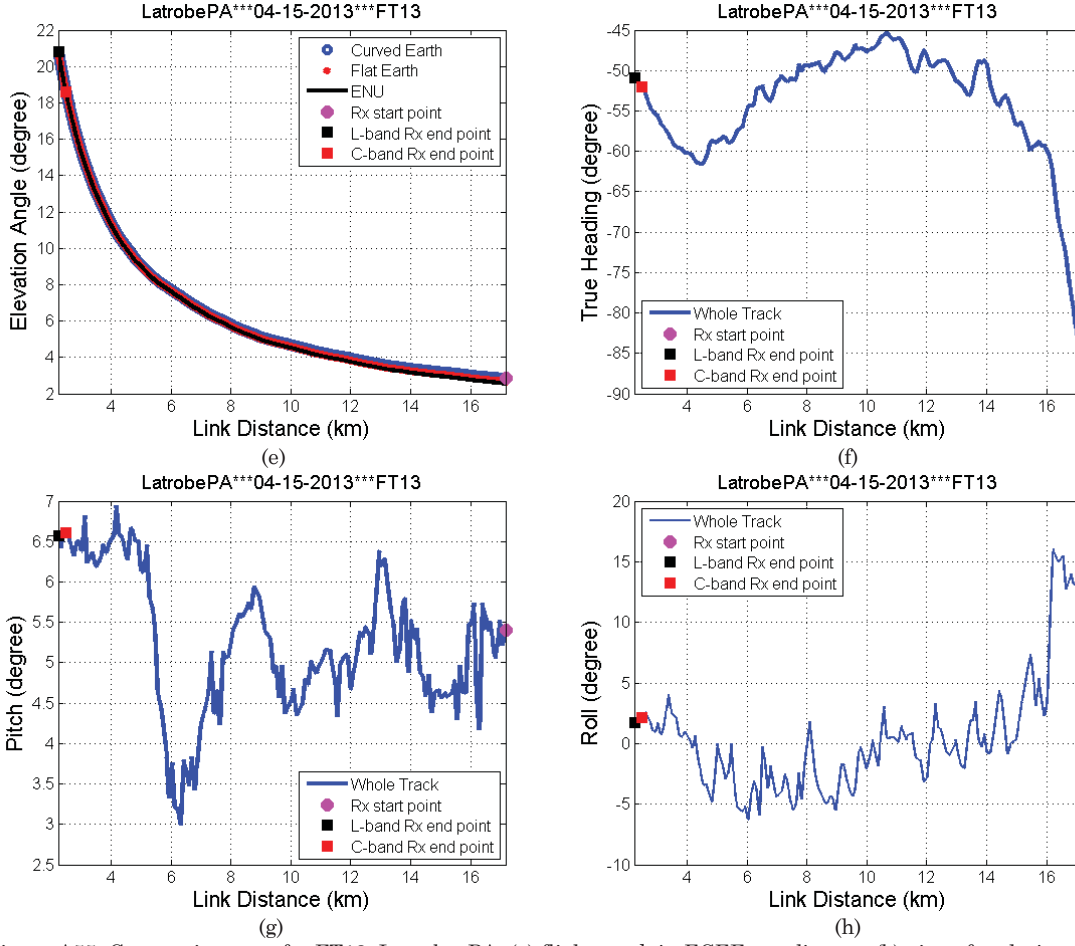
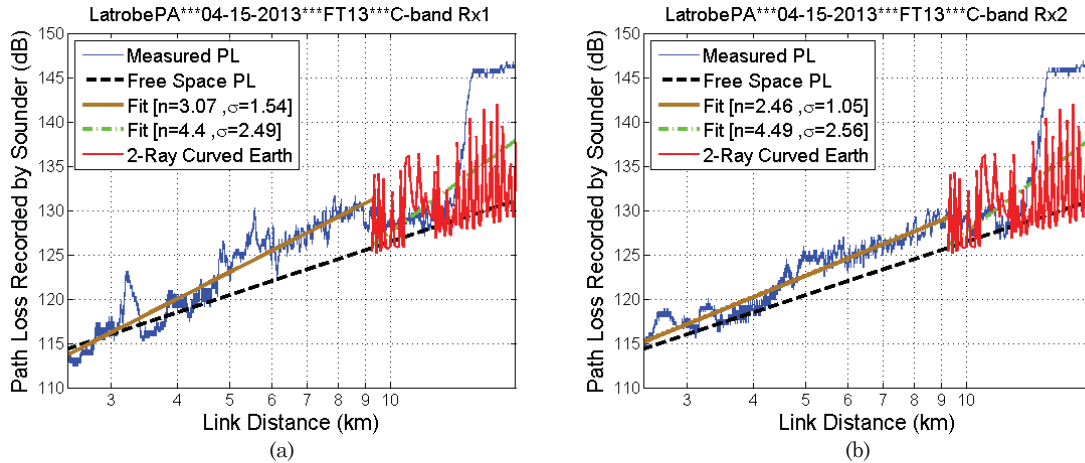


Figure A55. Geometric traces for FT13, Latrobe, PA: (a) flight track in ECEF coordinates; (b) aircraft velocity; (c) altitude difference between aircraft and ground station; (d) azimuth angle; (e) elevation angle; (f) heading of aircraft; (g) pitch angle of aircraft; (h) roll angle of aircraft.

As noted for hilly terrain FTs 8 and 9, the path loss for hilly terrain FT13 is likely not valid for large values of distance, due to terrain shadowing. RMS-DS and K -factor results for the large-distance section of FT13 are also likely inaccurate.



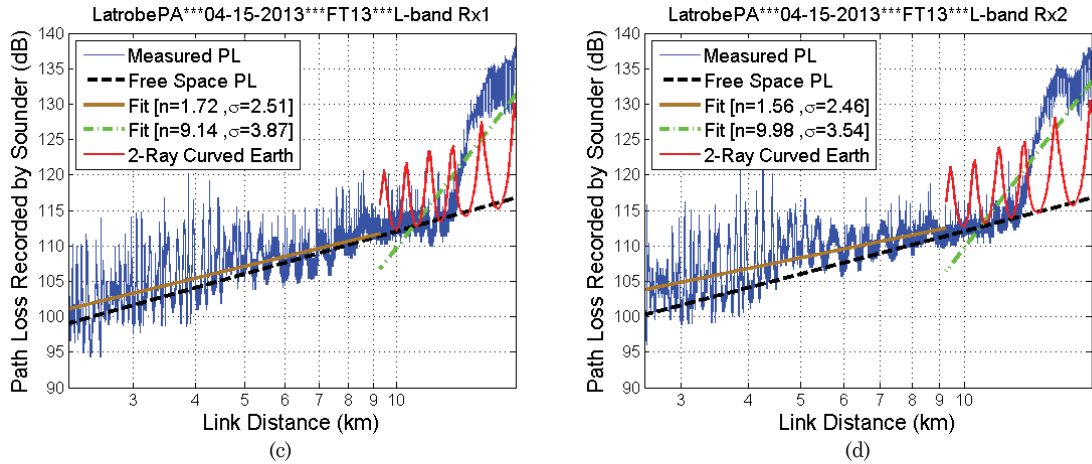


Figure A56. Measured path loss vs. distance for FT13, Latrobe, PA (a) C-band Rx1; (b) C-band 2; (c) L-band Rx1; (d) L-band Rx2.

Table A37. Path loss model parameters, FT13, Latrobe, PA, 15 April 2013, flight straight toward GS.

	$d < d_t (\theta > \theta_t)$							$d > d_t (\theta < \theta_t)$									
	Log-distance linear PL model			Elevation angle range (degree)		Distance range (km)		Log-distance linear PL model			CE2R (dB)		Elevation angle range (degree)		Distance range (km)		
	$A_{0,S}$ (dB)	n_S	$\sigma_{XL,S}$ (dB)	$\theta_{min,S}$	$\theta_{max,S}$	$d_{min,S}$	$d_{max,S}$	$A_{0,L}$ (dB)	n_L	$\sigma_{XL,L}$ (dB)	L_0	σ_{X2}	$\theta_{min,L}$	$\theta_{max,L}$	$d_{min,L}$	$d_{max,L}$	
	C-Rx1	-82.9	3.1	1.5	5.0	18.6	2.5	9.2	180.7	4.4	2.5	2.5	4.0	2.8	5.0	9.2	17.2
	C-Rx2	-42.4	2.5	1.1	5.0	18.6	2.5	9.2	186.6	4.5	2.6	2.5	4.0	2.8	5.0	9.2	17.2
	L-Rx1	-8.2	1.7	2.5	5.0	20.8	2.2	9.2	529.8	9.1	3.9	3.5	7.2	2.8	5.0	9.2	17.2
	L-Rx2	3.6	1.6	2.5	5.0	18.1	2.6	9.2	589.0	10.0	3.5	3.9	7.5	2.8	5.0	9.2	17.2

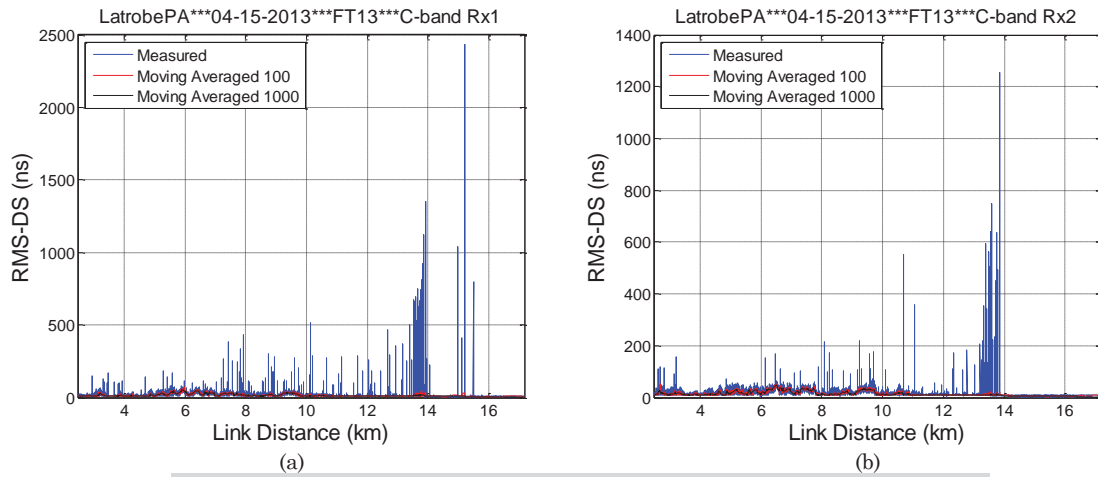


Figure A57. RMS-DS vs. distance for FT13, Latrobe, PA of C-band (a) Rx1; (b) Rx2.

Table A38. Statistics of spatial correlation, FT13, Latrobe, PA.

	C1C2	L1L2	C1L1	C1L2	C2L1	C2L2
Window Length	79	79	79	79	79	79
Mean	-0.01	0.55	0.01	-0.03	-0.03	-0.03
Median	-0.06	0.87	0.03	-0.07	-0.07	-0.07
Max	1.00	1.00	1.00	1.00	1.00	1.00
Min	-1.00	-0.99	-1.00	-1.00	-1.00	-1.00
Standard deviation	0.74	0.57	0.74	0.74	0.74	0.72

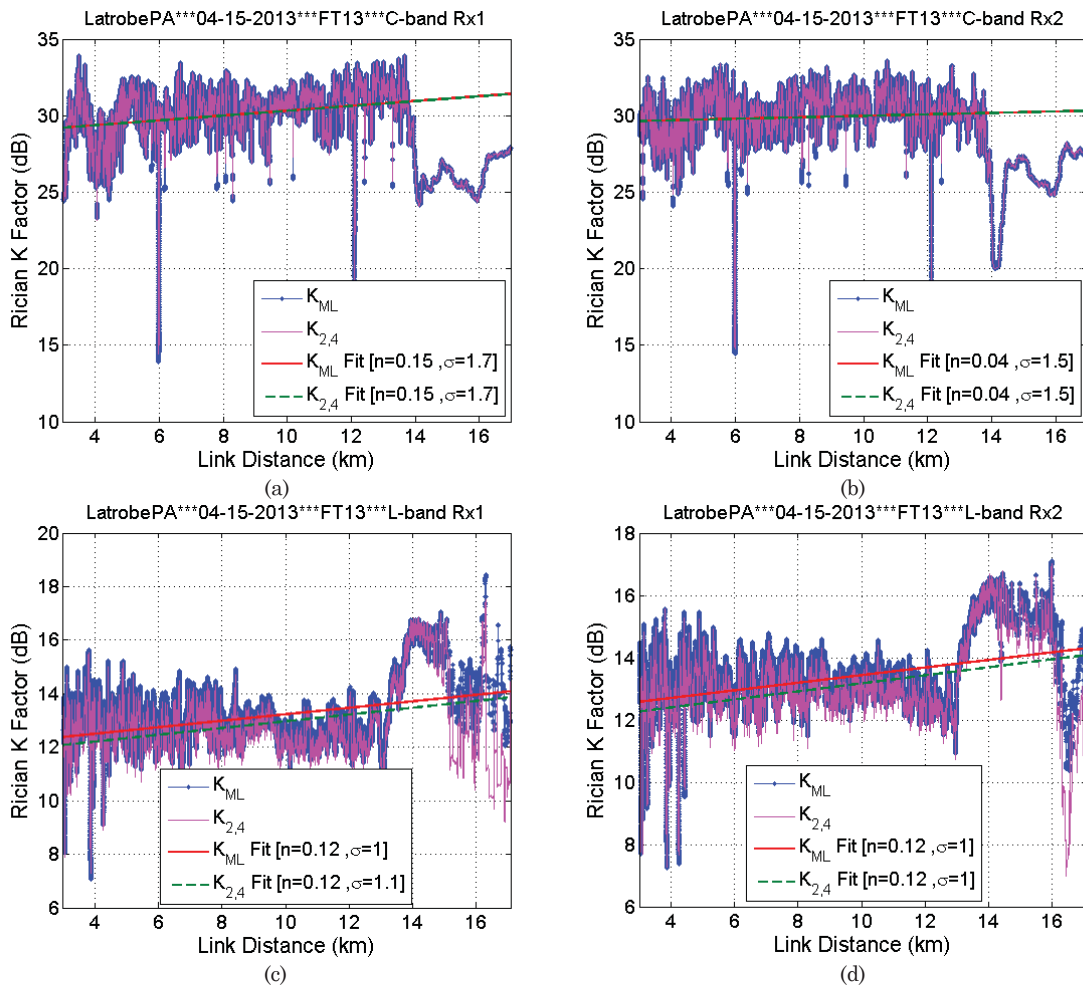


Figure A58. Ricean K factor for FT13, Latrobe, PA (a) C-band Rx1; (b) C-band Rx2; (c) L-band Rx1; (d) L-band Rx2.

Table A39. Statistics of Ricean K factor, FT13, Latrobe, PA.

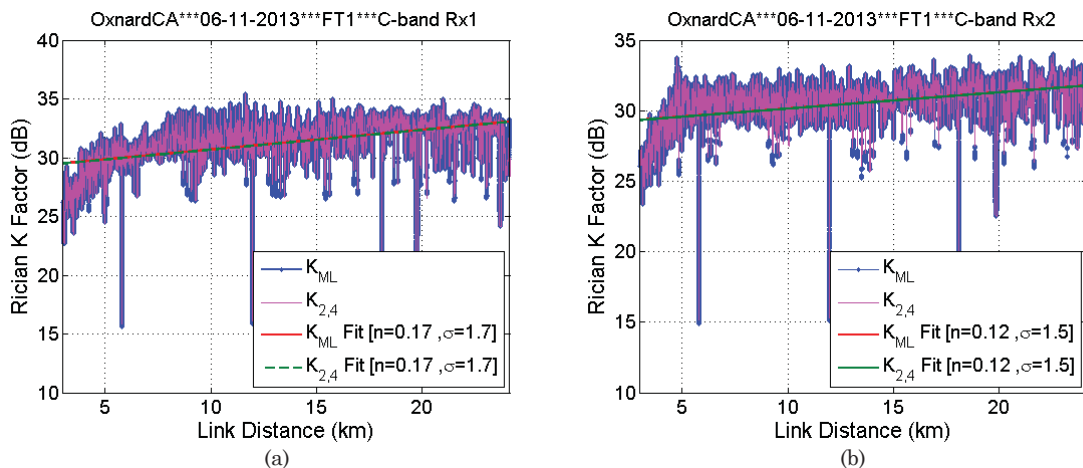
		C-band						L-band					
		Rx1			Rx2			Rx1			Rx2		
Moving Window Length		250λ						15 m					
Overall K factor (dB)		29.4			29.3			13.0			13.2		
Methods		K_{ML}	K_2	$K_{2,4}$									
Linear fit of K factor	A (dB)	28.8	26.3	28.8	29.5	27.7	29.5	12.0	10.2	11.7	12.2	10.3	11.9
	n	0.16	0.30	0.16	0.05	0.14	0.05	0.12	0.26	0.13	0.12	0.27	0.13
	σ_x (dB)	1.7	2.4	1.7	1.6	2.1	1.6	1.1	1.5	1.2	1.0	1.5	1.1
	D_{max} (km)	3.0	3.0	3.0	3.0	3.0	3.0	3.0	3.0	3.0	3.0	3.0	3.0
	D_{Min} (km)	17.2	17.2	17.2	17.2	17.2	17.2	17.2	17.2	17.2	17.2	17.2	17.2
Statistics of K factor (dB)	Max	33.9	34.0	33.9	33.6	33.5	33.6	18.4	19.9	19.8	17.1	17.1	17.0
	Min	13.9	11.2	14.3	14.4	11.5	14.8	7.1	-0.5	7.3	7.2	-5.8	7.0
	Median	30.1	28.9	30.1	29.9	28.9	29.9	13.2	12.6	12.9	13.4	12.8	13.1
	μ	30.5	29.5	30.5	30.2	29.4	30.1	12.9	12.5	12.7	13.2	12.8	12.9
	σ	1.8	2.6	1.8	1.6	2.2	1.6	1.2	1.7	1.2	1.1	1.7	1.2

A.15 Over Sea Flight Track 1

The inter- and intra-band spatial correlations reported previously for the over-sea FTs in [6] were based on arbitrarily-selected values of window length. Since we have now determined the appropriate stationarity distance, we provide updated results for spatial correlation for the over sea setting, computed over the stationarity distance. The Ricean K -factors for the over sea setting are also included in this section.

Table A40. Statistics of spatial correlation, FT1, Oxnard, CA.

	C1C2	L1L2	CIL1	C1L2	C2L1	C2L2
Window Length	79	79	79	79	79	79
Mean	0.60	0.37	0.00	0.00	0.00	0.00
Median	0.98	0.80	0.00	0.00	0.00	0.00
Max	1.00	1.00	0.63	0.64	0.64	0.72
Min	-1.00	-0.97	-0.75	-0.77	-0.77	-0.70
Standard deviation	0.64	0.69	0.14	0.14	0.14	0.14



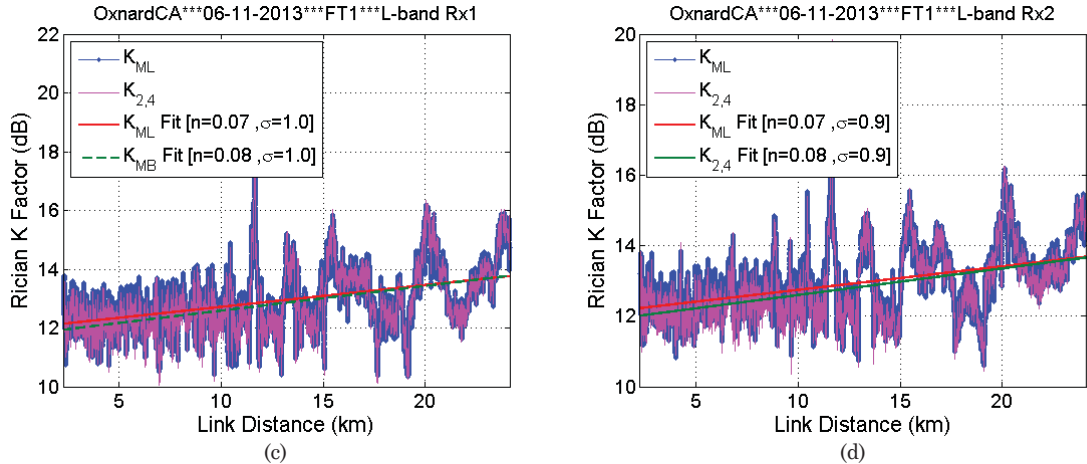


Figure A59. Ricean K factor for FT1, Oxnard, CA (a) C-band Rx1; (b) C-band 2; (c) L-band Rx1; (d) L-band Rx2.

Table A41. Statistics of Ricean K factor, FT1, Oxnard, CA.

		C-band						L-band					
		Rx1			Rx2			Rx1			Rx2		
Moving Window Length		250λ						15 m					
Overall K factor (dB)		30.4			29.9			12.8			12.8		
Methods		K_{ML}	K_2	$K_{2,4}$									
Linear fit of K factor	A (dB)	29.1	25.1	29.0	29.0	25.6	29.0	12.0	11.4	11.8	12.1	11.5	11.9
	n	0.17	0.22	0.17	0.12	0.15	0.12	0.07	0.10	0.08	0.07	0.10	0.08
	σ_X (dB)	1.7	3.4	1.7	1.5	3.2	1.5	1.0	1.0	1.0	0.9	0.9	0.9
	D_{max} (km)	3.0	3.0	3.0	3.0	3.0	3.0	2.2	2.2	2.2	2.2	2.2	2.2
	D_{Min} (km)	24.1	24.1	24.1	24.1	24.1	24.1	24.1	24.1	24.1	24.1	24.1	24.1
Statistics of K factor (dB)	Max	35.5	34.4	35.4	34.0	33.6	34.0	20.2	19.9	20.4	19.7	19.6	19.9
	Min	13.0	11.3	13.4	13.4	11.3	13.8	10.3	7.4	10.0	10.6	4.2	10.4
	Median	31.3	28.0	31.3	30.6	27.6	30.6	12.9	12.7	12.8	12.9	12.7	12.8
	μ	31.7	28.7	31.6	30.9	28.4	30.9	12.7	12.5	12.6	12.8	12.5	12.6
	σ	2.0	3.6	2.0	1.7	3.3	1.6	1.1	1.2	1.1	1.0	1.1	1.0

A.16 Over Sea Flight Track 2

Table A42. Statistics of spatial correlation, FT2, Oxnard, CA.

	C1C2	L1L2	C1L1	C1L2	C2L1	C2L2
Window Length	79	79	79	79	79	79
Mean	0.72	0.78	0.00	0.00	0.00	0.00
Median	0.96	0.97	0.00	0.00	0.00	0.00
Max	1.00	1.00	0.76	0.71	0.71	0.78
Min	-1.00	-1.00	-0.73	-0.78	-0.78	-0.86
Standard deviation	0.48	0.41	0.13	0.14	0.14	0.14

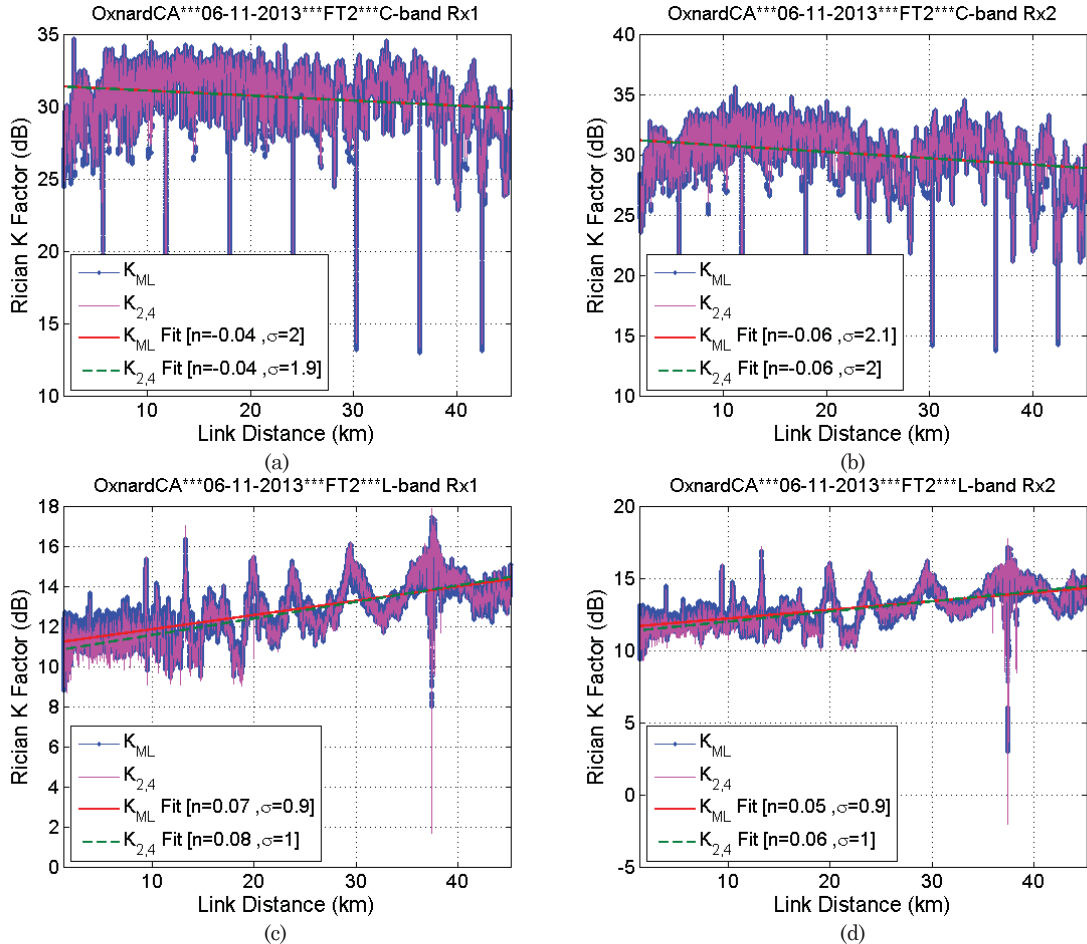


Figure A60. Ricean K factor for FT2, Oxnard, CA (a) C-band Rx1; (b) C-band 2; (c) L-band Rx1; (d) L-band Rx2.

Table A43. Statistics of Ricean K factor, FT2, Oxnard, CA.

		C-band			L-band								
		Rx1		Rx2	Rx1		Rx2						
Moving Window Length		250λ						15 m					
Overall K factor (dB)		29.6			29.0			12.6		12.8			
Methods		K_{ML}	K_2	$K_{2,4}$	K_{ML}	K_2	$K_{2,4}$	K_{ML}	K_2	$K_{2,4}$			
Linear fit of K factor	A(dB)	31.4	26.5	31.4	31.3	26.3	31.3	11.1	10.4	10.7	11.6	11.0	11.3
	n	-0.03	0.08	-0.03	-0.05	0.06	-0.05	0.07	0.09	0.08	0.06	0.08	0.07
	σ_X (dB)	2.0	3.3	2.0	2.1	3.4	2.1	0.9	1.1	1.0	0.9	1.1	1.1
	D_{max} (km)	1.8	1.8	1.8	1.8	1.8	1.8	1.2	1.2	1.2	1.2	1.2	1.2
	D_{Min} (km)	45.2	45.2	45.2	45.2	45.2	45.2	45.2	45.2	45.2	45.2	45.2	45.2
Statistics of K factor (dB)	Max	34.7	34.5	34.7	35.6	34.8	35.6	17.5	17.5	17.9	17.2	-17.0	17.8
	Min	11.1	10.6	11.8	11.4	10.7	12.1	8.0	1.3	1.7	3.0	0.0	3.7
	Median	30.6	28.3	30.6	30.1	27.8	30.1	12.8	12.5	12.6	13.0	12.8	12.9
	μ	31.0	29.1	31.0	30.4	28.6	30.4	12.7	12.6	12.6	12.9	12.8	12.8
	σ	2.0	3.4	2.0	2.2	3.4	2.2	1.3	1.6	1.5	1.2	1.5	1.4

A.17 Over Sea Flight Track 3

Table A44. Statistics of spatial correlation, FT3, Oxnard, CA.

	C1C2	L1L2	C1L1	C1L2	C2L1	C2L2
Window Length	82	82	82	82	82	82
Mean	0.72	0.44	0.00	0.00	0.00	0.00
Median	0.97	0.85	0.00	0.00	0.00	0.00
Max	1.00	1.00	0.38	0.52	0.52	0.46
Min	-1.00	-0.95	-0.40	-0.39	-0.39	-0.68
Standard deviation	0.52	0.65	0.10	0.10	0.10	0.10

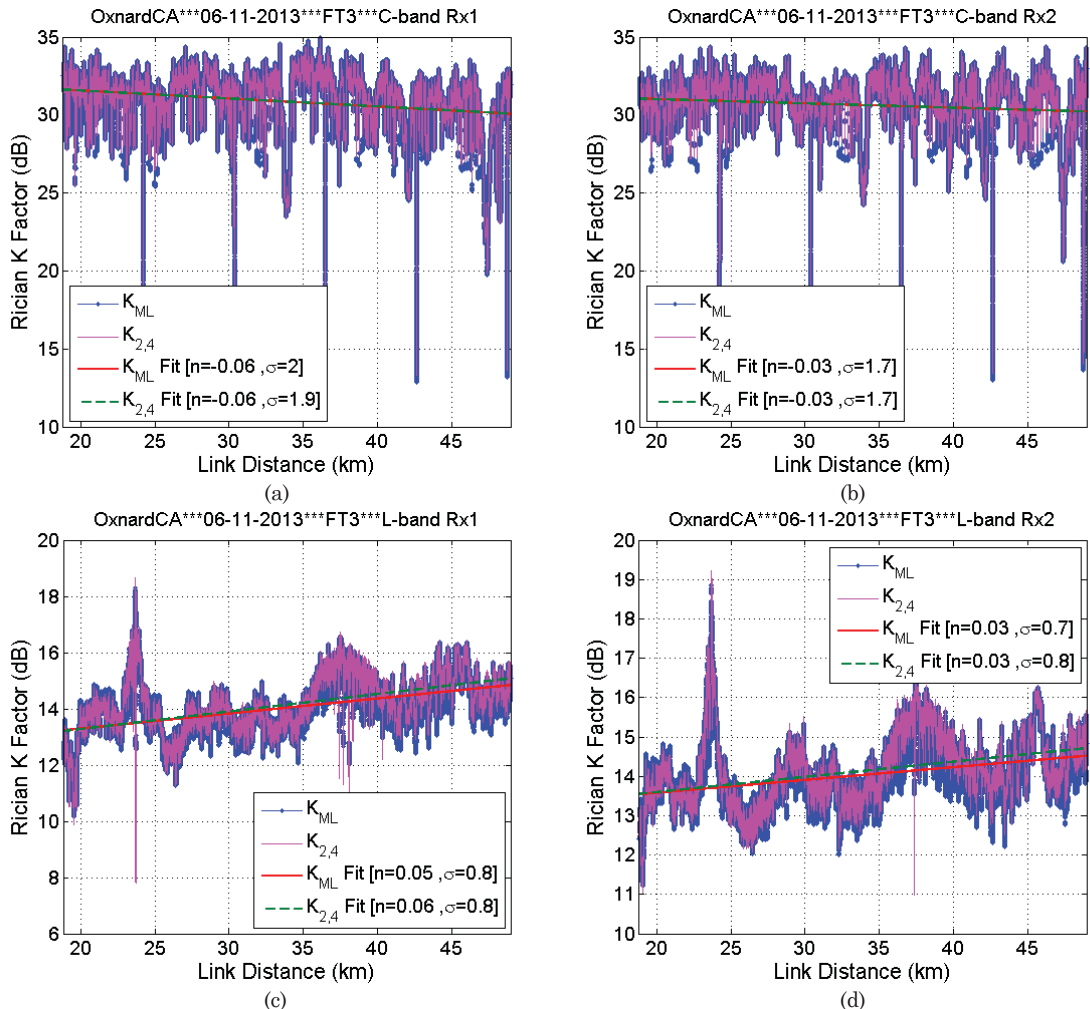


Figure A61. Ricean K factor for FT3, Oxnard, CA (a) C-band Rx1; (b) C-band 2; (c) L-band Rx1; (d) L-band Rx2.

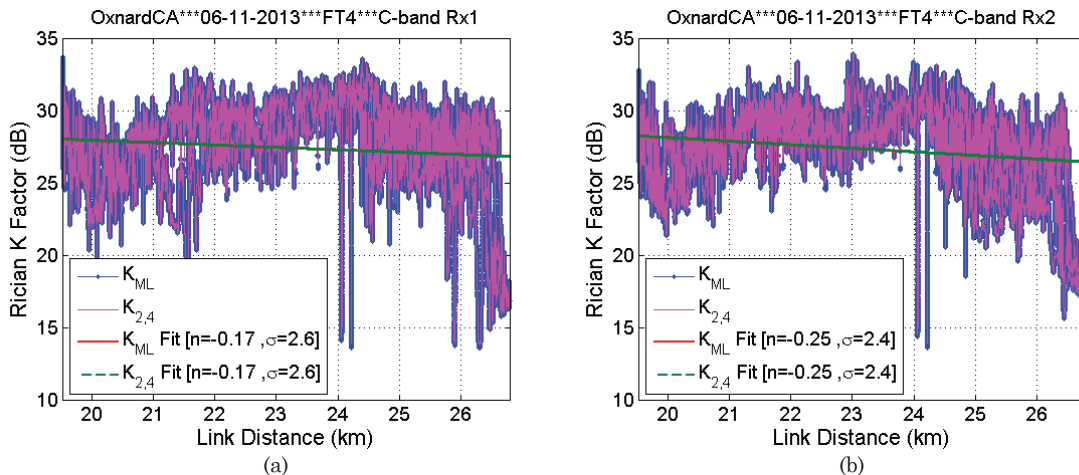
Table A45. Statistics of Ricean K factor, FT3, Oxnard, CA.

		C-band						L-band					
		Rx1			Rx2			Rx1			Rx2		
Moving Window Length		250λ						15 m					
Overall K factor (dB)		29.9			29.9			13.9			14.0		
Methods		K_{ML}	K_2	$K_{2,4}$									
Linear fit of K factor	A(dB)	32.6	29.6	32.6	31.6	28.8	31.6	12.2	12.0	12.0	12.9	12.8	12.8
	n	-0.05	0.00	-0.05	-0.03	0.02	-0.03	0.05	0.06	0.06	0.03	0.04	0.04
	σ_X (dB)	2.0	2.7	2.0	1.8	2.6	1.8	0.8	0.9	0.9	0.8	0.8	0.8
	D_{max} (km)	18.8	18.8	18.8	18.8	18.8	18.8	18.8	18.8	18.8	18.8	18.8	18.8
	D_{Min} (km)	49.0	49.0	49.0	49.0	49.0	49.0	49.0	49.0	49.0	49.0	49.0	49.0
Statistics of K factor (dB)	Max	35.0	34.8	34.9	34.4	34.3	34.4	18.3	18.4	18.7	18.9	19.0	19.2
	Min	12.8	11.3	13.3	13.0	11.6	13.4	10.2	7.1	7.8	11.2	10.9	11.0
	Median	30.9	29.5	30.9	30.7	29.4	30.7	14.1	14.1	14.2	14.0	14.1	14.1
	μ	31.4	30.2	31.4	31.0	30.0	31.0	14.0	14.1	14.1	14.0	14.0	14.0
	σ	2.1	2.7	2.0	1.8	2.6	1.8	1.0	1.0	1.0	0.8	0.9	0.9

A.18 Over Sea Flight Track 4

Table A46. Statistics of spatial correlation, FT4, Oxnard, CA.

	C1C2	L1L2	C1L1	C1L2	C2L1	C2L2
Window Length	85	85	85	85	85	85
Mean	0.30	0.68	0.00	0.00	0.00	0.00
Median	0.69	0.96	0.00	0.00	0.00	0.00
Max	1.00	1.00	0.87	0.85	0.85	0.83
Min	-1.00	-1.00	-0.86	-0.87	-0.87	-0.83
Standard deviation	0.75	0.56	0.13	0.13	0.13	0.13



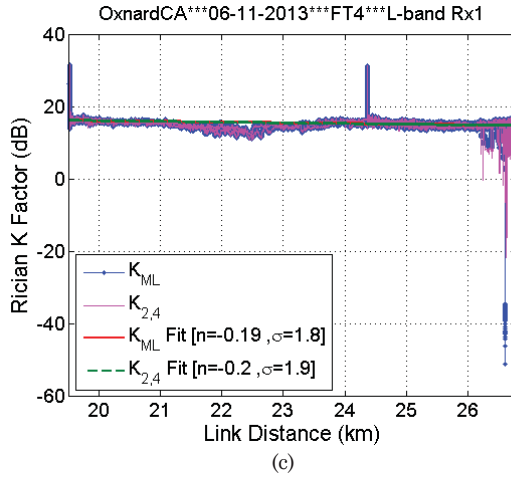


Figure A62. Ricean K factor for FT4, Oxnard, CA (a) C-band Rx1; (b) C-band 2; (c) L-band Rx1.

Table A47. Statistics of Ricean K factor, FT4, Oxnard, CA.

		C-band						L-band					
		Rx1			Rx2			Rx1			Rx2		
Moving Window Length		250λ						15 m					
Overall K factor (dB)		26.2			26.4			15.2			14.0		
Methods		K_{ML}	K_2	$K_{2,4}$									
Linear fit of K factor	A(dB)	31.3	29.9	31.3	33.1	31.0	33.1	19.8	19.2	20.1		19.0	19.9
	n	-0.17	-0.17	-0.17	-0.25	-0.22	-0.25	-0.19	-0.17	-0.20		-0.16	-0.19
	σ_X (dB)	2.7	3.1	2.7	2.5	2.9	2.5	1.8	1.6	1.9		1.7	2.0
	D_{max} (km)	19.5	19.5	19.5	19.5	19.5	19.5	19.5	19.5	19.5	19.5	19.5	19.5
	D_{Min} (km)	26.8	26.8	26.8	26.8	26.8	26.8	26.8	26.8	26.8	26.8	26.8	26.8
Statistics of K factor (dB)	Max	33.7	33.3	33.7	34.0	33.8	33.9	31.6	30.8	31.6		30.4	31.2
	Min	13.6	6.8	13.8	13.6	11.3	13.9	-51.3	0.0	0.0		0.0	0.0
	Median	27.4	25.9	27.4	27.4	25.9	27.4	15.5	15.3	15.4		15.4	15.5
	μ	27.9	26.2	27.9	27.7	26.2	27.7	15.4	15.4	15.4		15.5	15.6
	σ	2.7	3.1	2.7	2.5	3.0	2.5	1.9	1.7	2.0		1.8	2.1

A.19 Over Sea Flight Track 5

Table A48. Statistics of spatial correlation, FT5, Oxnard, CA.

	C1C2	L1L2	C1L1	C1L2	C2L1	C2L2
Window Length	84	84	84	84	84	84
Mean	0.25	0.55	0.00	0.00	0.00	0.00
Median	0.62	0.87	0.00	0.00	0.00	0.00
Max	1.00	1.00	0.74	0.78	0.78	0.80
Min	-1.00	-1.00	-0.81	-0.83	-0.83	-0.77
Standard deviation	0.77	0.60	0.12	0.12	0.12	0.12

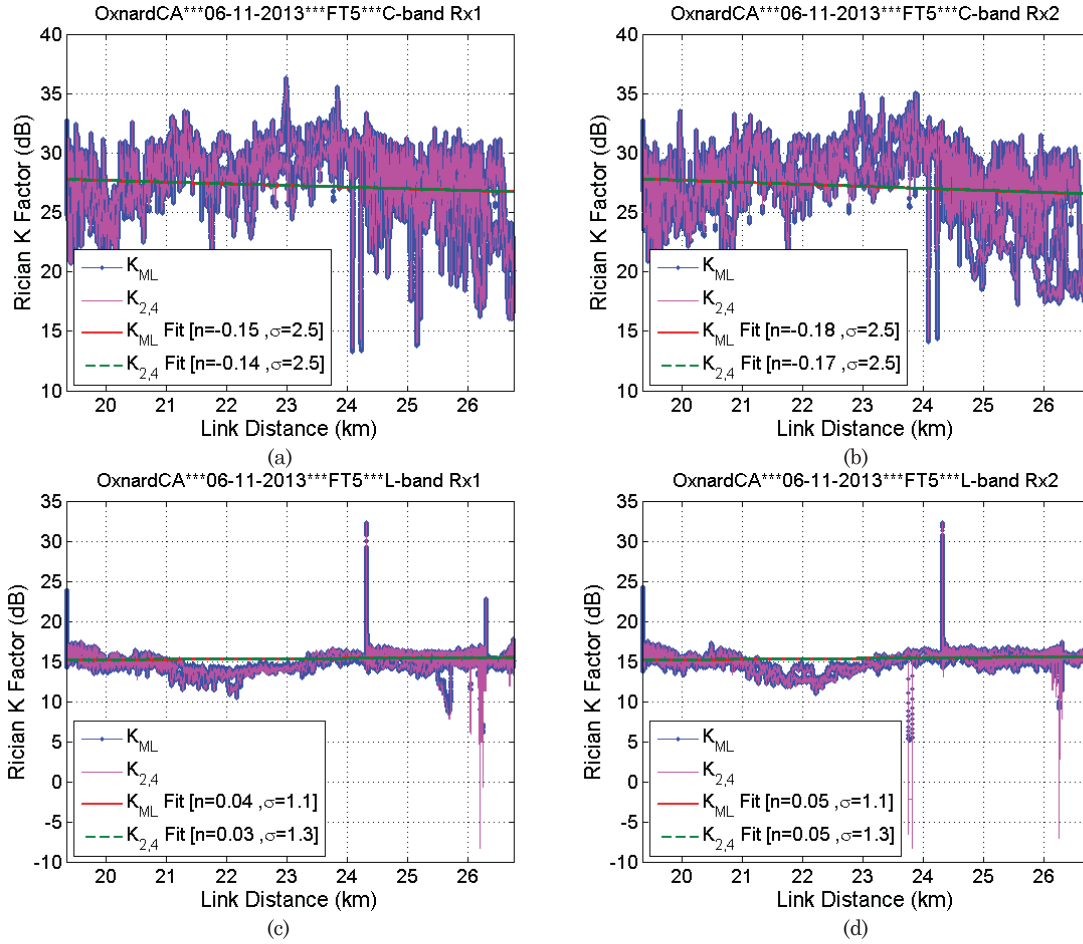


Figure A63. Ricean K factor for FT5, Oxnard, CA (a) C-band Rx1; (b) C-band 2; (c) L-band Rx1; (d) L-band Rx2.

Table A49. Statistics of Ricean K factor, FT5, Oxnard, CA.

		C-band						L-band					
		Rx1			Rx2			Rx1			Rx2		
Moving Window Length		250λ											
Overall K factor (dB)		26.2			26.2			15.2			15.2		
Methods		K_{ML}	K_2	$K_{2,4}$									
Linear fit of K factor	A(dB)	30.5	28.9	30.5	31.1	29.3	31.1	14.3	14.4	14.5	14.0	14.1	14.2
	n	-0.14	-0.14	-0.14	-0.17	-0.16	-0.17	0.05	0.04	0.04	0.06	0.05	0.05
	σ_X (dB)	2.6	3.1	2.6	2.5	3.0	2.5	1.2	1.2	1.3	1.2	1.2	1.3
	D_{max} (km)	19.3	19.3	19.3	19.3	19.3	19.3	19.3	19.3	19.3	19.3	19.3	19.3
	D_{Min} (km)	26.8	26.8	26.8	26.8	26.8	26.8	26.8	26.8	26.8	26.8	26.8	26.8
Statistics of K factor (dB)	Max	36.3	35.5	36.3	35.1	34.7	35.0	32.3	31.5	32.3	32.3	32.3	32.3
	Min	13.2	5.8	13.6	14.1	8.9	14.4	6.1	0.0	4.9	5.2	0.1	0.0
	Median	27.2	25.6	27.3	27.2	25.7	27.2	15.3	15.3	15.3	15.4	15.3	15.4
	μ	27.6	25.9	27.6	27.5	26.0	27.5	15.5	15.4	15.5	15.5	15.5	15.5
	σ	2.6	3.1	2.6	2.6	3.0	2.6	1.2	1.2	1.3	1.2	1.2	1.3

A.20 Over Sea Flight Track 6

Table A50. Statistics of spatial correlation, FT6, Oxnard, CA.

	C1C2	L1L2	C1L1	C1L2	C2L1	C2L2
Window Length	83	83	83	83	83	83
Mean	0.11	0.54	0.00	0.00	0.00	0.00
Median	0.35	0.87	0.00	0.00	0.00	0.00
Max	1.00	1.00	0.74	0.78	0.78	0.66
Min	-1.00	-1.00	-0.75	-0.84	-0.84	-0.70
Standard deviation	0.80	0.60	0.12	0.12	0.12	0.12

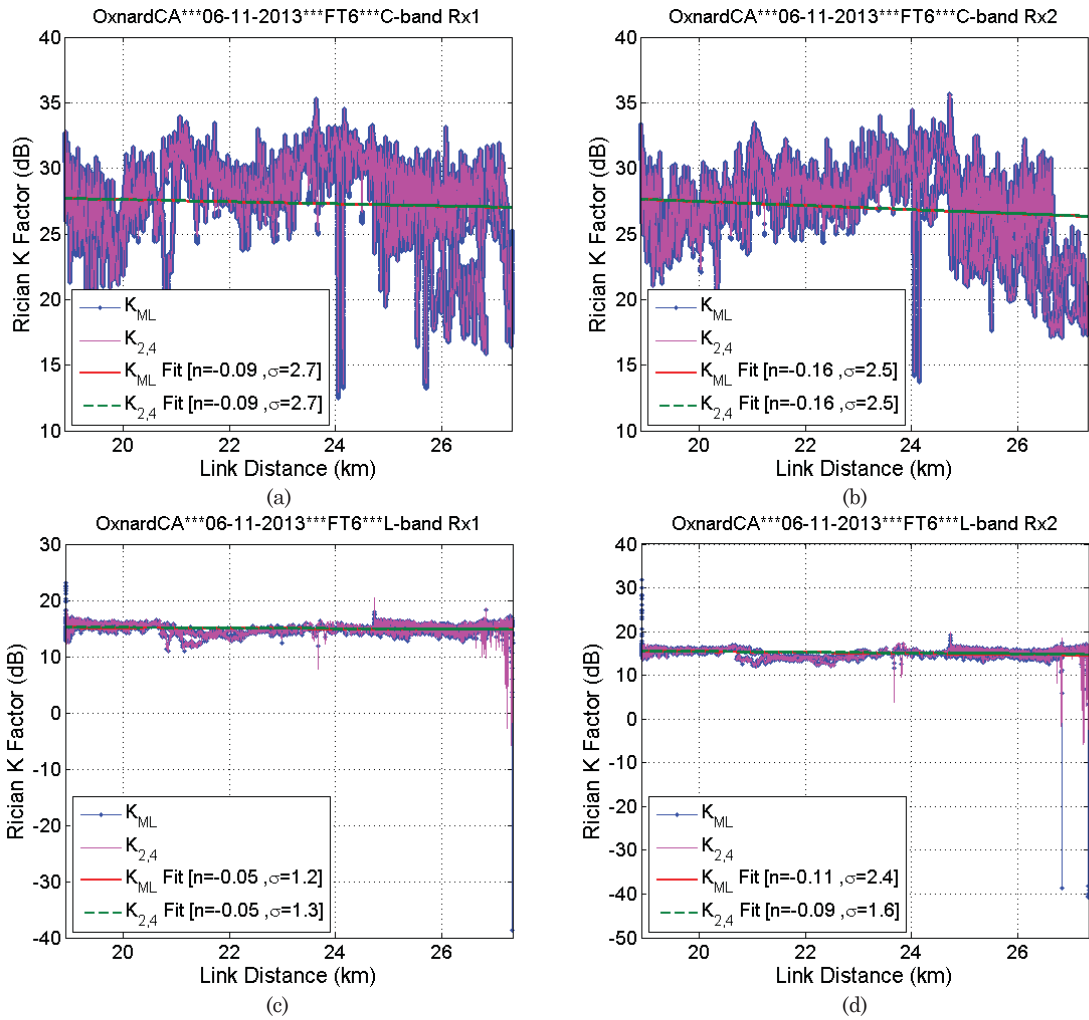


Figure A64. Ricean K factor for FT6, Oxnard, CA (a) C-band Rx1; (b) C-band 2; (c) L-band Rx1; (d) L-band Rx2.

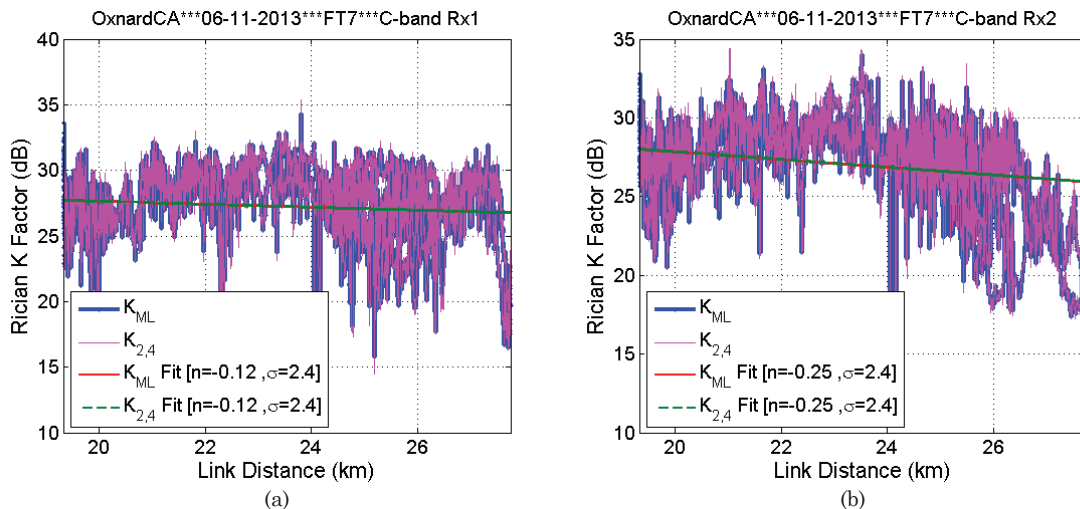
Table A51. Statistics of Ricean K factor, FT6, Oxnard, CA.

		C-band			L-band		
		Rx1		Rx2	Rx1		Rx2
Moving Window Length		250λ			15 m		
Overall K factor (dB)		26.1		26.0	14.9		14.7
Methods		K_{ML}	K_2	$K_{2,4}$	K_{ML}	K_2	$K_{2,4}$
Linear fit of K factor	A (dB)	29.3	28.9	29.2	30.6	29.3	30.6
	n	-0.08	-0.13	-0.08	-0.16	-0.16	-0.15
	σ_X (dB)	2.8	3.1	2.8	2.5	2.9	2.5
	D_{max} (km)	18.9	18.9	18.9	18.9	18.9	18.9
	D_{Min} (km)	27.3	27.3	27.3	27.3	27.3	27.3
Statistics of K factor (dB)	Max	35.3	34.2	35.3	35.7	35.6	35.7
	Min	12.5	7.5	12.9	13.7	9.9	14.0
	Median	27.4	25.8	27.4	27.0	25.6	27.0
	μ	27.8	26.1	27.8	27.3	25.9	27.3
	σ	2.8	3.1	2.8	2.6	2.9	2.6

A.21 Over Sea Flight Track 7

Table A52. Statistics of spatial correlation, FT7, Oxnard, CA.

	C1C2	L1L2	C1L1	C1L2	C2L1	C2L2
Window Length	83	83	83	83	83	83
Mean	0.07	0.52	0.00	0.00	0.00	0.00
Median	0.22	0.84	0.00	0.00	0.00	0.00
Max	1.00	1.00	0.58	0.68	0.68	0.55
Min	-1.00	-1.00	-0.64	-0.61	-0.61	-0.60
Standard deviation	0.80	0.60	0.12	0.12	0.12	0.12



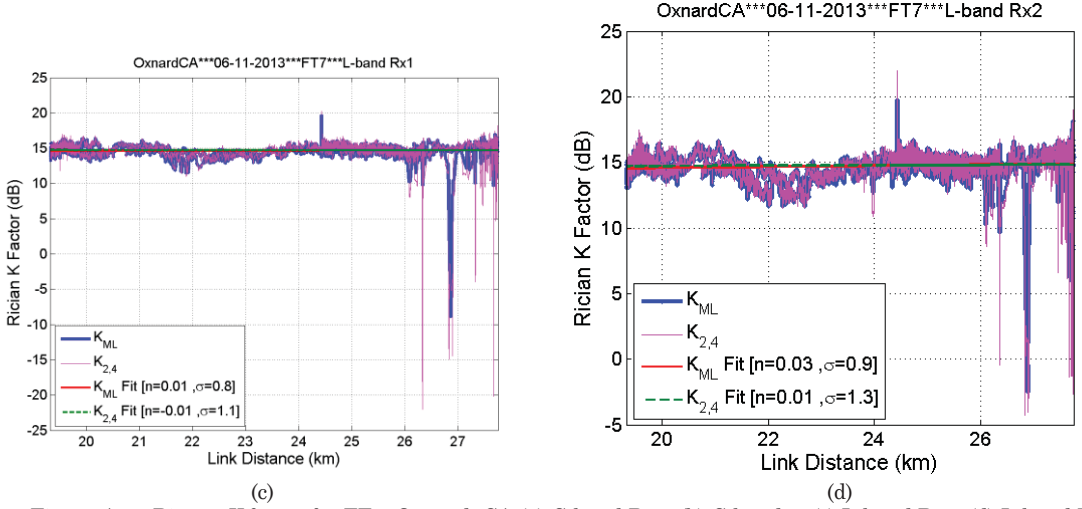


Figure A65. Ricean K factor for FT7, Oxnard, CA (a) C-band Rx1; (b) C-band 2; (c) L-band Rx1; (d) L-band Rx2.

Table A53. Statistics of Ricean K factor, FT7, Oxnard, CA.

		C-band						L-band					
		Rx1			Rx2			Rx1			Rx2		
Moving Window Length		250λ						15 m					
Overall K factor (dB)		26.3			26.1			14.6			14.6		
Methods		K_{ML}	K_2	$K_{2,4}$									
Linear fit of K factor	A (dB)	29.9	28.7	29.9	32.7	31.7	32.8	14.3	14.8	14.9	13.8	14.3	14.4
	n	-0.11	-0.13	-0.11	-0.24	-0.27	-0.25	0.02	0.00	-0.01	0.04	0.02	0.01
	σ_X (dB)	2.4	3.0	2.4	2.5	2.9	2.4	0.8	1.1	1.1	0.9	1.3	1.3
	D_{max} (km)	19.3	19.3	19.3	19.3	19.3	19.3	19.3	19.3	19.3	19.3	19.3	19.3
	D_{Min} (km)	27.8	27.8	27.8	27.8	27.8	27.8	27.8	27.8	27.8	27.8	27.8	27.8
Statistics of K factor (dB)	Max	34.3	35.6	35.4	34.0	34.2	34.4	19.7	-18.7	-22.1	19.8	21.2	22.0
	Min	13.7	8.0	13.9	15.8	10.0	14.9	-8.9	0.0	0.1	-2.5	0.0	0.0
	Median	27.2	25.6	27.2	27.0	25.5	27.1	14.7	14.7	14.7	14.7	14.7	14.8
	μ	27.5	25.9	27.5	27.4	26.0	27.4	14.7	14.8	14.8	14.8	14.9	14.9
	σ	2.4	3.1	2.4	2.5	3.0	2.5	0.8	1.1	1.1	0.9	1.3	1.3

A.22 Over Sea Flight Track 8

Table A54. Statistics of spatial correlation, FT8, Oxnard, CA.

	C1C2	L1L2	C1L1	C1L2	C2L1	C2L2
Window Length	85	85	85	85	85	85
Mean	0.57	0.51	0.00	0.00	0.00	0.00
Median	0.96	0.88	0.00	0.00	0.00	0.00
Max	1.00	1.00	0.90	0.88	0.88	0.83
Min	-1.00	-1.00	-0.86	-0.91	-0.91	-0.76
Standard deviation	0.66	0.61	0.14	0.14	0.14	0.13

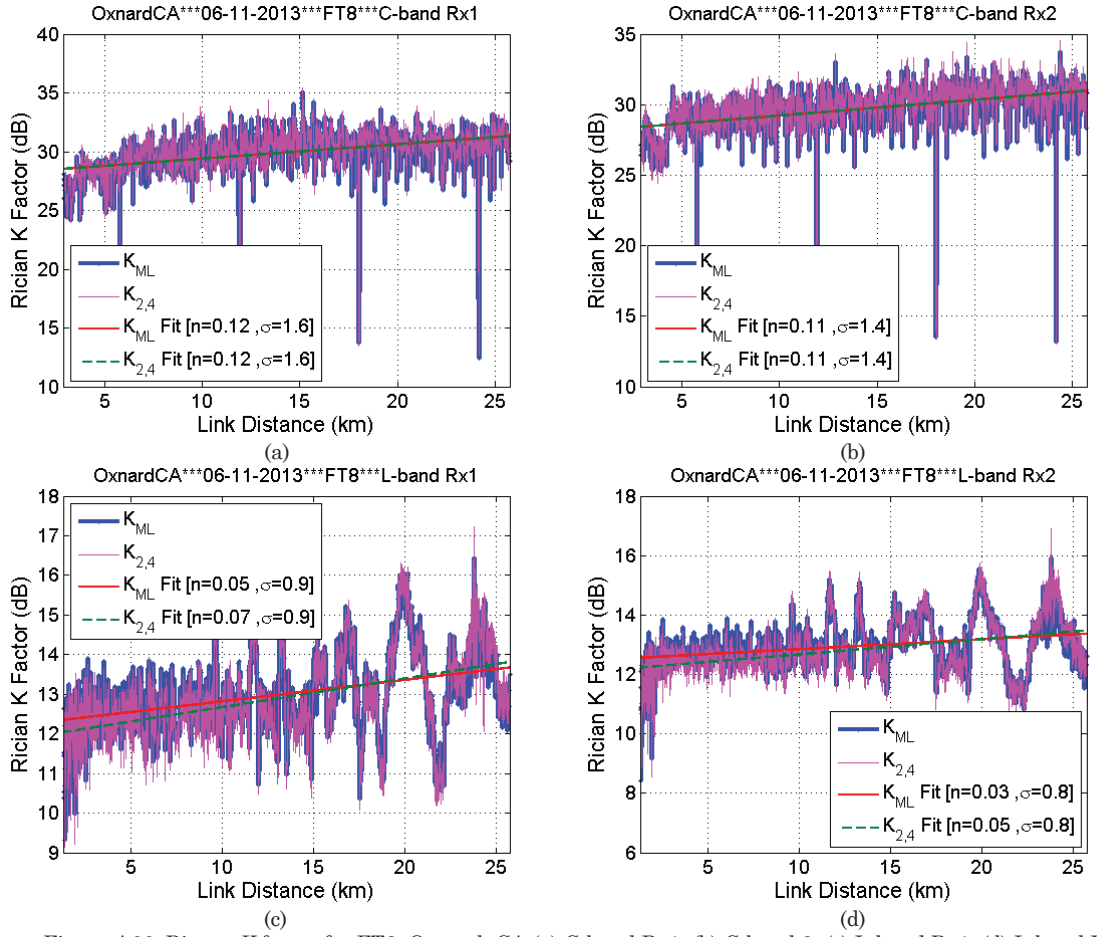


Figure A66. Ricean K factor for FT8, Oxnard, CA (a) C-band Rx1; (b) C-band 2; (c) L-band Rx1; (d) L-band Rx2.

Table A55. Statistics of Ricean K factor, FT8, Oxnard, CA.

		C-band						L-band					
		Rx1			Rx2			Rx1			Rx2		
Moving Window Length		250λ						15 m					
Overall K factor (dB)		29.1			29.0			12.9			12.9		
Methods		K_{ML}	K_2	$K_{2,4}$									
Linear fit of K factor	A (dB)	28.2	24.9	28.2	28.1	25.0	28.1	12.3	11.4	12.0	12.5	11.7	12.2
	n	0.12	0.18	0.12	0.11	0.17	0.11	0.05	0.10	0.07	0.03	0.08	0.05
	σ_X (dB)	1.7	3.0	1.6	1.5	2.9	1.4	0.9	1.1	1.0	0.8	1.0	0.9
	D_{max} (km)	2.9	2.9	2.9	2.9	2.9	2.9	1.3	1.3	1.3	1.3	1.3	1.3
	D_{Min} (km)	25.8	25.8	25.8	25.8	25.8	25.8	25.8	25.8	25.8	25.8	25.8	25.8
Statistics of K factor (dB)	Max	35.1	34.3	35.4	33.7	34.5	34.5	16.4	17.2	17.2	15.9	16.9	16.9
	Min	12.4	10.6	12.7	12.5	10.5	12.9	9.3	2.4	9.1	8.4	3.6	7.8
	Median	30.0	27.4	30.0	29.7	27.3	29.7	13.0	12.8	12.9	13.0	12.7	12.9
	μ	30.2	28.0	30.2	30.0	27.9	30.0	12.9	12.7	12.8	12.9	12.6	12.7
	σ	1.8	3.2	1.8	1.6	3.1	1.6	1.0	1.3	1.1	0.8	1.2	1.0

A.23 Over Sea Flight Track 9

Table A56. Statistics of spatial correlation, FT9, Oxnard, CA.

	C1C2	L1L2	C1L1	C1L2	C2L1	C2L2
Window Length	87	87	87	87	87	87
Mean	0.75	0.86	0.00	0.00	0.00	0.00
Median	0.98	0.98	0.00	0.00	0.00	0.00
Max	1.00	1.00	0.78	0.82	0.82	0.77
Min	-1.00	-0.98	-0.82	-0.81	-0.81	-0.83
Standard deviation	0.45	0.29	0.11	0.11	0.11	0.12

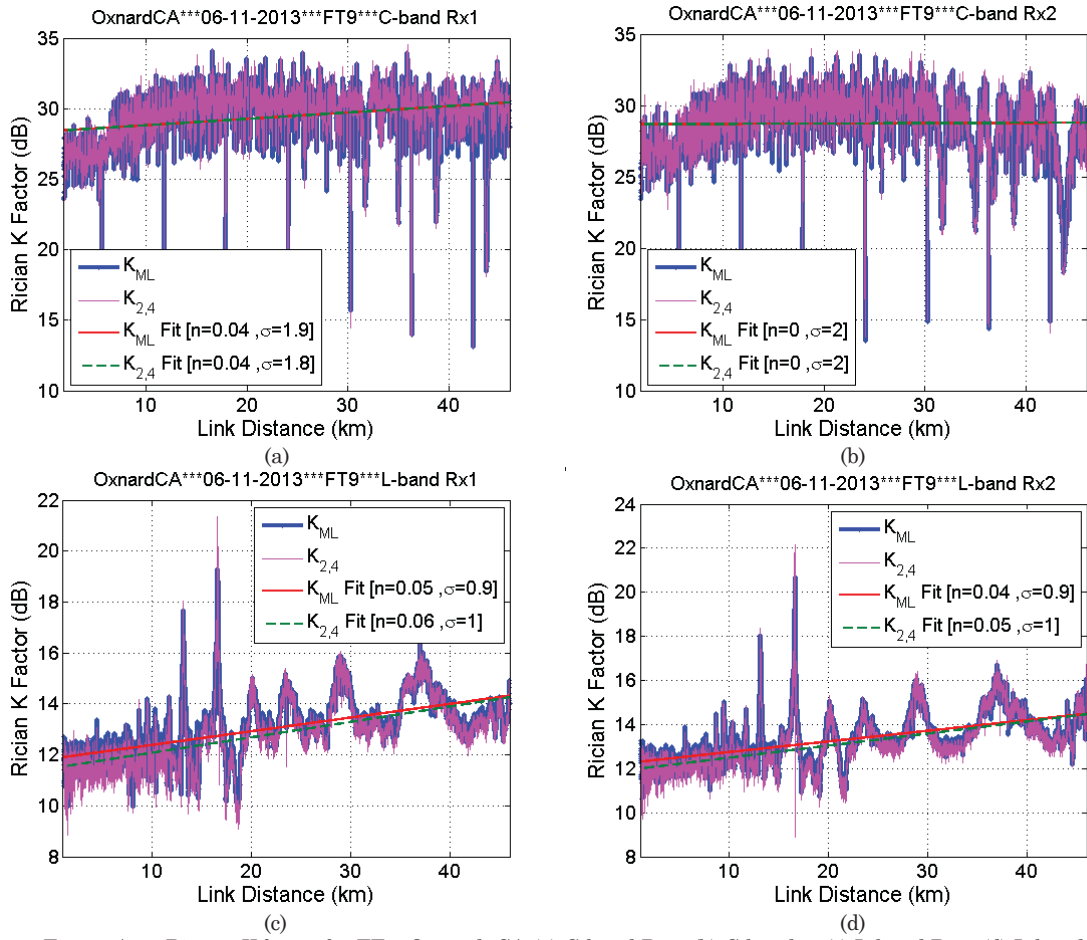


Figure A67. Ricean K factor for FT9, Oxnard, CA (a) C-band Rx1; (b) C-band 2; (c) L-band Rx1; (d) L-band Rx2.

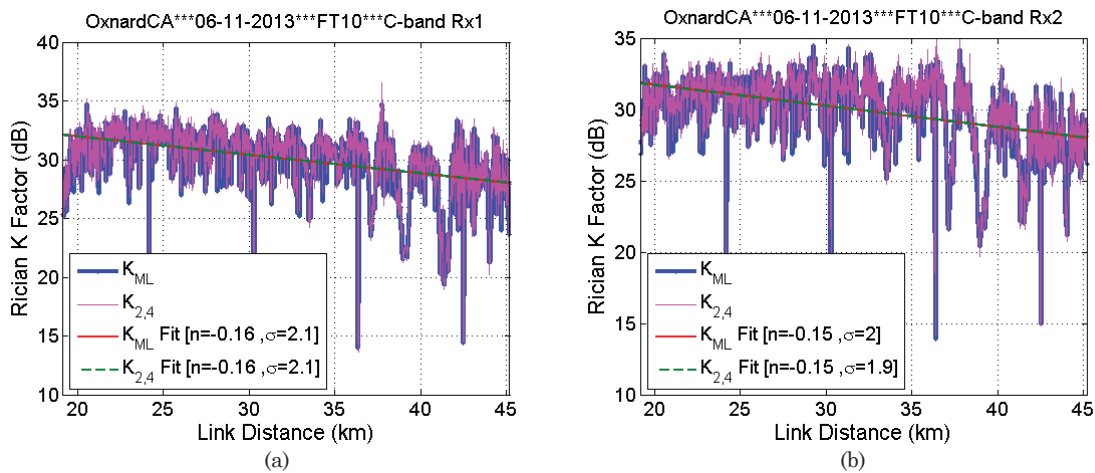
Table A57. Statistics of Ricean K factor, FT9, Oxnard, CA.

		C-band						L-band					
		Rx1			Rx2			Rx1			Rx2		
Moving Window Length		250λ						15 m					
Overall K factor (dB)		28.6			28.0			12.9			13.2		
Methods		K_{ML}	K_2	$K_{2,4}$									
Linear fit of K factor	A (dB)	28.4	25.4	28.4	28.7	25.7	28.7	11.8	11.2	11.5	12.3	11.6	11.9
	n	0.04	0.10	0.05	0.00	0.06	0.00	0.05	0.07	0.06	0.05	0.06	0.05
	σ_x (dB)	1.9	2.8	1.9	2.0	2.9	2.0	1.0	1.1	1.1	0.9	1.1	1.0
	D_{max} (km)	1.8	1.8	1.8	1.8	1.8	1.8	1.0	1.0	1.0	1.0	1.0	1.0
	D_{Min} (km)	46.0	46.0	46.0	46.0	46.0	46.0	46.0	46.0	46.0	46.0	46.0	46.0
Statistics of K factor (dB)	Max	34.1	34.5	34.5	33.6	33.9	34.0	19.3	20.8	21.4	20.7	21.3	22.1
	Min	13.1	10.3	13.1	13.5	10.2	13.8	9.7	2.9	8.9	10.6	4.7	8.9
	Median	29.4	27.7	29.4	28.7	27.0	28.7	13.1	12.8	12.9	13.4	13.1	13.2
	μ	29.9	28.4	29.9	29.1	27.5	29.1	13.1	12.9	12.9	13.2	13.0	13.0
	σ	2.0	3.0	2.0	2.0	3.0	2.0	1.2	1.4	1.3	1.1	1.3	1.3

A.24 Over Sea Flight Track 10

Table A58. Statistics of spatial correlation, FT10, Oxnard, CA.

	C1C2	L1L2	C1L1	C1L2	C2L1	C2L2
Window Length	83	83	83	83	83	83
Mean	0.57	0.52	0.00	0.00	0.00	0.00
Median	0.92	0.91	0.00	0.00	0.00	0.00
Max	1.00	1.00	0.56	0.48	0.48	0.55
Min	-1.00	-1.00	-0.45	-0.51	-0.51	-0.45
Standard deviation	0.62	0.62	0.11	0.11	0.11	0.11



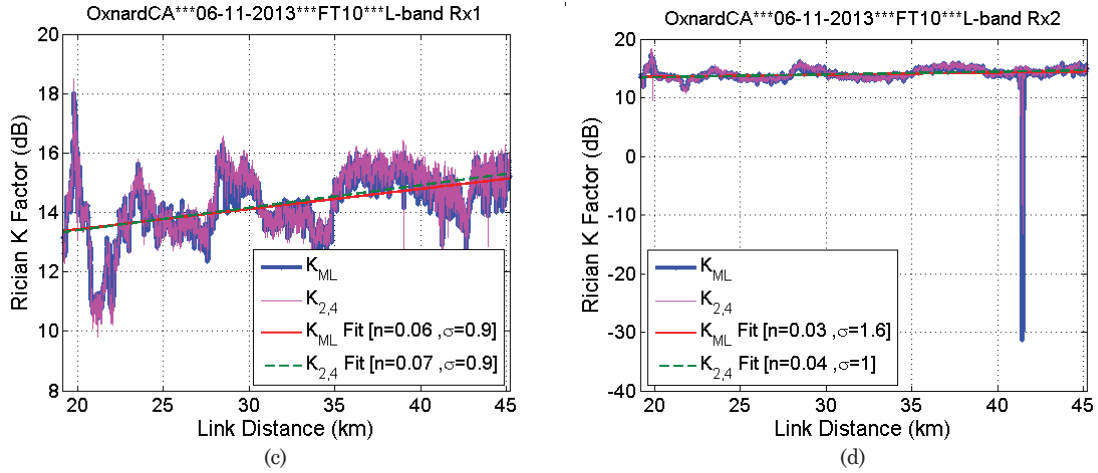


Figure A68. Ricean K factor for FT10, Oxnard, CA (a) C-band Rx1; (b) C-band 2; (c) L-band Rx1; (d) L-band Rx2.

Table A59. Statistics of Ricean K factor, FT10, Oxnard, CA.

		C-band						L-band					
		Rx1			Rx2			Rx1			Rx2		
Moving Window Length		250λ						15 m					
Overall K factor (dB)		28.8			28.9			14.2			9.7		
Methods		K_{ML}	K_2	$K_{2,4}$									
Linear fit of K factor	A (dB)	35.2	31.6	35.1	34.7	31.7	34.7	12.1	11.8	11.9	12.9	12.5	12.6
	n	-0.16	-0.10	-0.16	-0.15	-0.10	-0.15	0.07	0.08	0.08	0.04	0.05	0.05
	σ_X (dB)	2.2	3.2	2.2	2.0	3.1	2.0	0.9	1.0	1.0	1.7	1.0	1.1
	D_{max} (km)	19.1	19.1	19.1	19.1	19.1	19.1	19.1	19.1	19.1	19.1	19.1	19.1
	D_{Min} (km)	45.2	45.2	45.2	45.2	45.2	45.2	45.2	45.2	45.2	45.2	45.2	45.2
Statistics of K factor (dB)	Max	34.8	36.4	36.5	34.5	34.9	35.0	18.0	17.1	18.5	17.4	17.0	18.4
	Min	12.2	10.3	12.1	12.4	10.7	12.7	10.4	9.8	9.8	-31.4	-8.8	-0.3
	Median	30.0	28.5	30.1	29.9	28.4	29.9	14.3	14.4	14.4	14.1	14.1	14.1
	μ	30.6	29.1	30.6	30.5	29.0	30.5	14.4	14.5	14.5	14.1	14.1	14.1
	σ	2.5	3.3	2.5	2.3	3.2	2.3	1.1	1.1	1.1	1.7	1.1	1.2

A.25 Over Sea Flight Track 11

Table A60. Statistics of spatial correlation, FT11, Oxnard, CA.

	C1C2	L1L2	C1L1	C1L2	C2L1	C2L2
Window Length	94	94	94	94	94	94
Mean	0.25	0.55	0.00	0.00	0.00	0.00
Median	0.64	0.89	0.00	0.00	0.00	0.00
Max	1.00	1.00	0.79	0.78	0.78	0.81
Min	-1.00	-1.00	-0.70	-0.71	-0.71	-0.75
Standard deviation	0.78	0.60	0.13	0.13	0.13	0.13

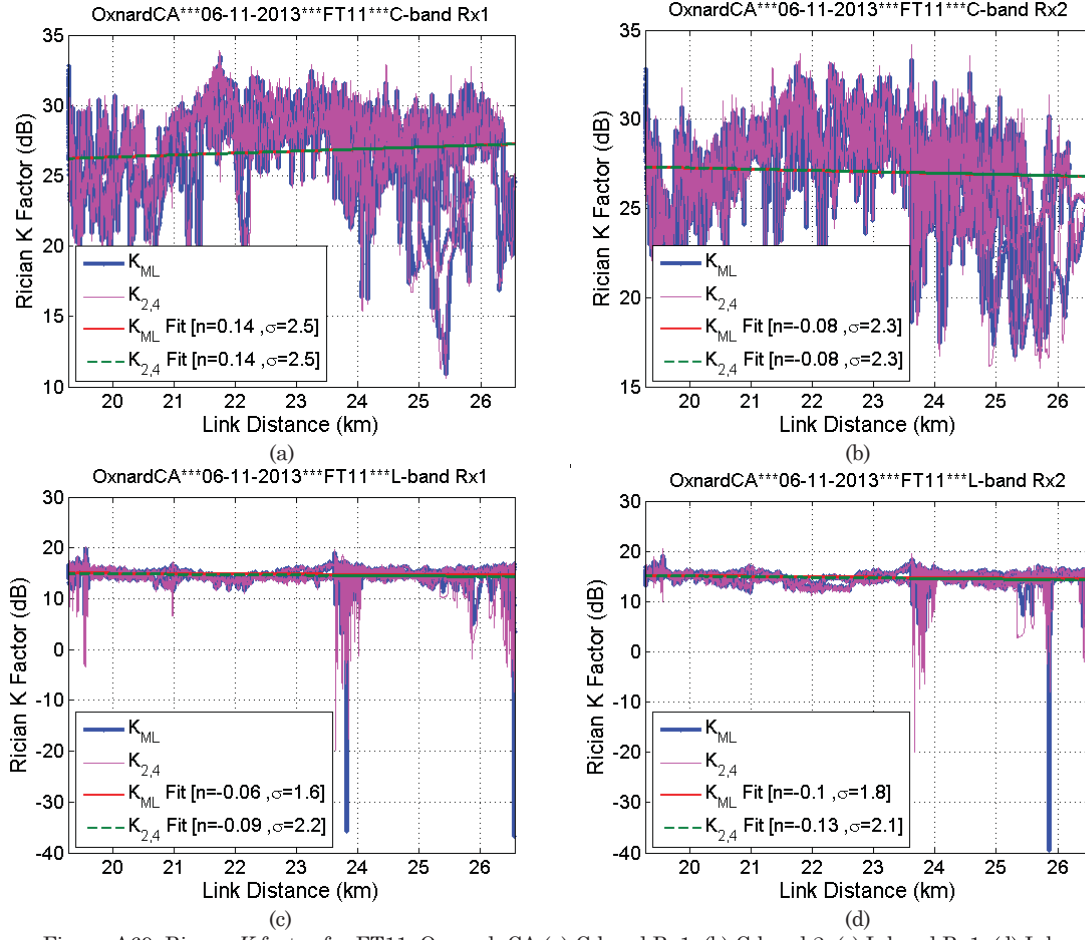


Figure A69. Ricean K factor for FT11, Oxnard, CA (a) C-band Rx1; (b) C-band 2; (c) L-band Rx1; (d) L-band Rx2.

Table A61. Statistics of Ricean K factor, FT11, Oxnard, CA.

		C-band						L-band					
		Rx1			Rx2			Rx1			Rx2		
Moving Window Length		250λ						15 m					
Overall K factor (dB)		25.8			26.3			14.6			14.6		
Methods		K_{ML}	K_2	$K_{2,4}$									
Linear fit of K factor	A (dB)	23.5	24.7	23.5	28.7	29.5	28.8	16.1	16.5	16.6	17.0	17.3	17.5
	n	0.14	0.03	0.14	-0.07	-0.16	-0.07	-0.06	-0.09	-0.09	-0.09	-0.12	-0.12
	σ_X (dB)	2.6	2.8	2.6	2.4	2.8	2.4	1.6	2.2	2.2	1.9	2.1	2.1
	D_{max} (km)	19.3	19.3	19.3	19.3	19.3	19.3	19.3	19.3	19.3	19.3	19.3	19.3
	D_{Min} (km)	26.6	26.6	26.6	26.6	26.6	26.6	26.6	26.6	26.6	26.6	26.6	26.6
Statistics of K factor (dB)	Max	33.5	33.9	33.9	33.3	34.3	34.2	19.9	-19.5	20.1	19.1	-22.8	-20.6
	Min	10.9	5.9	10.6	16.7	7.0	16.1	-36.7	0.0	0.0	-39.5	0.0	0.0
	Median	26.7	25.5	26.7	27.1	25.9	27.1	14.9	14.6	14.6	14.9	14.6	14.7
	μ	27.0	25.6	27.0	27.3	26.2	27.4	14.9	14.8	14.9	15.0	14.9	15.0
	σ	2.6	2.8	2.6	2.4	2.8	2.4	1.6	2.2	2.2	1.9	2.1	2.2

A.26 Over Sea Flight Track 12

Table A62. Statistics of spatial correlation, FT12, Oxnard, CA.

	C1C2	L1L2	C1L1	C1L2	C2L1	C2L2
Window Length	94	94	94	94	94	94
Mean	0.22	0.54	0.00	0.00	0.00	0.00
Median	0.55	0.86	0.00	0.00	0.00	0.00
Max	1.00	1.00	0.73	0.72	0.72	0.84
Min	-1.00	-1.00	-0.78	-0.77	-0.77	-0.70
Standard deviation	0.78	0.59	0.13	0.13	0.13	0.13

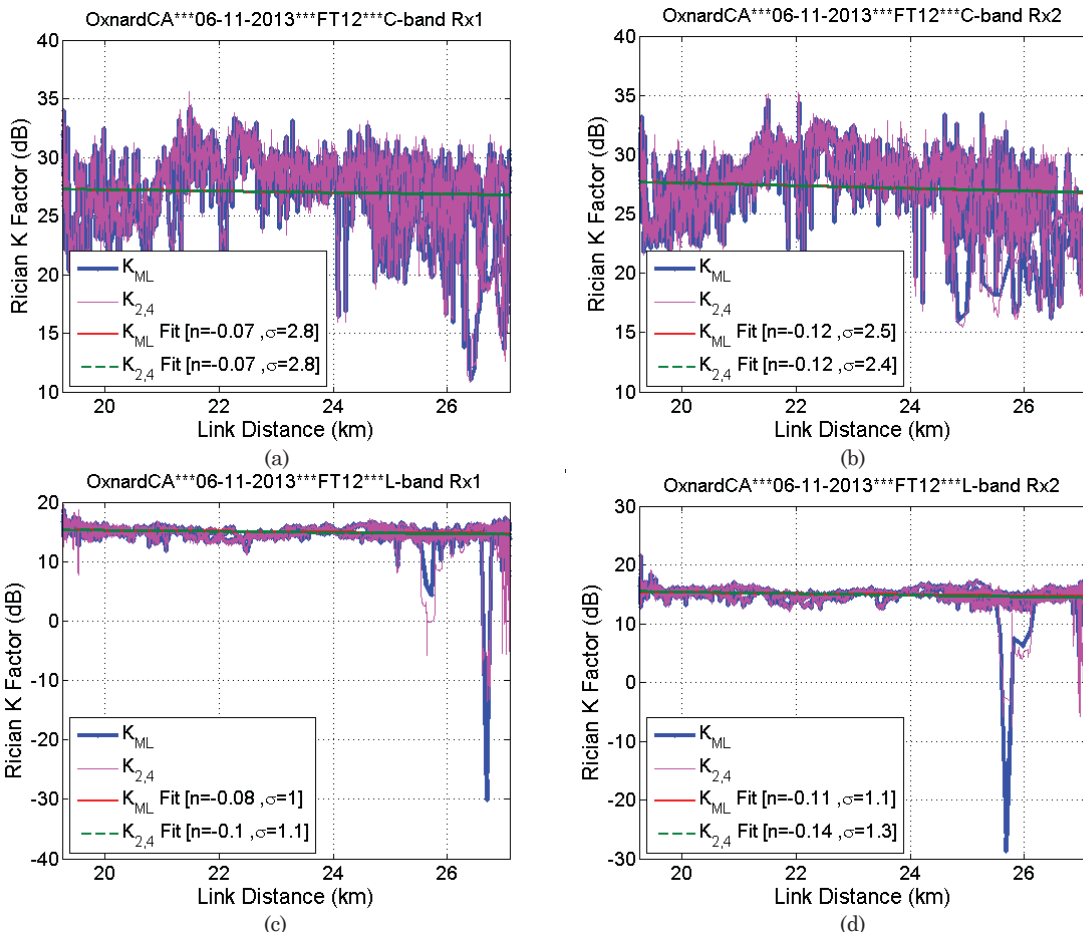


Figure A70. Ricean K factor for FT12, Oxnard, CA (a) C-band Rx1; (b) C-band 2; (c) L-band Rx1; (d) L-band Rx2.

Table A63. Statistics of Ricean K factor, FT12, Oxnard, CA.

		C-band						L-band					
		Rx1			Rx2			Rx1			Rx2		
Moving Window Length		250λ						15 m					
Overall K factor (dB)		25.9			26.4			14.9			14.9		
Methods		K_{ML}	K_2	$K_{2,4}$									
Linear fit of K factor	A (dB)	28.5	28.4	28.5	29.9	29.5	29.9	16.8	17.1	17.2	17.4	18.0	18.1
	n	-0.06	-0.11	-0.06	-0.12	-0.15	-0.11	-0.08	-0.09	-0.10	-0.10	-0.13	-0.14
	σ_X (dB)	2.9	3.0	2.9	2.5	2.9	2.5	1.1	1.2	1.2	1.1	1.3	1.3
	D_{max} (km)	19.3	19.3	19.3	19.3	19.3	19.3	19.3	19.3	19.3	19.3	19.3	19.3
	D_{Min} (km)	27.1	27.1	27.1	27.1	27.1	27.1	27.1	27.1	27.1	27.1	27.1	27.1
Statistics of K factor (dB)	Max	34.2	35.5	35.6	34.6	35.1	35.2	18.8	19.5	19.6	21.5	21.9	21.9
	Min	11.1	8.1	10.8	13.4	6.7	12.9	-30.1	0.0	0.0	-28.7	0.0	0.0
	Median	27.0	25.8	27.0	27.3	26.1	27.3	15.0	14.9	14.9	15.0	14.9	14.9
	μ	27.3	25.9	27.3	27.5	26.3	27.5	15.1	15.0	15.0	15.1	15.0	15.1
	σ	2.9	3.1	2.9	2.5	2.9	2.5	1.1	1.2	1.2	1.1	1.4	1.4

Appendix B: Additional Stationarity Distance Statistics

Here we provide some additional statistics on (C-band) stationarity distance, for two over-freshwater FTs. These are termed “urban” statistics since we *did* include the strong MPCs at large delays from buildings in downtown Cleveland. Results are comparable to those found in the over-sea case, i.e., an SD of $250\lambda_C$ ($\sim 15m$) is sufficient.

Table B1. C-band stationarity distance statistics, urban FT5.

		Rx1	Rx2
Lognormal	μ (m)	2.70	2.64
	σ (m)	0.74	0.77
Mean	(m)	19.15	18.41
	(λ 's)	323.00	310.55
Median	(m)	15.22	14.40
	(λ 's)	256.71	242.93
10 th percentile	(m)	5.51	5.04
	(λ 's)	92.87	84.96
Min	(m)	0.84	0.91
	(λ 's)	14.23	15.29

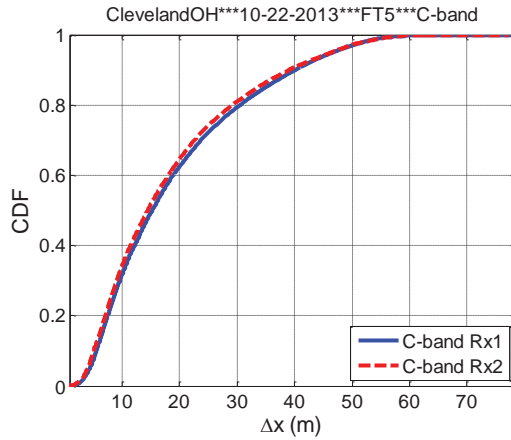


Figure B1. SD CDFs for straight flight track (FT5).

Table B2. C-band stationarity distance statistics, urban FT6.

		Rx1	Rx2
Lognormal	μ (m)	2.67	2.67
	σ (m)	0.66	0.67
Mean	(m)	17.66	17.83
	(λ 's)	297.86	300.74
Median	(m)	14.45	14.54
	(λ 's)	243.78	245.21
10 th percentile	(m)	6.08	6.02
	(λ 's)	102.47	101.59
Min	(m)	0.82	0.86
	(λ 's)	13.91	14.50

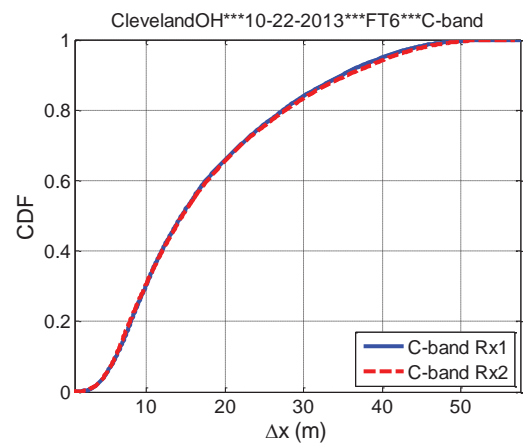


Figure B2. SD CDFs for straight flight track (FT6).

Appendix C: Ricean K-Factor Estimation

The envelope probability density function (pdf) of the Ricean distribution is given by [52]

$$p_r(r) = \frac{r}{\sigma^2} \exp\left(-\frac{r^2+s^2}{2\sigma^2}\right) I_0\left(\frac{rs}{\sigma^2}\right) \quad (\text{C.1})$$

where $I_0(\cdot)$ is the modified Bessel function of the first kind and zero order, s is the mean of the dominant (often, LOS) component, and $2\sigma^2$ is the power in the remaining (Rayleigh distributed) components. Often the pdf is normalized to have a mean-square value of unity. In this case it is given by

$$p(r, K) = 2r(1 + 10^{K/10}) \exp[-r^2(1 + 10^{K/10}) - 10^{K/10}] I_0\left(2r10^{K/20}\sqrt{1 + 10^{K/10}}\right) \quad (\text{C.1a})$$

The K factor in decibels is defined as

$$K \text{ (dB)} = 10 \log_{10}\left(\frac{s^2}{2\sigma^2}\right) \quad (\text{C.2})$$

If $K=0$, the Ricean degenerates into the Rayleigh distribution; if $K>>1$ the PDF looks like a Gaussian density with mean value s . Three K factor computation methods are considered.

C.1 Method I: Maximum Likelihood (ML) Fitting of Empirical Data

For this method we collect histograms of the measured data, and employ a maximum-likelihood (ML) fitting procedure. The steps employed to compute the empirical K factor are as follows:

1. Collect data (PDPs); the link distance d of each individual PDP is known. Find the narrow band received power¹ P_r in dBm.
2. Estimate local moving average value of P_r with a sliding window

$$P_{Avg}(d) = \sum_{i-W/2}^{i+W/2} \frac{P_r(d_i)}{W} \quad (\text{C.3})$$

where the window length W is determined by the stationarity distance (SD), the PDP update rate R_{PDP} and aircraft velocity V as

$$W = SD \cdot R_{PDP}/V \quad (\text{C.4})$$

We then remove the local moving average from the empirical data to create the residuals P_{Rsd}

$$P_{Rsd}(d) = P_r(d) - P_{Avg}(d) \quad (\text{C.5})$$

Alternative 1: We can also use a linear fit to P_r (~path loss model) to estimate the local average instead of the sliding window, but the linear fit does not fit the empirical data as well in some segments of data.

¹ Our power is the sum of the power in all chip samples. Note that the power recorded by the sounder directly can *not* be used to compute the K factor since the values are quantized in steps of approximately 0.25 dB; this would significantly degrade the estimation of the amplitude distribution.

Alternative 2: Another alternative to remove the large scale path loss is to subtract the free space path loss. However, since the window length is only a few meters, the variation of free space path loss is very small (it is almost a constant). This method is not recommended for removing the local average although it can still be used for the computation of the K factor for the complete FT.

3. Convert P_{Rsd} from decibel scale to linear scale.
4. Find amplitude A_{Rsd} by taking the (positive) square root of P_{Rsd} .
5. Find the Ricean fit of $A_{Rsd}(d_i: d_{i+W})$ via the Matlab® function “fitdist(A_{Rsd} , ‘rician’)", where W is the length of another sliding (or stepped) window; $W=250\lambda$ in C-band and 15 m in L-band. The function “fitdist” is a command within the Matlab® distribution fitting tool, in Matlab’s statistics toolbox. Detailed descriptions of W (stationarity distance) appear in Section 4.2 and Appendix B. The “fitdist” function returns the maximum-likelihood values of s and σ , from which K_{ML} can be calculated by (2).

Processing steps 1-4 are also used in the other K -factor estimation methods. Step 5 can be replaced by two other moment-based methods, as we describe next.

C.2 Method II: Second Order Moment

The authors of [53] proposed a second-order moment-based K -factor computation method for the fixed wireless channel (Tx & Rx motionless). The sliding window length in (C.3) is only a few meters, which is much smaller than the link distance. The signal amplitude within this window can be treated as a fixed value, hence the moment method in [53] can be applied for the AG channel. Assume $r(d)$ is the received signal, V is a fixed complex value and $v(d)$ is a zero mean complex random variable with standard deviation of σ .

$$r(d) = V + v(d) \quad (\text{C.6})$$

The second moment G_v is the RMS fluctuation of received power P_r about its moving average P_{Avg} :

$$G_v(d_i) = \sqrt{\frac{1}{W} \sum_{i-W/2}^{i+W/2} [P_r(d_i) - P_{Avg}(d_i)]^2} \quad (\text{C.7})$$

From this, $|V|^2$ and σ^2 can be obtained as

$$|V|^2 = \sqrt{P_{Avg}^2 - G_v^2} \quad (\text{C.8})$$

$$\sigma^2 = P_{Avg} - \sqrt{P_{Avg}^2 - G_v^2} \quad (\text{C.9})$$

Finally, the K -factor in linear scale is obtained as follows:

$$K_2 = |V|^2 / \sigma^2. \quad (\text{C.10})$$

C.2 Method III: Fourth Order Moment

In [54], the authors provided a widely used K -factor computation method based on fourth moments. The Rician K factor in linear scale is given by,

$$K_{2,4} = \frac{-2\mu_2^2 + \mu_4 - \mu_2\sqrt{2\mu_2^2 - \mu_4}}{\mu_2^2 - \mu_4}, \quad (\text{C.11})$$

where μ_2 and μ_4 are the second and fourth moments, respectively,

$$\mu_2 = \sum_{i=W/2}^{i+W/2} \frac{A_{Rsd}^2(d_i)}{W} \quad (\text{C.12})$$

$$\mu_4 = \sum_{i=W/2}^{i+W/2} \frac{A_{Rsd}^4(d_i)}{W}. \quad (\text{C.13})$$

C.4 Example K-factor Results

The signal amplitude within a window follows the Ricean distribution well (it is actually nearly Gaussian since $K > 1$). Some example results for both bands are shown in Figures C.1-C.6.

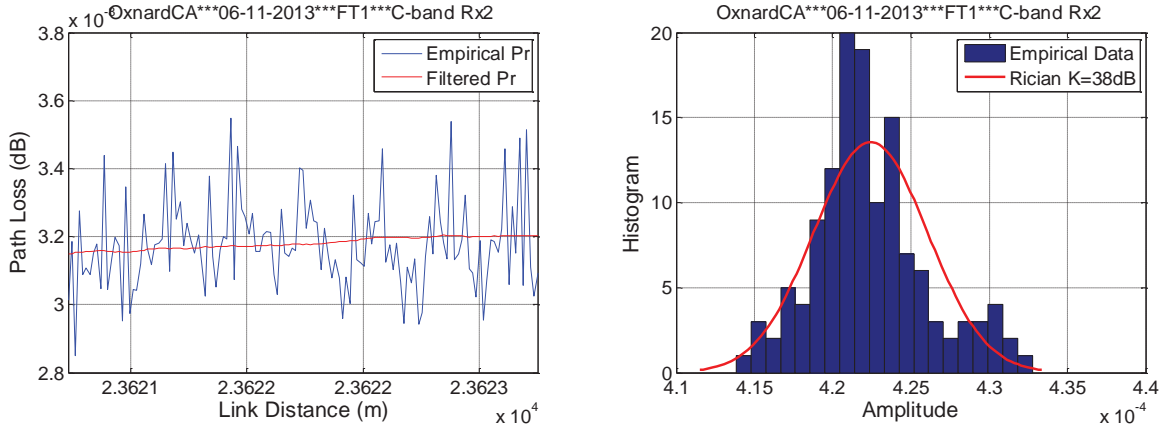


Figure C.1. Path loss (left) and amplitude histogram and fit (right) for 1000th stepped window, C-band Rx2.

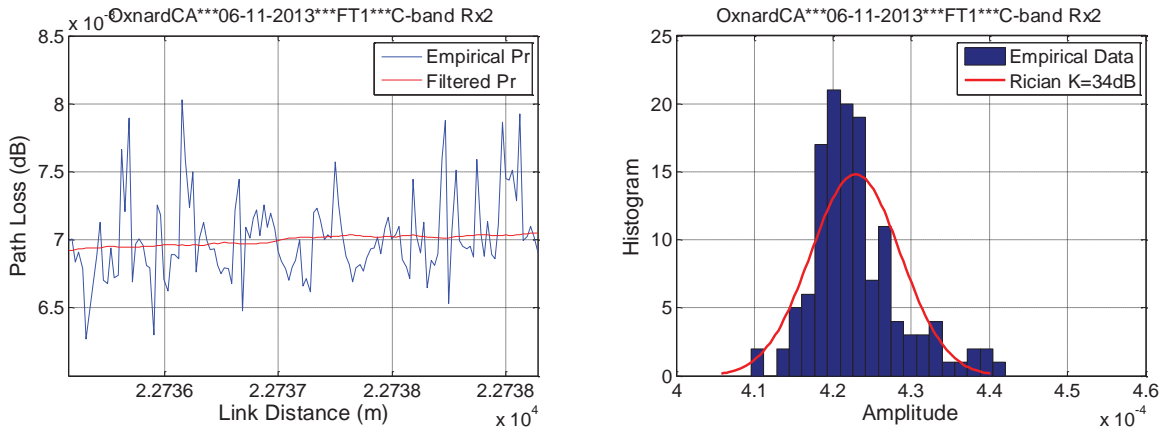


Figure C.2. Path loss (left) and amplitude histogram and fit (right) for 2000th stepped window, C-band Rx2.

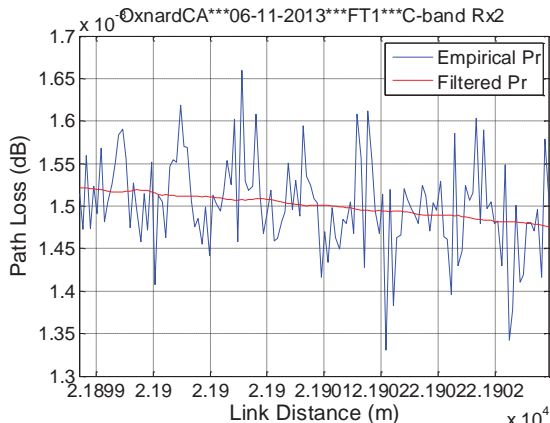


Figure C.3. Path loss (left) and amplitude histogram and fit (right) for 5000th stepped window, C-band Rx2.

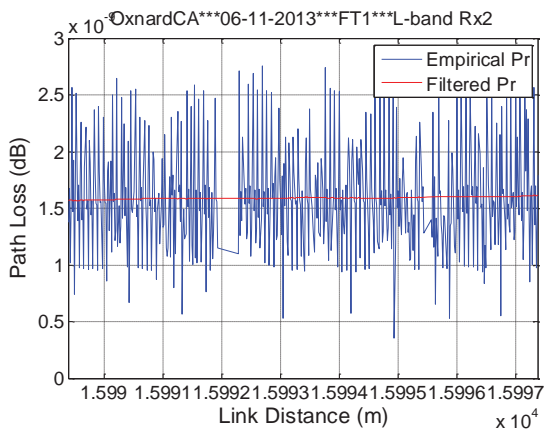


Figure C.4. Path loss (left) and amplitude histogram and fit (right) for 500th stepped window, L-band Rx2.

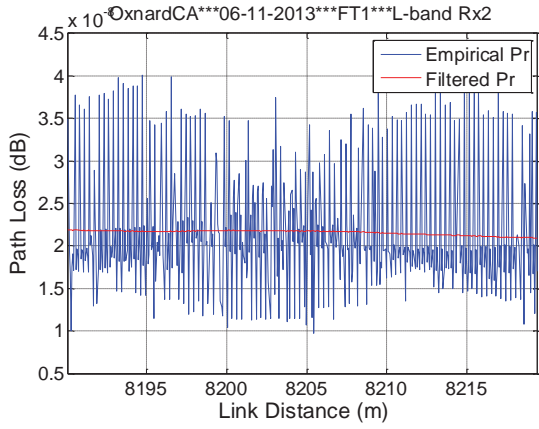


Figure C.5. Path loss (left) and amplitude histogram and fit (right) for 1000th stepped window, L-band Rx2.

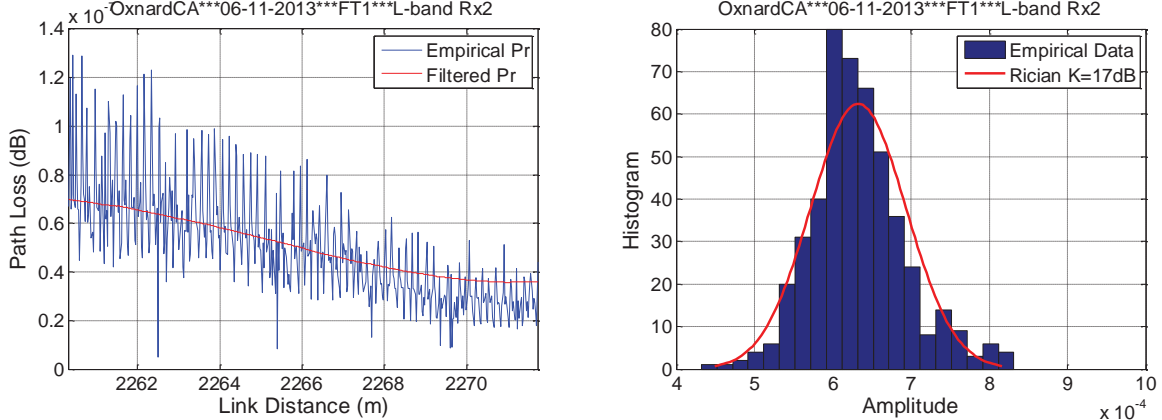
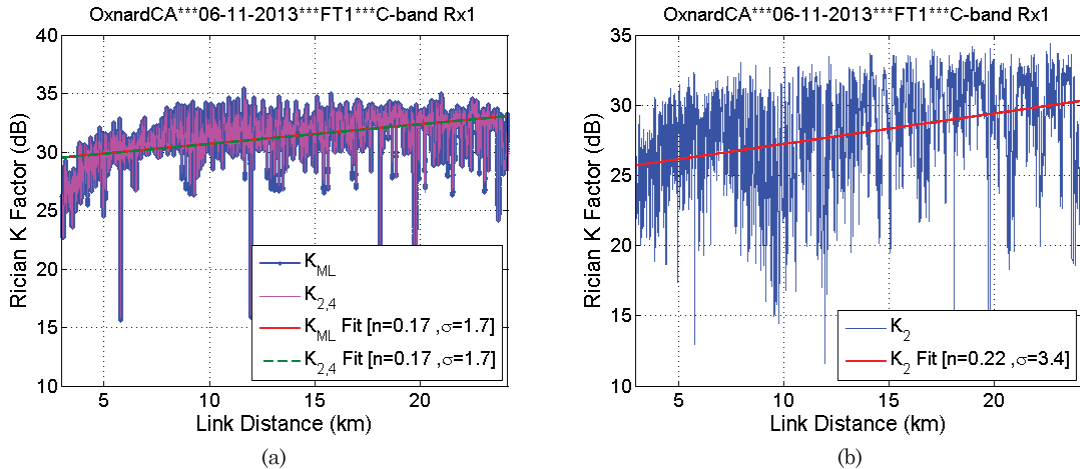


Figure C.6. Path loss (left) and amplitude histogram and fit (right) for 1415th stepped window, L-band Rx2.

The K -factor results for the three methods for the over sea FT1 are shown in Figures C.7-C.10. The statistics and linear fit parameters are listed in Table C.1. Method I is the most accurate, but the slowest for processing, and on rare occasions, the Ricean fit may not converge. Computing K_2 by Method II yields results that are always smaller than the results of the other two methods. Note that K_2 was developed for a *fixed* Tx & Rx, so it may not be best for the AG channel, even though Method II is the fastest computationally. Method III has been widely used in recent years, but the term $2\mu_2^2 - \mu_4$ in (C.4) may on occasion be negative, making $K_{2,4}$ a complex number with a very small imaginary part. For these rare results we used only the real part for our estimates.



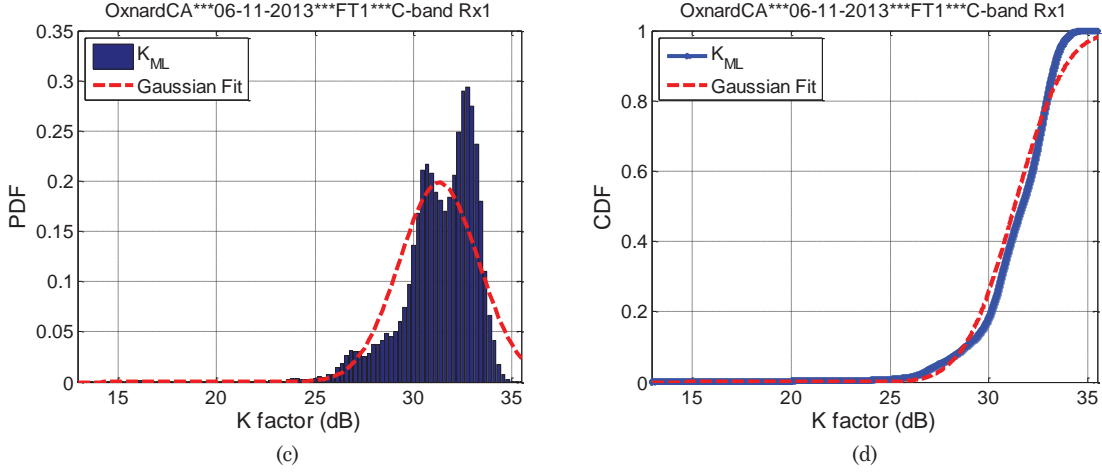


Figure C.7. K factor for C-band Rx1, over sea FT1. (a) Method I: ML fit & Method III; (b) Method II: moments; (c) PDF of Method I; (d) CDF of Method I.

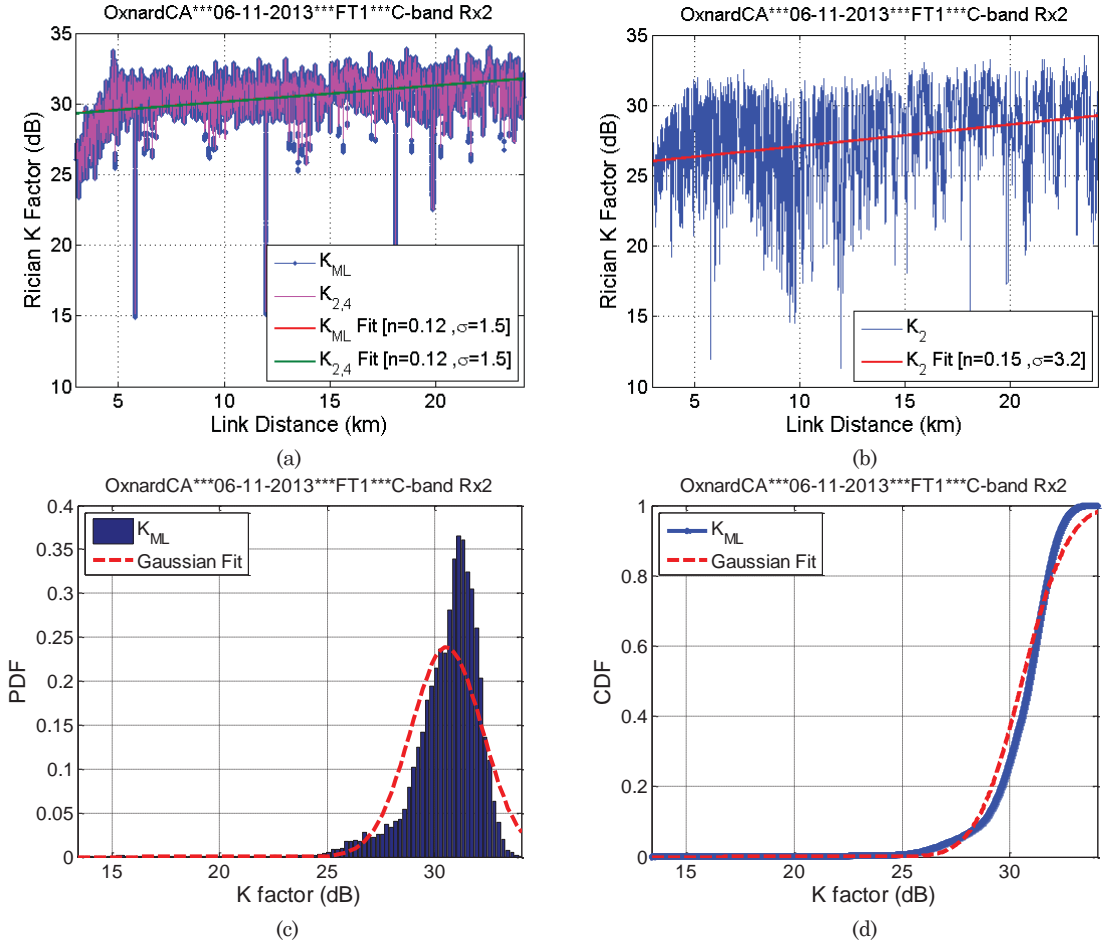


Figure C.8. K factor for C-band Rx2, over sea FT1. (a) Method I: ML fit & Method III; (b) Method II: moments; (c) PDF of Method I; (d) CDF of Method I.

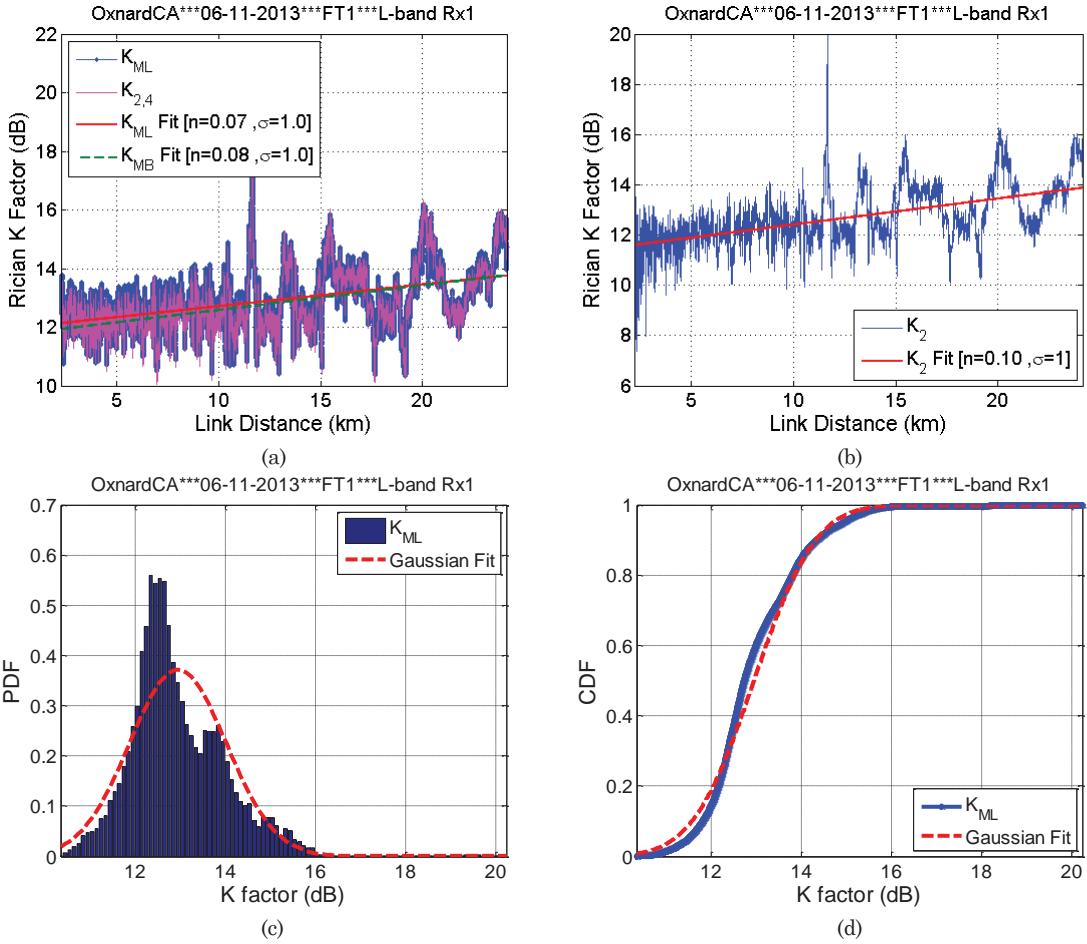
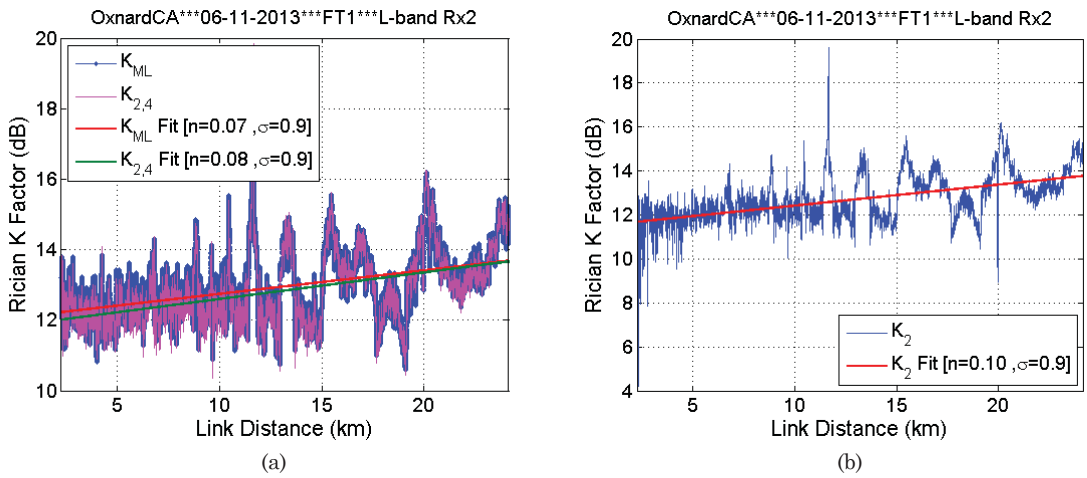


Figure C.9. K factor for L-band Rx1, over sea FT1. (a) Method I: ML fit & Method III; (b) Method II: moments; (c) PDF of Method I; (d) CDF of Method I.



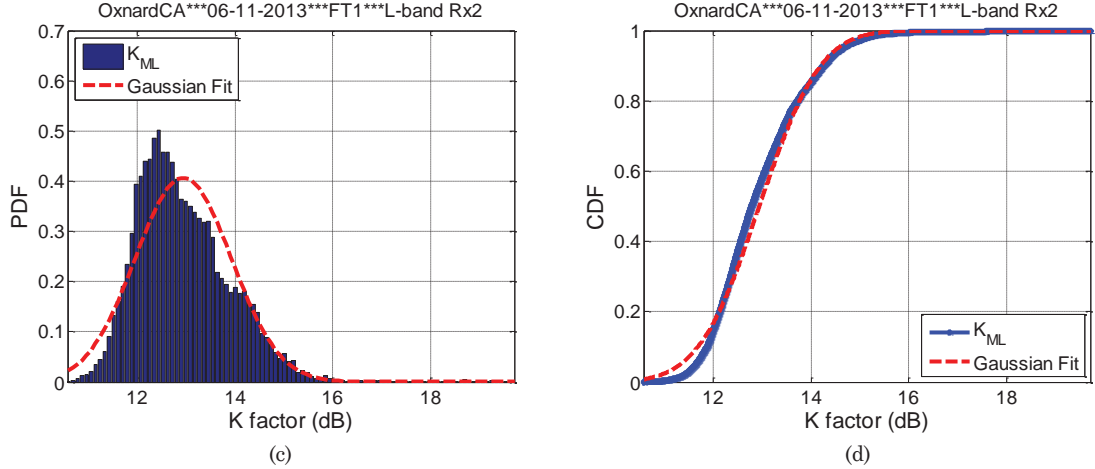


Figure C.10. K factor for L-band Rx2, over sea FT1. (a) Method I: ML fit & Method III; (b) Method II: moments; (c) PDF of Method I; (d) CDF of Method I.

Table C.1. Statistics of Ricean K factors, over-sea FT1, 11 June 2013, Oxnard, CA, with aircraft flown straight toward GS.

		C-band						L-band					
		Rx1			Rx2			Rx1			Rx2		
Moving Window Length		250λ						15 m					
Overall K factor (dB)		30.4			29.9			12.8			12.8		
Methods		K_{ML}	K_2	$K_{2,4}$									
Linear fit of K factor	A (dB)	29.1	25.1	29.0	29.0	25.6	29.0	12.0	11.4	11.8	12.1	11.5	11.9
	n	0.17	0.22	0.17	0.12	0.15	0.12	0.07	0.10	0.08	0.07	0.10	0.08
	α_X (dB)	1.7	3.4	1.7	1.5	3.2	1.5	1.0	1.0	1.0	0.9	0.9	0.9
	D_{max} (km)	3.0	3.0	3.0	3.0	3.0	3.0	2.2	2.2	2.2	2.2	2.2	2.2
	D_{Min} (km)	24.1	24.1	24.1	24.1	24.1	24.1	24.1	24.1	24.1	24.1	24.1	24.1
Statistics of K factor (dB)	Max	35.5	34.4	35.4	34.0	33.6	34.0	20.2	19.9	20.4	19.7	19.6	19.9
	Min	13.0	11.3	13.4	13.4	11.3	13.8	10.3	7.4	10.0	10.6	4.2	10.4
	Median	31.3	28.0	31.3	30.6	27.6	30.6	12.9	12.7	12.8	12.9	12.7	12.8
	μ	31.7	28.7	31.6	30.9	28.4	30.9	12.7	12.5	12.6	12.8	12.5	12.6
	σ	2.0	3.6	2.0	1.7	3.3	1.6	1.1	1.2	1.1	1.0	1.1	1.0

C.5 Discussion

The K factor for both bands is on average more than 12 dB. Although from some results (e.g., Fig. C8, C.10) it appears to increase with link distance, this is not true for all data or all flight tracks: in some cases K stays nearly constant, and in some it decreases. Since all increases or decreases are small, it is reasonable to model the mean K -factor as constant with link distance. The AG channel K factor is larger than that of terrestrial (e.g., V2V and cellular) environments. This is as expected because the LOS component is strong and the environment provides only a few, often intermittent, MPCs. Ricean K -factors for the AG channel were also estimated in [55]. In this work, the authors computed K for the VHF band over land. Values of K ranged from 2-20 dB, with a mean value of 16 dB; no other statistics were reported. From Figures C.1-C.10 and Table C.1 it is also clear that the C-band K -factors are considerably larger than those in L-band, and this is most likely due to the stronger surface-ray cancellation that occurs in L-band.

Although some reflecting objects may be present near the GS, the reflected rays and the sea surface reflection(s), as seen at the Rx antenna, arrive from nearly the same direction as that of the LOS component. A close inspection of the plots of K vs. distance also shows that the K -factor roughly follows a two-ray pattern. Figure C.11(a) shows total received power via measurements, and Figure C.11(b) shows the analytical value of received power, from the CE2R model. Figure C.12 shows the corresponding fading values from the measurements and analysis, with respect to the means. As can be seen, when the total received power (Fig. C.11) “fades” to a null, the “fading about the mean” (Fig. C.12) decreases, and a smaller variation corresponds to a larger K -factor. The absolute values of K are much larger for the analytical CE2R computation, which does not account for any noise, antenna effects, equipment variation, etc.

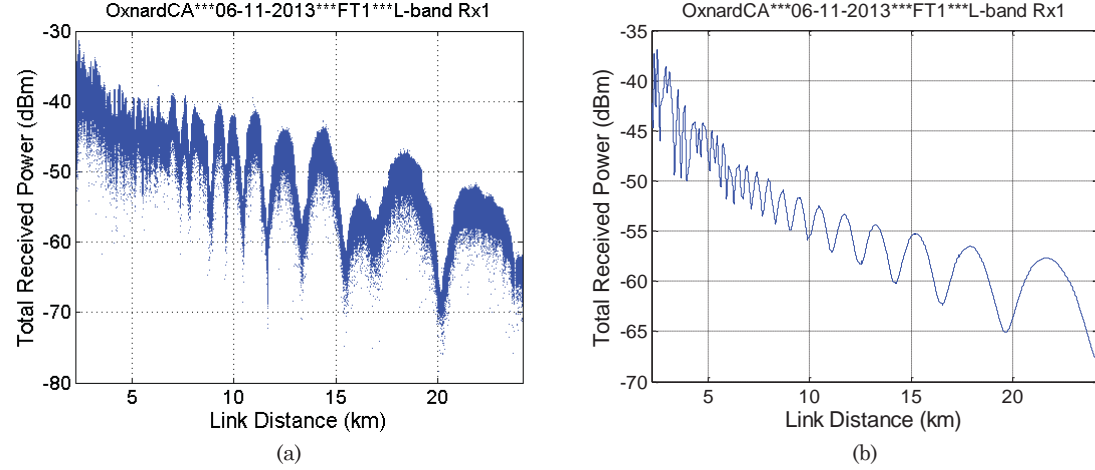


Figure C.11. Received power vs. link distance for (a) empirical data; (b) analytical CE2R.

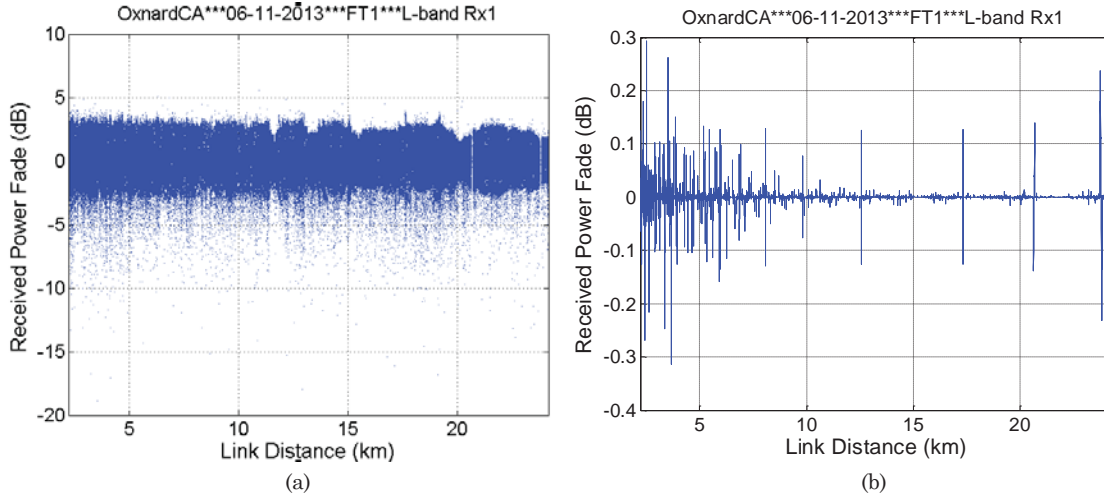


Figure C.12. Power fade, with respect to mean, vs. link distance, for (a) empirical data; (b) analytical CE2R.

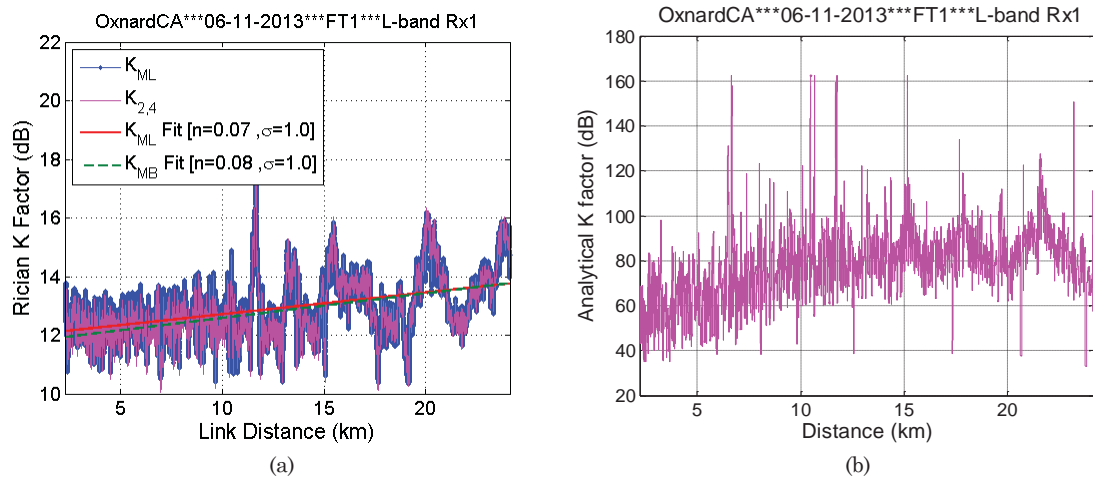


Figure C.13. Rician K factor vs. link distance for (a) empirical data; (b) analytical CE2R.

Appendix D: PDP Update Rate

The rate at which power delay profiles (PDPs) are recorded by the sounder is not a constant. This is due to the fact that the actual data recording rate and data transfer rate inside the sounder is slower than the rate at which correlation measurements are made. The sounder's PDP length is 2046 samples (two samples per the 1023 chips of the underlying *m*-sequences). The actual time duration of a 2046-sample PDP is 204.6 microseconds in L-band, and 20.46 microseconds in C-band, from the 200 ns and 20 ns chip durations for these bands, respectively. The aircraft's flight recorder gathers GPS information, from which a UNIX timestamp is generated. The UNIX timestamp is recorded for each PDP, and the accuracy is on the order of 10^{-7} seconds. If t_i is the UNIX timestamp of the i^{th} PDP, the recording duration for one PDP Δt_i is $t_i - t_{i-1}$. The minimum recording duration Δt_{\min} is 333.31 microseconds (reciprocal of 3002 Hz), which is much larger than the time duration of any single PDP (for either band).

Since a 25 (or 30) dB threshold is used in the air-ground channel measurements, only a few samples above the threshold are recorded when the channel contains a line-of-sight (LOS) component and very few multipath components. If the LOS is blocked, and/or many multipath components are present, more samples must be recorded, hence the recording time for such a PDP increases. We have found that the practical PDP recording duration can only be integer multiples of Δt_{\min} , i.e.,

$$\Delta t_i = N \Delta t_{\min}, \quad (\text{D.1})$$

where N is a positive integer. The PDP update rate K is the reciprocal of the PDP recording time duration Δt :

$$K_i = \frac{1}{\Delta t_i} = \begin{cases} 3002 \text{ Hz} & N = 1 \\ 1501 \text{ Hz} & N = 2 \\ 1000 \text{ Hz} & N = 3 \\ 750 \text{ Hz} & N = 4 \\ 600 \text{ Hz} & N = 5 \\ \dots \dots & \end{cases} \quad (\text{D.2})$$

Since the PDP update rate is the reciprocal of the recording time, the average update rate \bar{K} cannot be

$$\bar{K} = \frac{M}{\sum_{i=1}^M \frac{1}{K_i}} \quad (\text{D.3})$$

where M is the number of PDPs.

The PDP update rate vs. link distance for the four sounder receivers is shown in Figure 1. These results are based on flight track (FT) 2, with flight straight away from the ground site (GS), taken over Lake Erie on 22 October 2013. The histogram of PDP update rate for the C-band Rx1 is shown in Figure D.2, and statistics of the PDP update rate are provided in Table D.1. The average update rate is approximately 2.9 kHz, which is close to the maximum of 3 kHz. The percentage at the maximum value is more than 97%. Note that FT2 is one of the “cleanest” FTs, which always has a clear LOS, hence the number of samples in each PDP is relatively small. For FTs (or segments of FTs) in which the LOS is blocked, e.g., FTs in Telluride where the LOS was blocked by mountain ridges, or FTs with a large number of multipath components, the number of samples per PDP is expected to be much larger, and the PDP update rate is consequently expected to be much smaller.

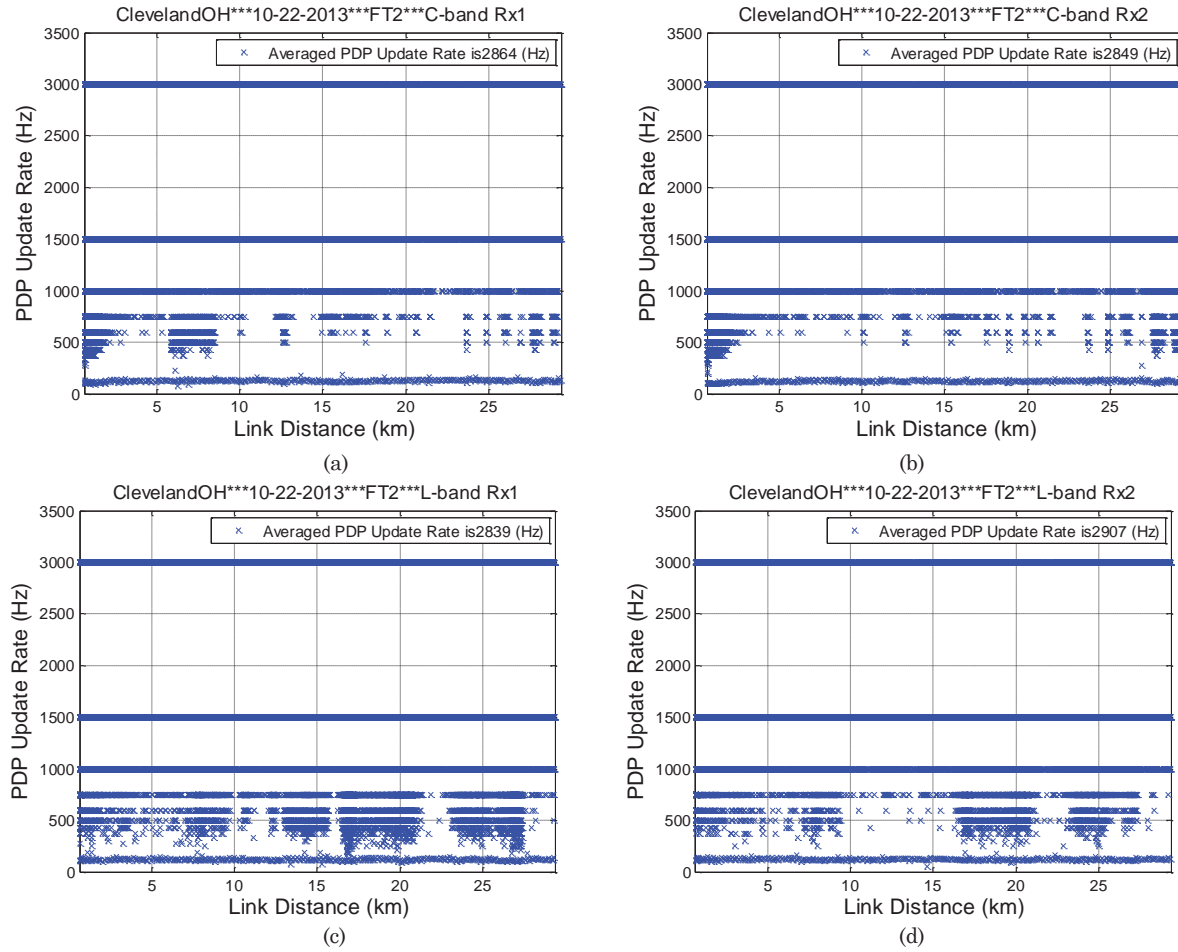


Figure D.1. PDP update rate for FT2 (straight away from GS) over Lake Erie, 22 October 2013. (a) C-band Rx1; (b) C-band Rx2; (c) L-band Rx1; (d) L-band Rx2.

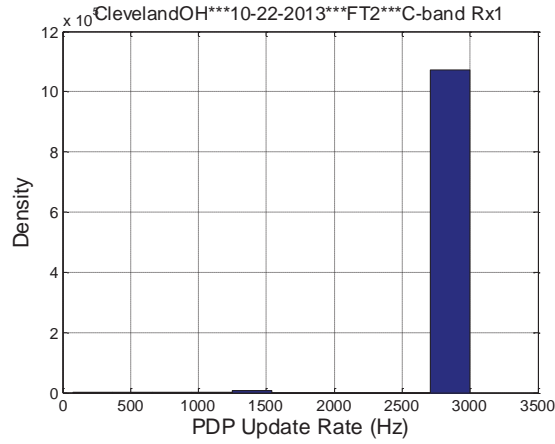


Figure D.2. Histogram of PDP update rate for Figure D.1(a).

Table D.1. Statistics of PDP update rate for over-freshwater flight, FT2, Lake Erie, 22 October 2013 (see also eq. (D.2)).

Band Receiver	# of PDPs M	Time duration Δt (s)	Average update rate K (Hz)	% with $N=1$	% with $N=2$	% with $N=3$	% with $N=4$	% with $N=5$	
C	Rx1	1,149,310	401.31	2864	97.88%	0.88%	0.68%	0.39%	0.09%
	Rx2	1,143,111	401.26	2849	97.56%	1.01%	0.84%	0.43%	0.08%
L	Rx1	1,139,534	401.32	2839	97.49%	1.27%	0.59%	0.34%	0.11%
	Rx2	1,166,408	401.29	2907	98.55%	0.81%	0.34%	0.16%	0.04%

